University Of Southampton

Faculty Of Natural and Environmental Sciences

School of Chemistry

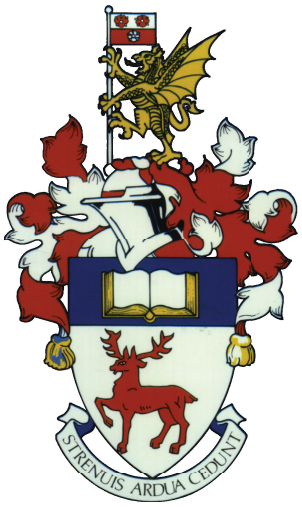

Nuclear Magnetic Resonance of Novel Type-II Superconductors

Richard William Bounds

Thesis for the degree of Doctor of Philosophy

August 31, 2016

UNIVERSITY OF SOUTHAMPTON

ABSTRACT

FACULTY OF NATURAL AND ENVIRONMENTAL SCIENCES
School of Chemistry

Doctor of Philosophy

NUCLEAR MAGNETIC RESONANCE OF NOVEL TYPE-II SUPERCONDUCTORS

Richard William Bounds

Nuclear magnetic resonance was crucial in the vindication of the theory of superconductivity in 1957, it still continues to provide vital information today in the ongoing challenge that is the determination of the mechanism for type-II superconductors.

This forms the basis of this piece of work, which details the preparation, characterisation and cryogenic measurements of two new superconductors based on the cage like fullerides. In light of recent synthetic developments it has now become possible to encapsulate small molecules inside the fullerene cage, which may then be doped with alkali metals to form the superconducting materials. In this thesis the encapsulated molecules are water and hydrogen, and the topic is the study of normal and superconducting states from their response to the magnetic resonance technique.

The materials are made using a vapour doping method, and their characterisation suggests high purity, with the superconducting transition temperatures modestly affected by the larger water molecule. The spectral lineshape suggests a unique window into the vortices in the superconducting state from both endohedral molecules, and the magnetic shift decays concomitant with s-wave symmetry of superconducting gap. The nuclear spin lattice relaxation rate is vastly different between molecules, highlighting the unique information available from these new probes.

Magnesium diboride is also studied using a sample enriched with carbon-13, which allows a new window into this multiple-band superconductor. Measurements of the lineshape reveal the role of carbon as a flux pinning centre, and combined with Knight shift measurements suggest the doping procedure favours the chemical substitution scenario. Also ab-initio calculations yield results which match this scenario and agree well with experimental values.

CONTENTS

LIST OF FIGURES

DECLARATION

I, Richard Bounds declare that the thesis entitled *Nuclear Magnetic Resonance on Novel Type II Superconductors* and the work presented in the thesis are both my own, and have been generated by me as the result of my own original research. I confirm that:

- this work was done wholly or mainly while in candidature for a research degree at this University;
- where any part of this thesis has previously been submitted for a degree or any other qualification at this University or any other institution, this has been clearly stated;
- where I have consulted the published work of others, this is always clearly attributed;
- where I have quoted from the work of others, the source is always given. With the exception of such quotations, this thesis is entirely my own work;
- I have acknowledged all main sources of help;
- where the thesis is based on work done by myself jointly with others, I have made clear exactly what was done by others and what I have contributed myself;
- none of this work has been published before submission

Signed:.....

Date:.....

PUBLICATIONS

The following works have been published in the field of materials science

- Krachmalnicoff, A.; Bounds, R.; Mamone, S; Alom, S.; Concistre, M.; Meier, B.; Horsewill, A. J.; Shugai, A.; Nagel,U.; Room, T.; Carravetta, M.; Levitt, M. H.; Whitby, R. J. The dipolar endofullerene HF@C_{60}. Nature Chemistry, Accepted.

- Sardar, K.; Bounds, R.; Carravetta, M.; Cutts, G.; Hargreaves, J. S. J.; Hector, A. L.; Hriljac, J. A.; Levason, W.; Wilson, F. Sol-Gel Preparation of Low Oxygen Content, High Surface Area Silicon Nitride and Imidonitride Materials. Dalt. Trans. 2016, 45, 5765–5774.

- Krachmalnicoff, A.; Bounds, R.; Mamone, S.; Levitt, M. H.; Carravetta, M.; Whitby, R. J. Synthesis and Characterisation of an Open-Cage Fullerene Encapsulating Hydrogen Fluoride. Chem. Commun. 2015, 51, 4993–4996.

- Dzielendziak, A. S.; Blake, J. I. R.; Bounds, R.; Wilkinson, K. A.; Carravetta, M.; Chambers, A. R.; Skylaris, C.-K.; Raja, R. Spectroscopic Chemical Insights Leading to the Design of Versatile Sustainable Composites for Enhanced Marine Application. RSC Adv. 2015, 5, 101221–101231.

- Cholerton, M. E.; Potter, M. E.; Kezina, J.; Bounds, R.; Carravetta, M.; Manzoli, M.; Gianottii, E.; Lefenfeld, M.; Raja, R. The Role of Isolated Acid Sites and Influence of Pore Diameter in the Dehydration of Ethanol. ACS Catal. 2014, 4, 4161–4169.

ACKNOWLEDGEMENTS

There are many people that I wish to thank that I have met and worked with over the course of my PhD, I will try to do this justice but I apologise if I miss anyone out!

Firstly, I would like to thank and acknowledge my supervisor Marina Carravetta, for her help and patience during the process. Marina has been an absolutely fantastic supervisor, she has given me great academic freedom to pursue and learn things that I was interested in, and always supported me throughout. I have really learnt a lot from her and cannot thank her enough. Also the rest of the Carravetta group, for sharing with me the trials and tribulations of doing a PhD. I'd like to thank Ibraheem Haies for his friendship and all the engaging discussions we had about our cultural differences, I wish you all the best for the future. James Jarvis who has been a great friend, for the countless hours we've spent laughing about everything, all the NMR theory we have hashed through together and the great conferences we attended. Emma Withers for getting me into martial arts, climbing and for all the office antics. I would also like to thank Maria Concistre for her good humour and friendly attitude. There is also Phil Williamson, his group, and Stuart Findlow from the Bio-NMR side. They've been great people to know, both for experimental advice and for their jovial natures, I especially enjoyed the conference to the Peak district.

Malcolm Levitt and his group have been a brilliant bunch to get to know, not least for the fascinating science that they do, but also they are an interesting and eclectic group that I've made many friends from. I thank Benno Meier, Stefan Glöggler, Stuart Elliot, Karel Kouril, Gabriele Stevanato, Graeme Finch and Zenawi Welderufael and Giuseppe Pileio. I'd like to thank Malcolm for his interest and help in my work, both academically and otherwise throughout the last year. From discussing all the ideas on the fulleride work, to teaching me a great deal about solid-state NMR from his lectures and general advice which is always incredibly clear and interesting. Ole Johannessen has given me a great deal of experimental help, thanks for fixing all the probes I broke and for all the humorous times in the lab we shared! Ilya Kuprov for his lectures, all his help with the simulations and his great stories in the pub. I would also like to thank Salvo Mamone, it was a pleasure to work with him on so many occasions and he taught me a great deal about science in many areas.

I've been lucky to visit the national NMR facility at the University of Warwick on many occasions. I'd like to thank all the people I've met there and Dinu Iuga for all his experimental help.

All my starting materials came from Richard Whitby and his group, Shamim Alom,

Andrea Krachmalnicoff and John Grasvik, who I cannot thank enough for their time and effort. They helped me on so many occasions and dedicated their precious time explicitly to provide material for my work, thanks guys! Also I want to thank Shamim again, for all the disasters he helped me out of. I must also thank Mark Denning for the invaluable advice he gave me on the synthesis of the fullerides.

Most of my experimental work was carried out in Tallinn. I would like to thank Raivo Stern and Ivo Heinmaa for letting me use their facilities. I would also like to further thank Ivo for the incredible amount of help he has given me over the last few years, not least for the long hours I put him through during the experimental sessions, but also for the engaging discussions and welcoming nature that he always has. I'd also like to thank my table tennis rival, Alex Leitmae, for all the experimental help he has given me and all the great days and nights out in Tallinn.

Finally and most of all, I would like to thank my parents for helping me pursue this difficult challenge and supporting me in so many ways. I've always been able to count on them for their love and support especially during this truly tough but incredibly rewarding period of my life, I cannot thank them enough for their support through it. I also thank my brother and sister, who are always there to lift my mood, and my dog Rocky, for being the sounding board for all my ideas.

Dedicated to my parents

CHAPTER

ONE

INTRODUCTION

Nuclear magnetic resonance (NMR) was a key technique in the vindication of the BCS theory of Superconductivity in 1957[1]. Hebel and Slichter[2] first observed nuclear spins connected to the superconducting state using a field cycling technique which allowed them to cycle a magnetic field from 0-500 Gauss in 1 ms. Field cycling allowed polarisation of the nuclear spins in field, and the evolution of the spins in the superconducting state in zero field. This was necessary because type-I superconductors expel an applied magnetic field, an issue for NMR experiments. They used a sample of Al for their experiments, which has a low T_c (1.2 K) but crucially has a long enough relaxation time, which allowed for the field switching time.

The theory of superconductivity at this time was still under development, so it was not clear what might happen if one attempted to indirectly observe the superconducting state using NMR. They expected that if they measured the relaxation rate of the nuclear spins, then the rate should be slower in the normal state than in the superconducting state. This was based on the idea of an energy gap opening at the Fermi-level in the superconducting state, which was a known concept at this time. However, they found that the rate *increases* just below T_c by a factor of two. The explanation they gave was that the energy gap opens at the Fermi-level pushing electronic states up and down. This piling up of the density of states near the edges of the energy gap leads to an increase in the relaxation rate, because T_1 is related to the integral of the square of the density of states.[3] This fit neatly into the Bardeen Cooper Schreiffer (BCS) theory of superconductivity which had been developed at around the same time. It is now accepted that the BCS theory of superconductivity is a good description of the mechanism of type-I superconductors.

The discovery of type-II superconductors has unveiled many new questions, mainly relating to the high T_c values and appropriateness of BCS theory to their description. Although some type-II materials do follow BCS[4], there are a range of superconductors in which the theory breaks down[5, 6], it is thought that these materials are described by a different theory and there is currently a great deal of ongoing experimental and theoretical work in an attempt to unveil it. A description of this mechanism may

allow higher T_c superconductors to be developed, and perhaps even one day room temperature superconductors[7], an achievement that would be truly revolutionary in terms of the current landscape of the energy economy. It is therefore of interest to study type-II materials using novel methods and samples, with the aim of extracting information that may aid the determination of this mechanism.

NMR is a particularly powerful tool in this venture as it has the somewhat unique ability to probe locally. One may select individual elements and this may give local or bulk information depending on the nuclei selected and its distribution across a lattice. This is especially advantageous in the study of superconductivity because the electron-phonon coupling interaction varies between elements and atomic sites. A example of this is in magnesium diboride, which has two superconducting gaps arising from two different electron bands coupling to the same phonon mode.[8] In this specific case different NMR nuclei reside in each band and NMR measurements of the superconducting gap yield values reflective of this. In order to take advantage of the local resolution afforded by NMR, one must ensure the nuclear isotopes are NMR active, in some cases a material must be isotopically enriched, in others the isotopes natural abundance may already suffice.

NMR is not limited to materials that follow the electron-phonon coupling mechanism though, for example it has provided key information regarding spin density[9, 10] and charge density[11] waves, which may underpin the type-II mechanism. Other relevant NMR studies elucidating type-II materials include those investigating their phase diagram, which is not limited to just metallic and superconducting states. There may also be antiferromagnetic spin fluctuation[12] and pseudogap regions[13] as well as Mott-insulators[14], Jahn-Teller metals[15] and more.

It is of interest then to study novel materials using NMR and this forms the basis of this thesis, which details the investigation of two type-II superconductors, Rb_3C_{60} and MgB_2. The motivations for these particular materials are now outlined in detail.

1.0.1 Motivation for studying Rb_3C_{60}

The Alkali-doped fullerides have the general composition A_3C_{60}, where A=Rb, K or Cs. They have the highest superconducting transition temperatures of the molecular superconductors ($T_c \approx 39$ K) and the general consensus is that they follow the BCS theory of superconductivity, in which the electrons are coupled in pairs mediated by the phonons. This came about from a highly influential publication outlining a theory and suggesting the maximum T_c was around 30 K.[16] This value was vindicated experimentally shortly afterwards.[17] After this, the problem was considered solved, even though there was still questions regarding the physical mechanism. There were

for example different spectroscopic techniques, that indicated different phonon modes responsible for the electron pairing and some questions regarding the isotope effect, as discussed in section 3.4.1.

This situation was slightly altered after the discovery that the fullerides have a Mott-insulating magnetic state and can transition to a metallic and superconducting one.[14, 18–21] This is an interesting point because it raises the question of how the conventional s-wave superconductivity can exist close to the Mott-insulating state without being suppressed, and may even be enhanced, by the strong repulsive interactions.[22]

The majority of previous NMR studies, have focused on ^{13}C NMR and a range of metallic nuclei such as ^{87}Rb, ^{133}Cs or ^{39}K NMR, depending on the material. In most of these works, the appropriateness of BCS theory is usually ratified, this is discussed in more detail in section 3.3 . However recent developments involving cryogenic magic angle spinning (cryoMAS) allow one to spin at cryogenic temperatures, which extends the temperature range in which one may average the NMR interaction anisotropies and record high resolution spectra. This has opened a new avenue of possible NMR experiments, for example a recent cryoMAS study has shown how important the Jahn-Teller effect is to the superconducting state.[15]

Clearly there is more to learn about these materials beyond the standard techniques and NMR nuclei already used to probe the fullerides, it is therefore of interest to design NMR experiments which can provide this information either through new experimental techniques such as cryoMAS or by designing new samples.

One area of chemistry which is rapidly developing, and may enhance the information gained by NMR on the fullerides is the synthesis of endofullerenes.[23, 24] Recent success in synthetic organic chemistry have expanded the cage like fullerenes to allow encapsulation of atoms and small molecules, known as atomic and molecular endofullerenes respectively. These materials are stable analogues of the fullerenes (or fullerides), but contain an extra atom or molecule which is trapped inside the C_{60} cage. The enclosed atom or molecule is sometimes referred to as the guest species and is not bonded to the cage chemically. Due to the disconnected nature of the guest species, these materials are sometimes known as nano-laboratories, as they allow the study of isolated molecules.

Endofullerene chemistry and physics is developing at a fast pace, it has already given a fascinating insight into some physical processes such as the Ortho-Para conversion in H_2O encapsulated inside a fullerene cage[25]. Superconductivity in the endofullerides remains a relatively unexplored area. There has only been a couple of studies which have detailed the reaction of the endofullerenes with an alkali metal to form endofulleride superconductors.[26] In these studies, atomic endofullerides were synthesised and investigated using powder x-ray diffraction (pXRD) and the physical property

measurement system (PPMS). This is discussed further in section 3.3.4

There has not yet been any investigations using NMR, which can selectively probe the guest species (if NMR active). This is probably due to the fact that the atomic endofullerides that have been already made, lack an NMR 'friendly' nucleus. For example $K_3(Ar@C_{60})$ exists but ^{39}Ar NMR is very difficult to study due to the low abundance and radioactive nature of the isotope. There are other atomic endofullerenes which may be reacted with an alkali metal, and in principle one may select relatively more favourable NMR isotopes such as Y@C60, La@C60 and Ba@C60. Although there are some issues with these NMR nuclei in terms of their sensitivity, (some have low gyromagnetic ratios), in the end the most inhibiting step in the study of these superconductors is accessibility to the starting materials, which can often be only a few mg, and this makes subsequent reaction with alkali elements extremely difficult.

In light of these issues, one would ideally want an endohedral NMR nucleus that had a high abundance and a large gyromagnetic ratio, but also the preparation of the endofullerene should give a high enough yield to facilitate further reaction with alkali metal. These problems are both solved by the use of molecular endofullerenes, which are fullerenes which can encapsulate small molecules such as H_2O, H_2 and HF. These molecules have the benefit of containing the ^1H nucleus which satisfies all conditions just given. The preparation of molecular endofullerenes also yields 10's of mg, which is scalable depending on how much is required.[27]

The combination of NMR and endohedral fullerides is a potentially huge research area to explore because of the many combinations of molecules that may be used to probe and alter the electronic structure. But there is no precedent and it is unknown how the guest species will behave in terms of its NMR properties, such as Knight shift and T_1 measurements as a function of temperature. Questions that immediately arise are those related to the effect that an encapsulated guest atom or molecule would have on the superconducting state. Studies on $K_3(Ar@C_{60})$ already suggest that the endohedral component does influence the C_{60} cage, and this manifests through a shift in T_c.[26]

The two encapsulated molecules (H_2O and H_2) studied in this thesis are held inside molecules of C_{60} and the NMR experiments focus around the ^1H nucleus. The principle aim is to investigate the normal and superconducting states using these new endohedral NMR probes, and also evaluate their usefulness in the study of the normal and superconducting states of the fullerides. There are also some more specific points to address which are now outlined.

The synthesis of the molecular endofullerides has never been attempted and therefore it is an open question whether the typical alkali fulleride synthesis procedures will be appropriate. The bulk properties are also of interest, for example how the endohe-

dral component affect the T_c and lattice parameters. These properties may be probed using standard methods, i.e. Vibrating sample magnetometer as part of a Physical Property Measurement System (VSM-PPMS) and pXRD

Other properties that may be studied are those related to NMR, for example the extent to which the ^{13}C and ^{87}Rb NMR is altered, and if the ^{1}H NMR is sensitive to the superconducting state. The fullerides show a temperature independent electronic susceptibility, verified through electron spin resonance (ESR) and ^{13}C NMR measurements of Knight shift and Korringa product. In contrast ^{87}Rb NMR shows a temperature dependent magnetic shift, which often indicates the electronic susceptibility varies (through modification of the Knight shift).[28] It is currently unknown where this temperature dependence comes from, and measurements on other NMR active nuclei that occupy similar locations (^{133}Cs on Rb_2CsC_{60}) lead to similar effects. An endohedral component studied by NMR should probe inside the C_{60} cage and it is unknown how the susceptibility varies here, although it is likely that the variation should be similar to the susceptibility at the carbon atoms. Therefore a point of interest is how similar the ^{1}H and ^{13}C NMR shifts follow the same trend as a function of temperature, as the shift and susceptibility are correlated as discussed in section 4.8.2. This is a unique piece of information which can only be extracted using endohedral ^{1}H NMR.

An isotope effect was found to be present for ^{13}C and almost negligible for ^{87}Rb. This indicates an electron-phonon coupling mechanism and the importance of intramolecular phonons, however other techniques have suggested that the intermolecular phonons play are the most important. An endohedral NMR component might be able to investigate this further, as it may be coupled to the phonon modes on the C_{60} cage. Another more general point is the difference between the H_2O and H_2 encapsulated molecules, specifically in terms of electric dipole moment, size and interaction with the C_{60} cage. Is there a difference in the NMR properties of these molecules in the normal and superconducting state?

Finally, the Hebel-Slichter coherence peak has been observed using ^{13}C and ^{87}Rb NMR, which is strong evidence of an s-wave superconducting gap, and of the BCS mechanism. There has been no indication of the coherence peak at fields above 5 T and theoretical predications have suggested the peak is inhibited due to damping effects, this is discussed fully elsewhere[8]. It is worth investigating the NMR relaxation properties of an endohedral molecule to test for the presence of the coherence peak, with a comparison to literature. It is unknown if there is a connection between the endohedral species and the conduction electrons, and if the opening of the superconducting gap can be observed. If there is a coherence peak, then this is strong evidence of a BCS s-wave superconductor and is therefore a valuable piece of information.

1.0.2 Motivation for studying MgB_2

MgB_2 is a relatively new superconductor, discovered in 2001[29]. It has a high T_c (39 K) for a metallic superconductor and importantly it has less serious issues in terms of anisotropy and weak links at the grain boundaries which are prevalent in the cuprates[30]. Additionally MgB_2 is malleable, easy to synthesise and readily available. It is for these reasons that a large amount of both fundamental and applied research has been conducted on this superconductor, and applications are expected at liquid hydrogen temperatures, and MgB_2 magnets for MRI have already been implemented.[31] The work carried out in this thesis addresses two issues relating to MgB_2, the first is regarding the distribution of carbon in the doped sample and the second is more generally testing the applicability of BCS superconductivity. This is now outlined in greater detail.

There has already been fabrication of MgB_2 into tapes and wires toward practical uses and a key parameter to consider is the maximum current that may be applied (J_c). As this depends on a balance between the Lorentz and pinning forces, there has been a great deal of interest on the pinning mechanism. In general if one is able to increase the pinning, J_c is also increased. One typical method of increasing the amount of pinning is by chemically doping with carbon, which is achieved by addition of SiC[32] or B_4C[33]. The addition of C atoms is thought to cause substitution with B sites and this causes the structure of the boron graphite-like lattice to become distorted. The result of this is that the a-axis length is reduced and the c-axis is left unaffected. The improvement of J_c at high fields arises from the enhanced upper critical field (H_{c2}), which is brought about by the reduced coherence length due to the distortion of the crystal structure from C substitution[30]. Recent studies have shown that it may be boron vacancies which cause the enhancement of J_c not C substitution, and therefore there is still no full consensus on the role of carbon in MgB_2 superconductors. If doping is done with a ^{13}C labelled carbon source, then one may use NMR to investigate this process in more detail. The specific points to address are the extent to which carbon is substituted with boron and if there is significant carbon build up at the interstitial grain boundaries.

Beyond the role of carbon as a flux pinning centre, it is also interesting to study the effect on the superconducting state, specifically the extent to which the two superconducting bands are preserved on doping. This has also been studied before using ^{27}Al NMR[34–36] It has been noted previously that when doped with carbon, the E_{2g} phonon mode is stiffened, leading to a drop in T_c, but the two distinct gaps remain intact up to a critical doping point. This has been reported up to $x = 0.132$ in single crystals and there has been no reported gap merging in polycrystals.[37] ^{13}C NMR

offers a tool to investigate this by studying NMR properties which are sensitive to the opening of the gap, for example one may measure the normalised spin susceptibility. This has not yet been measured due to the different superconducting bands where the NMR active nuclei reside, which have different susceptibilities, and therefore one cannot use the usual procedure as discussed in section 4.3. This is not the case for carbon, which is thought to reside in the same band as boron, thereby allowing one to extract the gap ratio and also test for two superconducting gaps.

In general the superconducting state of MgB_2 is thought to be well described by the BCS theory of superconductivity. There are however some open questions to address, such as the mechanism which connects the two superconducting bands and the presence of the Hebel-Slichter coherence peak in the T_1 just below T_c. The two superconducting bands are thought to be connected by interband scattering which can be thought of as a energy transfer process between quasiparticles. It is thought that adding carbon enhances scattering between bands, which can lead to a more isotropic superconducting gap. In other words, the double gap becomes an averaged single gap and this is detectable using NMR methods. There has been a great deal of ambiguity regarding the Hebel-Slichter coherence peak. In general it has been noted to be absent, but there are ^{27}Al NMR studies which report it. It is interesting to follow the relaxation behaviour from the ^{13}C NMR probe because carbon is supposed to reside in the boron sublattice. If there is a mechanism that suppresses the peak for boron, then carbon might also have a reduced coherence peak.

This thesis investigates a sample of ^{13}C doped MgB_2, it is the first study using ^{13}C NMR. The main aspect of this investigation was an attempt to discover more about the nature of the dopant site, for example to its chemical position in the lattice, the nature of pinning in the superconducting state and effects on the NMR parameters such as $1/T_1$ and Knight shift in the normal and superconducting state. Boron and carbon are thought to be part of the same graphite-like lattice, therefore an additional benefit is the subtraction of the diamagnetic contribution to the decay of the Knight shift. As mentioned this can give information about the spin-susceptibility which is sensitive to one or two superconducting gaps. This has not been done before because of the very different lattice positions of other available NMR nuclei, such as ^{27}Al (If doped with Al) and ^{25}Mg which sit above the boron planes.

CHAPTER

TWO

INTRODUCTION TO MATERIALS

2.1 The Fullerides and Rb_3C_{60}

In 1985 carbon was seen to exhibit a new molecular structure known as C_{60} or fullerene[38]. It has a quasi spherical structure made up of 20 hexagons and 12 pentagons with a carbon atom at each vertex, shown in Fig.2.1. In a solid, C_{60} packs into a FCC lattice with a molecule centered at each point, with lattice constant a=14.17Å. This phase is maintained above ∼260 K and the C_{60} molecule rotates isotropically about its centroid and therefore the time-averaged shape of C_{60} is a simple sphere. This is also similar to the solid-state NMR reference compound adamantane, which has a similar averaging effect. In general these materials are known as plastic crystals and they are characterised by their narrow line widths in NMR spectra due to this intrinsic motional averaging of the NMR interactions such as the homonuclear dipolar and chemical shift anisotropy terms.[39] As C_{60} is cooled below 260 K, there is a first order phase transition[40] which causes the molecules to begin ratcheting among high symmetry orientations. This change in behaviour manifests itself in physical properties such as X-ray diffraction and magnetic susceptibility. The molecular rotation ceases below 20 K from evidence of an Einstein mode[41] in specific heat measurements . The molecules then freeze randomly, in one of two molecular orientations, this is known as merohedral disorder.

Each of the carbon atoms in C_{60} are bonded with sp^2 hybridised σ bonds similar to graphite, the remaining 60 2p atomic orbitals form a delocalised π system similar to the bonding in benzene. The lowest unoccupied molecular orbital (LUMO) is triply degenerate and can be filled by up to 6 additional electrons per C_{60}.[21] A diagram of this progression is given later in Fig. 2.4.

Fullerenes are usually synthesised using the arc discharge method, this involves the use of two graphite electrodes, which are immersed in an inert atmosphere such as He. A direct-current arc voltage is applied across the electrodes and fullerene is deposited in the form of soot inside the chamber.[42]

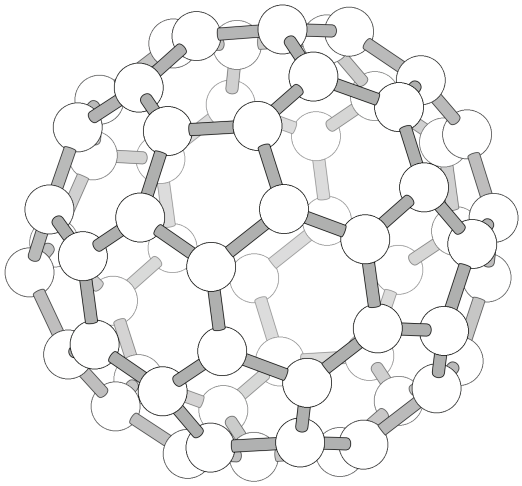

Figure 2.1: Structure of C_{60}

2.1.1 Endohedral Fullerenes

New forms of synthetic chemistry have allowed expansion of the field of fullerenes to encompass new materials, known as endohedral fullerenes. These new materials take advantage of the 'void' inside the C_{60} to house new atoms and molecules. Endohedral fullerenes are extremely interesting materials, not least because of their appealing structure, they also allow testing of various physical phenomena and have been described as nano-laboratories.[43]

The idea of encapsulating atoms inside has been achieved numerous times in the past with metal atoms, where the formation of C_{60} and entrapment of host species, occurs simultaneously. Metal atoms and C_{60} are vaporised at the same time so the atoms are trapped as the carbon cages form. This has been done with noble gases[44] to form metallofullerenes and with He and N to produce small non-metallic endofullerenes[45]. However the yield was often low, sometimes less than 0.4 %.

An alternative approach is the use of 'molecular surgery' which uses chemical reactions to open an orifice in the carbon cage and then additional reactions are usually done in order to widen the orifice. At this point various molecules can be inserted into the vacant cavity aided by elevated temperatures and pressures. [46] Initially the compounds were not closed after this point, and the guest molecules were chemically stable inside the open-caged fullerenes.

This procedure eventually culminated in an encapsulation of H_2 inside an open cage fullerene in 2003[47] with 100 % incorporation in the cages, showing the potential to enclose molecules. [48]

Soon after this accomplishment, an NMR investigation took place on the open

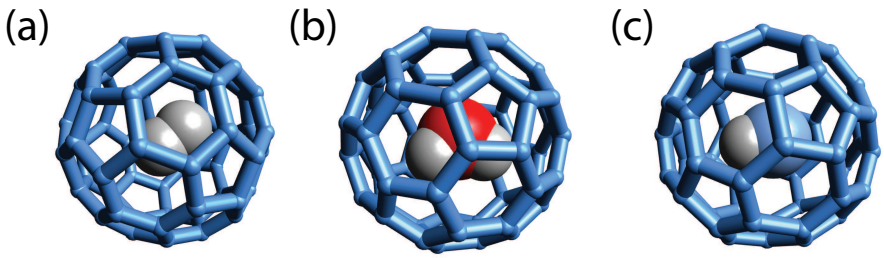

Figure 2.2: Illustration of endohedral molecules (a) $H_2@C_{60}$ (b) $H_2O@C_{60}$ (c) $HF@C_{60}$

caged fullerene, denoted H_2@ATOCF.[49] The authors were able to estimate the H_2 rotation correlation time, given to be 2.3 ps at 295 K and 15.3 ps at 119 K. They observed a small anisotropy from variable temperature measurements of the dipolar coupling. This indicates the motion of the endohedral H_2 is quite small, and that the unsymmetrical orifice only slightly affects the rotational motion. In 2005, the closure of the open caged fullerene was achieved by organic synthesis allowing the production of $H_2@C_{60}$[23] and also later in 2011 $H_2O@C_{60}$.[24]

The metal atoms inside metallofullerenes are often treated classically as they are relatively large. The endohedral component in the molecular endofullerenes is smaller and therefore quantum effects are important. The molecules are confined within a tight cavity, and they have a small mass and moment of inertia. Therefore the effects which arise from translation and rotational quantisation are quite large. For example in $H_2@C_{60}$ the energy spacing between the two lowest translational levels is 260 K, and the spacing between rotational levels is 175 K.[50, 51]

The trapped molecules are then better thought of in quantum mechanical terms, as a trapped 'molecular wave' as described previously[52]

2.1.2 Alkali Fullerides - Structure and electronic properties

Doping C_{60} with alkali atoms induces metallic behaviour, with almost complete charge transfer from the metal atoms to the C_{60} cages. The electrons are delocalised as in insulating C_{60}. On filling of the t_{1u} bands of C_{60} with additional electrons, insulating C_{60} becomes metallic. These class of materials are known as the fullerides and there are a variety of different stoichiometries, with the general form A_nC_{60}. A can be various alkali elements such as Rb, Cs and K.

The fullerides have a large amount of orientational disorder, at low temperatures there are two inequivalent C_{60} sites, oriented at 90° to each other. This is known as merohedral disorder and manifests through the observation of two inequivalent tetrahedral sites in ^{87}Rb NMR, which arises from the distinct local orders of C_{60} which

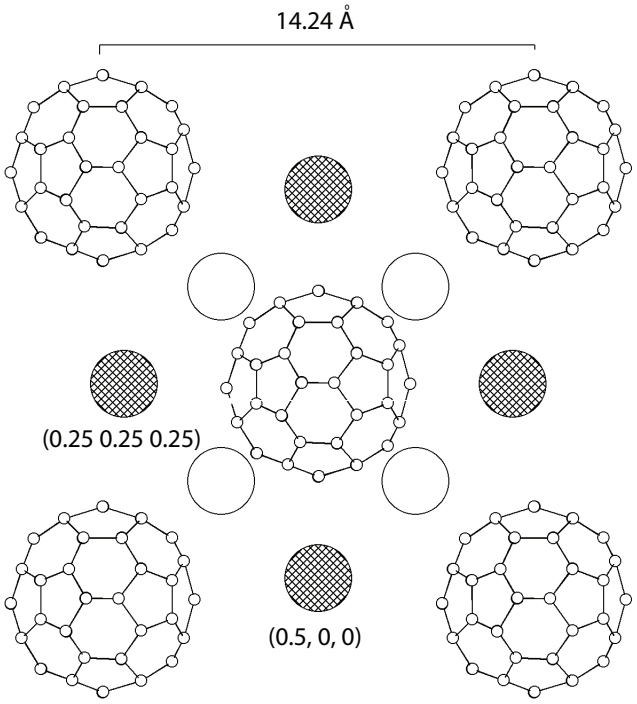

Figure 2.3: FCC unit cell of Rb_3C_{60} open and hatched spheres represent tetrahedral and octahedral Rb sites respectively. Adapted from[28]

surrounds the tetrahedral site.[21]

Alkali metals fill tetrahedral and octahedral 'voids' between C_{60} molecules, this implies that an alkali atom will be surrounded by 4 or 8 C_{60}'s respectively. As one moves down the periodic table, the ionic shell radius increases and therefore the atoms become effectively larger. This translates to different packing arrangements in the fullerides. K_3C_{60} and Rb_3C_{60} have the face centered cubic (FCC) structure[53, 54] whereas Cs_3C_{60} can be either FCC or A15.[18]. Another correlation with increasing ionic shell radius is the ^{13}C NMR linewidth, which increases as the motional averaging is damped by the presence of the dopant atoms.[28] An illustration of the FCC unit cell is given in 2.3, note that the unit cell is constrained in such a way that an alkali atom must face a hexagonal carbon ring. There are only two inequivalent orientations of C_{60} that satisfy this arrangement, which are the two orientations in merohedral disorder.

As mentioned previously, C_{60} is comprised of pentagons and hexagons, where the pentagons establish a curvature and the molecule becomes quasi-spherical. The electron bonding is similar to graphite, with three sp^2 σ bonds connecting neighbouring C atoms. The fourth electron is delocalised on the surface of the C_{60} 'cage', similar to the benzene ring. There are a total of 60 electrons which fill π molecular orbitals. The electrons fill the electronic states according to the Pauli exclusion principle, with

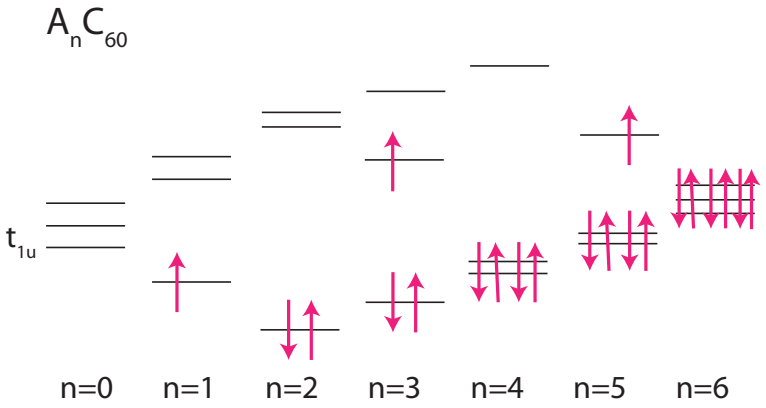

Figure 2.4: Simplified electronic energy level diagram of electron doping progression in A_nC_{60}, highlighting the Jahn-Teller distortion. Adapted from[21]

the highest occupied molecular orbital (HOMO) corresponding to the h_u orbital and the lowest unoccupied molecular orbital (LUMO) is the t_{1u} orbital. This orbital is triply degenerate and may contain up to 6 electrons, these states are filled during the adding of electrons by doping with alkali atoms. They may be filled up to A_6C_{60} but the superconducting stoichiometry is A_3C_{60}.

At temperatures below 260 K, there is a structural transition to a simple cubic lattice, this is true for both the pure C_{60} insulator, and the A_3C_{60} ion. [55]

The A_3C_{60} fullerides are metallic and have a temperature independent spin susceptibility, evidenced by electron spin resonance (ESR) studies. This has also been confirmed by following the Knight shift as a function of temperature, as well as studies of $1/T_1T$, these NMR parameters are discussed earlier in section 4.4.

Jahn-Teller distortions The Jahn-Teller effect is an important phenomenon to consider when doping C_{60} with electrons from rubidium. In a highly symmetric molecule, an electron-phonon coupling can induce a distortion, which occurs when a degenerate valence orbital is only partially filled. The resulting distortion causes the degeneracy to be lifted and the resulting electronic energy levels are now split higher or lower. There is therefore an energy gain when only the lower energy state is occupied. In A_3C_{60} the t_{1u} energy levels at the LUMO are initially degenerate, but the electrons donated from alkali atoms couple to the H_g vibrations in C_{60} and the degeneracy is lifted.

As more electrons are added, the electronic energy levels are progressively altered. A simplified outline of this progression is given in Fig 2.4, this is based on theoretical calculations[56]. At A_1C_{60} and A_2C_{60} there is axial elongation giving rise to a lower singlet and higher doublet levels, at A_3C_{60} the symmetry is lost and there are just three independent levels. As more electrons are added, the C_{60} cage is squeezed and the levels are inverted. The situation then corresponds to a doublet in the lower energy

state and a singlet in the higher energy state.[21]

2.2 Magnesium Diboride

MgB_2 is a simple bimetallic[1] inorganic compound, which was discovered to be a type II superconductor in 2001[29] with T_c=39 K. The structure of MgB_2 consists of boron atoms forming a hexagonal AlB_2 graphite-type structure, with the magnesium atoms located above the centre of the boron hexagons, in-between the planes. The space group of MgB2 is P6/mmm, the lattice parameters are a=3.0834 Åand c=3.5213 Å.

Due to its simple crystalline structure, availability and cost of starting materials, malleability into tapes and wires, chemical reactivity, relatively high transition temperature and reasonably good superconducting parameters (J_c and H_c) MgB_2 has instigated a significant amount of technological interest. The high critical transition temperature alone qualifies the material for use in cryogen-free operation and therefore is attractive for engineering applications. An example of this is in the development of cryogen free MRI magnets, which already exist in some hospitals today.[57]

It is generally believed to be a phonon mediated BCS superconductor from measurements of a large isotope effect[58] and ab-initio calculations of the electron phonon coupling[59], discussed more fully in section 3.4.

J_c in MgB_2 falls rapidly in high fields, due to poor grain connectivity and lack of pinning centres. One way to increase J_c is to dope MgB_2 with carbon, $Mg(B_{1-x}C_x)_2$. This has shown promising enhancements of the field dependence of J_c and also H_{c2}, with the reason often ascribed to lattice defects acting as flux pinning centers.[60] The addition of carbon also affects the structure as well, the a-axis parameter is altered, which causes a shift in the (100) reflection in pXRD, this can be exploited to calculate the doping level.[60, 61] In terms of the electronic structure, the DOS is also reduced and the phonon modes which are involved in the superconducting mechanism (E_{2g}) are hardened.[62]

The widely held view is that carbon replaces boron in the lattice, although the details of this process still have to be determined, for example carbon may be exchanged multiple times on a single ring of the boron sub-lattice or there may only be one boron carbon exchange per ring, alternatively neither of these situations may be correct. An alternative hypothesis often proposed is that carbon collects at the grain boundary, and there is experimental evidence that supports this[63]. However in general, studies which use microscopic tools to investigate the doping of carbon, such as electron energy loss spectroscopy (EELS) were not able to provide evidence on how this process occurs,

[1] A bimetallic compound is one made up of two metals

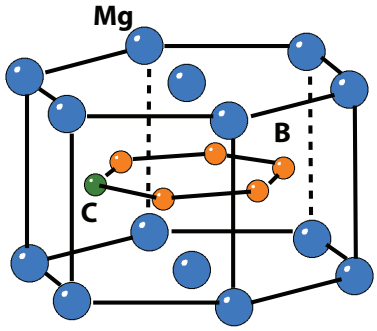

Figure 2.5: Structure of magnesium diboride doped with carbon, which is thought to substitute boron as indicated.

which is due to the limit of resolution of this technique. Despite this issue, EELS can still provide important information, for example there is evidence that boron vacancies generate stack faults within the MgB_2 grains, affecting the impurity scattering and enhancing H_{c2}.[62] Carbon doping may therefore be only increasing the imperfections in the crystal structure and enhancing superconducting properties this way.

2.2.1 Synthesis of MgB_2 and $Mg(B_{1-x}C_x)_2$

There are many different methods used to synthesise MgB_2 powders, films, tapes and wires since it was first synthesised[64] in the early 1950's, for a review see [65]. This thesis is concerned with MgB_2 powders, which are typically synthesised using a solid-state reaction, in which boron and magnesium are weighed in stoichiometric amounts and placed in a furnace, the magnesium vapor condenses onto the boron powder at elevated temperatures[58]. One may use an excess of magnesium to ensure a complete reaction. The furnace will have an inert gaseous atmosphere, argon for example, which will reduce side reactions involving magnesium. Typically the furnace is heated to above the melting point of magnesium(650°C), around 950°C.[4] The superconducting properties may vary according to the presence of impurities in boron, this situation may be improved by subliming boron powder, yielding a higher purity starting material and therefore less impurities in the product.

Carbon doped MgB_2 can be synthesised by adding carbon to MgB_2 using high speed milling or grinding, this requires nanoparticles which will agglomerate due to electrostatic interactions present at this length scale. This agglomerated powder is difficult to grind and therefore the doping will become inhomogeneous. This problem may be bypassed by a chemical vapor deposition technique, described in[60] and allows distribution of the dopant without contamination and more homogeneous doping to each precursor particle.

CHAPTER

THREE

SUPERCONDUCTIVITY: BACKGROUND AND LITERATURE REVIEW

3.1 Introduction

Superconductivity is a quantum mechanical phenomenon which may be observed on the macroscopic scale, it is typically characterised by exactly zero electrical resistance and no magnetic induction below a critical temperature, denoted T_c. The reason for this abrupt loss in resistance can be outlined using a simple phenomenological description[66] based on the Bardeen Cooper and Scheiffer (BCS) theory of superconductivity[1].

A superconductor like Aluminium is a metal, made up of electrons which obey Fermi-Dirac statistics. An electrical current can be visualised in terms of a Fermi liquid, where the electrons flow across an ionic lattice and collide with the heavy positive ions which creates resistance. When Aluminium is cooled below its T_c (1.2 K)[67], the electrons condense into a coherent quantum fluid of correlated pairs of electrons and consequently follow Bose-Einstein statistics. Now a conduction electron with a certain spin and momentum, will be weakly coupled to another electron with the opposite spin and momentum. These pairs of electrons are called Cooper pairs and their interaction is mediated by phonons in the lattice. This is known as the electron-phonon interaction. In this new state, the electrons move in one coherent motion and can be described by one wavefunction. There is now a certain quantity of energy which must be supplied in order to scatter the electrons known as the superconducting gap (Δ), illustrated in Fig.3.1. The gap is broadly defined as the energy needed to break a Cooper pair. Δ arises from the BCS theory and is related to the T_c by the relation:

$$2\Delta = 3.5 k_B \mathrm{T_c} \tag{3.1}$$

where k_B is Boltzmanns constant. If the thermal energy of the lattice is smaller than this quantity, then the quantum fluid will not be scattered by the lattice and there will be no resistance. It was shown from BCS theory that even a small interaction between

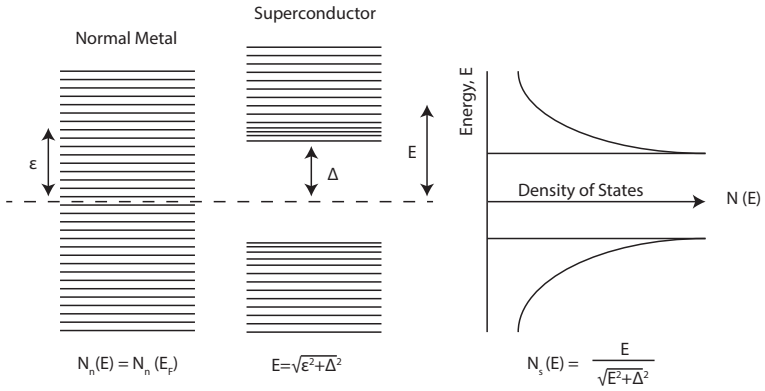

Figure 3.1: An illustration of the density of states in a normal metal and superconductor, adapted from[1]

electrons, such as from the electron-phonon interaction, can cause an instability in the Fermi-sea ground state of the electron gas, with respect to the pairing of electrons with opposite spin and momentum. These paired electrons are known as Cooper pairs, and form the charge carriers of the superconducting state[68].

An interesting and relevant result of BCS theory is the so-called coherence effect[68], which is now outlined. In a normal metal, a scattering event can take place where the momentum of an electron changes from one state to another, often denoted K↑ → K'↑, note that this is independent of -K↓ → -K'↓. However, this is not the case in a superconductor which has electrons paired with opposite spin and momentum, (K↑, -K↓). In this scenario a transition is coherent, and the probability amplitudes from these two events are added. This is known as the interference effect from quantum mechanics.

If one considers the normal electrons and superconducting electrons as two separate fluids, the scattering events in a normal metal should decrease below T_c simply because there are less normal electrons to scatter[66]. An example is the attenuation of sound (due to scattering by electrons) through a metal, which decreases below T_c. There are however, other properties which observe an increase below T_c followed by a decrease, this has been observed in NMR relaxation[2]. The cause of this difference relates to the BCS coherence factor which modifies the matrix element describing relaxation in different ways[28], this is discussed in greater detail in section 4.1.1.

3.1.1 Characteristics of the superconducting state

An additional characteristic of the superconducting state is the expulsion of an applied magnetic field when below T_c. This is known as the Meissner-Ochenfeld effect[69] and is related to surface super-currents generating a magnetic field which screens the applied field. This will happen if the applied magnetic field is lower than the critical field, which

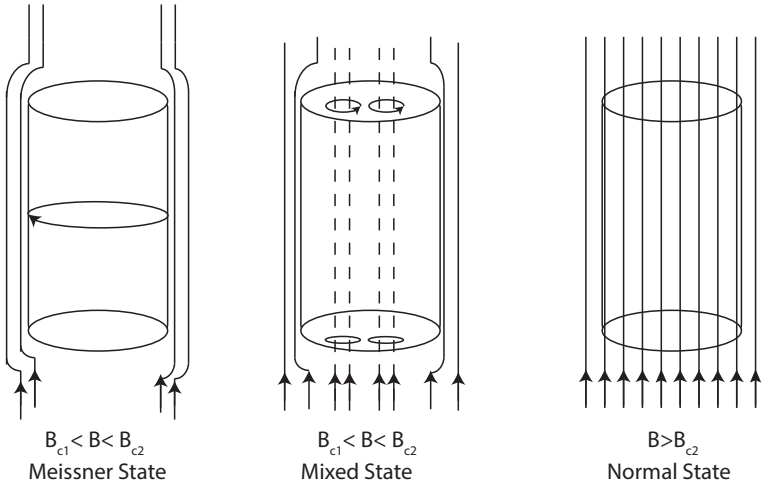

Figure 3.2: An illustration of the Meissner effect and flux penetration in Type-II superconductors

is a temperature dependent parameter with its maximum at 0 K ($H_c(0)$) and zero value at the critical temperature ($H_c(T_c)$)=0. If a superconductor is cooled below T_c and a magnetic field is applied which is greater than H_c(T), then the superconducting state will be destroyed and the magnetic field will penetrate the material as if it was a normal metal. The critical current (J_c) defines the amount of current a superconductor can withstand before the field generated exceeds the critical field.

In general the superconducting state can be described with a phase diagram, where the critical field and critical temperature are the axes (J_c may also be used), different materials will have a different set of parameters that define the boundaries of the superconducting state.

3.1.2 Type I and Type II

There are two types of superconducting materials, which can be simply defined from their response to an applied magnetic field (H). Type-I superconductors which are cooled below T_c and then subject to a magnetic field which is less than H_c are in the superconducting state, when the applied magnetic field is greater than H_c the sample returns to the normal state. Type-II materials have a H_{c1} and H_{c2}. When $H < H_{c1}$(T) then the material is in the superconducting state, then if $H > H_{c1}$(T) the material is penetrated by a periodic lattice of magnetic flux lines, which are inside vortices of super-current. This is known as the vortex state, or mixed state as there are areas of both superconductivity and thin tubes in the normal state. The difference between Type-I and Type-II superconductors is illustrated in Fig.3.2. As $H \rightarrow H_{c2}$(T) more flux lines penetrate the material, and they become closer packed together until H_{c2}(T) at which the material enters the normal state again.

3.1.3 Penetration depth and Coherence length

In the superconducting state the Meissner effect expels an applied magnetic field (H), leading to zero field within a given superconductor. The origin of this effect lies at the surface of the sample, where a non-resistive supercurrent generates magnetisation (M), which then leads to $M + H = 0$. The depth of the region in which these currents flow is known as the penetration depth and is denoted λ. It is a characteristic parameter and additionally is also present as the extension of supercurrent around the flux tubes in type-II superconductors. Typical values of the penetration depth are 100-1000Å in type-II superconductors.

An additional characteristic parameter is the coherence length (ξ), this is broadly defined as the distance between two Cooper pairs. However a more rigorous definition is the distance over which the superconducting gap (Δ) may vary. An example of this might be the boundary between a normal metal and a superconductor. The definition of the coherence length from BCS theory is given by

$$\xi = \frac{\hbar \nu_F}{\pi \Delta} \tag{3.2}$$

Where $\hbar$ is Plancks constant divided by 2π, ν_F is the Fermi-velocity and Δ is the superconducting gap. Typical values for ξ_0 for type-I and II superconductors are quite different, for example in Al ξ_0=16000Å whereas in YBCO ξ_0=10Å.

These two characteristic length parameters lead to a quantity which characterises materials into type-I or type-II categories, this is known as the Ginzburg-Landau Coefficient and is defined as:

$$\kappa = \frac{\lambda}{\xi} \tag{3.3}$$

The standard definition is that if κ<0.7, then the material is type-I and if κ>0.7 then this is known as type-II.

3.1.4 Vortices in Type II superconductors

In a Type-II superconductor, above H_{c1} there are vortices present which penetrate the superconductor in a periodic array as described previously. Each vortex contains a quantum of magnetic flux and forms a cylindrical region of normal material, the radius is of the order of the coherence length. The vortices are repelled from one another and in-between the material is in the superconducting state

If one applies a current it will pass unimpeded, so long as the current does not disrupt the vortices. However there is a tendency for this disruption to occur, as a current will exert a force (the Lorentz force) on the magnetic flux that tries to move it

sideways. This movement of flux through the lattice dissipates energy and is akin to resistivity. This can be a problem in the application of superconductors to problems which require a large current to flow. To circumvent these issues, one may use chemical or structural deformations to effectively 'pin' the vortices and allow the current to run between without dissipation caused by flux motion.

If one applies a magnetic field to a Type II superconductor in the region between H_{c1} and H_{c2}, then the superconductor allows thin filaments of flux to partially penetrate and this lowers the total free energy of the system. The flux passes through normal regions which arise from vortices of supercurrent which generate their own magnetic field. Each vortex carries a flux quantum

$$\phi_0 = \frac{\hbar}{2e} = 2.07 \times 10^{-16}\text{Wb} \tag{3.4}$$

Where $\hbar$ is Plancks constant divided by 2π, e is the elementary electron charge. The amount of flux lines increases with the applied magnetic field, and the structure is dependent on the penetration depth and coherence length. The radius of the vortex is given by the coherence length, and the density of Cooper pairs diminishes and falls to zero at the centre.

The applied magnetic field penetrates the core of the vortex, and this field region is essentially the same value as the field would be if the material were in the normal state, which consequently is the highest value, and the magnetic field decays exponentially over the characteristic length scale λ. Also the supercurrent vortices may interact over the length scale ξ.

Flux Pinning and Vortex Phases

As mentioned previously there are various non-superconducting inhomogeneities, which allow the vortex line to reduce its own total energy. These inhomogeneities are known as pinning sites, as the vortex line is effectively pinned to them. Examples of such sites include structural defects, impurities, chemical vacancies, grain boundaries and/or twin boundaries. There is a natural tendency for a vortex line to be attracted to a pinning site as both are non-superconducting. After a vortex line is pinned to one of these sites, there is an energy barrier which must be overcome in order for them to move, from a non-superconducting to a superconducting region.

This flux-pinning will mean that as the externally applied field is altered, the magnetic flux will not change in a reversible way. Therefore in the application of type-II superconductors in industry and applied science, one must take the intricacies of the pinning mechanism into account, especially in relation to the critical current.

The value of the critical current depends on a balance between the Lorentz forces

and the pinning forces acting on the flux lines. As mentioned previously, the effect of the Lorentz force is to drive the flux lines into motion, dissipating energy and destroying zero resistance. Flux pinning opposes the motion of the flux lines and cause an increase in critical current and therefore is a widely studied and relevant field in the application of type-II superconductors.

A type-II superconductor in the mixed state is penetrated by many vortex lines which adopt the lowest energy arrangement possible, which consists of a periodic array arranged in a hexagonal pattern, in the plane perpendicular to the field direction. This is known as the Abrikosov vortex lattice

In general however, a superconductor may contain disorder and therefore the vortex structure may differ and various phases have been proposed, including vortex solid, liquid and glass phases. A more detailed review can be found here[70]. The vortex phases

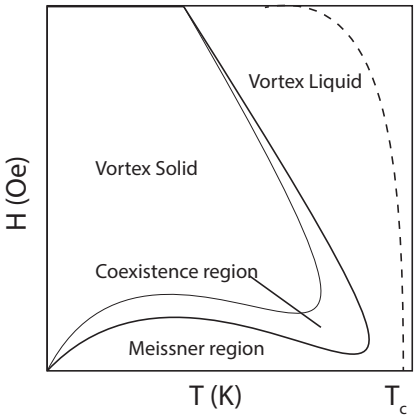

Figure 3.3: Vortex phase diagram

are accessible experimentally because they depend on various parameters which may be controlled such as magnetic field and temperature. An illustrative phase diagram is shown in Fig. 3.3. Typically below T_c the phase diagram first enters the vortex liquid state, characterised by fast correlation time of the magnetic field (flux line), as a function of position. As one cools the material, the vortices gain more order and they enter the vortex lattice or vortex solid phase. This is typically characterised by an ordered periodic array with a much slower correlation time. The Coexistence region has both solid and liquid vortices. The Meissner region completely expels the magnetic field and there are no vortices. Vortex lattice melting describes the first order phase transition between solid and liquid phases, this transition was first detected in transport measurements, as a sharp kink in the resistivity as a function of temperature.[71]

3.1.5 Isotope effect

A test of the electron-phonon coupling mechanism is measurement of the isotope effect. In BCS theory the isotope coefficient, denoted α is defined by the relation.

$$Tc \propto M^{-a} \tag{3.5}$$

Where M is the mass of the element and α is a numerical factor, BCS superconductors have α=1/2 and Type-I superconductors show experimental values of α close to this. The isotope effect in general is a useful tool to determine, not only if a superconductor follows the electron-phonon coupling model but also which phonons may be involved in the mechanism[58, 72–74].

3.2 Theories of superconductivity

The phenomenon of superconductivity was discovered in 1911, but an adequate theoretical description did not appear until 1957. This was helped by the understanding of superfluidity in ^{4}He (at 2.17 K), which is described by Bose-Einstein statistics. The bosons make up a coherent state, so when an individual boson attempts to scatter on an obstacle to its flow such as an impurity, the whole condensate forbids this individual particle to be scattered to leave the condensate. This is the origin of the superfluidity. Superfluidity is also seen in fermionic systems, such as ^{3}He, but the difference in transition temperature is stark (0.0026 K). In this instance the superfluid is made up of pairs of ^{3}He fermions. The description of superfluidity using a coherent state of bosons or pairs of fermions was thought to relate to superconductivity as well. The few orders of magnitude difference between transition temperatures seemed it might explain the early low (Hg at 4.2 K) and high temperature (Nb_3Ge at 23 K) superconductors. Electrons are fermions however, therefore the initial attempts to formulate a description included a bonding/pairing between electrons. These initial attempts failed because they did not include details regarding the Coulomb repulsion between electrons which would naturally stop such pairing from occurring. When Bardeen Cooper Schreiffer (BCS) formulated their famous theory, they proposed that two electrons can form a paired state, but it is of a relatively large dimension i.e. 10^4 times the average inter-electron spacing. The theory rested on an earlier idea which arose from Frohlich which suggested that conduction electrons at the Fermi energy could have an attractive interaction because of their weak interaction with the phonons in the lattice, in other words the vibrating ions of a crystal lattice could mediate an attractive interaction between electron pairs. Cooper showed that pairs of electrons are stable only due to

their quantum interaction with other pairs, known as Cooper pairs. The BCS theory showed that within a small shell at the Fermi energy, the electrons are correlated into pairs in momentum space, these pairs would then be strongly overlapping in real space. The theory was extremely successful at describing superconductors with low T_c values but not as good for high temperature T_c values, in fact many theorists stated that BCS theory put an upper limit of superconductivity of 30 K. The BCS theory was eventually extended to include an electron-phonon interaction and the result suggested that a Bose liquid of tightly bound electron pairs would surround the lattice deformation. This is known as the Migdal-Eliashberg extension of BCS theory, which includes the electron phonon coupling. In the interest of brevity, this is just referred to as 'BCS theory' throughout this thesis.[75]

3.3 Superconductivity in the Fullerides

Superconductivity was discovered in the K_3C_{60} system of the fullerides in 1991[76] with T_c=18 K. Since then superconductivity has been found in other alkali derivatives such as caesium[17, 77, 78] and rubidium[79], there are also fulleride salts which contain ammonium ions[80]. A vast body of work[8, 28, 81–91] has been dedicated to study the superconductivity in these materials and even in the past few years, there has been a revolution in experimental[14, 15, 92] and theoretical efforts[22, 93, 94] to understand the mechanism.

3.3.1 Electron-phonon coupling

The A_3C_{60} fullerides are thought to be regular Fermi liquids from the observation of a temperature independent electronic susceptibility, recorded in the normal state using electron spin resonance (ESR)[95] and supported by NMR measurements of Knight shift and $1/T_1T$[81]. In other words ESR and NMR have shown that the fullerides behave as regular metals. For more details on the Knight shift and $1/T_1T$, and their relation to the susceptibility see sections 4.2 and 4.4 respectively.

The pairing mechanism in the fullerides is usually discussed in the traditional framework, which is within the Migdal-Eliashberg extension of BCS theory. In order to match the experimentally determined T_c, the electron-phonon coupling constant and the high phonon frequency has been determined experimentally[96, 97] and also calculated[16, 98, 99]

NMR studies have shown show a decrease of the Knight shift in the superconducting state, which implies singlet pairing, typical of the BCS theory. There is also evidence of a Hebel-Slichter coherence peak in the relaxation rate of NMR[28, 100] and muon

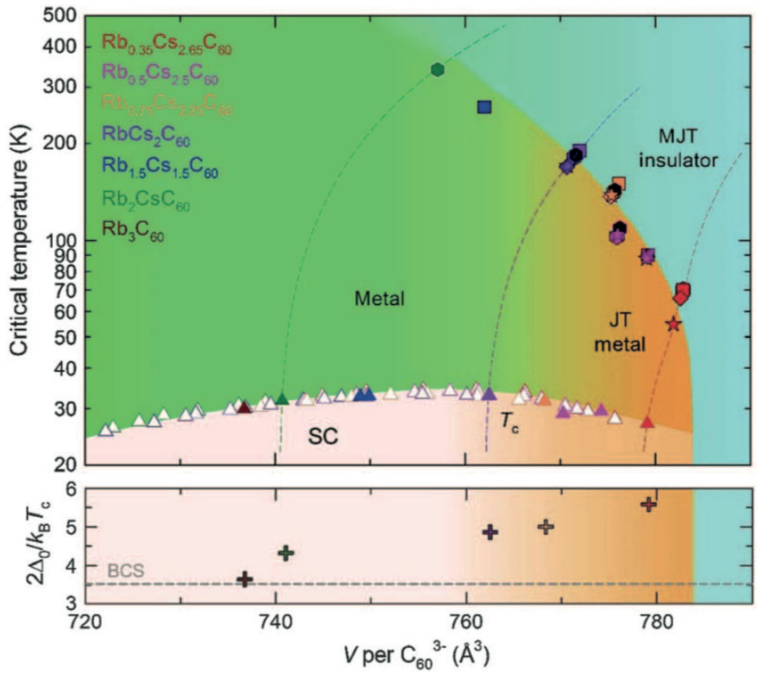

Figure 3.4: Phase diagram of Rubidium doped C_{60}, reproduced from[101]

spin resonance[91], which has been observed at 2 T. An important experimental finding was the dependence on the variation of T_c with chemical or mechanical pressure.[102–104] A positive correlation between the lattice constant and the T_c was found which supports BCS theory, the lattice is expanded which causes the bandwidth to decrease and thereby the DOS increases. This fits into BCS theory and therefore was thought to be strong evidence of an electron-phonon mediated mechanism.

There are two elements which may be substituted in Rb_3C_{60} to test for the presence of the isotope effect. The ^{13}C isotope effect has been measured by Ebbesen et al. who prepared C_{60} with various quantities of the ^{13}C isotope. The exponent was large, a value of α_{Rb}=1.4±0.5[82], which is much higher than the BCS value, around 0.5.

The ^{13}C isotope effect has also been measured to be α_C=0.37±0.05, with a substitution of 75% ^{13}C for ^{12}C[83] and α_C=0.21±0.012, with a substitution of 99% ^{13}C for ^{12}C.[72] This indicates the presence of an electron-phonon coupling mechanism, but does not highlight a specific phonon mode. For example, there are intermolecular and intramolecular phonons in Rb_3C_{60}, and both would be sensitive to the ^{13}C isotope effect compared to ^{87}Rb, which specifically probes the intermolecular optic phonons. The ^{87}Rb isotope effect exponent was measured to be α_{Rb}=0.028±+0.036[73], which implies intermolecular optic phonons are not involved in the mechanism of superconductivity. As there is a isotope effect with carbon, it suggests the phonon modes which are important to the pairing interaction are intramolecular in origin.

3.3.2 Strong Correlations in the Fullerides

As discussed in the previous section, many techniques have indicated the BCS theory as the most appropriate description of superconductivity in the fullerides. In conventional superconductors there is a repulsive interaction between electrons (Coulomb repulsion), which opposes electron-phonon pairing and causes the T_c to decrease as electron correlations increase. Conversely there are a group of materials that are classed as *strongly correlated*[105]. This implies there is a stronger interaction between electrons, and interestingly in some superconductors the stronger electron-electron correlations do not suppress superconductivity but actually enhance it, for example this is the case in the cuprates. The definition of strongly correlated is given by the ratio of the intramolecular Coulomb repulsion (U) and the bandwith (W). When U/W exceeds unity, then the material can be regarded as strongly-correlated.

The fullerides are molecular conductors, they have a narrow bandwidth of W$\approxeq$0.5 eV, they also have U$\sim$1.6 eV measured using Auger spectroscopy[106]. Therefore there is increasing evidence that the fullerides belong to the strongly correlated class of materials[107], similar to the cuprates.

A major difference between the cuprates and the fullerides however is the symmetry of the superconducting gap. In the cuprates the superconducting gap has a d-wave order parameter, whereas the fullerides are of s-wave order. Evidently in the fullerides there is a mechanism which allows superconductivity to be induced in spite of the relatively large value of U.

As U is larger than W, there has been some speculation that superconductivity arises from off-stoichiometry and the A_3C_{60} system is in fact a magnetic insulator. This has spurred some to consider an electronic mechanism[108] and there have been many works which take into account both the conventional pairing mechanism, and the electronic correlations[109–111]. An important discovery was the Mott insulating phase in Cs_3C_{60}, which was surprising as it was thought this phase could not co-exist with conventional BCS superconductivity[18, 19].

The alkali-doped fullerides are thought to provide a unique opportunity to study strongly correlated s-wave superconductivity. This alongside the recent synthetic developments in encapsulating molecules inside the C_{60} cavity, has brought an interesting opportunity to study the superconducting state using a new NMR probe.

3.3.3 Penetration Depth and Coherence Length in Rb_3C_{60}

In Rb_3C_{60} the samples are mostly polycrystalline and thus transport-determined values of the penetration depth are unreliable. In this case resonance methods are more

accurate such as NMR[81] and muon spin resonance[112] (μSR). Measurements using NMR have indicated that $\lambda = 4600$ Å whereas μSR gives $\lambda = 4200$ Å. This is in contrast to optical measurements which yield a value of $\lambda = 6000$ Å. The coherence length can be extracted from the upper critical field measurements, which is in turn may be determined from ac susceptibility measurements, this method applied to Rb_3C_{60} has yielded a value of 30 Å[113].

3.3.4 Superconductivity in Endohedral Fullerides

The idea of encapsulating molecules or single atoms inside superconducting fullerides is interesting in its novelty alone, however there are also questions raised about the effect on the electronic structure and the lattice. One might expect the encapsulated species to exert an effect on the cage radius for example, and/or alter the intermolecular interactions. Superconductivity in enohedral fullerides has been studied previously[26], but the work so far has been limited to encapsulated noble gases such as Ar and He. This is most likely due to the difficulty in obtaining the endohedral fullerene precursor, and even the noble gas endofullerenes are studied on a scale of 1-2 mg. Yakigaya et. al. first studied $Rb_3(Ar@C_{60})$ and $K_3(Ar@C_{60})$. They find that the insertion of Ar atoms into the cage leads to a decrease in T_c of 2 and 1 K respectively, compared to the empty caged fulleride compounds. Also there appears to be a difference in lattice constant measured by pXRD between the empty and filled derivatives.

3.4 Superconductivity in MgB_2

In this thesis, a ^{13}C doped sample of MgB_2 is studied. As a prelude to these experiments, an overview of the current understanding of superconductivity in MgB_2 and doped MgB_2 is now given. An outline of superconductivity is given in chapter 3, details of the theory behind NMR on metals and superconductors is given in chapter 4. More explicit details of the NMR experiments on MgB_2 are given in section 4.9.

3.4.1 Electron-Phonon Coupling

Superconductivity in the magnesium diborides is thought to arise from an electron-phonon coupling mechanism[114]. The electronic structure of MgB_2 is well described by band theoretical methods and there is excellent agreement between calculations and experiment of the electron-phonon spectrum, leaving little room for other more exotic mechanisms such as those based on an all electron one.[115]

The isotope effect has been measured in MgB_2[58], the difference in T_c is ≈ 1 K between $Mg^{10}B_2$ and $Mg^{11}B_2$ (α_B=0.25) and there is a much smaller shift between the two Mg isotopes($\alpha_M g$=0.02), this strongly suggests the mechanism of superconductivity resides in the boron planes. This is in agreement with ab-initio calculations[59, 116, 117] which suggest there is a strong coupling between the E_{2g} phonon mode[1] and the conduction electrons in the sigma and pi bands.[59] The difference in coupling strength between these bands and the phonon modes is what drives the double-gapped nature of MgB_2. There is however still a discrepancy with the isotope effect, which is approximately half the expected value for BCS superconductors. The solution to this problem lies in the nature and extreme strength of the electron-phonon coupling, which is the main reason for the relatively high T_c value.[118, 119] The specific coupling between electronic states and phonons in the magnesium diborides is a key feature of these materials and is also related to its double gap superconductivity.

3.4.2 Double Gap Superconductivity

The first specific heat measurements[120] on MgB_2 revealed a strong field-dependent feature at low temperature suggesting the presence of two distinct superconducting gaps. Further experimental evidence such as Raman[121], photoemission[122], point-Contact[123] and scanning tunnelling microscopy[124] measurements have yielded evidence that ratifies the double gap nature of MgB_2. Electronic structure calculations[59] identified two bands which the two gaps derive from, notably the σ and π bands which form quasi two-dimensional cylindrical sheets and 3D tabular networks. This is shown in Fig. 3.5.

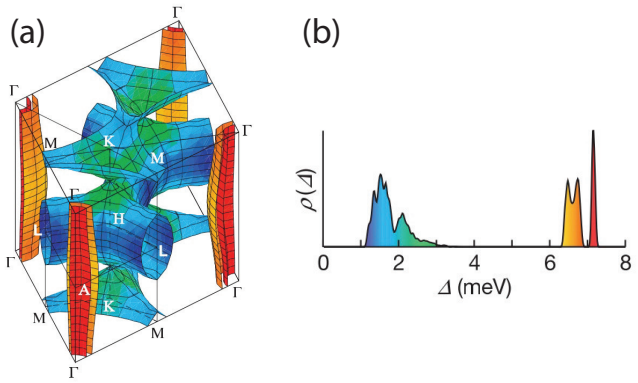

Figure 3.5: (a) The superconducting energy gap on the Fermi surface at 4 K given a colour scale, highlighting the double gap superconductivity for MgB_2. (b) Superconducting gap values given in meV. Reproduced from [59]

[1]The E_{2g} phonon mode involves boron atoms moving in opposite directions in the boron plane adjacent to each other about their equilibrium positions

The σ band arises from the $p_{x,y}$ orbital of boron and the π band from the p_z orbital. The difference in coupling strength between the phonon modes and sigma/pi bands is the origin of the two superconducting gaps, with a ratio $\Delta_\sigma/\Delta_\pi = 2.63$. Although there is good agreement amongst these various experimental techniques, ^{11}B NMR has proven to be an exception with $1/T_1$ data that fits better to a single gap of $2\Delta/k_BT_c$=5.[125, 126] The reason for this may be linked to interband scattering which should be taken into account for two-band superconductors, then one would expect more single band behaviour[34].

3.4.3 Flux-pinning in MgB_2

Practical applications of superconductors sometimes requires knowledge of vortices and pinning centres, the latter of which can be induced by a variety of techniques such as chemical doping[127] or neutron irradiation[128]. As discussed in section 3.1.4, a supercurrent is dissipated unless the vortices are 'pinned' in some way. The Lorentz force, which usually drives them into motion, is then rendered ineffective and the balance between the depinning force (force required to de-pin vortex from pinning centre) and Lorentz force determines J_c.

MgB_2 is a good superconductor for applications because its grain boundaries are highly transparent to supercurrents, which flow around the polycrystalline fragments.[129] This is in stark contrast to the cuprates, where a polycrystalline sample has an assembly of disconnected grains, except in lowest applied fields.[129] A disadvantage of MgB_2 is that although J_c is high, it rapidly decreases with increasing field and therefore to become more useful the vortex pinning energy must be enhanced.

A common route to enhance J_c is chemically doping with carbon, using SiC[32] or B_4C[33]. Fig. 3.6 shows J_c as a function of field for a series of carbon doped MgB_2 samples. It is immediately obvious that even modest carbon doping (x=0.04) leads to beneficial effects, for example at x=0.08 the J_c value is 24 times higher than the pure sample at 6 T and 10 K. The curves become broader with nano-carbon doping, with respect to the undoped sample, and this arises due to flux pinning, which then results in increased critical field values and thereby larger critical current densities.[130] The mechanism of flux pinning is of interest to help design and improve superconductors for applications. pXRD measurements have suggested that carbon mainly replaces boron in the lattice, leading to an intrinsic pinning mechanism. Any additional carbon then builds up at the grain boundaries, which facilitates an extrinsic flux pinning mechanism.[130] The general consensus is that carbon substitutes for boron, but there has been evidence from transmission electron microscopy (TEM) that carbon is located exclusively outside the MgB_2 phase and that flux pinning results from boron vacancies

rather than boron-carbon substitutions. The boron vacancies lead to boron stacking faults, shown in Fig. 3.6. These structural defects lead to an increase in impurity scattering rate, which in turn enhances the upper critical field and critical current density. It is unclear if this mechanism is appropriate to all forms of carbon doped MgB_2 or that it is specific to the reaction of magnesium and boron with malic acid.

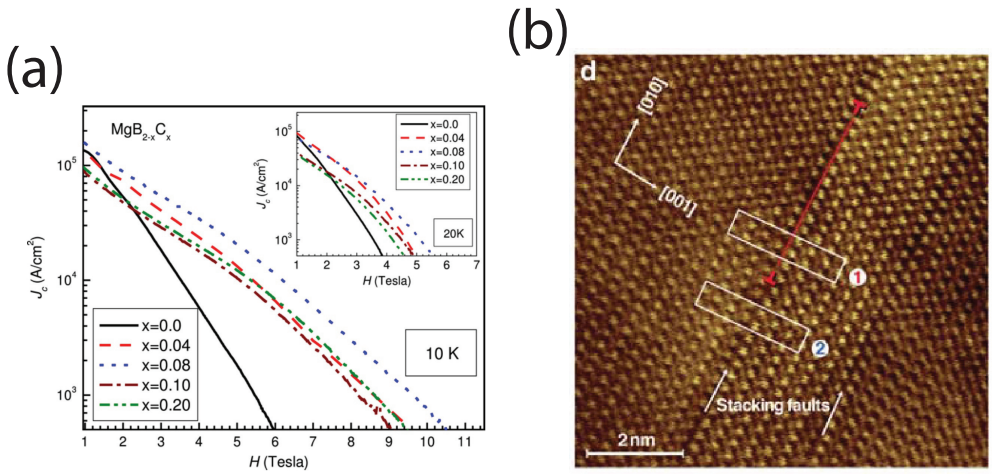

Figure 3.6: (a) Variation of J_c as a function of H for a series of carbon doped MgB_2. Reproduced from [130] (b) TEM spectrum of carbon doped MgB_2 indicating that carbon doping causes boron vacancies, leading to stacking faults. Reproduced from[131]

CHAPTER

FOUR

NMR OF METALS AND SUPERCONDUCTORS

4.1 Introduction

This section introduces the concepts behind NMR on metals and superconductors. The hyperfine interaction is first introduced, this is the coupling between the conduction electrons and nuclei, the underpinning to this chapter. Then more specific NMR parameters such as T_1 and Knight shift are discussed. This provides a prelude to the literature review of the NMR experiments on the fullerides and magnesium diborides toward the end of the chapter. For an outline of the basics of NMR, there are a variety of excellent textbooks available[132, 133]

4.1.1 The Hyperfine interaction

The Hyperfine interaction is the interaction between the nuclear spin and the electron spin, and acts as a small perturbation on the Zeeman Hamiltonian. It is described as follows:

$$H_{el-n} = \gamma\hbar\hat{\boldsymbol{I}} \cdot \sum_i (2\mu_B)\left(\frac{\boldsymbol{l}_i}{r_i^3} - \frac{\boldsymbol{S}_i}{r_i^3} + 3\frac{\boldsymbol{r}_i(\boldsymbol{S}_i \cdot \boldsymbol{r}_i)}{r_i^5} + \frac{8}{3}\pi \boldsymbol{S}_i \delta(\boldsymbol{r}_i)\right) \tag{4.1}$$

Where $\boldsymbol{l}$ and $\boldsymbol{S}_i$ are the orbital and spin angular momentum for the electron, $\hat{I}$ is the nuclear spin angular momentum, μ_B is the Bohr magneton and $\boldsymbol{r}$ is position vector of the electron with respect to the nucleus.

The first term describes the interaction responsible for the chemical shift, it arises from orbital angular momentum of the electrons and nuclei. The second and third terms describe the dipolar interaction between nuclei and electrons, which can give rise to an anisotropy of the Knight shift and relaxation rate in metals. The last term describes the Fermi-contact interaction between electrons and nuclei, it arises from the s electrons which have a finite spin density at the nuclear spin site, as opposed to p electrons which have a zero probability at the nucleus. The Fermi-contact interaction generates an additional shift in the NMR spectrum and this is known as the Knight

shift.

4.1.2 The Skin-depth

An important difference between the study of diamagnetic insulators and conducting metal samples by NMR is the consideration of the skin depth. To obtain spectra which are representative and quantitative, it is important to use powder samples which have a particle size smaller than the skin depth[133]. The skin depth is the distance at which eddy currents are generated after the application of a radio-frequency field to conducting metallic powders. The NMR signal is proportional to the area of the metal, not to the volume and this is because the radiofrequency field only penetrates the surface. The skin depth is given by the following equation[134]

$$d = \frac{1}{\sqrt{\pi \mu_0}} \sqrt{\frac{\rho}{\mu_r f}} \tag{4.2}$$

where f is the resonance frequency (the Larmor frequency), μ_0 is the vacuum permittivity constant ($= 4\pi \times 10^{-7}$ m kg A^{-2} s^{-2}), μ_r is the relative permeability of the metal and ρ is the resistivity of the metal. It is clear from equation 4.2 that a higher magnetic field will also lead to a smaller skin depth.

It is therefore advantageous to work with small particle sizes in order to maximise the amount of signal arising from the sample. A common method for particle size reduction is by grinding in an agate mortar, the smallest particle size achievable by this method is dependent on the material, for example C_{60} may be reduced to 5 nm[135] and MgB_2 may be reduced to 9 μm[136].

To ensure the maximum benefit from the reduction of particle size, one must also consider the electrical insulation between particles. A thin natural oxide layer may provide this, but if it is not present or not effective, then one may disperse the particles in oil or set in wax[133]. Alternatively an insulator may be mixed with the conducting metal powder[137].

4.2 The Knight shift in metals

Applying a magnetic field lifts the degeneracy of the nuclear spin energy levels and the splitting is known as the Larmor frequency, which depends on the nucleus and increases with field strength. However due to local magnetic fields, which vary according the interactions present, the resonance line for a particular atomic site will be shifted.

$$H_Z = -\gamma \hbar \cdot (H_0 + \Delta H) \tag{4.3}$$

where $\hbar$ is Plancks constant divided by 2π, γ is the gyromagnetic ratio, H_0 is the applied magnetic field and ΔH is defined as follow

$$\Delta H = H_{orb} + H_{spin} \tag{4.4}$$

Where H_{orb} is the orbital shift also known as the chemical shift, this interaction is discussed in more detail elsewhere[132]. H_{spin} is the Knight shift, it can be defined as the interaction of the nuclear spins with the magnetic moments associated with electron spin of charge carriers in the conduction band. This is now broadly outlined in more detail.

In a metal, the conduction electrons hop rapidly between atomic sites and therefore to describe their effect on the nucleus, one must average over all electron spin orientations. When there is no magnetic field, this average is equal to zero because there is no preferential orientation and thus there is effectively no Knight shift. When a magnetic field is applied, the electrons are polarised. The change in electron spin populations, denoted $n_{\pm 1/2}$ creates magnetisation

$$M = \mu_B(n_{1/2} - n_{-1/2}) \tag{4.5}$$

where μ_B is the Bohr magneton. There is now a non-zero coupling between the nucleus and the electrons. The distribution of electrons at the Fermi-level is given by the Fermi distribution function

$$f(E) = \frac{1}{1 + \exp^{(E-E_f)/k_B T}} \tag{4.6}$$

where E is the electron energy, E_f is the Fermi energy, k_B is the Boltzmann constant and T is temperature. The Fermi function is plotted in Fig. 4.3(b). The magnetisation can be expressed as

$$M = \mu_B^2 B \int nf(E)dE \tag{4.7}$$

where B is the magnetic field and n is the density of states, when the energy at the Fermi-level is much greater than k_BT then

$$M = \mu_B B_0 n(E_f) \rightarrow \chi_p = \mu_0 \mu_B^2 n(E_f) \tag{4.8}$$

where $n(E_f)$ is the density of states at the Fermi level. The polarisation of the electron spin states, leading to a net magnetisation is known as Pauli susceptibility (χ_p). The electrons in the s-orbital are predominately involved in this coupling, as there is a large attractive potential of the nuclear charge. The magnetic field produced by the s-state electrons is perpendicular to their electron magnetic moment, and this is oriented

parallel to the applied field. This means that the additional field produced at the nuclear site will be positive, as has been determined experimentally for almost all cases[138]. By calculating the magnetic field produced by the electrons, one may determine the shift in field experienced by the nucleus. This is defined via the hyperfine field arising from the conduction electrons

$$\Delta B = \frac{\mu_0}{4\pi}\frac{8\pi}{3}\chi_P \Omega \langle|\psi(0)|^2\rangle_F B_0 \tag{4.9}$$

The field (B) is determined by the wavefunction (ψ) at the nucleus, which is averaged over the Fermi-surface and Ω is the volume factor known as the volume per electron. In NMR this additional field was originally discovered by Walter Knight, who found an additional shift in metallic copper with respect to CuCl which is an insulator. These shifts are common to all metals and are an order of magnitude larger than diamagnetic shifts, such as the chemical or Van Vleck shifts. The Knight shift is a diamagnetic shift and is positive, it does not depend on field, it is approximately independent of temperature and increases with nuclear charge.

$$K = \frac{\Delta B}{B_0} = \frac{2}{3}\chi_P \Omega \langle|\psi(0)|^2\rangle_F \tag{4.10}$$

As seen in eq. 4.9 and 4.10, the Knight shift depends on the wavefunction density at r=0, which is at the nucleus. This means that the shift is mainly dominated by the s-electrons, however it is possible to have p or d electron contributions. The s-electrons are close to the nucleus and the effect arising from the other contributions is small, and are known as core polarisation effects due to their mechanism of interaction. The d or p electrons polarise the s-electrons and this produces a field at the nucleus. This term can actually be negative, due to the way that the flux lines curve around and produce a field in the opposite direction. To summarise, the magnetic shift in an NMR spectrum is comprised of orbital and spin contribution which is also known as the chemical and Knight shifts respectively. These contributions combine to give the overall shift as follows

$$K_{tot} = K_{spin} + K_{orb} = K_{dip} + K_{FC} + K_{cp} + K_{orb} \tag{4.11}$$

The K_{spin} term is only relevant in metals and is further broken down according to the Fermi-contact, dipolar and core polarisation terms.

4.3 Knight Shift in the Superconducting State

The behaviour of the Knight shift in the superconducting state can be a useful tool to determine the symmetry of the superconducting gap. In a BCS s-wave superconductor, electrons start to pair up into a singlet state below T_c and the susceptibility (and therefore the Knight shift) goes to zero, this is shown in Fig. 4.1(a). In contrast a superconductor with p-wave symmetry has electrons which pair up into a triplet state, and the Knight shift therefore does not decay below T_c, an example is shown in Fig.4.1(b).

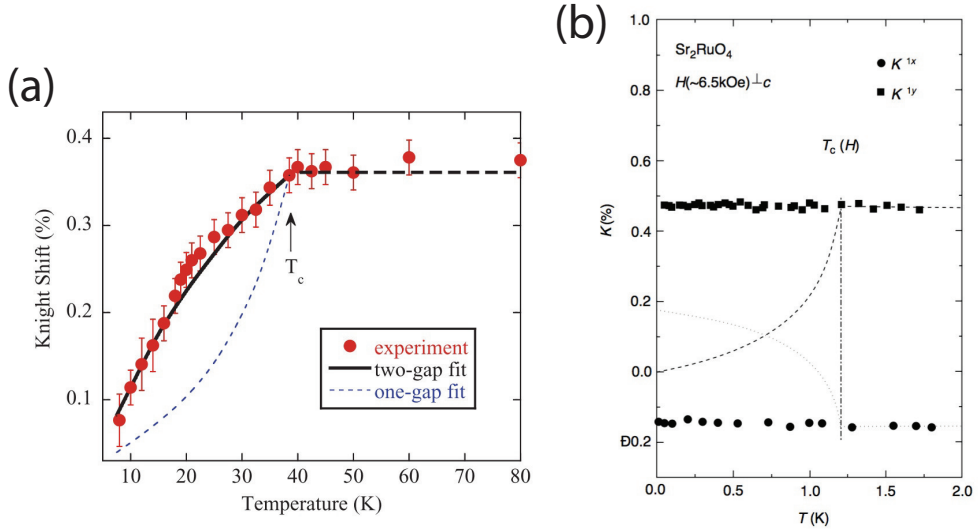

Figure 4.1: (a) Temperature dependence of ^{75}As Knight shift in $PrFeAsO_{0.89}F_{0.11}$, an example of spin-singlet superconductivity. Reproduced from[139](b) temperature dependence of ^{17}O Knight shift in Sr_2RuO_4, an example of spin-triplet superconductivity. Reproduced from[140]

4.3.1 Spin Susceptibility

In the superconducting state the external magnetic field induces a diamagnetic shielding current and therefore an additional screening of the internal field at the nucleus, this is also known as the Meissner screening current. The diamagnetic shielding term reduces the internal field and is therefore a negative contribution to the total magnetic shift as follows:

$$K^{\alpha}_{total} = K^{\alpha}_{spin}(T) + K^{\alpha}_{orbital} + K^{\alpha}_{Q} - \frac{\Delta H(T)}{H_0} \tag{4.12}$$

Where K^{α}_{spin} and $K^{\alpha}_{orbital}$ represent Knight and chemical shift respectively. α is the nuclear isotope and K_Q is the shift from the second order quadrupolar interaction and ΔH represents the demagnetisation field. This value is not known and therefore there

is an uncertainty in determining the other components of equation 4.12. There can be a large broadening effect from this contribution, and to determine accurately K_{spin} one needs to measure K_{total} of two different nuclei.

A relevant term in the analysis of the superconducting state is the Knight shift, which can be decomposed into

$$K^{\alpha}_{spin} = \overleftrightarrow{A}\chi^{S} \tag{4.13}$$

where $\overleftrightarrow{A}$ is the hyperfine coupling tensor and χ^S is the dimensionless Pauli spin susceptibility. A useful approach to test the appropriateness of the BCS picture is to measure the spin susceptibility, which allows extraction of the BCS gap at zero temperature (Δ_0) by fitting it to the Yosida function[141]. The temperature dependence of $\chi^S(T)$ cannot be measured directly because of the Meissner screening currents in the vortex state, which are in general much greater than the Knight shift and are field dependent. There are also orbital and quadrupolar contributions to the shift, but these typically act as a temperature independent offset. The diamagnetic shift may be removed by subtracting two isotopic nuclear species by some simple rearrangement of equation 4.13 as follows

$$K^{\alpha}_{total}(T) - K^{\beta}_{total}(T) = (A_{\alpha} - A_{\beta})\chi^{S}(T) + const \tag{4.14}$$

where *const* arises from the K_{orb} contributions. The spin susceptibility is scaled by the difference between hyperfine coupling tensors, therefore after normalisation gives the normalised spin susceptibility. This quantity can then be fitted with the Yosida function[141], which allows determination of the superconducting energy gap. To calculate the Yosida function the following expressions are used[142]:

$$\frac{K_s(T)}{K_s(T_c)} = Y(T) = 1 - 2\pi k_B T \sum_{n=0}^{\infty} \frac{\Delta^2(T)}{[\epsilon_n^2 + \Delta^2(T)]} \tag{4.15}$$

Where $K_s(T)$ is the Knight shift, k_B is the Boltzmann constant, Δ is the superconducting gap and $\epsilon_n = 2\pi(n + 1/2)k_BT$. An example calculation is given in Fig.4.2b, compared with tabulated values given by Muhlschlegel[143]. The superconducting gap is calculated using the following:

$$\Delta(T) = \Delta_0(0)\tanh\frac{k_B T c\,\pi}{\Delta_0(0)}\sqrt{\frac{2}{3}\left(\frac{T_c}{T} - 1\right)\frac{\Delta C}{C}} \tag{4.16}$$

Where $\frac{\Delta C}{C} = 1.43$. An example calculation of the energy gap for a BCS gap ratio of 3.53 is given in Fig.4.2a, again compared with tabulated values[143] for a BCS gap ratio of 3.53. By fitting Eq. 4.15 to the normalised spin susceptibility, determined

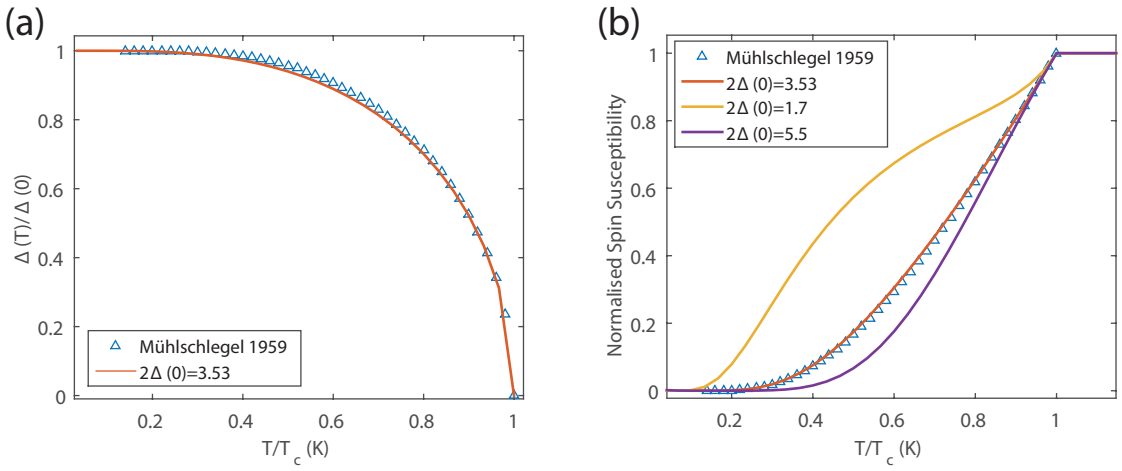

Figure 4.2: (a) Superconducting energy gap (b) Yosida Function

experimentally via Eq. 4.14, one may extract the superconducting gap ratio. Other superconducting gap ratios are also calculated in Fig. 4.2a, for the strong coupling the gap ratio is larger (5.5) and shows a more rapid deviation.

4.4 Nuclear Spin Relaxation in a metal

The hyperfine interaction between electrons and nuclei provides a powerful channel for relaxation in a metal, usually this arises from the on-site Fermi contact interaction which describes the electrons in the s-orbitals. It is also possible for the dipolar, orbital and core-polarisation terms to contribute, and in some circumstances these are the largest terms.

Nuclear spin-lattice relaxation in a metal can be framed in terms of a scattering process and sketched out as follows according to Slichter[144]. The assumptions are a dominant Fermi-contact term and the nuclear spins within a gas of free electrons. An electron, which is initially in spin state $\downarrow$ and has wavevector $\mathbf{k}$, comes into contact with a nucleus in spin state s=$\uparrow$. In the presence of a magnetic field, the collision causes both electron and nucleus to have changed their Zeeman energies, and the differing γ means that the electron also changes its kinetic energy. Now the electron is in spin state $\uparrow$ with wavevector **k'** and the nuclues with spin state s'=$\downarrow$. This is illustrated in Fig. 4.3.

In order to describe the scattering one may use Fermi's Golden Rule, which describes the probability per second of the transition of an electron from initial state i to final state f and is given by

$$W_{if} = \frac{2\pi}{\hbar}|\langle i|\hat{V}|f\rangle|^2\delta(E_f - E_i - \Delta E) \tag{4.17}$$

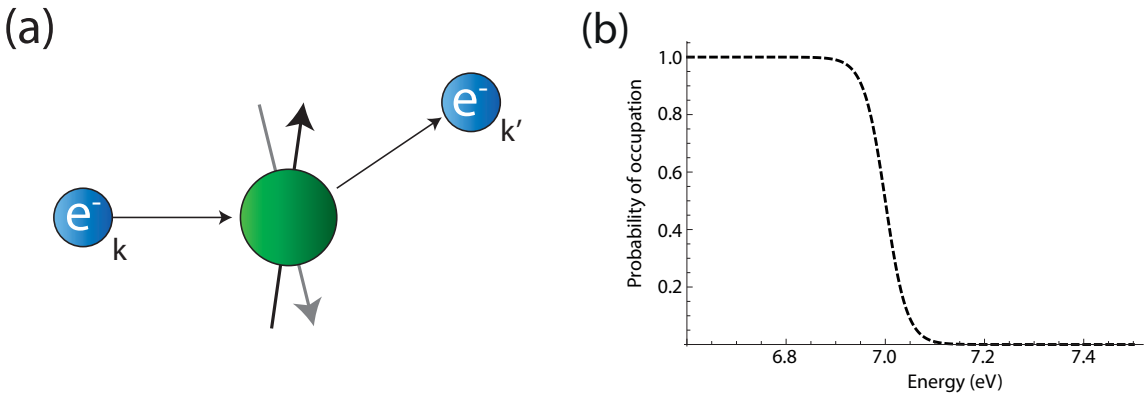

Figure 4.3: (a) Illustration of relaxation process between nuclei and electrons (b) Fermi distribution function at 250 K

Where ΔE is the change in nuclear Zeeman energy, $\hat{V}$ is the hyperfine coupling energy operator, given in this case by the Fermi-contact interaction and E_i and E_f are the energies of initial and final states respectively. The conduction electrons in a metal follow Fermi-statistics, this has two important consequences.

Firstly, the average kinetic energy of the electrons is much larger than the thermal energy (k_BT) and are of the same order of the Fermi energy (E_F). Secondly, the Pauli-exclusion principle means that only electrons within a narrow band at the Fermi-level can participate in the scattering process. This is described by the Fermi Function $f(E)$, which gives the probability that an initial state is empty. The probability that the final state is empty is given by $1 - f(E)$. The probability of a flip of the nuclear and electron spins is given by

$$W = \frac{2\pi}{\hbar} \int |\langle i|\hat{V}|f\rangle|^2 f(E_i)(1 - f(E_i + \Delta E))\rho(E_i)\rho(E_i + \Delta E)dE_i \tag{4.18}$$

The difference between the initial and final electron states after the scattering event is just the change in nuclear Zeeman energy, and this is a very small change with respect to the thermal energy of the lattice (k_BT). Therefore by neglecting the energy difference and integrating over the final energy

$$W = \frac{2\pi}{\hbar} \int |\langle i|\hat{V}|f\rangle|^2 f(E_i)(1 - f(E_i))\rho(E_i)^2 dE_i \tag{4.19}$$

Then by neglecting any changes in the energy of $|\langle i|\hat{V}|f\rangle|$ and $\rho(E)$, that are comparable to k_BT, the spin-lattice relaxation rate may be defined as

$$\frac{1}{T_1} = W = \frac{2\pi}{\hbar}[|\langle i|\hat{V}|f\rangle|^2_{E_F} \rho(E_F)^2 k_BT \tag{4.20}$$

As this expression depends on k_BT it is clear that $1/T_1$ will be inversely proportional

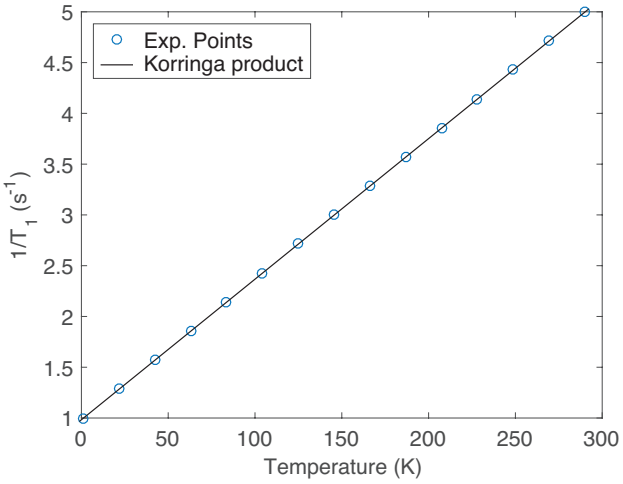

Figure 4.4: Nuclear spin lattice relaxation in a metal following a linear dependence on temperature, known as the Korringa law

to temperature, as shown in Fig. 4.4, this is known as the Heitler-Teller relaxation law.

$$\frac{1}{T_1} \propto T \tag{4.21}$$

The nuclear spin-lattice relaxation rate in metals may also be related to the Knight shift, as both originate from the Hyperfine interaction. This is known as the Korringa relation and is discussed in the following section.

4.4.1 Korringa relation

The Knight shift (K) and relaxation rate (T_1) can be related through the Korringa expression[145], which is defined as

$$\frac{1}{T_1 T} = \frac{4\pi k_B}{\hbar}\left(\frac{\gamma_n}{\gamma_e}\right)^2 K^2 \tag{4.22}$$

where γ_n and γ_e is the nuclear and electron gyromagnetic ratio respectively. The Korringa relation is useful because it helps to determine other mechanisms of relaxation. If one rearranges the above equation, the right-hand side is made up of constants

$$T_1 T K^2 = S \tag{4.23}$$

Where S is defined as

$$S = \frac{\hbar}{4\pi k_B}\frac{\gamma_e^2}{\gamma_n^2} \tag{4.24}$$

This relationship allows one to predict T_1 values (or K values) depending on the information known[67]. In a simple (Fermi-gas) metal, one expects the Korringa relation to hold and S is constant, depending only on γ_n. In reality there are often deviations which arise from electron-electron correlations and one may use the relation

$$T_1 T K^2 = \alpha S \tag{4.25}$$

where α measures the strength of electron correlations by the deviation from unity. $1/T_1$ probes the dynamic spin susceptibility and can be enhanced by either ferromagnetic or antiferromagnetic correlations. Whereas K probes the static susceptibility and only ferromagnetic correlations can enhance it[146].

The standard analysis is that when α is greater than unity, this implies the presence of ferromagnetic correlations and conversely in the presence of anti-ferromagnetic correlations then $\alpha < 1$. In a metal, the Knight shift is usually independent of temperature and T_1T is a characteristic value known as the Korringa product, this varies between superconductors.

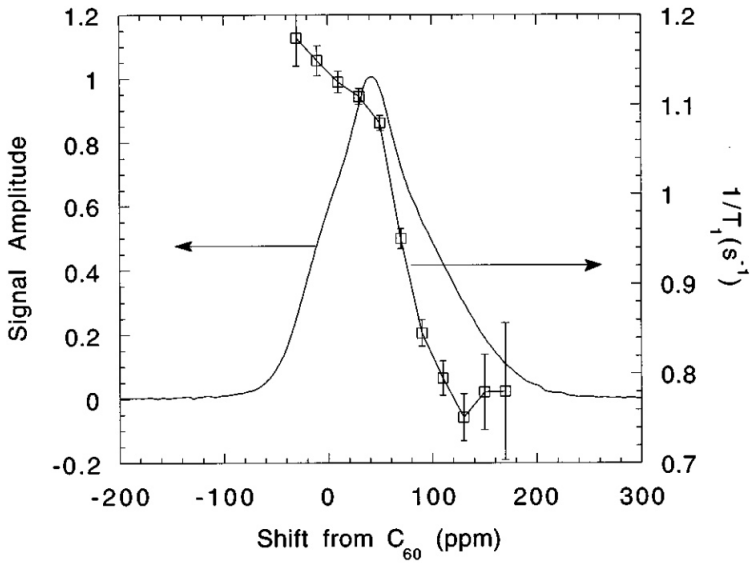

Figure 4.5: ^{13}C NMR spectrum of Rb_3C_{60}. Frequency dependent T_1 measurements over lineshape to test for dipolar relaxation mechanism. Reproduced from[28]

Additionally a deviation from unity implies that the relaxation mechanism does not originate solely from the Fermi-contact mechanism. This often indicates that another term in the hyperfine hamiltonian is large, or sometimes dominant. The other terms include the dipolar, core polarisation or orbital parts. One may test the dipolar term by integrating across the spectrum as shown in Fig. 4.5.

If one integrates in 'strips' across the spectral lineshape, the dipolar relaxation mechanism will be dependent on frequency. The ratio between the lowest and highest frequency is predicted to be 2.5 for the dipolar relaxation mechanism *only*.[28] If the ratio is less, then there may be additional relaxation mechanisms from the orbital or core terms. To determine the mechanism in more detail one requires ab-initio calculations, discussed in more detail elsewhere.[36, 147, 148].

4.5 Nuclear Spin Relaxation in the Superconducting State

The spin-lattice relaxation rate is a crucial tool in the study of superconductors, both in the normal and superconducting states.

4.5.1 Hebel-Slichter coherence peak

A classical signature of the BCS theory is the enhancement of $1/T_1$ at the superconducting transition temperature, followed by an exponential fall off at lower temperatures. This is also known as the coherence peak and is shown in Fig.4.6. It was first predicted by and then observed experimentally by Hebel and Slichter in 1957[2]. They used BCS theory to calculate the ratio, R_s/R_n ($R=1/T_1$) of the normal and superconducting state at T_c. The Hebel-Slichter peak has two origins[28] as follows: (a) The temperature is lowered below T_c, and there is a 'piling up' of the density of states at the Fermi-level (b) The coherence factor from the BCS model can be positive or negative, in the case of NMR it is positive and this leads to an enhancement. At $E = \Delta$ there is

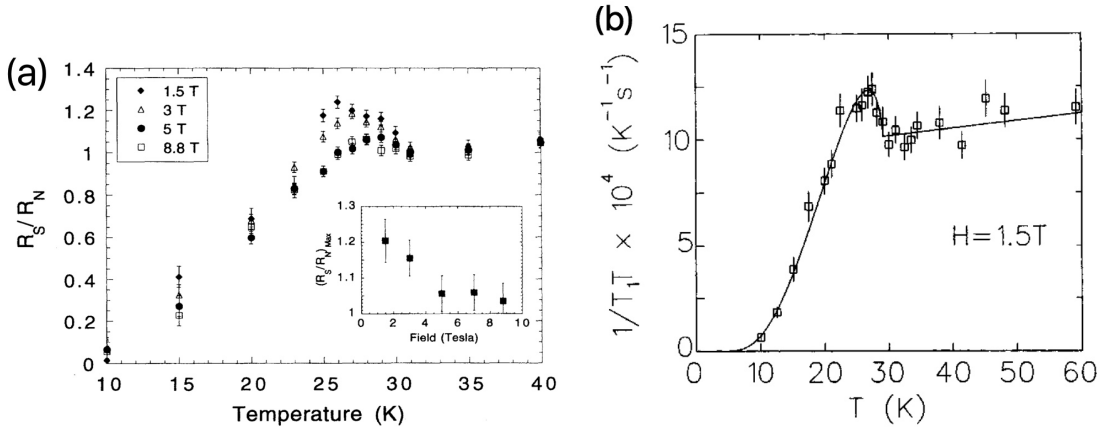

Figure 4.6: Temperature dependence of (a) ^{13}C NMR relaxation and (b) μSR relaxation. Both techniques show Hebel-Slichter peak below T_c. Reproduced from[149] and [91] respectively.

a logarithmic divergence, however in reality there are mechanisms which suppress the peak. These include, the magnetic field, pair-breaking interactions, anisotropy of the gap, d-wave pairing and anisotropy of the upper critical field. [8]. This is taken into account in the calculation of the relaxation rate in NMR by including a broadening function $B(E'-E)$. The expression to calculate R_s/R_n, taken from[150], is given as follows

$$\frac{R_s}{R_n} = \frac{2}{k_B}\int_{\Delta}^{\infty}[N_s^2(E)+M_s^2(E)]f(E)[1-f(E)]dE \tag{4.26}$$

where k_B is the Boltzmann constant, $f(E)$ is the Fermi function and $N_s(E)$ is the normal density of states which is given by

$$N_s(E) = \int B(E'-E)\frac{E'}{(E'^2-\Delta^2)^{1/2}}dE' \tag{4.27}$$

and $M_s(E)$ is known as the anomalous density of states and is defined by

$$N_s^2(E)C_+(E) = N_s^2 + M_s^2(E) \tag{4.28}$$

and is given by

$$M_s(E) = \int B(E'-E)\frac{\Delta}{(E'^2-\Delta^2)^{1/2}}dE' \tag{4.29}$$

The term $B(E'-E)$ is the broadening function and from Hebel and Slichter[2, 3], is set to be a rectangle with a breadth of between $1-10\%$ centered around $E'=E$. The coherence factor is given by

$$C_{\pm}(\boldsymbol{k},\boldsymbol{k'})\frac{1}{2}[1\pm(\Delta^2/E_kE_{k'})] \tag{4.30}$$

where the sign is positive for NMR and negative for ultrasonic attenuation. The BCS theory also predicts a fall off at temperatures below T_c which is given by

$$\frac{1}{T_1} \propto \exp^{\Delta(T)/k_BT} \tag{4.31}$$

where Δ is the superconducting gap value. Therefore T_1 measurements in the superconducting state allow extraction of Δ and therefore $2\Delta/k_BT_c$.

4.6 Peak shape and vortex structure

The NMR spectrum is a linear map of the magnetic field inside a material and therefore it is a powerful tool to probe Type II superconductivity. This is because in the region between H_{c1} and H_{c2} a type-II superconductor is penetrated by a regular array of super-

current vortices which generate a magnetic field. This magnetic field varies spatially with intensity and this is reflected in an NMR spectrum whilst in the superconducting state.

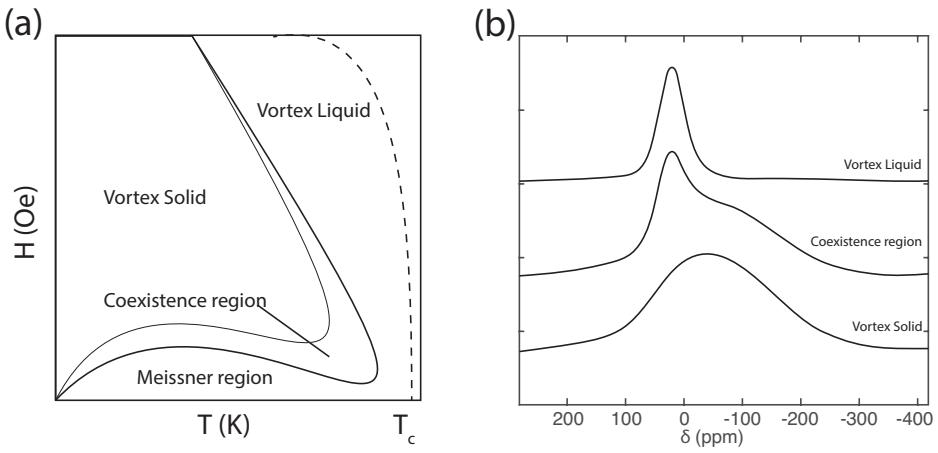

Figure 4.7: (a) Vortex phase diagram (b) Corresponding NMR peak shape

The periodic array of vortices in type-II superconductors is known as the Abrikosov lattice. Vortices have their own phase diagram which describes the motion of flux lines, as described in section 3.1.4 and shown in Fig. 4.7(a). At temperatures just below T_c they are in the liquid phase, characterised by rapid fluctuations of the flux line. At T$\ll T_c$ they enter the solid phase, which is also known as the Abrikosov lattice. This is characterised by a periodic array of flux lines that is static. The coexistence region has regions of both solid and liquid vortices. There is also a Meissner region in which the magnetic field is completely expelled, this region corresponds to fields below H_{c1}

In terms of NMR one may collect information regarding these phases by following the lineshape and linewidth as a function of temperature. The corresponding NMR lineshapes are shown in 4.7(b). The nuclear spins probed using magnetic resonance will experience a local magnetic field from the fluctuations of the vortices, which can be described in terms of a correlation time τ_c. When τ_c is long with respect to the NMR acquisition time, as for liquid vortices, one observes a time average of the local field and the NMR signal is narrow. If τ_c is longer than the NMR acquisition time, as for solid vortices, then this averaging does not occur and the corresponding NMR signal is broad and featureless[151]. The transition between phases is described as vortex melting and is the point at which τ_c changes rapidly.

An example of this is shown in Fig. 4.8, which shows the ^{17}O NMR parameters as a function of temperature for $YBa_2Cu_3O_7$. Fig. 4.8(a) shows the temperature dependence of the peak shape and 4.8(b) shows the linewidth and frequency. As the sample is cooled the NMR peakshape changes from a relatively narrow line which remains unshifted until T_c. At this point there is a slight change in position characteristic of the

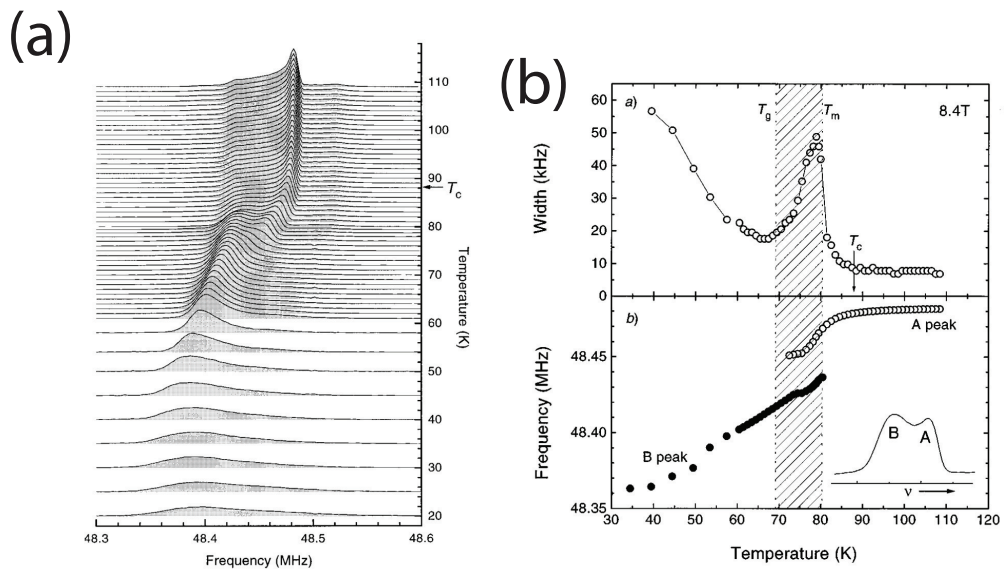

Figure 4.8: ^{17}O NMR parameters for $YBa_2Cu_3O_7$ in the normal and superconducting state. (a) Peak shape variation showing solid and liquid vortices (b) NMR linewidth and frequency. T_m shows transition from liquid to solid vortices, at T_g there is only solid vortices. Reproduced from [151]

onset of the superconducting state and the linewidth also increases. Then at T_m there is a dramatic drop in linewidth characteristic of the liquid vortices which have rapid fluctuations averaging the local field. Also the lineshape gains an additional double peak structure, which corresponds to the coexistance region of both solid and liquid vortices shown in Fig. 4.7. Then as the temperature is lowered further to T_g, there is only a single broad peak which is characteristic of the inhomogeneous distribution of the solid vortices and the linewidth begins to increase again.

4.7 Penetration depth

In the superconducting state there is an inhomogeneous distribution of magnetic fields which arises from the vortices. Although detrimental to determining the spin shift, this line broadening may be exploited to extract the London penetration depth. This is accomplished using the following procedure. The Abrikosov lattice is made up of a periodic array of quantised magnetic flux, the largest value of the magnetic field is in the vortex cores and decays across the characteristic length, λ. The distribution of fields may then be expressed as[152]

$$\Delta B_{local} \sim 0.0609 \frac{\phi_0}{\lambda} \tag{4.32}$$

Where ϕ_0=2.07×10^{-7} Oe/cm^2, λ is the penetration depth. The NMR linewidth is $\Delta f = \gamma_n \Delta B_{local}$ and this becomes broader as the temperature is lowered below T_c reflecting the change in penetration depth. The peak shape may be fit to a Gaussian lineshape, and then the parameter Δf may be extracted from this fit as a function of temperature, therby allowing determination of the penetration depth[152]. Examples of this analysis are given[81]

4.8 Literature Review: NMR on the Fullerides

4.8.1 NMR on Rb_3C_{60}

NMR studies of the fullerides have principally consisted of ^{13}C and the respective NMR active alkali isotope. This thesis is mainly concerned with the rubidium fulleride Rb_3C_{60}. The relevant NMR parameters are as follows. ^{13}C is I=1/2, has natural abundance=1.11% and γ_n=10.705 MHz/T, ^{87}Rb is I=3/2, natural abundance=27.85% and γ_n=13.801 MHz/T.

The static ^{87}Rb NMR spectrum of Rb_3C_{60} shows three distinct sites at room temperature, shown in Fig 4.9(a). These sites correspond to one octahedral site, denoted O and two tetrahedral sites, denoted T and T′.[153]. The first experiments using ^{87}Rb NMR to probe Rb_3C_{60}[154, 155] revealed an unexpected lineshape, there were three sites instead of the two which would arise from an ideal fcc lattice. The third site was shown to be an intrinsic property of these materials and not sample impurity[153–155]. This extra site is thought to be linked to the tetrahedral site, from observations of the T and T′ peaks merging at temperatures above 370 K, shown in the inset of Fig.4.9(a)). Furthermore 2D exchange spectroscopy confirms no exchange between O and T or O and T′ sites measured both static and under MAS. The T′ site was then attributed to modified tetrahedral sites. The origin of the third site is still not fully understood, but there are numerous hypotheses. For example merohedral disorder has been cited as a source of the third site.[156] Mehring et al. have challenged this idea and proposed a model based on diffusion between tetrahedral sites[153].

The static ^{13}C NMR lineshape for Rb_3C_{60} is a typical powder pattern shape found in static solids shown in Fig. 4.9(b). The chemical shift has been reported to be between 175-205 ppm[157]. The broad linewidth is related to the structural dynamics. The parent compound, C_{60}, rotates rapidly about its centroid and thus the ^{13}C NMR lineshape is usually narrow. This is in contrast to the fullerides, where the alkali atom restricts motion and causes the lineshape to become broader. This broadening is dependent on the size of the alkali atom, with size varying as follows (K<Rb<Cs). The larger the ionic radius the more the C_{60} rotation is inhibited and the broader the

^{13}C spectrum becomes.[28]. The ^{13}C T_1 of Rb_3C_{60} has been reported[81] to be quite rapid (0.25s) with respect to the C_{60}, which is known to be of the order of 120s.[158]

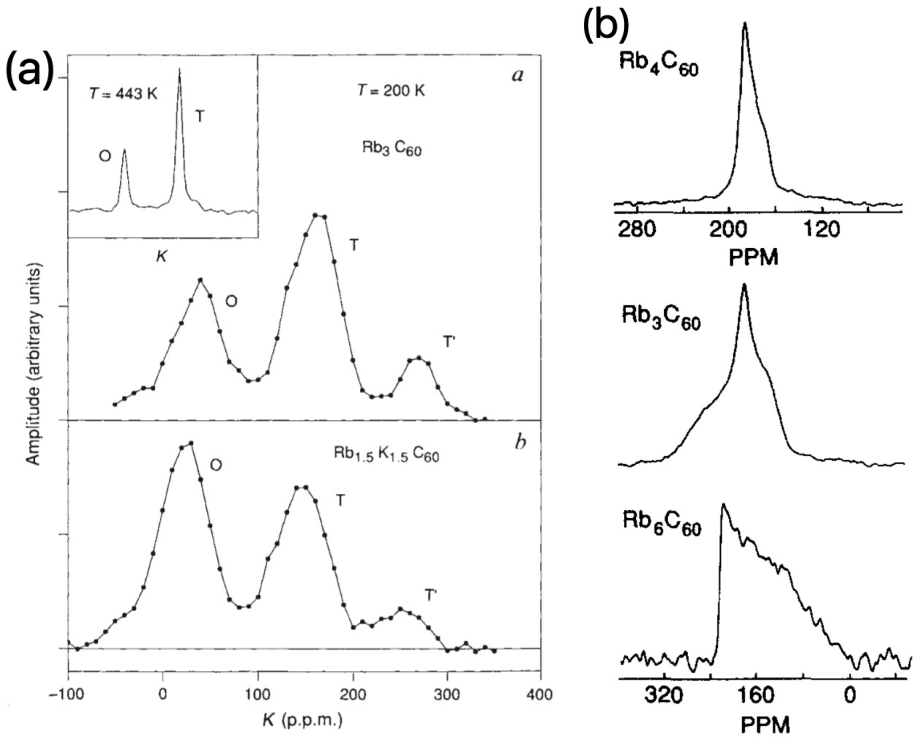

Figure 4.9: (a) ^{87}Rb NMR spectra of rubidium fullerides showing octahedral and two tetrahedral sites. Upper panel shows Rb_3C_{60}, inset shows merging of tetrahedral peaks at 443 K. Lower panel shows $Rb_{1.5}K_{1.5}C_{60}$. Data reproduced from [154] (b) ^{13}C NMR spectra of Rb_4C_{60}, Rb_3C_{60} and Rb_6C_{60}. Data reproduced from [159]

Studies of other fullerides containing various stoichiometries of rubidium and other alkali metals have shown the preferential order of filling of sites. For example when ^{87}Rb NMR is used to study K_2RbC_{60}, one observes a single peak corresponding to the octahedral site. Instead if Rb_2CsC_{60} is studied, then one finds the rubidium distributed amongst T and T′ sites, with no signal at the position of the O site. There is clearly a size ordered occupation of sites, with the relatively larger ions always filling the larger octahedral cavities. In K_2RbC_{60} the larger Rb ions occupy this space, but in Rb_2CsC_{60} Cs is the larger ion and Rb is pushed to the smaller tetrahedral sites.There is a further line splitting of both the O and T lines and an additional O' site is observed when one uses MAS techniques to increase resolution.[153]

4.8.2 Rb_3C_{60} Knight shift

The determination of the Knight shift is an important parameter to study the electronic structure of metals and superconductors, as outlined in section 4.2. The temperature

dependence of the magnetic shift gives information on the variation of the Knight shift, which is related to the spin susceptibility. Typically in metals the susceptibility does not depend on temperature, but in a superconductor the pairing of electrons causes the susceptibility to decrease, this is outlined in more detail in section 4.3. The value of the Knight shift, as well as its temperature dependence is outlined here for Rb_3C_{60}.

^{13}C NMR

The ^{13}C Knight shift has been reported by various authors in the Rb_3C_{60} system but there is discrepancy between values reported. Tycko 1992 et al. gives a Knight shift value of 30-40 ppm[81], but they comment that one must take into account Meissner screening currents which screen the applied field, and further suggest that the 30-40 ppm Knight shift extracted might be due purely to the diamagnetism of the sample in the superconducting state. They use the relationship

$$B = H_0 + 4\pi M(1 - n). \tag{4.33}$$

Where H_0 is the applied field, M is the magnetisation taken from susceptibility measurements and n is the demagnetising factor. They calculate the average internal field ($\langle B \rangle$) is reduced by approximately 20 G (200 ppm) and therefore conclude that the reduction in shift might be explained by this alone. Mehring et al. reported 47 ppm[155], they use MAS-NMR data of C_{60} (143 ppm), Rb_3C_{60} (196 ppm) and Rb_6C_{60} (157 ppm). They then assume a shift of 2 ppm per electron doped on C_{60}[1], therefore Rb_3C_{60} has a chemical shift of 149 ppm. To extract the Knight shift one simply subtracts the chemical shift from the magnetic shift of Rb_3C_{60}, that is K_s+K_{orb}. The resulting quantity is the Knight shift. This is consistent with later measurements reporting the shift to be 52 ppm, also extracted from the shift with respect to the parent insulator C_{60}.[160]

One may also use the magnetic shift value in the superconducting state as an approximate value for the chemical shift, as the Knight shift is expected to decay (for an s-wave superconductor). The lowest temperature point should ideally be used, where the slope is zero, implying the spin susceptibility has fully decayed and the resulting shift is just the chemical shift term. This method has been used previously, and yields a chemical shift of σ_{iso}=155 ppm[90] and is consistent with K_s proposed by other studies.[81, 155, 160]

The total shift is shown in Fig. 4.10, the temperature dependent variation shows the susceptibility is constant at temperatures above T_c characteristic of a normal metal. At temperatures below T_c there is a decrease in shift, which arises due to the pairing

[1]They take the shift value of Rb_6C_{60} and compare this with the undoped C_{60} shift, the assumption is that for every Rb ion doped onto C_{60} there is a 2 ppm shift

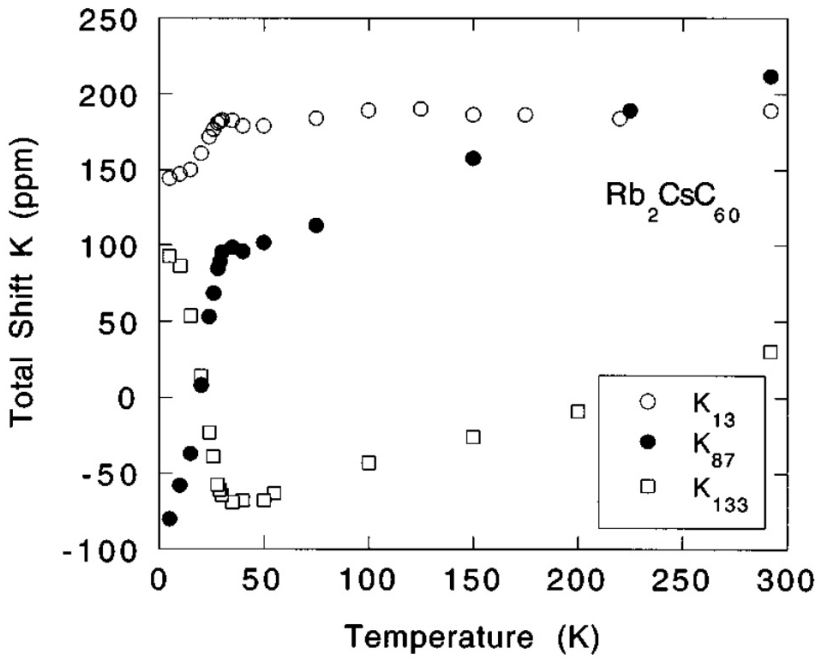

Figure 4.10: Variation of total shift, showing the indirect measure of the susceptibility, observed using static ^{13}C, ^{87}Rb and ^{133}Cs NMR on a polycrystalline sample of Rb_2CsC_{60}. Data recorded at 8.8 T and referenced to the free alkali ions. Reproduced from[28]

of electrons in the superconducting state, this is also concomitant with typical *s*-wave superconductivity.[28]

^{87}Rb NMR

The ^{87}Rb Knight shift is difficult to determine because there are three peaks which overlap in the static NMR spectrum of the polycrystalline solid. However one may follow the weighted average of the peaks. The magnetic shift is temperature dependent in both the normal and superconducting states, this is shown in Fig. 4.10. In the superconducting state this is clearly due to the decrease of spin susceptibility, arising from the pairing of electrons. In the normal state the mechanism was not as obvious, and it was proposed that the spin susceptibility must change between 298-30K (normal state) as well. An agreement was found between NMR shift and magnetic susceptibility data[155] which both depend on the Pauli spin susceptibility, and also a weak temperature was found for ^{13}C shifts.[2] This would usually imply that the bulk susceptibility is temperature dependent, but the variation in ^{13}C and magnetic susceptibility measurements was significantly weaker than the ^{87}Rb shifts, leaving the

[2]Additional terms such as the chemical shift also influence the total magnetic shift but just act as an offset and can be ignored.

problem still unresolved. It is likely that the susceptibility change is a local effect, as other measurements of the ^{13}C shift are not temperature dependent, for example in Fig. 4.10.

The temperature dependence of the shift for ^{113}Cs and ^{87}Rb nuclei in Rb_2CsC_{60} was later studied, shown in Fig. 4.10[28]. The data shows that in the normal state there is a temperature dependence for both nuclei which follows a very similar trend, but the entire curve is offset by approximately 200 ppm. The offset is easily explained by a difference in hyperfine interaction, which is expected for different nuclei. In the superconducting state the ^{87}Rb magnetic shift falls to lower frequency, which as discussed previously, is due to electrons pairing up in the superconducting state, the spin susceptibility drops and so does the Knight shift. There is also a diamagnetic shielding of the applied field in the superconducting state, which also contributes. However the ^{113}Cs magnetic shift *increases* in frequency after T_c. A simple explanation given in literature is that ^{133}Cs has a negative Knight shift in the normal state, although this then negates the normal state shift explanation if ^{87}Rb and ^{133}Cs have opposite signs. As ^{87}Rb has spin I=3/2, a nuclear quadrupole moment is present, however as reported previously the octahedral and tetrahedral quadrupolar interaction is small[90]. This is consistent with the cubic nature (FCC) of the unit cell.

4.8.3 Rb_3C_{60} Spin Susceptibility

The spin susceptibility decays in both ^{87}Rb and ^{13}C spectra below T_c as discussed in the previous section. One may follow the decay and fit the Yosida function to extract the superconducting gap ratio, as discussed in section 4.3.1. Although one must first remove the diamagnetic contribution which arises from Meissner screening currents. This may be removed by subtracting the shifts of two different nuclei, the resulting quantity after normalisation is the normalised spin susceptibility as discussed in section 4.3. This has been done previously in the Rb_2CsC_{60} system using ^{13}C, ^{87}Rb and ^{133}Cs shifts. This is shown in Fig. 4.11, the solid points are fit to different Yosida functions which represent different superconducting gap ratios. The gap ratio best fit to the subtractions is $2\Delta_0 = 3.52kT_c$, which is the predicted ratio from BCS theory, indicating the fullerides are conventional *s*-wave superconductors.[100]. Other Yosida functions are shown, such as $2\Delta_0 = 4kT_c$ and this may also be representative of the experimental points. Interestingly measurements of ^{13}C $1/T_1$ studies[81] give this same gap ratio. The discrepancy may be related to the accuracy of the method used, and it is commonly suggested that T_1 measurements are a more reliable way to determine the superconducting gap.[36] This is because there is often an error on the Knight shift value due to the typically large linewidths in static polycrystalline solids.

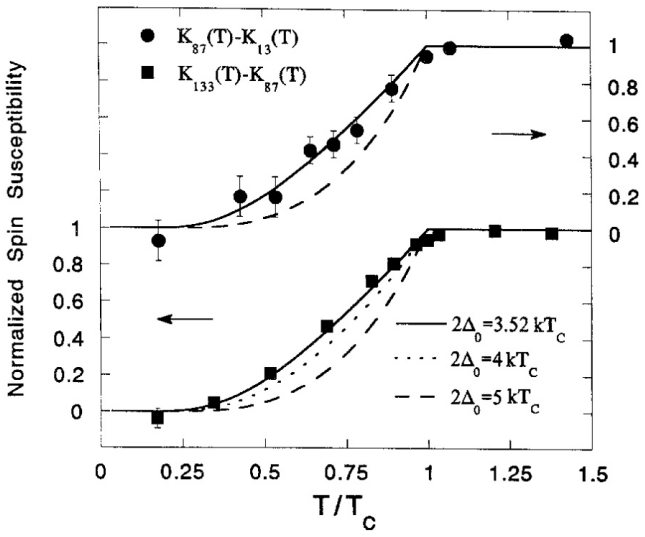

Figure 4.11: NMR Knight shift differences for Rb_3C_{60} (K_{87}-K_{13}) and Rb_2CsC_{60} (K_{133}-K_{87}) fit to the Yosida function to extract the superconducting gap ratio. Reproduced from [100]

4.8.4 Rb_3C_{60} T_1 in the normal state

The determination of T_1 is an important parameter as discussed in section 4.4. In a metal the temperature dependence should follow the Korringa law, in a superconductor there is a deviation at T_c with a coherence peak for BCS s-wave superconductors, as discussed in section 4.5.1. Another useful parameter to determine is the Korringa product (T_1T) which can help to determine the mechanism of relaxaion, as described in section 4.4.1.

A key parameter for superconductivity is the electronic density of states at the Fermi level ($N(E_F)$) in the normal state. It may be theoretically predicted using the local density function approximation, but this can fail if electronic correlations or orientational order are important. NMR can help to provide an experimental determination, as $1/T_1T$ is proportional to the square of the density of states at the Fermi-level as

$$\frac{1}{T_1T} = \frac{\pi k}{\hbar} A^2 N(E_F)^2 \tag{4.34}$$

A is the hyperfine coupling constant, which was determined to be A=1.1x10^{-20} erg, $\hbar$ is plancks constant divided by 2π.

^{13}C NMR

Tycko et al. determined $N(E_F)$ to be 22 eV^{-1} for Rb_3C_{60}[81]. They also used the Korringa ratio to calculate the Knight shift to be K_{iso}≈160-260 ppm. This was rather

large compared to the observed value of K_s determined experimentally, this is evidence that the relaxation mechanism may have a relatively large contribution from the spin-dipolar hyperfine hamiltonian. Subsequent experimental[84, 155] and theoretical[161] studies also vindicated this.

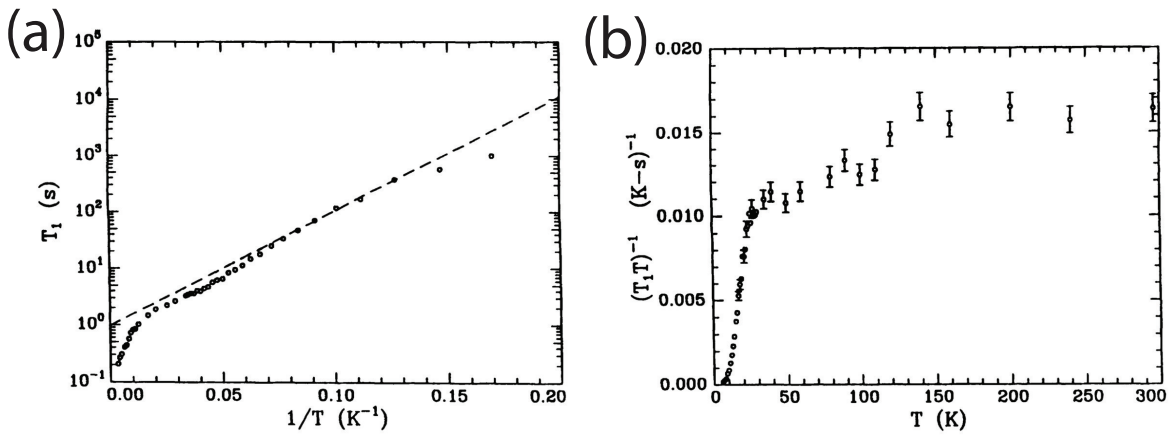

Figure 4.12: Temperature dependence of the ^{13}C NMR spin-lattice relaxation time T_1 on a polycrystalline sample of Rb_3C_{60} data recorded at 9.39 T. (a) Temperature dependence of T_1 plotted as logT_1 vs T^{-1}, solid line is Arrhenius fit yielding 2Δ=94 K (b) Temperature dependence of Korringa product plotted as $(T_1T)^{-1}$ vs T. Reproduced from[81]

The ^{13}C Korringa product was determined to be 0.01 $(sK)^{-1}$ from previous works[159]. LDA calculations[161] have confirmed the dipolar mechanism is the dominant contribution to relaxation in the fullerides. This implies that the ^{13}C nuclei interact with electron spin density on the $2p_z$ orbital, which points radially from the centroid of the C_{60} molecule. Following this study was an effort to vindicate the dipolar mechanism experimentally[162]. It was found that this contribution to the relaxation was only half of the total, and that an additional isotropic relaxation mechanism was involved. The authors suggested various sources such as an admixture of 2s into $2p_z$ orbitals or core polarisation of the 1s orbitals and spin polarisation of the three sp^2 orbitals, that are involved in bonding.

Although it was clear that there was a spin-dipolar contribution, there was still a remaining term to be accounted for as the dipolar mechanism did not fully account for the anisotropy which was seen experimentally. The suggested mechanisms were core polarisation of the 1s orbital and spin polarisation of the sp^2 orbitals involved in bonding. Another proposed mechanism arises from admixture of the 1s and $2p_z$ orbitals from the curvature of the fullerene.[162]

The superconducting gap has been determined to be Δ=46.8 K from temperature dependent T_1 measurements at 9.39 T.[81] The gap is extracted by using the Arrhenius law described in section 4.5.1. The T_c determined from NMR measurements (23±1),

gives a superconducting gap ratio of $2\Delta_0/k_BT_c$=4.1, which is larger than the BCS ratio of 3.5.

The deviation from the Arrhenius line at lower temperatures is from an additional relaxation mechanism which arises due to vortices in the superconducting state, the last two points are therefore not taken into consideration when determining the superconducting gap ratio[81].

^{87}Rb NMR

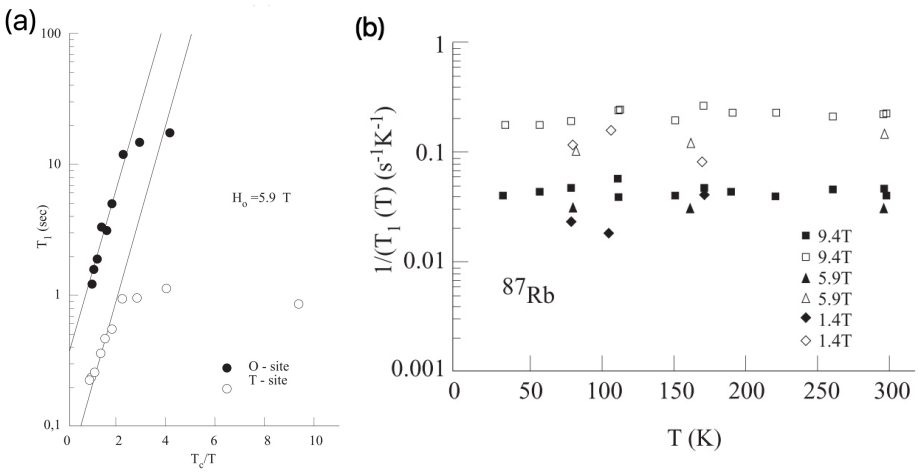

Figure 4.13: Temperature dependence of the ^{87}Rb NMR spin-lattice relaxation time T_1 on a polycrystalline sample of Rb_3C_{60} data recorded at 5.9 T. (a) Temperature dependence of T_1 plotted as T_1 vs T_c/T, solid line is Arrhenius fit yielding 2Δ=90 K (b) Temperature dependence of Korringa product plotted as $(T_1T)^{-1}$ vs T. Reproduced from [163]

The T_1 measured using ^{87}Rb NMR follows the Korringa law of relaxation common to metals, shown in Fig. 4.13. The superconducting gap may be extracted using the Arrhenius law (solid line in Fig. 4.13(a)), yielding Δ=45 K at fields of 5.9 and 2.3 T[163]. This corresponds to a gap ratio of $2\Delta = 3.2T_c$, which is characteristic of BCS theory. There is a deviation from this law at low temperatures is due to an additional relaxation mechanism from the vortices.

The ^{87}Rb Korringa product $1/(T_1T)^{-1}$ of Rb_3C_{60} is reported to be field dependent[163], as shown in Fig. 4.13(b). This has not been reported in other works[28] and it is unclear if it is an intrinsic effect or an experimental error.

4.8.5 Hebel-Slichter peak in Rb_3C_{60} T_1

The Hebel-Slichter coherence peak was absent from early NMR measurements at 2.37 T[81] but this has since been shown to be incorrect as following studies have shown

that the coherence peak is indeed present. μSR was the first definitive technique to show the peak at 2 T.[164] Then also Sasaki et al.[165] observed a broadened peak at 2.93 T using NMR. This was later confirmed in the Rb_2CsC_{60} system, in ^{13}C, ^{87}Rb and ^{133}Cs NMR by Stenger and Pennington[166] at fields between 1.5-5 T. The peak has also been reported in an ammonia intercalated fulleride using ^{1}H NMR.[167].

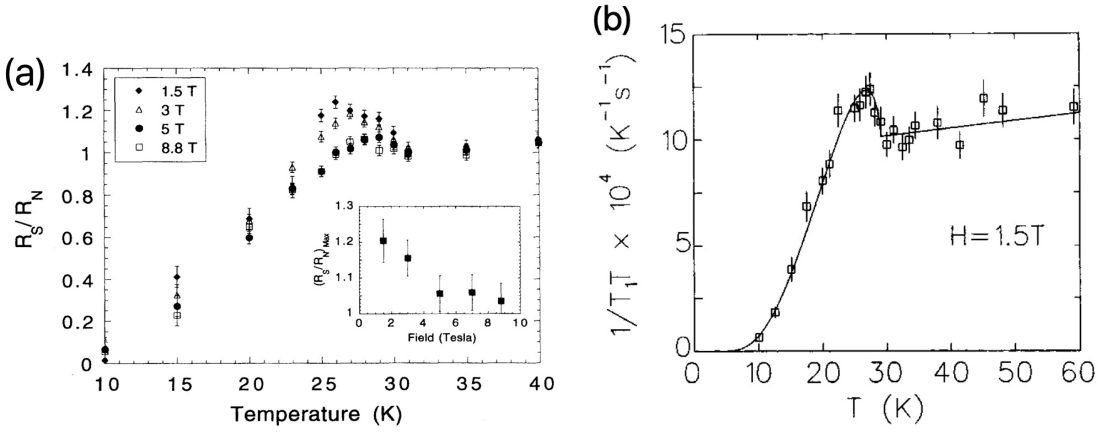

Figure 4.14: (a) ^{13}C NMR relaxation data showing Hebel-Slichter peak. R_s/R_n vs T for several magnetic fields. Inset shows maximum of R_s/R_n vs applied field. Reproduced from[149] (b) Temperature dependence of μSR relaxation rate of $Mu@C_{60}$ at a field of 1.5 T on a polycrystalline sample of Rb_3C_{60}. Reproduced from [91]

The maximum enhancement of the relaxation rate (R_s/R_n) is expected to be 1.1-1.2[165] in zero field using μSR. The enhancement reported before is similar to this but if one takes into account the characteristic phonon frequency for fullerides then the expected maximum enhancement of R_s/R_n is 2-3.[8] Therefore the peak is thought to be suppressed, and this has been noted elsewhere[28, 81, 100]. By definition, high-T_c superconductors work at higher temperatures, and this implies there are many electron-phonon decay channels open to the electronic excitations[168], this can lead to a suppression of the coherence peak. The theoretical studies which have been done on Rb_3C_{60} suggest a damping mechanism which arises from the Coulomb interactions.[8]

4.9 Literature Review: NMR on Magnesium Diboride

NMR studies of the magnesium diborides have principally consisted of ^{11}B NMR and if doped, ^{27}Al, ^{13}C or ^{25}Mg NMR. ^{11}B is I=3/2, has natural abundance=80.1% and γ_n=13.484 MHz/T, ^{27}Al is I=5/2, has natural abundance=100% and γ_n=10.705 MHz/T, ^{13}C is I=1/2, has natural abundance=1.11% and γ_n=10.958 MHz/T and ^{25}Mg is I=5/2, has natural abundance=10.0% and γ_n=-2.5743 MHz/T.

4.9.1 MgB_2 Knight shift

The ^{11}B MAS-NMR spectrum of MgB_2 shows one crystallographically unique site with a magnetic shift of 95 ppm at 8.5 T.[137]. The second-order quadrupolar interaction[132] produces a field dependent shift, as shown in Fig.4.15. The field dependence of the static powder lineshape is shown in Fig.4.15(b), there is a splitting resolved which is due to the dipole-dipole interaction between boron atoms[36] not observed under MAS.

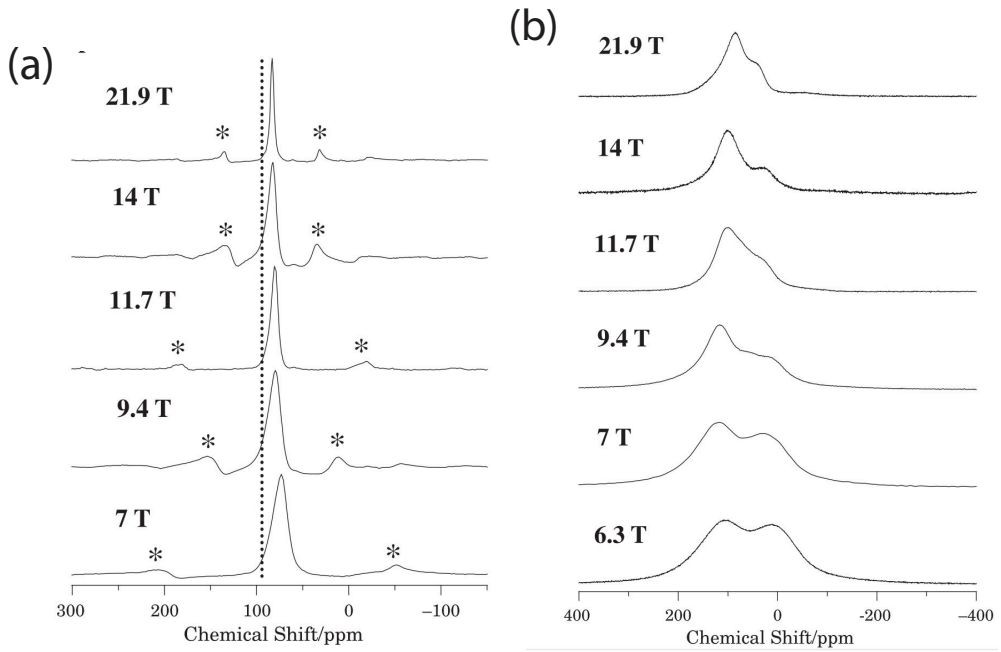

Figure 4.15: Field dependence of ^{11}B NMR lineshape of MgB_2 (a) MAS-NMR (b) Static NMR. Reproduced from [169]

An important quantity to determine is K_{spin} as discussed in section 4.2. The spin shift may be used to test mechanisms of relaxation through the Korringa ratio, it also allows one to indirectly follow the temperature dependence of the spin susceptibility. The latter is easy to follow as the temperature dependence of the spin susceptibility and therefore the Knight shift, is monitored through the temperature dependence of the

total magnetic shift. The former must be evaluated by extracting other contributions to the total magnetic shift, such as the chemical and second order quadrupolar shift (if applicable). However there is considerable disagreement in literature in evaluation of the Knight shift of MgB_2, which is due to various reference compounds used. It is also not completely clear if values reported are simply extracted from the room temperature shift or use a procedure to determine K_{spin} based on low temperature measurements.

The magnetic shift (K_{tot}) in Fig. 4.15 is 85 ppm at 7 T referenced to H_3BO_3[169]. This is in contrast to other studies, for example investigations on non-oriented powders have reported 80 ppm referenced to $NaBH_4$ and 40 ppm referenced to BF_3[36], 70 ppm with respect to $B(OH)_3$[125] and 41 ppm with respect to $C_6H_{15}B$ [148]. A study[170] on a single crystal of MgB_2 gives $K^{tot}_{iso} = \frac{1}{3} \times (K^{tot}_c + 2K^{tot}_{ab}) = 81(5)$ppm and $K^{tot}_{aniso} = \frac{1}{3} \times (K^{tot}_c - K^{tot}_{ab}) = 19(4)$ppm.

The temperature dependence of the total magnetic shift and thereby the Knight shift, is shown in Fig.4.16. The peak position in the normal state is generally constant, which is the expected behaviour for a metal. However Fig.4.16(a) shows a change in peak position at temperatures above T_c (39 K), whereas Fig.4.16(b) shows the change within a region more closely associated with T_c. It is not clear why there is a stark difference in the temperature dependence between these two studies, although it may be related to sample quality. Fig.4.16(b) also contains cryogenic MAS data (black squares), which also suggests the peak position is constant. The decrease in total magnetic shift is concomitant with the onset of the superconducting state, which is typical of BCS *s*-wave superconductors. This is strong evidence that the superconducting gap is of *s*-wave symmetry.

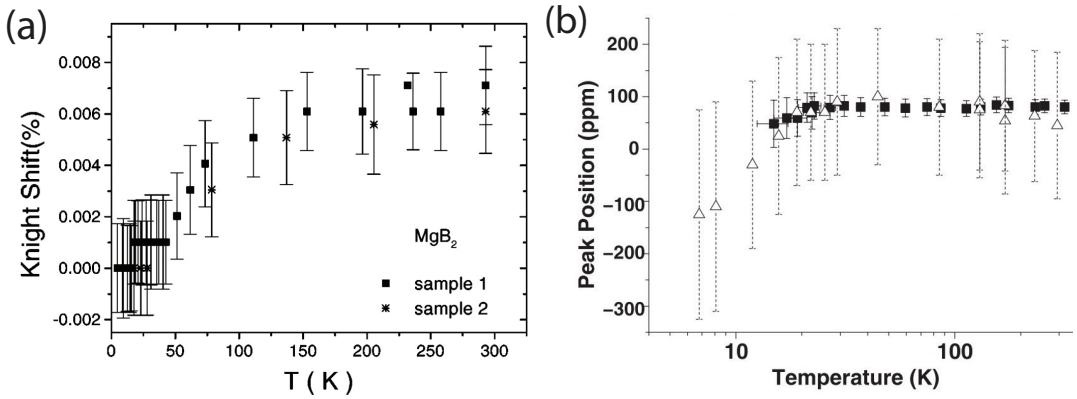

Figure 4.16: Temperature dependence of ^{11}B Knight shift on a polycrystalline sample of MgB_2. In the normal state the shift is relatively constant, below T_c it decreases concomitant with the onset of the superconducting state. (a) Static NMR measurements of Knight shift at 7.2 T expressed in % reproduced from [171] (b) Static (triangles) and MAS (squares) measurements expressed in ppm reproduced from [137].

Ab-initio calculations of the Knight shift

As discussed in the previous section there is an uncertainty in measurements of the Knight shift. An excellent way to test the validity of conjectures from experimental measurements is to simulate the NMR parameters such as Knight shift and T_1 using ab-initio methods, such as those described in refs.[36, 148, 172]. This has been done for ^{11}B and ^{25}Mg NMR, the results are reproduced in table 4.1.[147]. The Knight shift is reported to be mainly due to the hyperfine coupling with the s-electrons and the total Knight shift is reported to be 0.0044% which corresponds to 44 ppm, close to some of the experimental investigations reported previously.[36, 148] It is clear from table 4.1 that the largest contribution to the Knight shift is the Fermi-contact interaction as expected for metals. The dipolar and core polarisation contributes little to the shift, and the orbital part is zero.

	dipole (xy)	dipole (z)	orbital	Fermi-contact	core	Total (xy/z)
Mg	0.0005	-0.0010	0	0.0260	0.003	0.0271/0.0256
B	-0.0004	0.0008	0	0.0027	-0.0007	0.0016/0.0028

Table 4.1: Calculated dipole-dipole, orbital, Fermi-Contact and core polarisation contribution to the Knight shift in MgB_2. The label $\alpha = xy, z$ indicates the direction of the applied external magnetic field. Data reproduced from[147].Calculated using the approach described in Refs.[36, 148, 172].

4.9.2 Vortices studied using NMR

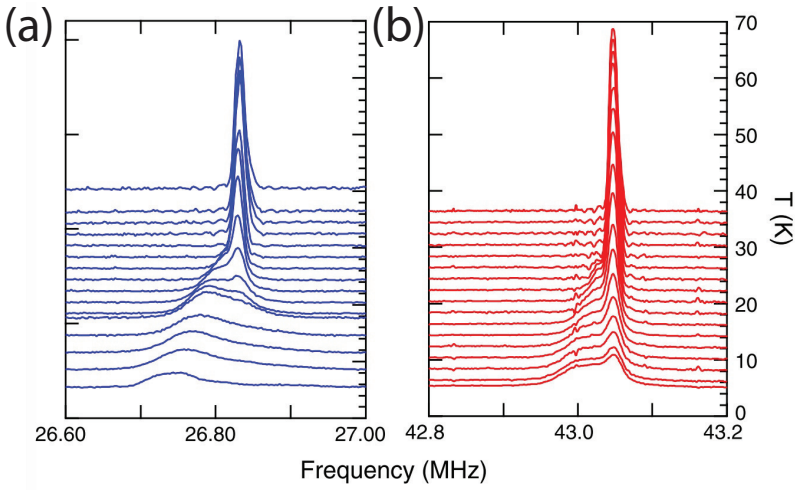

Figure 4.17: Temperature dependence of ^{11}B NMR lineshape of MgB_2 at fields of (a) 1.97 T and (b) 3.15 T. Reproduced from [173]

NMR may be used to study the vortex structure in the superconducting state, as discussed in section 4.6. The temperature dependence of the static NMR lineshape at

1.97 T is shown in Fig. 4.17(a) and at 3.15 T shown in Fig. 4.17(b) As the temperature is lowered below T_c a broad and asymmetric line appears, this is characteristic of the solid vortex phase and represents an inhomogeneous field distribution as well as diamagnetic screening currents.[173]. The solid phase vortex region has a flux correlation time that is slower than the signal acquisition time and this causes the peak shape to appear broad[151, 173].

The broad component increases with decreasing temperature and the narrow component decreases. The narrow peak is representative of the liquid phase vortex state and has a correlation time faster than the signal acquisition time, therefore the NMR signal is time-averaged and appears isotropic. There is a point at which both peaks exist, and this is known as the coexistence region where both solid and liquid vortex phase regions contribute to the spectral lineshape. At a field of 1.97 T the sample eventually reaches the solid phase vortex region only, and then only the broad component contributes to the spectrum. At 3.15 T the sample remains in the coexistence region even at 5 K.

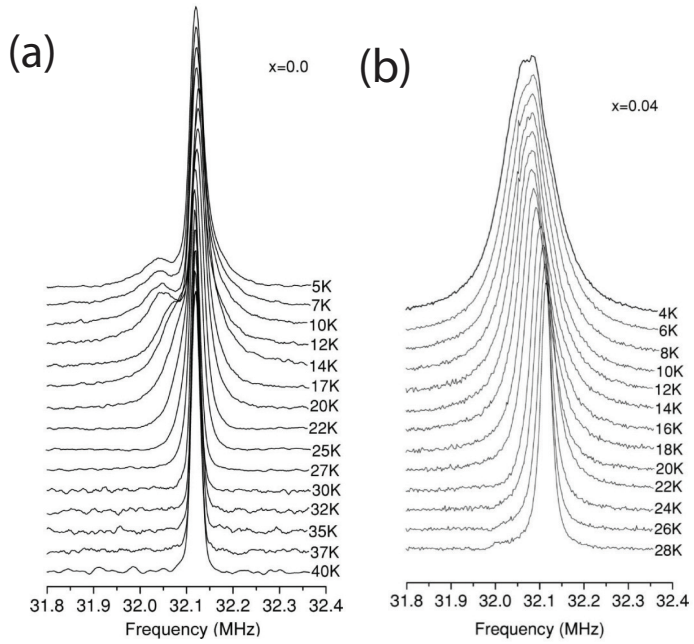

Figure 4.18: Temperature dependence of ^{11}B NMR lineshape on a sample of (a) MgB_2 (b) $MgB_{1.96}C_{0.04}$. Reproduced from [174]

As noted previously[173], the distribution is also related to the anisotropy of H_{c2} which arises from the temperature and orientation dependent superconducting gaps of MgB_2. This can be described as follows:

$$H_{c2}(\theta, T) = \frac{H_{c2}^{ab}(T)}{\sqrt{1 + (\gamma_\eta^2 - 1)\cos^2\theta}} \tag{4.35}$$

A polycrystalline powder has a distribution of crystal sites, and this means in MgB_2 the c-axis, which bisects the boron planes, will be oriented at a distribution of angles with respect to the applied magnetic field, B_0. Below T_c, at some angles H_{c2} will equal or be smaller than B_0 and the sample will remain in the normal state, there will also be a fraction which has a H_{c2} higher than the applied field and this part will be superconducting.

As the temperature is lowered, H_{c2} increases and there is a point in which all H_{c2} distributions are larger than B_0 and all of the powder will enter the superconducting state. Although as B_0 is still higher than H_{c1}, the sample will be penetrated by vortices.

The temperature dependence of the static ^{11}B NMR lineshape for the carbon doped MgB_2 system is shown in Fig.4.18. The additional peak at x=0.0 (Fig. 4.18(a)) shows the characteristic peak assigned to the vortex lattice as discussed previously, at a carbon doping level of x=0.04 (Fig. 4.18(b)) the normal state signal disappears below T_c. This is likely due to an enhancement of H_{c2} which arises from the addition of carbon and has also been noted in ^{27}Al NMR studies.[175]

4.9.3 MgB_2 T_1 in the normal state

The temperature dependence of the ^{11}B NMR spin-lattice relaxation, shown in Fig.4.19, has been widely studied[36, 125, 126, 171, 176, 177] and follows the expected behaviour for metals, i.e. the Korringa law of relaxation. The ^{11}B Korringa product (T_1T) is reported to be 178[174], 170[36], 165[171], 150[177] and 125[178] K sec. By combining the Knight shift and Korringa product, one can calculate the Korringa ratio (R) as discussed in section 7.3.6. R has been reported to be 0.2[171] and 0.1[36] for ^{11}B , this is highly suggestive that the ^{11}B relaxation mechanism in MgB_2 is unlikely to be mainly due to the Fermi-contact interaction. A possible explanation is that the relaxation is dominated by the orbital contribution, arising due to p electrons, as discussed in the next section. This contribution is proportional to the DOS at the Fermi level and to temperature, it supports the hypothesis that T_1T and the Knight shift originate from different mechanisms, this is vindicated by ab-initio calculations in the next section.

The Korringa ratio has also been reported to be near to unity for ^{25}Mg[176] and ^{27}Al, which is expected for metals. There has also been reports of R=0.4-1.0 for ^{27}Al, depending on Al doping [35], other literature reports [148] $R \approx 0.5$. It has been suggested that $1/T_1T \propto N(E_F)^2$ decreases as Al content increases, which demonstrates a reduction in DOS at the Fermi level as electrons are doped. Applying the McMillan equation allows estimation of the electron-phonon coupling constant and the characteristic phonon frequency, $\lambda \sim 0.87$ and $\omega \sim 700$ K respectively. [126]

^{25}Mg NMR has a small magnetic moment and low natural abundance, despite this

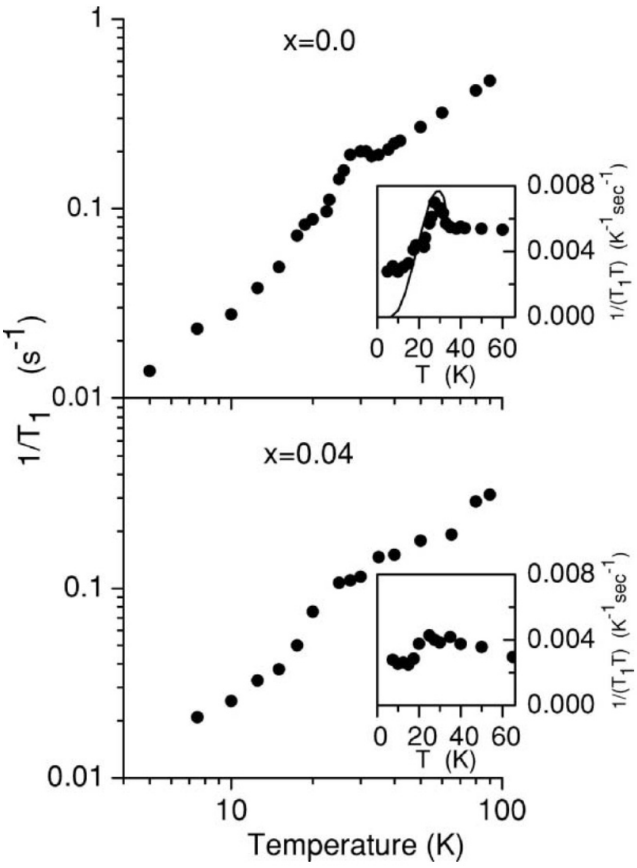

Figure 4.19: Temperature dependence of ^{11}B NMR spin-lattice relaxation rate for MgB_2 and $MgB_{1.96}C_{0.04}$ in a magnetic field of 2.35 T. Reproduced from[174]

there has been an investigation on MgB_2.[176] The Korringa ratio is 0.95, which is close to the unity value expected for *s*-electrons. This is consistent with ab-initio calculations which suggest the dominant relaxation mechanism is the Fermi-contact interaction, this is also true for the Knight shift.[147]

Ab-Initio Calculations of the Relaxation Rate

The data from LDA simulations reported in table 4.2 support the notion that the main source of relaxation in MgB_2 is the coupling between the nuclear spin and conduction boron *p* electrons. The data shows that relaxation is mainly due to *p* states and that the orbital relaxation rate is 3 times larger than the dipole rate and 10 times greater than the Fermi-contact rate. The reason the orbital contribution is much larger than the dipolar contribution, is that all three Boron *p* orbitals are at the Fermi level(E_F).[147] This is in contrast to the fullerides for example, which have only one *p* orbital (p_z) at E_F, and therefore the orbital term is reduced. This is supported by experimental studies in the previous section, which show the Korringa ratio to deviate from unity,

	orbital	dipole	Fermi-contact	core	Total	R
Mg	0.02	0.01	1.0	0.0001	1.0	1.0
B	2.6	0.8	0.28	0.02	3.7	0.27

Table 4.2: Calculated relaxation rate $1/T_1T$ in 10^{-3}/(K sec). R is the Korringa ratio, defined as the inverse of the total. Calculated using the approach described in Refs.[36, 148, 172]. Data reproduced from[147]

the experimentally determined ratio of R=0.1-0.2, is similar to the calculated value of R=0.27. After renormalisation(discussed in literature[147]), the theoretical value is more in line with the experimental result i.e. R=0.19. The mechanisms which underpin ^{11}B NMR relaxation and Knight shifts have also been studied as a function of Al doping, when x=0 relaxation is dominated by the orbital contribution. As x$\rightarrow$1, the relaxation becomes dominated by the Fermi-contact interaction as in most superconductors.[36]

4.9.4 Hebel-Slichter peak in MgB_2 T_1

NMR is a probe into the DOS in the superconducting state, in the case of a fully isotropic gap there is a coherence peak and exponential decay in $1/T_1$ with decreasing temperature, for an anisotropic gap $1/T_1$ is expected to follow a T^3 and T^5 for line and point nodes respectively.[144, 179]

In MgB_2 there is disagreement on the presence of a Hebel-Slichter coherence peak, some studies have reported that there is no peak[36, 171, 177], mainly citing a suppression mechanism due to the anisotropic nature of MgB_2. Although there have been other investigations which clearly show the coherence peak for MgB_2[125, 126, 180]. The peak has also been observed in similar analogues such as $MgB_{2-x}{}^{12}C_x$[174] and $MgB_{2-x}Al_x$[34, 126, 180]. An example of data reproduced[174] that shows the coherence peak is given in Fig.4.19.

The decay in relaxation was fit to single gap of $2\Delta/k_BT_c$=5, this is considerably larger than the BCS gap ratio of 3.5. There are some discrepancies from typical $1/T_1$ Korringa behaviour BCS behaviour below 15 K, which has been ascribed to vortex dynamics contributing to the relaxation mechanism[174]. In boron this deviation is enhanced from the presence of a dopant (carbon), this has also been noted in previous works[137]

CHAPTER

FIVE

EXPERIMENTAL METHODOLOGY

5.1 NMR

5.1.1 Room temperature NMR measurements

Static and Magic-angle-spinning (MAS) NMR experiments data were acquired on a 9.4 T Bruker Ascend 400WB spectrometer and a CMX chemagnetics infinity console, and a 14.1 T Bruker Avance-II 600WB spectrometer. The MAS experiments used nitrogen gas, for bearing and drive gases to maintain air sensitive samples in an inert atmosphere. Experiments using this equipment were primarily done for characterisation of samples after synthesis.

5.1.2 Cryogenic NMR measurements

Cryogenic experiments on the MgB_2 and fulleride materials were performed on 4.7 T or 8.5 T widebore magnets using an upgraded Bruker AMX 360 console. Experiments at 14.1 T were performed on an AMX 600 console. All experiments were run static using a helium gas flow cryostat from Janis Research Inc. The temperature was measured using a calibrated Lakeshore Cernox sensor, which has an accuracy of at least 0.1 K.

The probe used in the cryogenic experiments had an inductively coupled resonance circuit, the trimmer capacitor is a nonmagnetic NMQM22 from Voltronics. There is an additional capacitor series to this one to divide the voltage and a parallel capacitor to obtain lower frequencies. These capacitors are nonmagnetic multilayer chip-capacitors from TEMEX-ceramic.

All samples were stored and handled in an argon or nitrogen glovebox, MgB_2 samples were studied in zirconium oxide rotors and fulleride samples were sealed in glass under vacuum. The probe used in the variable temperature experiments was home built and had one channel. The coil size was adjustable depending on sample dimensions. All vacuum fittings in the probe and cryostat were Swagelok.

The procedure used in the variable temperature NMR experiments is as follows. (a) The probe is inserted into the cryostat, an o-ring mediates the connection and is

sealed. (b) The outer chamber of the cryostat is evacuated using a turbo pump to a pressure of 1.0×10^{-5} Torr, this provides an additional layer of thermal insulation. (c) The cryostat is inserted into the bore of the magnet and then a Janis Research inc. transfer line is slowly lowered into a 20 L helium dewer, a positive pressure is allowed to build to facilitate a flow of helium down the transfer line. (d) The transfer line is inserted into the cryostat and all connections are closed. Then the transfer line is fully opened until the Lakeshore Cernox sensor detects a change in temperature. (e) The transfer line flow is then adjusted to a point where there is an equilibrium between the heater inside the cryostat and the helium flow. With consideration to keep the heater below 80% of its maximum power, when working on medium heat mode. (f) The heater may be set to regulate the temperature automatically but the pressure flowing through the transfer line requires constant monitoring and adjusting.

5.1.3 Pulse sequences

Pulse sequences describe one or more defined blocks of radiofrequency energy typically applied at the Larmor frequency of the nuclei being studied in the NMR experiment. There are many different types which can be employed for a large number of practical uses, such as measuring relaxation rate, distances between atoms and obtaining NMR parameters such as the direct dipole-dipole coupling. There are three main pulse sequences used in this thesis, the Hahn-echo which is used to record spectra and the saturation and inversion recovery experiments, designed to monitor the T_1 time constant characterising nuclear spin-lattice relaxation.

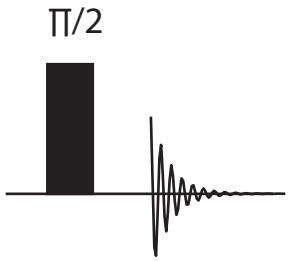

Figure 5.1: Illustration of a simple pulse acquire RF sequence

Hartman-Hahn echo

After application of a $\pi/2$ pulse, the net magnetisation vector will be tipped into the xy plane. It will then evolve by precessing about the B_0 field and a signal is induced in the NMR coil, which is the vector sum of all the magnetisation. As there is a distribution

of precession frequencies arising from the inhomogeneity of the B_0 field, the vector sum diminishes as the components 'fan out' or dephase. This is reflected in the FID which decays exponentially according to the time constant T_2. The Hartman-Hahn echo, or spin-echo was discovered in 1950 by Erwin Hahn[181] and is illustrated in Fig. 5.2. The application of a pulse rotates the net nuclear spin magnetisation from the axis parallel to the direction of the static magnetic field (B_0) to the y axis. Then during an evolution time, denoted τ, magnetisation will begin to dephase moving away from the +y axis causing the vector sum to decrease. A π pulse then flips the magnetisation to the other side of the xy plane and is now aligned along the -y axis. The magnetisation continues to dephase, but now is precessing in the same direction as before which means it now moves toward the -y axis and the vector sum increases. There is a point in time at which the vector sum is at its maximum, and the effects of field inhomogeneity have been removed and the FID is usually collected from this point.

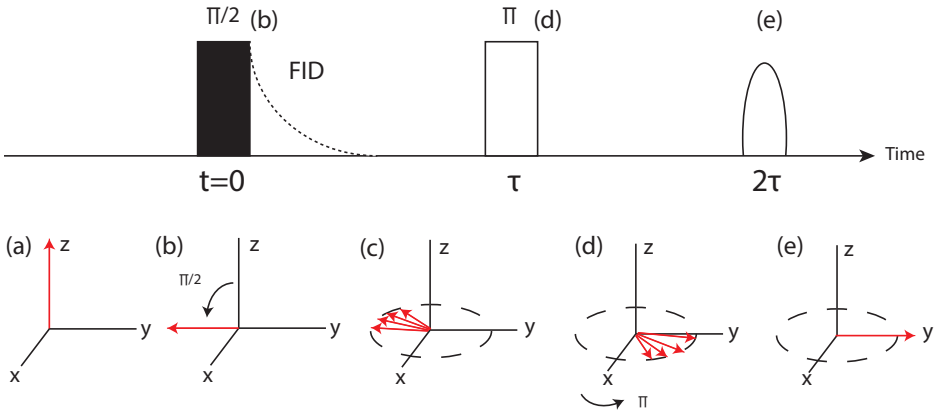

Figure 5.2: Hartman-Hahn echo. (a) Nuclear magnetisation builds up along the z-axis (b) a 90° pulse rotates net magnetisation into the xy plane (c) the nuclear spins begin to lose coherence(d) after a period of time the magnetisation is refocused by a 180° pulse (e) the nuclear spins come back into alignment and an FID is recorded.

Inversion recovery

The inversion recovery experiment begins with a π pulse which inverts the net nuclear spin magnetisation from +z to -z, this equates to inverting the populations of the nuclear spin energy levels. A variable delay time is left and then a $\pi/2$ pulse is applied, which has the effect of creating transverse magnetisation in the xy plane. This magnetisation precesses back to equilibrium and is detected as a FID. After the signal is recorded, one waits a time period of 3-5 times T_1 to allow the magnetisation to fully recover. The experiment is repeated with successively larger values of τ, up to the maximum time given by the experimenter. The magnetisation builds up after each

experiment according to

$$M(\tau) = M(0)[1 - 2\exp(-\tau/T_1)] \tag{5.1}$$

where $M(0)$ is the magnetisation at τ=0, T_1 is the time constant characterising spin-lattice relaxation. As this experiment relies on an inversion pulse, which may differ between signals in a spectrum, it is a useful technique to selectively monitor T_1, but can have the disadvantage of long experiment times.

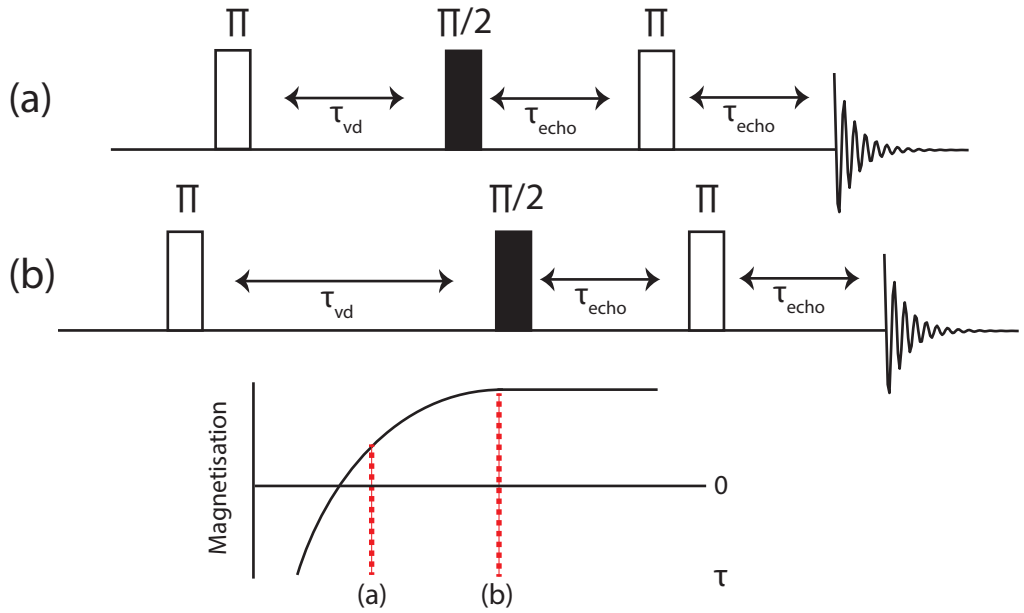

Figure 5.3: The inversion recovery experiment begins with a 180° inversion pulse which inverts the net nuclear spin magnetisation. Then a variable delay is left which allows the magnetisation to partly recover to thermal equilibrium, an echo sequence then reads out the recovered magnetisation along the z axis. The experiment is then repeated with an increment in the delay and the magnetisation builds up as a function of τ. In (a) τ is not long enough and the magnetisation has only partly recovered, in (b) τ is long enough in relation to the T_1 of the system

Saturation recovery

Another common technique to measure T_1 is the saturation recovery experiment, an outline of this technique is now given. A comb of $\pi/2$ pulses saturates the nuclear magnetisation along the z axis, this has the effect of returning the system to reproducible state after each experiment. The experiments conducted throughout this thesis typically used 80-100 pulses in the saturation train, with 80μs between pulses, although these values are usually optimised depending on the sample. After this a variable time is left to allow the system to recover, this increases on subsequent experiments to a

maximum value which is dependent on the spin system under study as discussed later. A pulse is then applied after this delay which reads out the net nuclear magnetisation built up along the z axis, as shown in Fig 5.4. In this work, an echo sequence was appended to the usual saturation recovery sequence, to suppress background signals and the variable delay list was controlled using an extra parameter denoted L1 as discussed later. The magnetisation builds up in the variable delay period according to

$$M(t) = M(0)[1 - \exp(-t/T_1)] \tag{5.2}$$

In terms of nuclear spin energy levels for a spin 1/2 nuclei the saturation pulse has the effect of equalising the two energy levels, then after the variable delay there is an increase in population in the lower energy state concomitant with a build up of M_z along B_0.

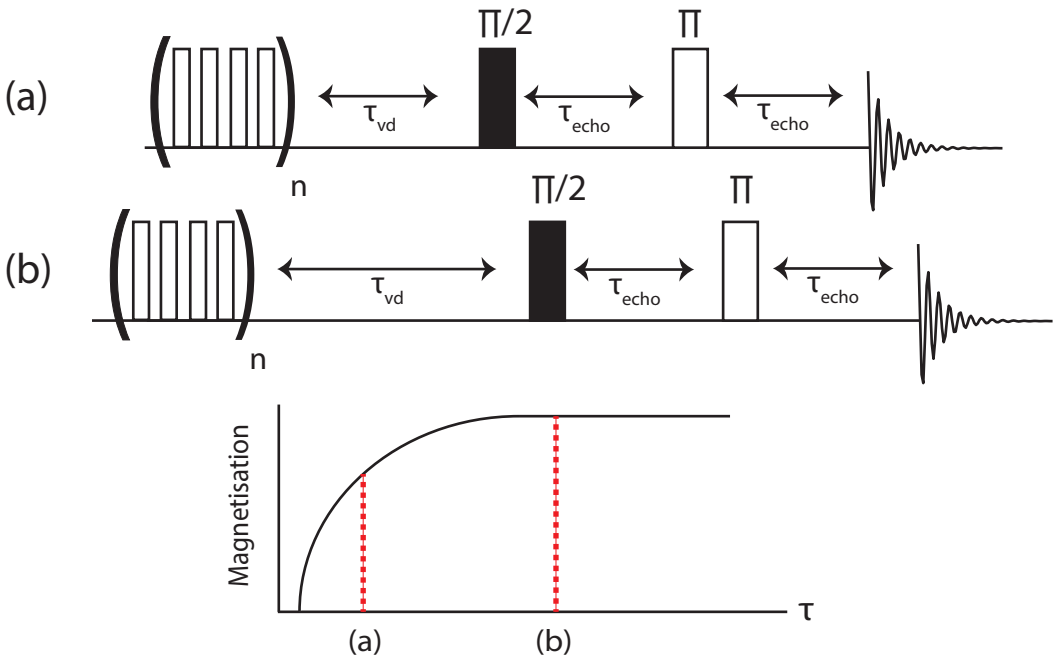

Figure 5.4: The saturation recovery experiment begins with a train of pulses applied in quick succession, destroying magnetisation along the z axis (M_z). Then a variable delay is left which allows M_z to begin to return to equilibrium. An echo sequence reads out the value of M_z, after the delay and then the experiment is repeated and τ is incremented. After a series of slices the magnetisation builds up as τ approaches the appropriate T_1 value and by integrating the signal in each slice, M_z may be monitored over time. Two example slices are presented, in (a) the time τ is not sufficient and the M_z has not fully reached its equilibrium value whereas in (b) τ is sufficiently long to enable M_z to build up to its maximum value

Data analysis

NMR data was processed in MatNMR[182] and analysed using a large number of home built scripts in MATLAB and Mathematica.

Analysis of T_1 The experiments described above offer the method to measure T_1 of nuclear spin, in addition to complete irradiation of the bandwidth necessary to excite the spins of interest, the variable delay list must have a maximum which is typically set as 3-5 times T_1. Although in some cases the T_1 is not known and therefore an estimate is usually taken, guided by previous literature. In the case where the magnetisation curve, given in Fig. 5.3 and Fig. 5.4 does not plateau, the experiment is repeated with a longer variable delay list.

The experiments conducted in this thesis focus strongly on measurement of T_1 as a function of temperature. The T_1 and therefore the maximum value in the variable delay list vary according to temperature, the reasons for this are outlined in section 4.4. Therefore an experimental delay list at room temperature may not be appropriate at temperatures of 5 K. In order to reduce the complexity of the experiment, an extra loop is created in the pulse program which has the effect of multiplying the variable delay list by a constant which is chosen according to the set temperature. For example, if a variable delay list has a 32 element list with a maximum value of 1 second at room temperature, the whole list is multiplied by 5, to give a list which has a maximum value of 5 seconds appropriate for longer T_1 values usually found at lower temperatures. This multiplicative factor is known as L1. In general the methodology to measure T_1 was based upon this, typically the value of L1 is increased as the temperature is lowered but not in every case.

In the simplest case, the build up of nuclear spin relaxation builds up following a single exponential given by

$$M(\tau) = A[1 - \exp(-\tau/T_1)] + C \tag{5.3}$$

where A is the amplitude of the magnetisation curve, typically set to unity as the data is normalised between 0-1, τ is the time from the variable delay list, T_1 is the time constant associated with spin-lattice relaxation and C is an offset term which accounts for incomplete saturation. In some instances the magnetisation build up follows a bi-exponential function given by

$$M(\tau) = A_1[1 - \exp(-\tau/T_{1a})] + A_2[1 - \exp(-\tau/T_{1b})] + C \tag{5.4}$$

More terms can also be added, depending on the spin system. No more than two terms

were used to describe the experiments outlined in this thesis. However, in some cases it was required to describe the magnetisation by a superposition of relaxation curves, typically this occurs when studying a superconductor below T_c. The function used for this is the stretched exponential[100, 183–185] given by

$$M(\tau) = A\exp(-\tau/T_1)^{\beta} + C \tag{5.5}$$

The additional coefficient β is commonly used to describe the distribution of relaxation rates in the superconducting state. The value of β is unity in the normal state, representing a single exponential fit. In the superconducting state, the value of β deviates, representing the superposition of relaxation curves due to the distribution of T_c's, in general $\beta \to 0$ as there is a larger distribution of relaxation rates.

Analysis of peak position The static NMR spectrum of polycrystalline solids can be complicated due to a given nucleus experiences many different dipolar interactions, this causes broadening of the lineshape and complications in interpreting the spectra. Often the lineshape may be well approximated by the Gaussian distribution which has the form

$$f(x) = A\exp\left(\frac{(x-x_0)^2}{2\sigma^2}\right) + C \tag{5.6}$$

Where A is the height of the curves peak, x_0 is the peak position at the center of the Gaussian and σ is the Gaussian RMS width. C is an offset term to account for a non-zero baseline. σ is the standard deviation of the line which can be converted into the full width half maximum by

$$FWHM = 2.355\sigma^2 \tag{5.7}$$

There is also the method of moments which was first introduced by Van Vleck, the second moment is most often used and this is given by

$$M_2 = \sigma^2 \tag{5.8}$$

This is the general case, however there may be additional terms required in Eq.5.6, for example if there is an overlap of peaks in a spectrum then a sum of Gaussian terms may be required, given by

$$f(x) = A_1\exp\left(\frac{(x_1-x_0^a)^2}{2\sigma_a^2}\right) + A_2\exp\left(\frac{(x_2-x_0^b)^2}{2\sigma_b^2}\right) \tag{5.9}$$

5.2 Glovebox

The samples studied throughout this thesis were stored and handled in an MBraun LABstar glovebox, an illustration of this is given in Fig. 5.5. A N_2 cylinder ($\sim$200 bar) is connected to a double stage pressure regulator with working pressure 4 bar. This feeds a supply of N_2 to a stainless steel box. The gas is circulated over heated copper metal and molecular sieves to continuously remove O_2 and H_2O respectively. The oxygen and moisture level is monitored by an LED readout, and values are typically $<$0.5 ppm

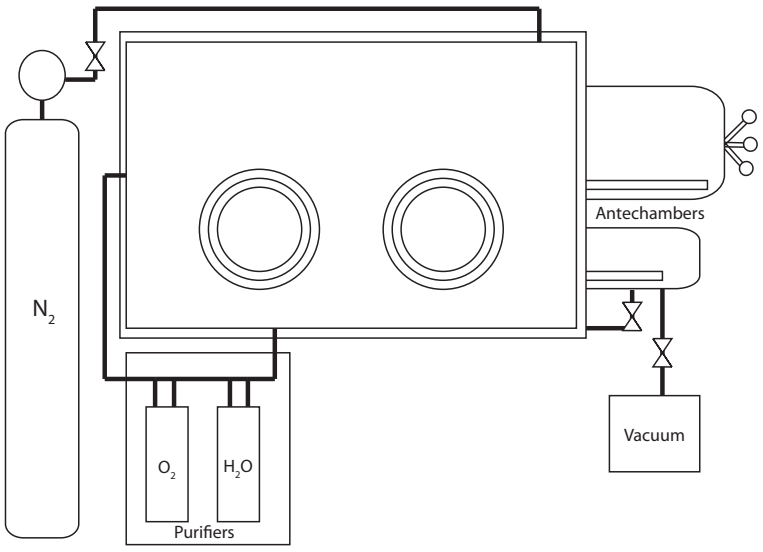

Figure 5.5: Illustration of Glovebox

5.3 Powder x-ray diffraction

Powder x-ray diffraction (pXRD) is an important technique used to characterise materials and determine structural parameters, and was used throughout the course of this thesis. A brief outline of the main concepts is now given.

A copper-anode tube generates x-rays and these are projected onto a polycrystalline sample, illustrated in Fig. 5.6a. The x-rays are scattered by the atoms, which act like a diffraction grating and this constructive interference is monitored at a detector, as shown in Fig. 5.6b. The measurement of the angle at which this interference occurs allows one to calculate the atomic spacing. This is described by an equation known as

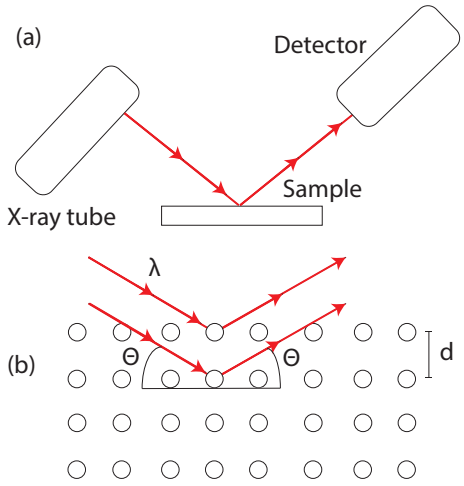

Figure 5.6: Schematic of powder x-ray diffraction and illustration of Braggs equation. (a) Copper-anode tube generates x-rays which are projected onto sample, the reflections are recorded in a detector (b) x-rays scattered by atoms at an angle θ

Bragg's law, which is given by:

$$n\lambda = 2d_{hkl}sin\theta \tag{5.10}$$

where n is an integer, λ is the wavelength of radiation, d_{hkl} is the lattice spacing and θ is the diffraction angle[186]. The measurements in this thesis were carried out on a Bruker D2 Phaser using Cu Kα1/α2 radiation with λ=1.5418Å. The samples were mounted in FMMA sample holders and flattened with a glass slide. The fulleride samples were placed inside sealed sample holders to avoid degradation.

The resulting powder patterns were analysed using the rietveld method[187]. This method allows the refinement of atomic positions, unit cell and displacement parameters and site occupancies and was carried out using the GSAS-EXPGUI software package[188].

5.4 Physical property measurement system

A Physical Property Measurement System (PPMS) from Quantum Design, is used to characterise the superconducting properties of the superconductors presented in this thesis. A vibrating sample magnetometer (VSM) measures the magnetic properties in a variety of different materials, such as powders, liquids, single crystals and thin films. When a sample is placed inside a static magnetic field, a diamagnetic response induces a magnetic moment. The VSM works by mechanically vibrating a sample under sinusoidal motion within distance of some sensing coils, the magnetic flux changes

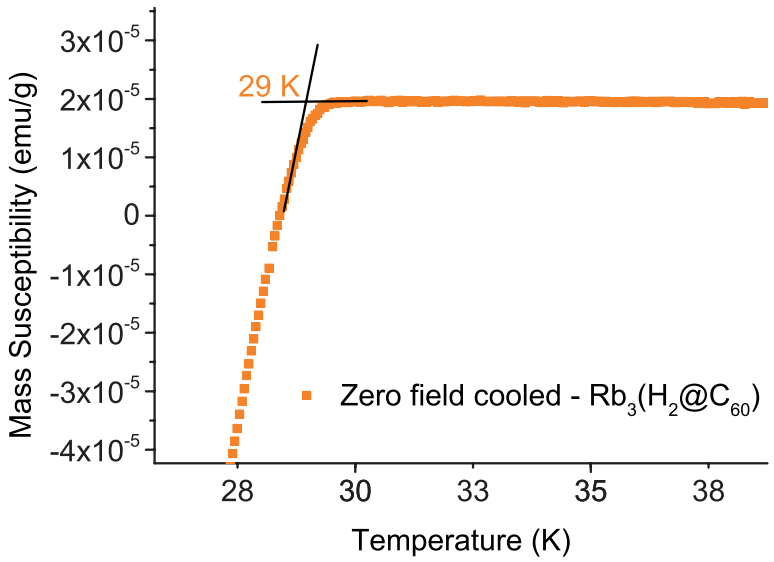

Figure 5.7: Typical ZFC measurement showing definition of T_c as the intercept of linear extrapolation of the susceptibility curve at M(T) and M(0)

induce a voltage in the coils and this is proportional to the magnetic moment of the sample.

In an ideal case, perfect diamagnetic shielding would be indicated by an experimental susceptibility which is described by

$$\chi_e = \frac{M}{H_e} = \frac{M}{H_i + 4\pi DM} = -\frac{1}{4\pi(1-D)} \tag{5.11}$$

Where M is magnetisation, H_e and H_i is the external and internal magnetic field respectively, D is the demagnetisation factor. The VSM option of the PPMS was used to measure T_c on the magnesium diboride and the fulleride samples. The magnesium diboride powder samples were mixed with an epoxy and cured into a pellet, then loaded into a VSM sample holder.

The fulleride samples were too air sensitive to handle using the standard method for powders outlined above. These samples were placed into a borosilicate tube, and firmly pressed down to ensure good thermal contact, then they were flame sealed under vacuum, a glass spacer was added either side of the sample. The tube or pellet is placed inside a sample rod which is attached to a motor, this motor is driven sinusoidally near a detection coil and simultaneously the induced voltage is read. The system is able to resolve changes in magnetisation of less that 10^{-6} emu. The $T_c(H)$ is defined as the intercept of a linear extrapolation of the susceptibility curve at $M(T)$ and $M(0)$, as shown in Fig 5.7.

CHAPTER

SIX

SYNTHESIS AND CHARACTERISATION OF FULLERIDE SUPERCONDUCTORS

This chapter outlines the synthesis and characterisation of the fulleride materials studied in this thesis. Two endohedral materials have been synthesised, they are $Rb_3(H_2O@C_{60})$ and $Rb_3(H_2@C_{60})$. In the interest of clarity; this notation implies a C_{60} molecule contains inside it either a single molecule of H_2O or a single molecule of H_2. Additionally a sample of Rb_3C_{60} is synthesised and characterised for comparison.

The starting material to produce $Rb_3(H_2O@C_{60})$, i.e $H_2O@C_{60}$ was provided by Andrea Krachmalnicoff and Shamim Alom from Southampton University chemistry department. The initial sample from Andrea was doped with Rb atoms but the reaction produced a sample which contained impurities, and the data is not presented in this thesis. The second sample, with the parent compound from Shamim, produced a purer sample which is studied in this chapter and the following chapter. This sample has 98% of the C_{60} cages containing a single water molecule, which was deduced from HPLC measurements from Shamim (shown in appendix).

The starting material for the production of $Rb_3(H_2@C_{60})$ was provided by John Grasvik and Yusujiro Murata from Southampton and Kyoto University respectively, both from the chemistry departments. The sample from Yusujiro is studied in this chapter and the following chapter, and has 95% of the C_{60} cages containing a single hydrogen molecule.

The following discussion attempts to lay out the steps to synthesise the Rb_3C_{60} superconductors, explicit detail is given on the basis of the difficulty of the reaction. The method was developed over 8 syntheses using ordinary fullerene, only a few of which succeeded. The perfected method was applied to the endohedral fullerene samples and then these samples are characterised and studied at low temperature in this and the following chapter.

6.1 Review of Fulleride Syntheses

In principle the synthesis of the A_3C_{60} fullerides is a simple procedure, only involving the heating of stoichiometric amounts of alkali metal with C_{60} in a sealed tube under vacuum, although in practice it can be more difficult. The difficulty mainly arises from the air sensitive nature of Rb, which then necessitates the use of an inert environment, such as a glovebox, to carry out the preparation. In all the methods one requires an amount of C_{60} and alkali metal, but the amounts and additional materials may vary according to the synthesis method. Some of these different methods are now outlined and although some minor details such as temperatures or reaction times may differ, generally they may be used to synthesise Rb_3C_{60}, K_3C_{60} or Cs_3C_{60} etc. The samples prepared and studied in this thesis were made using a variation of the vapour transport method, this is fully discussed in section 6.2

The C_{60} molecule can be prepared by collecting soot which is generated by a DC carbon arc in a water-cooled vacuum chamber[189] or an alternative is to use a Benzene-Oxygen flame[190]. In general however, C_{60} is now widely available and relatively cheap to purchase from manufacturers. Also the alkali metals are generally not generated *de novo*, as high quality materials may be ordered straight from the manufacturer.

The simplest way to produce the alkali fullerides is by the vapour transport method[76, 80, 159, 191–193], the procedure generally consists of three heat treatment stages which are as follows, described for Rb_3C_{60}. (a) A given amount of Rb is mixed in a stoichiometric ratio with C_{60} and sealed under vacuum in a 5-8mm diameter Pyrex tube. The tube is placed inside a furnace at 200°C for 24 hr and during this time the Rb completely adheres to the C_{60} powder. A slightly different procedure which promises better control of the stoichiometry, is to dope C_{60} with excess alkali metal to form A_6C_{60} and then mix with more C_{60} to yield the superconducting A_3C_{60}.[194]

The solution-phase route[195] uses alkali metal salts of the decamethylmanganocene anion, which leads to production of discrete THF-solvated alkali metal salts of the C_{60} trianion, A_3C_{60}-xTHF. This is then used as a precursor to the A_3C_{60} phase, which can be generated by heating the THF precursor with mild heating under vacuum. Some advantages of this method include a shorter reaction time and more mild reaction temperatures. Also there is a greater control of stoichiometry and more homogeneity of the final product. Although this method requires excess alkali metal which has to be removed from the product and there may be residual solvent.

An approach to circumvent some of those issues is the liquid ammonia route[189] to the preparation, which is as follows. 5 mL of liquid ammonia is condensed onto stoichiometric amounts of C_{60} and Rb metal, which are inside an evacuated silica quartz tube at a temperature of -78° C. The tube is then carefully warmed to -55° C

for 30-60 min and occasionally stirred with an enclosed quartz stirrer bar. The mixture is gently heated (< 100°) under a dynamic vacuum in order to remove any residual ammonia. The resulting product is then removed by scraping from the tube whilst inside an inert atmosphere glovebox. It is then pressed into a pellet and sealed inside another quartz tube under vacuum and then annealed for 25 h at 375 °C. The product is thought to be highly reproducible although does add additional complexity handling ammonia.

6.2 Synthesis of fullerides and endohedral fullerides

The synthesis of alkali-metal fullerides has various stages, which are broken up into sections and discussed below. All glassware used in the following procedures is first cleaned with Aqua-Regia and then flame dried under 1x10^{-5} Torr dynamic vacuum[1]. The glassware is allowed to cool and the Youngs tap is closed to seal the cold tube under vacuum. The tubes are then transferred to a N_2 glovebox for subsequent steps. This chapter is laid out in the following way, first the sublimation of C_{60} to provide high quality starting materials is described, then the alkali metal synthesis reaction is discussed, this is followed by the flame sealing and heating procedures. An important note is that there are no altered or additional steps to the procedure between the synthesis of fullerides or endofullerides. The rest of the chapter describes X-ray, NMR and PPMS characterisation of the materials studied by variable temperature NMR in the subsequent chapter.

6.2.1 Sublimation

The sublimation of C_{60} is performed in two steps. The first step is designed to remove residual solvent; the second step is the actual sublimation, which provides pure C_{60} for further syntheses. 200mg C_{60} is loaded into a 30 cm borosilicate tube with an OD of 8mm; the tube is placed inside a horizontal tube furnace and connected to a turbo-molecular pump. The tube is evacuated to 1x10^{-5} Torr and heated to 350°C under dynamic vacuum at a heating rate of 1°C/min, this temperature is held for 2 hours. The tube is then allowed to cool at a natural rate back to room temperature and the vacuum is removed. The C_{60} is then taken from the tube and is sublimed in smaller batches, 10mg was found to be an appropriate amount.

10mg of C_{60} is loaded into a 30cm quartz silica tube with an OD of 4mm using a glass funnel, with a drawn out spout to span the length of the quartz silica tube. It is

[1]Dynamic vacuum implies the system is evacuated continuously whilst further work is carried out, instead of evacuating and then closing off the Youngs tap for further work

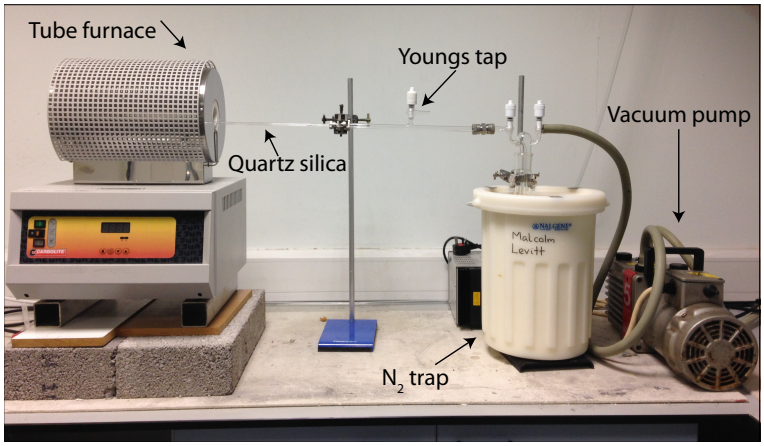

Figure 6.1: Photograph of apparatus designed to sublime fullerides to produce high purity starting materials. Commercially bought C_{60} is loaded into a silica quartz tube and the tube is placed inside the center of a horizontal tube furnace. The system is evacuated using a rotary vane pump to $1x10^{-5}$ Torr. Then the furnace is set to a heating programme which is described in the main text.

important when filling the tube not to contaminate the sides with C_{60}, as sublimed C_{60} will condense at the point coincident with the gradient of the tube furnace. Once the tube is loaded it is placed inside a horizontal tube furnace and connected to a turbo-molecular pump, the tube is then evacuated to $1x10^{-5}$ Torr and heated to 550°C under dynamic vacuum at a heating rate of 2°C/min, this temperature is held for 12 hours. The tube furnace is isolated from outside air currents by plugging both ends with glass wool. After the heating procedure, the tube is allowed to cool at a natural rate back to room temperature and the vacuum is removed. The sublimed C_{60} condenses towards the centre of the quartz silica tube, along the gradient of the furnace; it may be harvested by cutting the tube open using a glass knife. The yield is usually high, around 90%.

6.2.2 Preparation Inside Glovebox

Alkali metal fullerides are extremely sensitive to air and moisture, therefore special techniques are required in order to circumvent degradation, during synthesis and also whilst under experimental study. The preparation of fullerides needs to be performed under an inert gas (nitrogen) inside a glovebox, where moisture and oxygen levels are kept at <0.5ppm. Sublimed C_{60} is transferred into a glovebox and it is weighed several times to ensure an accurate reading. This is vital as the balance is sensitive to the unstable atmosphere inside the glovebox and actual weights can be misrepresented. Once an accurate reading is achieved the C_{60} is loaded into a 50x5mm stainless steel tube and the tube is then weighed.

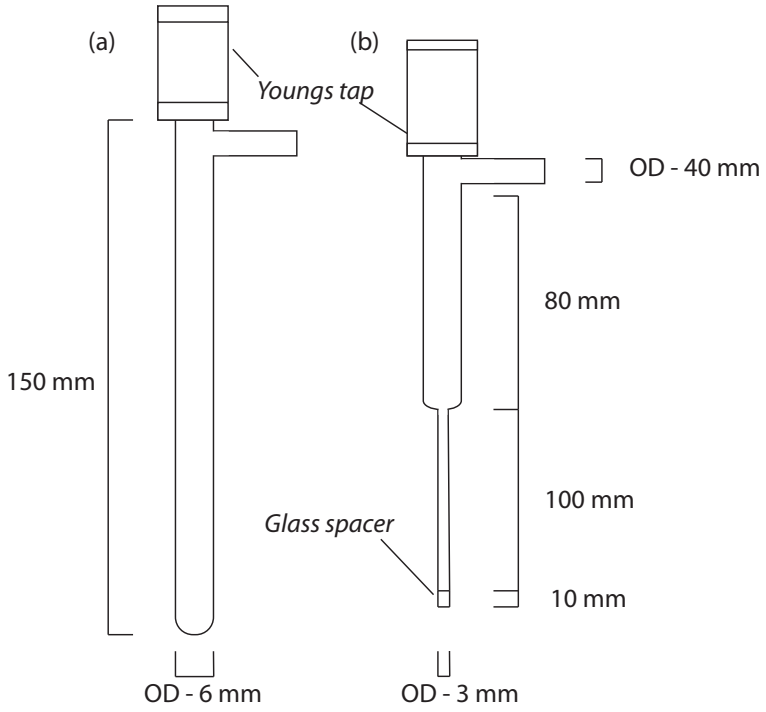

Figure 6.2: Schematic of glassware used in fulleride synthesis, samples are loaded inside a glovebox, evacuated using dynamic vacuum and then flame sealed. (a) Reaction vessel for vapour doping (b) Sample tube for NMR study, dimensions fit to NMR coil

For the endohedral fullerides a stoichiometric amount of Rb is added based on the weight of C_{60} provided. In the synthesis of the H_2O fulleride 55.5 mg of $H_2O@C_{60}$ was provided as starting materials, which required 19.27 mg of Rb. When calculating the amount of Rb, the extra weight of the H_2O molecule is taken into account, especially if the filling factor is high, in this case it was close to 100%. For the H_2 fulleride, 29.2 mg $H_2@C_{60}$ was provided which required 10.38 mg of Rb. In this case the H_2 molecule is not taken into account when weighing out the Rb, as the difference in weight between empty and filled cages is negligible.

A fresh shiny piece of Rb is then cut using a spatula, and this is smeared onto the inside of the stainless steel tube at the rim. The stainless steel tube is then weighed, the amount of Rb is adjusted and this is repeated until the weight is the same as the theoretical weight needed. When the weight is correct the stainless steel tube is placed inside a glass tube with a Youngs tap, dimensions are given in Fig. 6.2a.

6.2.3 Flame sealing

The next step is flame sealing the borosilicate glass (Pyrex) under vacuum using a blowtorch, some key thermal properties of Pyrex are given in Tab.6.1. The aim is to seal the tube approximately half way along, with extra care taken not to heat

Thermal Property	Temperature (K)
Strain Point	515°C
Annealing Point	565°C
Softening Point	820°C
Working Point	1245°C

Table 6.1: Summary of thermal properties of borosilicate glass

up the reaction vessel, which sits at the bottom of the tube. Alkali metals have a low vapor pressure and consequently are extremely sensitive to heat gradients, any localised heating will cause the alkali metal to condense and the stoichiometry will change significantly.

The 6mm OD borosilicate tube is taken from the glovebox with the Youngs tap firmly closed and is connected to a turbo-molecular pump. The pump is activated and the turbine speed is allowed to increase until a pressure of at least 1x10^{-5} Torr. The Youngs tap is slowly opened in stages, this will cause the pressure to drop as nitrogen gas flows out of the tube. It is important at this point to allow the pressure to drop before continuing, this cycle is repeated until the tap is fully opened and ensures 'bumping' does not occur. A butane-propane blowtorch is lit and allowed to warm up, typically this takes 10-15 seconds to reach a maximum temperature of 1970°C. The tip of the flame is used to gently warm the tube at roughly half way along, it is important to heat uniformly to ensure stress does not build on the glass. As the temperature of the glass rises, it begins to glow orange, at which point the cone of the flame is used to begin the sealing process.

The glass is heated uniformly with the cone of the flame, but this step should be done slower to ensure the temperature increases to the working point of the glass. At the working point the glass flows with high viscosity, therefore the tube can be gently pulled down whilst still applying the flame, causing the glass to collapse in and form a seal. The tube is pulled down until it is free from the rest of the apparatus, at which point it must be rotated inside the tip of the flame and then in air, this is to ensure the glass cools uniformly.[2] The glass is then allowed to cool. Glass parts that are hot should not be allowed contact with good thermal conductors, such as other metals, which would allow rapid local cooling and stress to build on the glass. Hot glassware is left on non-conductive materials such as wood or cork.

[2]The lower surfaces cool faster than the upper ones, as the latter become heated by hot air rising from the lower surfaces below.

Figure 6.3: Photograph of reaction tube after heat treatment, condensed Rb is observed as an orange hue implying a failed reaction

6.2.4 Heating procedure

The tube is wrapped in aluminium foil, to ensure isothermal conditions, and placed in the centre of a muffle furnace. It is then subjected to the following heat procedure; 168 hr at 200°C, 24 hr at 250°C, 24 hr at 300°C, 24 hr at 350°C then an intermittent grinding, in which the tube is broken open in the glovebox and the sample is thoroughly ground in a pestle and mortar, then loaded into a 6mm OD borosilicate tube and flame sealed using the same method above and then placed in the centre of the muffle furnace for 72 hr at 450°C. The tube should be completely clear when it is removed from the furnace, alkali metal condenses onto a borosilicate tube with an orange hue, an example is given in Fig. 6.3. At this point the reaction has failed and one must begin again.

6.2.5 Samples

The samples synthesised using the procedure outlined were as follows; 49.8 mg Rb_3C_{60}, 41mg $Rb_3(H_2@C_{60})$ and 71.5 mg $Rb_3(H_2O@C_{60})$. These samples are characterised and studied using variable temperature NMR in the following sections.

Sample	Peak Position (T′,T,O)	Intensity (T′,T,O)
$Rb_3(H_2@C_{60})$	77,-17,-135 ppm	0.30:1.0:0.53
$Rb_3(H_2O@C_{60})$	75,-15,-138 ppm,	0.18:1:0:0.51
Rb_3C_{60} (exp)	70 -26 -142 ppm	0.12:1.0:0.36
Rb_3C_{60} (literature)	70 -20 -139 ppm	0.17:1.0:0.55

Table 6.2: Summary of ^{87}Rb NMR parameters for fulleride samples. Reference values from[153, 155]

6.3 Characterisation of alkali fullerides and alkali endofullerides

The samples studied in this section: 10 mg of $Rb_3(H_2@C_{60})$ and 15 mg of $Rb_3(H_2O@C_{60})$ sealed in glass tubes under vacuum. For brevity they are referred to as the H_2 and H_2O fullerides in subsequent chapters. The H_2 fulleride was prepared using C_{60} with 95% of the cages were filled with H_2 molecules. The H_2O fulleride was prepared using C_{60} with 98% of the cages filled with H_2O molecules.

6.3.1 NMR spectroscopy

All ^{87}Rb NMR spectra were referenced to a sample of RbCl(aq) with a chemical shift of 0 ppm. ^{13}C NMR spectra referenced to adamantane with a chemical shift of 38.2 ppm (CH_2 peak)[196]. ^{1}H NMR spectra referenced to H_2O with a chemical shift of 4.8 ppm. ^{13}C is I=1/2, has natural abundance=1.11% and γ_n=10.705 MHz/T, ^{87}Rb in comparison is I=3/2, natural abundance=27.85% and γ_n=13.801 MHz/T.

^{87}Rb NMR

The static ^{87}Rb NMR spectrum of Rb_3C_{60} acquired at room temperature shows three distinct sites, shown in Fig 6.4. These sites correspond to one octahedral site, denoted O and two tetrahedral sites, denoted T and T′. The expected intensity ratios of these peaks are 0.55:1.0:0.17 (O:T:T′) at T<350 K.[153]. The NMR parameters measured from the spectrum are given in Table 6.2. There is a good agreement with literature values, which indicates the rubidium atoms in the endohedral fullerides are distributed similarly to the non-endohedral fulleride.

^{13}C NMR

^{13}C NMR acquired at room temperature is shown in Fig 6.5, the lineshape follows the typical powder pattern shape for NMR on static solids. C_{60} rotates rapidly about its

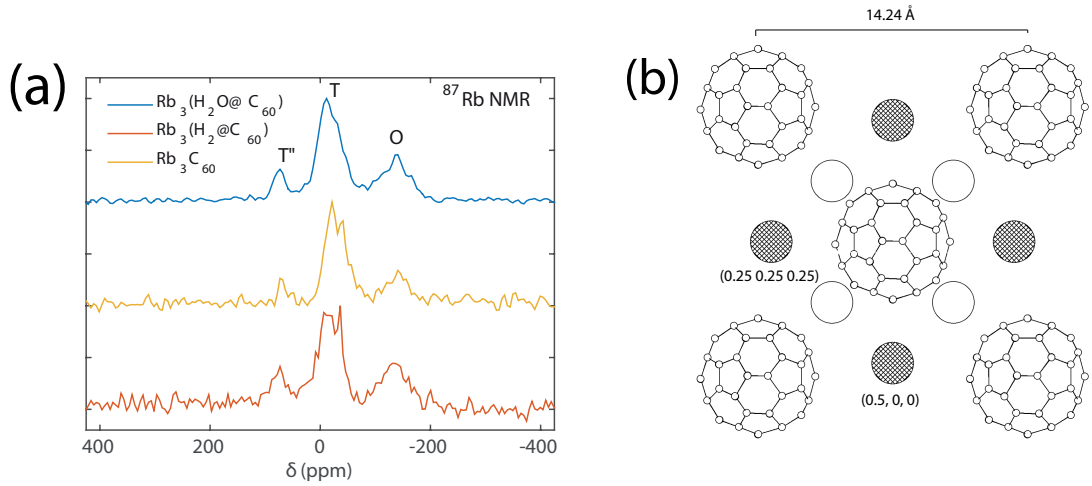

Figure 6.4: (a) Static ^{87}Rb NMR at 14.1 T at room temperature on samples of Rb_3C_{60}, $Rb_3(H_2@C_{60})$ and $Rb_3(H_2O@C_{60})$. The three signals observed are due to one octahedral and two tetrahedral sites, as discussed in the text. (b) FCC unit cell of Rb_3C_{60} open and hatched spheres represent tetrahedral and octahedral Rb sites respectively. Adapted from[28]

centroid and thus the NMR lineshape is usually narrow. In the case of the fullerides, the alkali atom restricts motion and causes the lineshape to become broader. The larger the alkali atom, the more the rotation is inhibited and the broader the ^{13}C spectrum becomes. This is true for all fullerides, even K_3C_{60} which has a relatively small ionic radius, however the linewidth is only slightly broader[28]. σ_{iso} has been reported to be between 175-205 ppm[157], this is consistent with the data recorded here. The ^{13}C T_1 of Rb_3C_{60} has been reported to be quite rapid (0.25s) with respect to the C_{60}, which is known to be of the order of 120s.

^{1}H NMR

^{1}H NMR was acquired in order to probe the local environment of the endohedral molecules, shown in Fig 6.6. On first evaluation it appears both $Rb_3(H_2@C_{60})$ and $Rb_3(H_2O@C_{60})$ have a similar magnetic shift. In undoped endohedral fullerenes, $H_2O@C_{60}$ and $H_2@C_{60}$ have proton chemical shifts of -4.7[197] and -1.1 ppm[198] respectively.

In the fulleride case, there is a shift due to the conduction electrons (Knight shift) and a paramagnetic contribution (Van Vleck shift). There is also a ring current shift, which describes the shift in the NMR spectrum due to currents moving around the C_{60} molecule, this will differ in the Rb_3C_{60} systems compared to the C_{60} molecule. The Knight shift is always positive[138] and the Van Vleck shift is negative[199]. In this case the overall shift is positive, which implies both the endohedral components of the H_2 and H_2O fullerides interact with the conduction electrons via the hyperfine interaction.

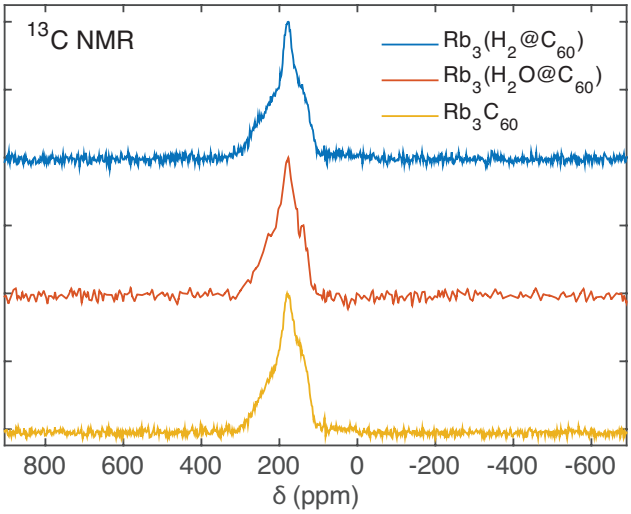

Figure 6.5: Static ^{13}C NMR at 14.1 T at room temperature on samples of Rb_3C_{60},$Rb_3(H_2@C_{60})$ and $Rb_3(H_2O@C_{60})$.

The distribution of crystallites in a polycrystalline material as well as the chemical shift and Knight shift anisotropy, (from the dipolar hyperfine term) results in a broad lineshape, whereas measurements on the endohedral insulators reveal narrow peaks. The endohedral component in these materials still rotates leading to an averaging of the anisotropies. In the endofulleride case the increased linewidth may be due to the anisotropy of the Knight shift rather than reduced rotation of the endohedral molecule, although it has been speculated that the addition of ions would affect the position of H_2O[200].

As the magnetic shifts are the same, the endohedral components may have similar couplings to the conduction electrons. In this case the Fermi-contact interaction gives rise to the isotropic Knight shift, this is associated density of states at the Fermi-level[201], which apparently is similar between endofulleride materials.

6.3.2 PPMS and powder X-ray diffraction

The endofullerides were characterised using powder x-ray diffraction and refined according to the Rietveld method[187] in GSAS-EXPGUI. Details of the diffractometer are given in section 5.3. The reference crystal structure used to calculate the x-ray profile was taken from the Inorganic Crystal Structure Database (ICSD)[202].

Fig. 6.7a shows the experimental powder pattern for the H_2 fulleride and refinement according to the literature structure, there is a very good match to the profile at all reflections, the reduced chi-squared measure of fit is 7.7. The calculated lattice parameters are a=b=c=14.45Å.

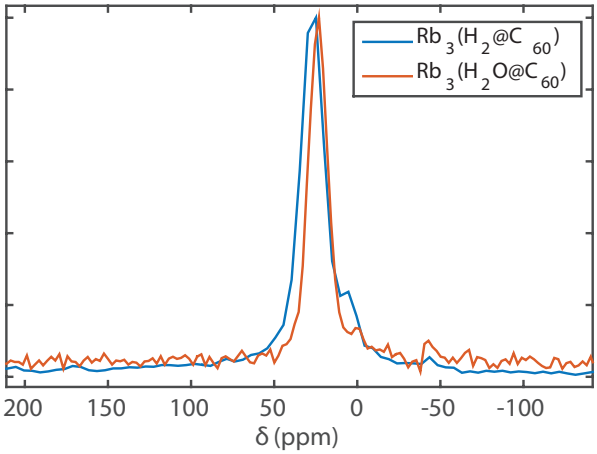

Figure 6.6: Static ^{1}H NMR at 4.7 T on samples of Rb_3C_{60}, $Rb_3(H_2@C_{60})$ and $Rb_3(H_2O@C_{60})$.

Fig. 6.8a shows the H_2O endofulleride x-ray pattern and Rietveld refinement. Unfortunately there was only a small amount of material available for powder x-ray studies and this is reflected in the low intensities of the peaks, the large peak at 2θ=13 and the broad component at 2θ=24 arises from the sample holder. The Rietveld fit gives the calculated lattice parameters as a=b=c=14.32Å. The reduced chi-squared measure of fit is 51.6. The smaller lattice constant in the H_2O fulleride appears to be consistent with previous works on noble gas endohedral fullerides[26], in which a sample of $K_3(Ar@C_{60})$ shows a smaller lattice constant than K_3C_{60}. Although the data are not good enough to carry out more quantitative analysis, the unit cell parameters are accurate and clearly show that encapsulating larger molecules (H_2O), has an effect on the structure. This is also mirrored in the T_c, as now discussed.

The superconducting transition temperature of the endohedral fullerides was determined from measurements of the temperature dependence of both the ZFC and FC temperature dc magnetic dipole moment (emu) of the polycrystalline material. This is shown in Fig 6.7b and Fig 6.8b for the H_2 and H_2O endofullerides respectively. All PPMS curves are given in the Appendix and the T_c values are summarised in Tab.6.3 Details of experimental methodology and concepts behind the measurement are given in section 5.4, but the main protocol is given here again.

The ZFC measurement is as follows, the sample was cooled from the normal state ($>$ 40 K) to 5 K in zero field, then a field was applied and the sample was warmed above the T_c. The DC magnetic moment is monitored during this process. The field cooled measurement applies the field above T_c and then monitors the magnetic moment upon cooling to 5 K. T_c was determined[3] to be 28.4 and 29.6 K for $Rb_3(H_2O@C_{60})$ and

[3]The nucleation temperature (T_c(H)) is defined using the intercept of a linear extrapolation from

	$Rb_3(H_2O@C_{60})$	$Rb_3(H_2@C_{60})$
Field (T)	T_c (K)	T_c (K)
0.001	28.4	29.7
4.7	27.7	28.5
8.5	26.7	27.6
14.1	25.6	26.5

Table 6.3: Summary of T_c values for endohedral fullerides collected using VSM option on a Quantum Design PPMS. T_c determined from ZFC measurements

$Rb_3(H_2@C_{60})$ respectively, by using the linear extrapolation method which is accurate for cubic crystals such as Rb_3C_{60}. This is similar to literature values of susceptibility measurements on single crystals[203] of Rb_3C_{60} and powders[159]. From the PPMS and XRD results it appears the encapsulatd H_2O molecule has an effect on the structure of the cage, and this manifests through the T_c and lattice constant. The H_2 molecule shows no discernable difference and this may be indicative that it has little interaction with the C_{60} cage. Of course the difference in T_c and lattice could be assigned to difference in sample quality and to test this idea a different alkali atom should be used. If the changes in bulk properties are an intrinsic effect then a larger alkali atom should give a larger drop in T_c and vice versa. In this case the ΔTc is 1.4 K. A sample of $K_3(H_2O@C_{60})$ and $K_3(H_2@C_{60})$ would give a smaller decrease, or alternatively the Cs doped compounds would give a larger decrease[26].

the susceptibility at M=0 and M(T). The point at which they cross is the T_c.

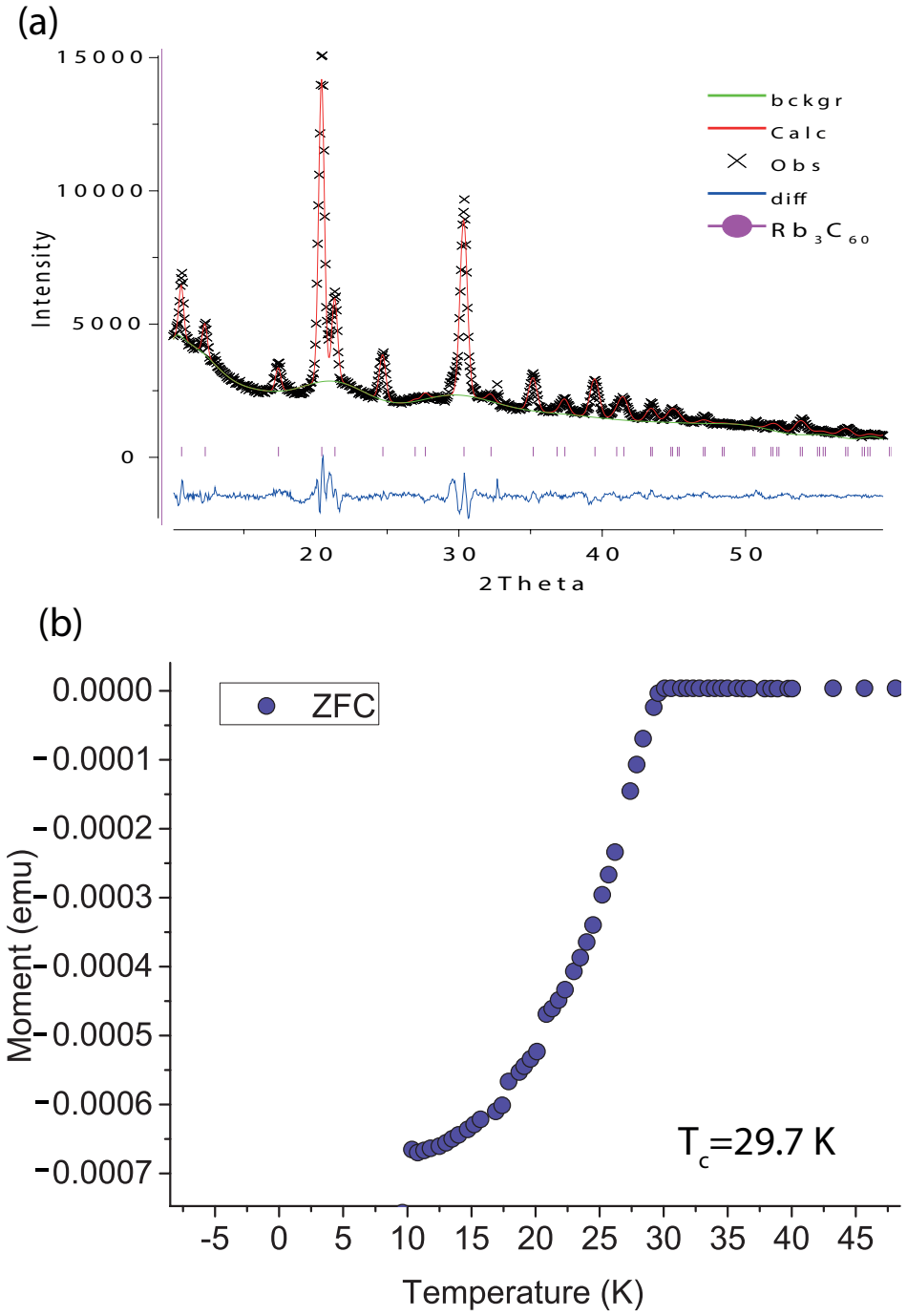

Figure 6.7: Characterisation of $Rb_3(H_2@C_{60})$ (a) pXRD pattern with Rietveld refinement (b) ZFC (0.001 T) susceptibility measured using VSM-PPMS

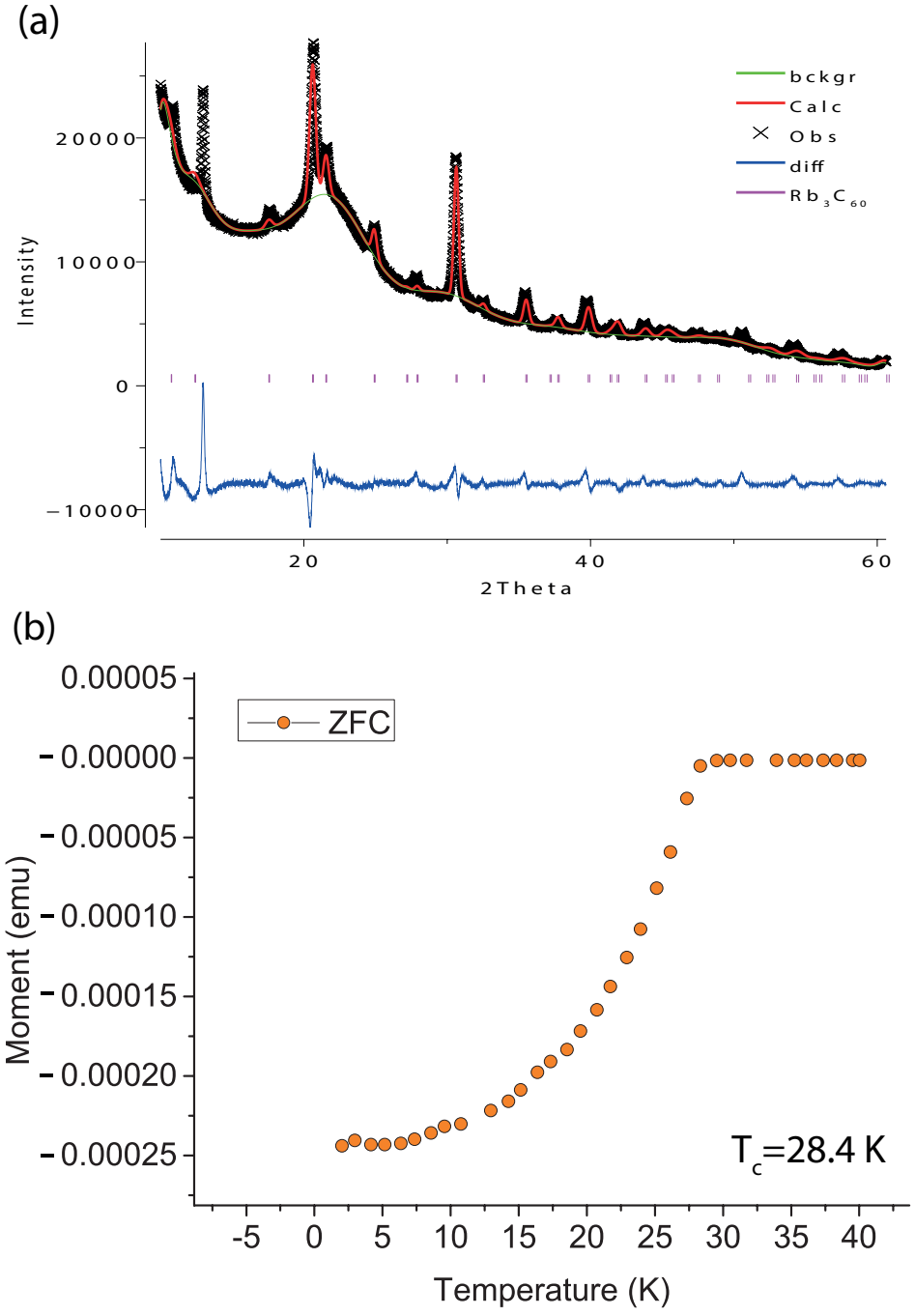

Figure 6.8: Characterisation of $Rb_3(H_2O@C_{60})$ (a) pXRD pattern with Rietveld refinement (b) ZFC (0.001 T) susceptibility measured using VSM-PPMS

CHAPTER

SEVEN

NMR OF ENDOHEDRAL FULLERIDES

7.1 Lineshape studies

Variable temperature static NMR experiments were recorded in the range of 298-5K on 10 mg of $Rb_3(H_2@C_{60})$ and 15 mg of $Rb_3(H_2O@C_{60})$ sealed in a glass tube under vacuum. ^{1}H, ^{87}Rb and ^{13}C NMR spectra have been recorded to characterise the normal and superconducting state of the endohedral fullerides. The peak shape, Knight shift and relaxation rate are followed as a function of temperature and discussed in this chapter. The majority of spectra presented for the analysis of peak shape and Knight shift were taken from the last slice of a 2D T_1 experiment, where the signal is most intense.

The NMR lineshape is first discussed for both endohedral fullerides and a comparison is made to normal Rb_3C_{60}, using all nuclei available. This is principally to monitor any structural transitions in the normal and superconducting state. The endohedral fullerides are also compared to the normal fulleride, to discern any major differences from implanting molecules inside C_{60} on the structure as a function of temperature.

7.1.1 ^{13}C and ^{87}Rb Peak shape

Figure 7.1 shows the variation in ^{13}C NMR peak shape for the fulleride and endohedral fullerides as a function of temperature. In the normal state the peak shape remains relatively unchanged, a typical powder pattern of a static solid. The distribution of crystallites in a powder, as well as the anisotropy of the chemical shift and Knight shift tensors results in the broadening of the lineshape, as reported previously.[28, 100, 204] Undoped C_{60} rotates about its centroid and the linewidth is narrow, in the fullerides there is still rotation[39] but it is hindered by the presence of the alkali ions, and there is a correlation between the alkali ion size and the NMR linewidth[28].

There are expected to be a number of phase transitions, although this is not clearly reflected in the ^{13}C lineshape. At 260 K there is expected to be a transition into a simple cubic structure, and the C_{60} molecules ratchet between two symmetry orientations

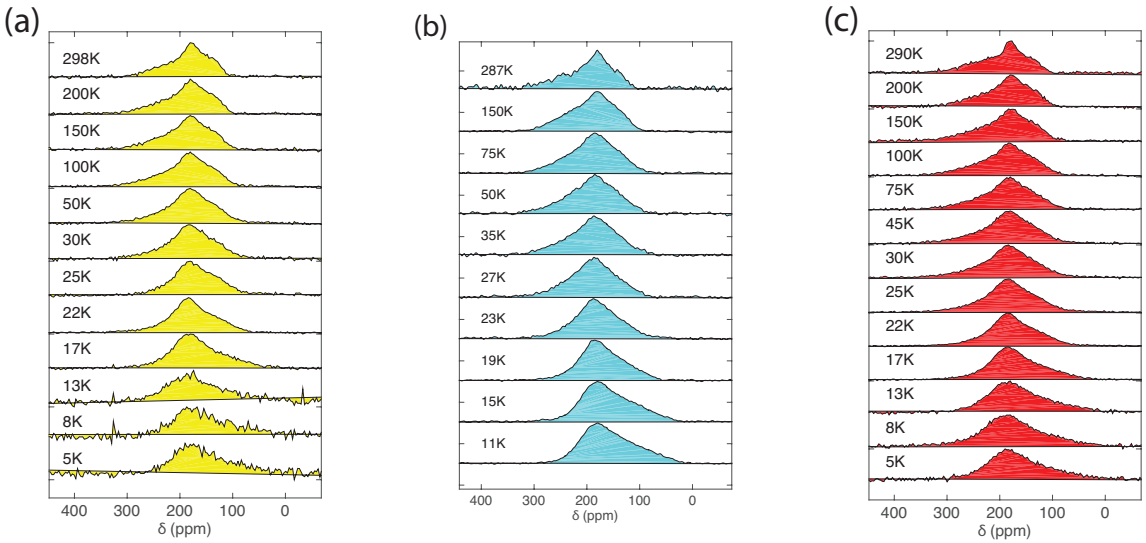

Figure 7.1: ^{13}C NMR spectra vs. temperature for the fulleride samples, recorded at 14.1 T using a Hahn-echo with τ=30μs. (a) Rb_3C_{60} (b) $Rb_3(H_2O@C_{60})$ with τ=40μs (c) $Rb_3(H_2@C_{60})$

which is based upon the distribution of electrons on the cage. Then at 80 K the ratchet behaviour stops and the C_{60} cages are set in either one of two orientations, this is known as merohedral disorder. The resolution is not high enough to observe any phase transitions here. There are no obvious differences in the lineshape between materials in the range 298-15K. At temperatures below 15K, the lineshape broadens more in the case of the H_2 fulleride and the lineshift is greater at the lowest temperatures. It is not clear why this is, although may be reflective of the difference in T_c between materials and small variations in sample quality.

As the temperature is lowered below T_c, an asymmetry develops which could be assigned to the Knight shift decaying as the materials become superconducting. The transition temperatures measured from PPMS studies are consistent with the change in lineshape reported here [1] There is a more marked variation in the ^{87}Rb NMR lineshape as a function of temperature, which is shown in Fig.7.2. A notable point is that for all three samples there is a temperature dependent magnetic shift above T_c, discussed in greater detail in section 7.2. At temperatures greater than 50 K, there are three distinct sites which are characteristic of the alkali fullerides and denote octahedral and tetrahedral sites as discussed previously. The lineshape broadens below 150 K and the sites are not as clearly resolved, below T_c the decay of the Knight shift is such that the peaks merge and the three sites are not distinguishable at T$\leq$25 K.

In Fig.7.2b, the data recorded on the H_2O fulleride shows the signal arising from the

[1] At 14.1 T, T_c is determined to be 25.6 and 26.5 K for $Rb_3(H_2O@C_{60})$ and $Rb_3(H_2@C_{60})$ fullerides respectively, from PPMS studies discussed in section 6.3.2.

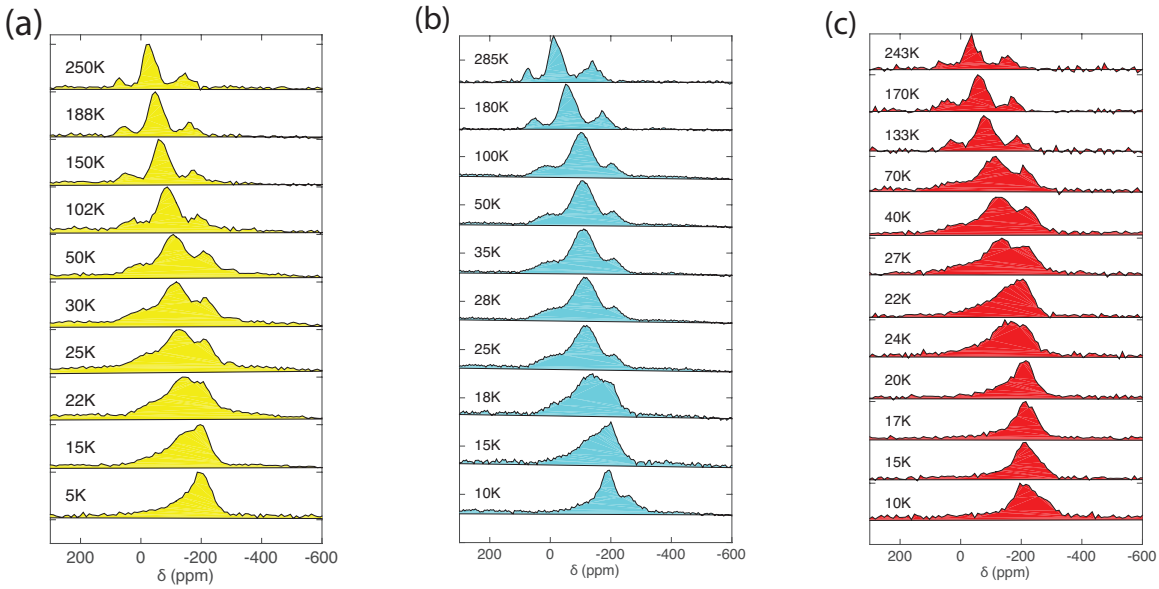

Figure 7.2: ^{87}Rb NMR spectra vs. temperature for the fulleride samples, recorded at 14.1 T using a Hahn-echo with τ=30μs. (a) Rb_3C_{60} (b) $Rb_3(H_2O@C_{60})$ (c) $Rb_3(H_2@C_{60})$

octahedral site is more pronounced, there appears to be a different evolution of peak shape compared to the H_2 and unfilled fullerides. All data was recorded with the same echo conditions, although the sample amounts vary by 50%, i.e. 10 and 15 mg for the H_2 and H_2O fullerides respectively. This would explain the difference in signal intensity, but not the variation in peak shape as a function of temperature. The variation might be intrinsic to the samples, one hypothesis might be a difference in Knight shift decays, this would arise from different critical temperatures, which would induce a variation in the resulting peak envelope across samples. Although it is difficult to resolve the three sites effectively, a weighted average fit, as discussed in section 7.2, shows no significant difference in the shift. On the other hand, the endohedral components might affect the structure of the carbon cage, for example in section 6.3.2 there is a variation of 1 K of the T_c between H_2 and H_2O fullerides, a similar effect is observed in other endohedral fullerides[26]. The change in peak shape may be a result of the varying structure due to a distortion induced by the endohedral component, this may then manifest through the lineshape. This effect is not seen in the H_2 fulleride, where the radius of H_2 is much smaller and there is no appreciable difference on the T_c.

The analysis given here is limited by the resolution and ideally future work should clarify these points using cryo-MAS at variable temperature to resolve the fine structure, a similar investigation has been done for Cs_3C_{60} and allowed high resolution ^{13}C and ^{133}Cs spectra to be collected at temperatures down to 5 K.[15]

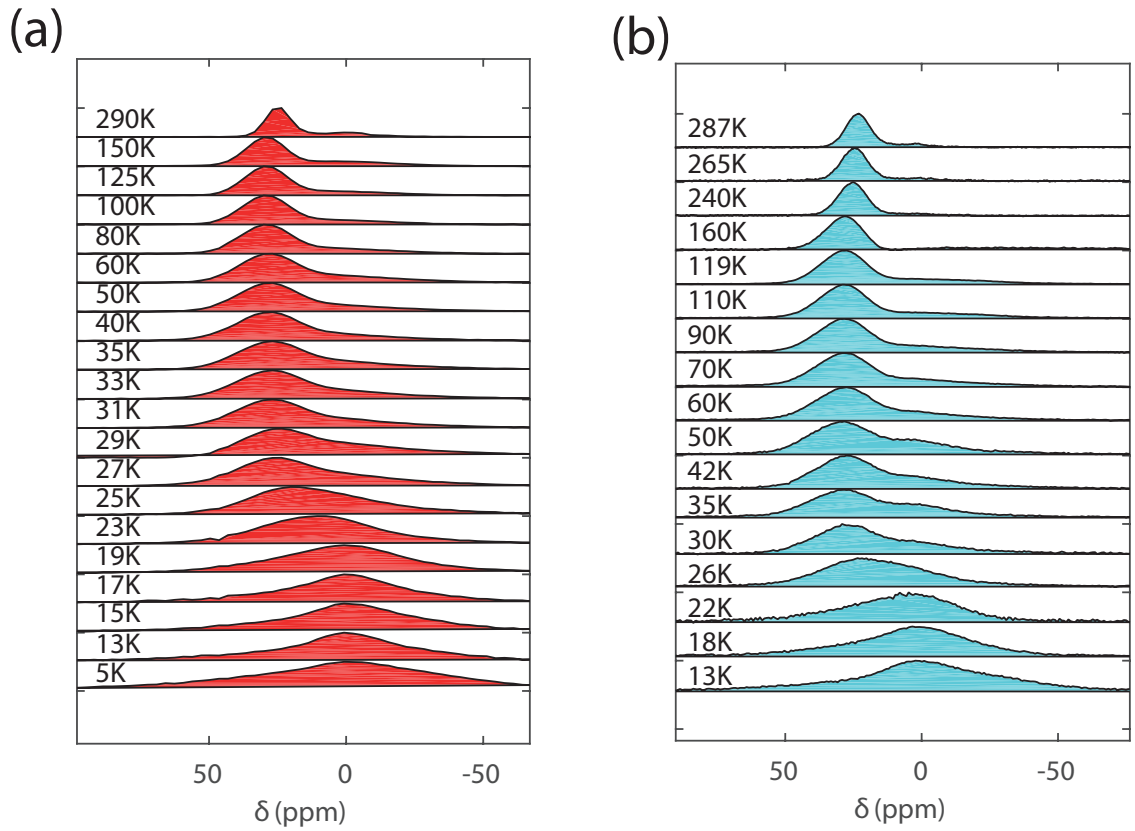

Figure 7.3: ^{1}H NMR Peak shape vs. temperature of endohedral fullerides at 14.1 T (a) $Rb_3(H_2@C_{60})$ recorded using Inversion Recovery (b) $Rb_3(H_2O@C_{60})$ recorded using Saturation Recovery

7.1.2 ^{1}H Peak shape

^{1}H NMR spectra were recorded at 14.1 T(600 MHz) and 4.7 T(200 MHz), shown in Fig. 7.3 and Fig 7.4. The extra signals in Fig. 7.3(b) at room temperature arise from the background. In both samples, at room temperature (298 K) the peaks are relatively narrow, characteristic of the rapid isotropic rotational motion of the endohedral component. As the sample is cooled, the peak broadens and this may be reflective of the rotational motion becoming more anisotropic. This has been reported previously for open-caged fullerenes[205], which have a lower symmetry than their endohedral fullerene analogues. In the case of the endohedral fullerides, the alkali metal also imposes a lower symmetry onto the C_{60} cages. This is consistent with both H_2O and H_2 endohedral fullerides, and therefore is likely to be a result of the alkali atoms rather than the endohedral component itself. At approximately 28 K at 4.7 T and 26 K at 14.1 T, there is a shift in peak position which is a characteristic signature of the superconducting state, arising from the decay of the Knight shift. This is consistent with PPMS measurements given in section 6.3.2. Additionally, a new peak appears

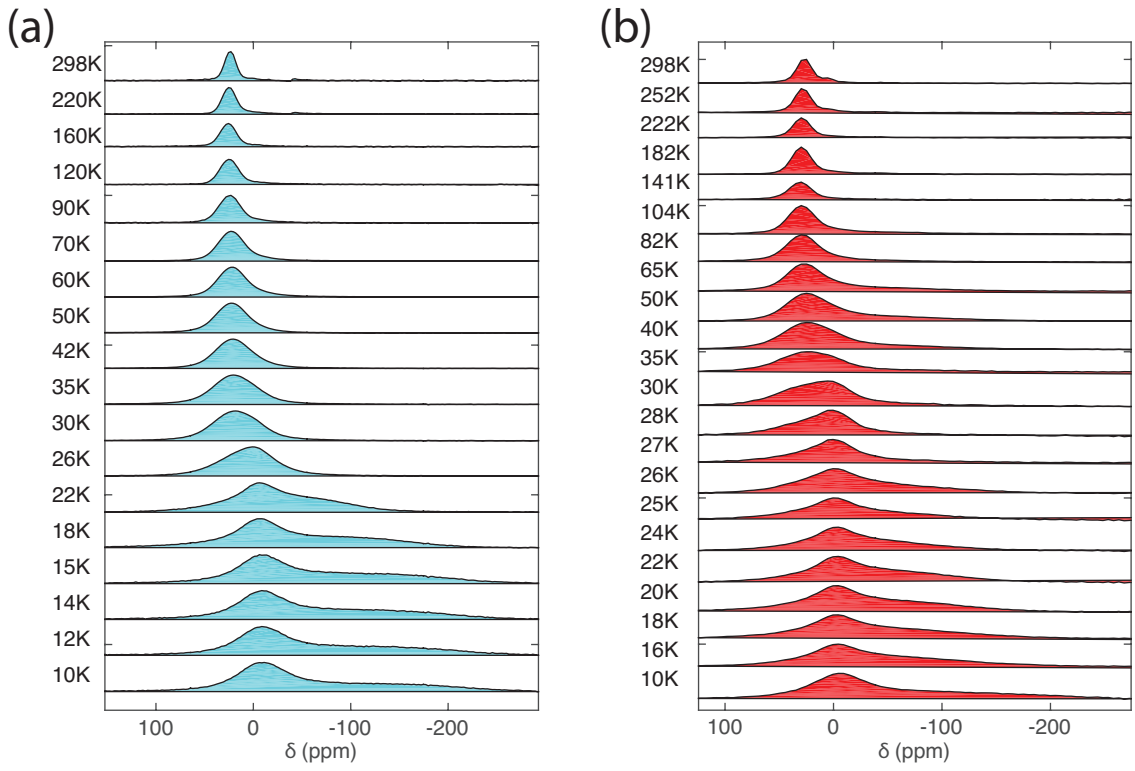

Figure 7.4: ^{1}H NMR Peak shape vs. temperature of endohedral fullerides at 4.7 T using a Hahn-echo with τ=25μs. Each spectrum was extracted from the last slice of 2D T_1 saturation recovery experiments and normalised. (a) $Rb_3(H_2O@C_{60})$ (b) $Rb_3(H_2@C_{60})$

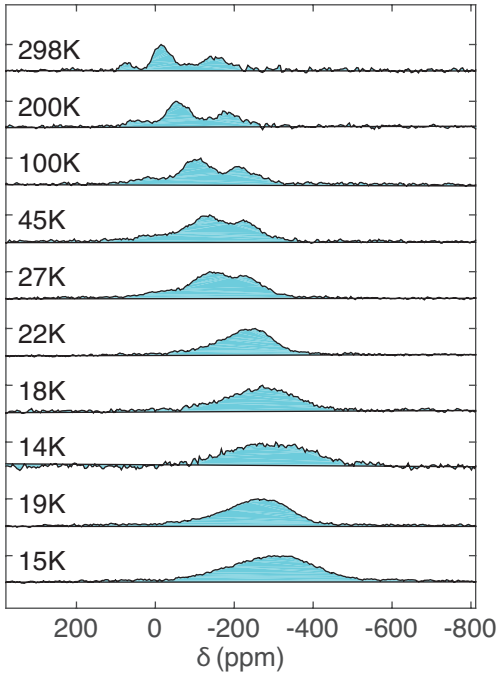

Figure 7.5: ^{87}Rb NMR spectra vs. temperature for the H_2O fulleride at 4.7 T, collected using a Hahn-echo with $\tau = 20\mu$s.

at temperatures below 26 K, on the negative ppm side, which corresponds to higher frequency. This new peak is characteristic of the inhomogeneous field distribution of the vortex state and is typically broad and featureless.[151]

This feature was only seen in ^{1}H spectra, for example Fig. 7.5 shows ^{87}Rb data collected at 4.7 T. There is no clear evidence of two separate domains, although the spectra is broader than at 14.1 T. As ^{87}Rb is quadrupolar, the difference in line broadening may be related to the inverse field dependence of the quadrupole interaction and not be related to the diamagnetic broadening in the superconducting state. To monitor the vortex state, one may fit the two peaks and extract the linewidth using the Gaussian equation discussed in section 5.1.3, a sum of two Gaussians were used to describe the lineshape below T_c, the FWHM is extracted from the Gaussian fit. Figure 7.6 shows the linewidth as a function of temperature for both endohedral materials. The linewidth increases from room temperature to T_c, which is approximately 28 K for both samples at 4.7 T.[2] This increase in linewidth is likely due to the reduced rotation of the C_{60} cage which has been noted to be the main source of anisotropy (in ^{1}H NMR) for the H_2O endohedral molecule[197], there appears to be a similar trend in the H_2 fulleride. Below T_c there are narrow and broad components which correspond to liquid and solid vortices respectively[151]. The initial drop in the linewidth is reflective of the

[2]From PPMS studies at 4.7 T: $Rb_3(H_2@C_{60})$ - 28.5 K and $Rb_3(H_2O@C_{60})$ - 27.8 K.

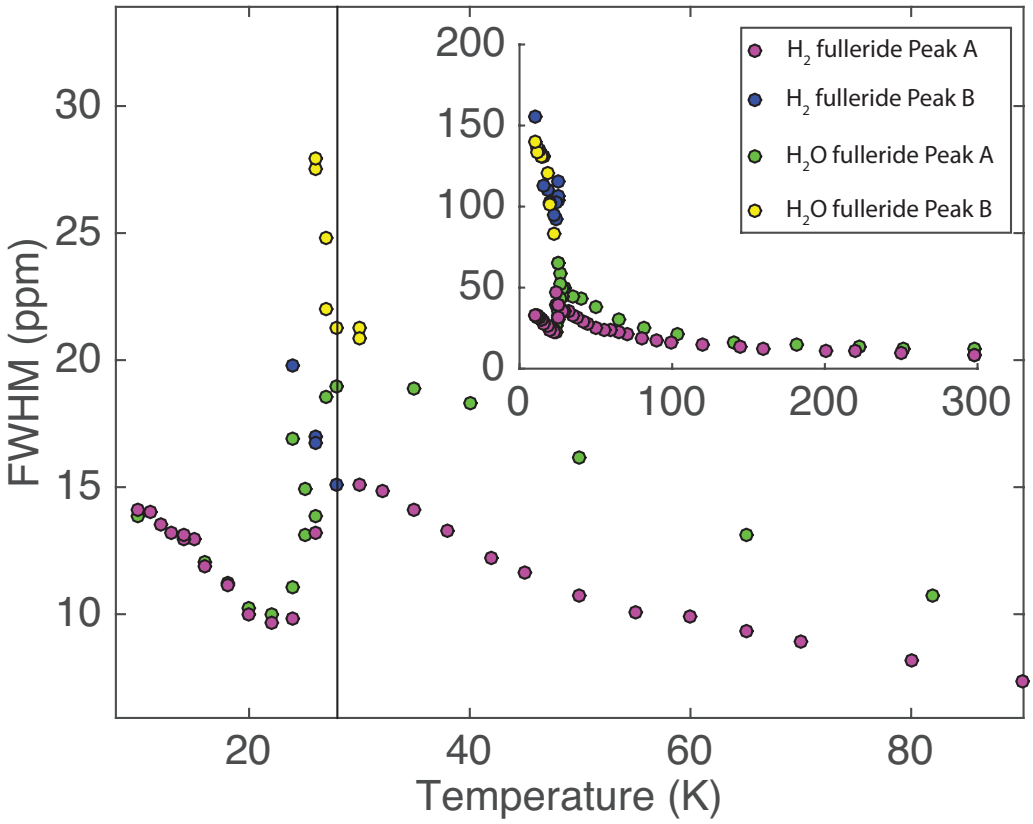

Figure 7.6: FWHM of ^{1}H NMR spectra as a function of temperature of the H_2 and H_2O endofullerides extracted using a Gaussian lineshape. For brevity $Rb_3(H_2@C_{60})$ and $Rb_3(H_2O@C_{60})$ are denoted H_2 and H_2O fulleride respectively. A sum of two Gaussians is used to describe the behaviour below T_c. Peak A is the normal state signal and below T_c follows the liquid vortices, Peak B is assigned to the inhomogeneous field distribution from vortices in the solid phase which continue to broaden at low temperatures[151]. Solid line is T_c determined from PPMS

liquid vortices, which typically have a short correlation time with respect to the echo time used in the experiments, this means the time average is recorded and the linewidth is narrow. The broad component represents the solid vortices, which have a relatively slower correlation time and are therefore not time-averaged. Both components exist in both samples simultaneously below T_c. The two components also increase in width, as temperature is lowered. This is the expected behaviour as the penetration depth decreases with decreasing temperature. This analysis is based on vortex melting in YBCO-123[151]

The broadening below T_c can be exploited to extract the penetration depth, by fitting the spectrum to two Gaussian functions and monitoring the change in σ. The peak associated with the solid vortices broadens below T_c and the difference between

the σ just above T_c and well below T_c allows an approximation of the penetration depth, as discussed in 4.7 and reported in previous works[152]. This is done for the H_2O and H_2 endofulleride yielding 520 and 587 nm respectively and is quite close to other NMR studies reporting the penetration depth as 420 nm[81] and μSR meausrements give 460 nm[112]. Optical measurements on the other hand give 800 nm for Rb_3C_{60} and AC susceptibility find λ=350 nm.[206]

7.2 Magnetic shift measurements

To investigate the superconducting state further, the magnetic shift was followed as a function of temperature. ^{13}C and ^{87}Rb measurements were used to characterise the materials and compare with existing literature, however ^{1}H NMR measurements are novel and therefore do not have an established precedent. All ^{87}Rb NMR spectra were referenced to a sample of RbCl(aq) with a chemical shift of 0 ppm. ^{13}C NMR spectra referenced to adamantane with a chemical shift of 38.2 ppm (CH_2 peak)[196] or toluene with a chemical shift of 128 ppm. ^{1}H NMR spectra referenced to water with a chemical shift of 4.8 ppm.

7.2.1 Experimental methodology

The ^{87}Rb NMR spectrum at room temperature consists of three sites as discussed previously[154]. This may be fit to three Gaussians as shown in Fig. 7.7a. As the temperature is decreased, the NMR signal shifts in the normal state. This means that the three resolved sites at room temperature become difficult to distinguish at low temperatures <50 K. An example fit with three Gaussians is shown in Fig. 7.7a. For ^{13}C NMR spectra the weighted average was taken by fitting to a Gaussian lineshape shown in Fig. 7.7b.

The ^{1}H NMR spectrum in the normal state consists of a single peak, which was well described by a Gaussian line shape, as shown in Fig 7.7c. In the superconducting state, there is an additional peak which is broad and featureless, an additional Gaussian is required to fit these spectra, shown in 7.7d.

7.2.2 Magnetic shift vs. Temperature

The ^{87}Rb NMR peak position was followed as a function of temperature, shown in Fig. 7.8 for the normal alkali fulleride and the two endohedral fullerides between 298-5 K, monitoring both the normal and superconducting state. The lineshape consists of three components, related to inequivalent sites discussed in section 6.3.1. Fig. 7.8a shows the

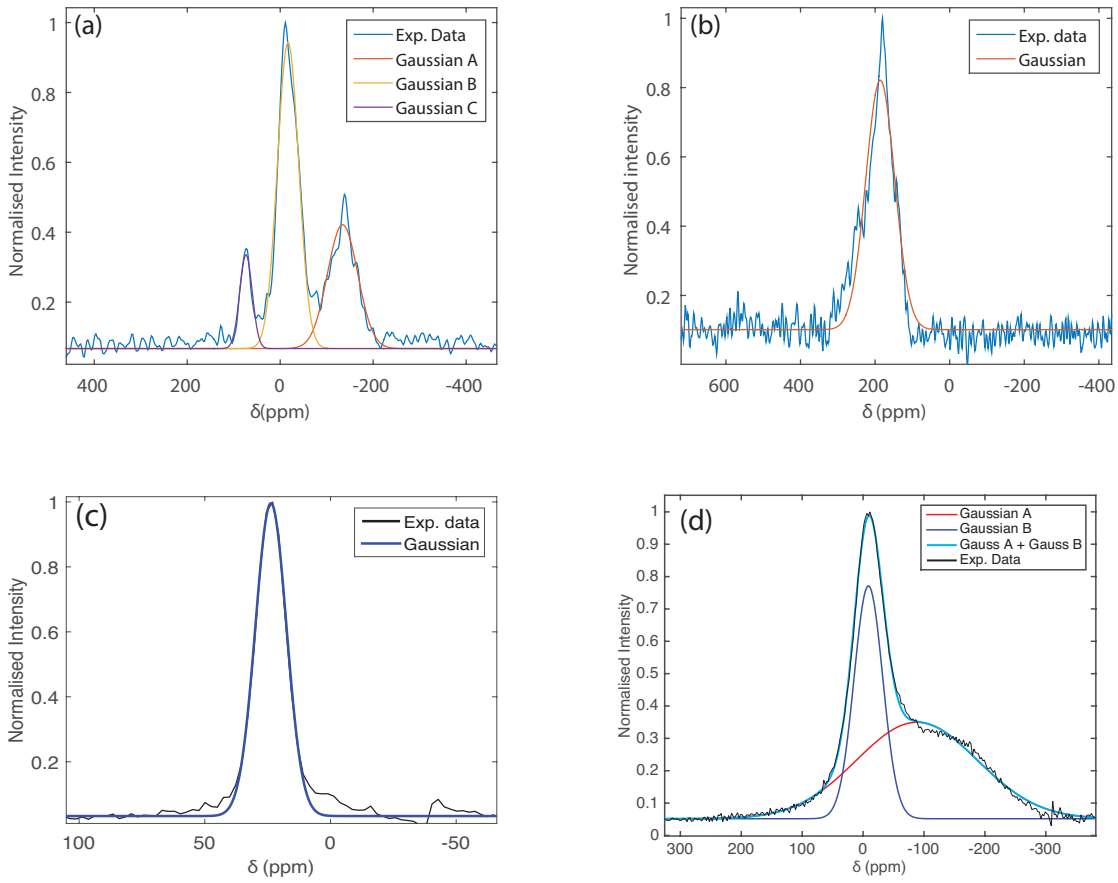

Figure 7.7: Gaussian fits of ^{87}Rb, ^{13}C and ^{1}H NMR spectra of $Rb_3(H_2O@C_{60})$ in the normal state at 14.1 T. (a) ^{87}Rb NMR spectra fit with three Gaussians (b) ^{13}C NMR spectra fit with one Gaussian (c) ^{1}H NMR spectra fit with one Gaussian (d) ^{1}H NMR spectra in the SC state fit with two Gaussians

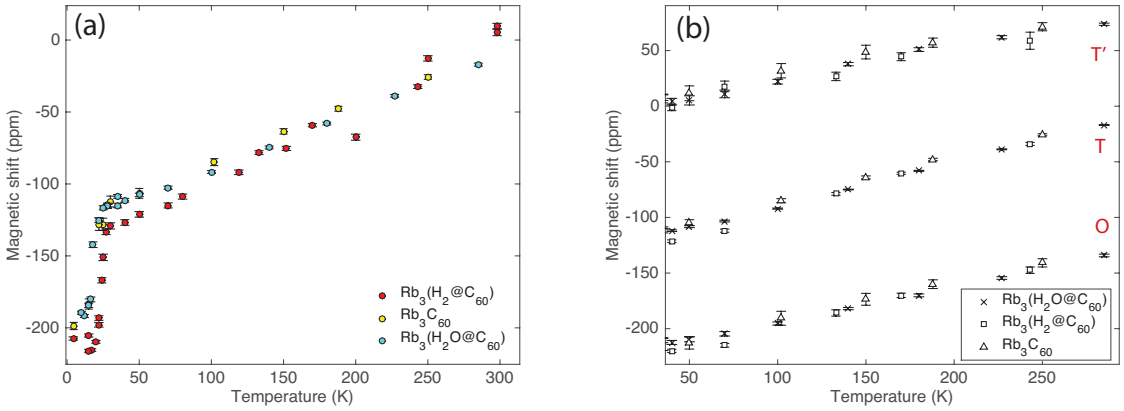

Figure 7.8: ^{87}Rb peak position vs. Temperature fit with one and three Gaussians. (a) One Gaussian fit to most intense signal (b) Three Gaussians, one fit to each signal

peak position resulting from the lineshape fit to a single Gaussian, which approximates the weighted average of the three components. In Fig. 7.8b, three Gaussians have been used to describe the lineshape as a function of temperature, this becomes difficult to reliably interpret below T_c, as the peaks merge.

Immediately in both figures it is apparent that there is a temperature dependent lineshift in the normal state, above the superconducting transition. This is in line with previous works, it has been suggested that this is an effect related to a temperature dependent susceptibility[28, 155]. The temperature dependence is similar for all three materials, which seems to suggest no appreciable effect is observed from NMR on the structure from implanting endohedral molecules inside C_{60}.

An approximation of the Knight shift can usually be extracted from comparison of the normal state magnetic shift with the low temperature shift, although there will still be a diamagnetic contribution. In this case there are three sites, which become indistinguishable at low temperatures and this makes obtaining the Knight shift difficult. Mehring et al.[155] have used the temperature dependent susceptibility of ^{87}Rb and ^{13}C to extract the isotropic hyperfine interaction, by correlating the temperature dependent shifts with the measured susceptibility from SQUID experiments. They obtained $^{87}K_s$ of -164, -188 and -98 ppm for the O, T and T′ sites respectively, although the temperature variation of the shifts is weak[3].

The variation of shift as a function of temperature for the endohedral fullerides, for each nucleus are compared in Fig. 7.9. Immediately it becomes clear that the ^{87}Rb signal varies considerably as a function of temperature, however there is no clear variation in ^{13}C or ^{1}H NMR in the normal state. This suggests that the ^{87}Rb nuclei

[3]The symbol $^{\alpha}K_s$ is used to denote the Knight shift, also known as the spin shift. α refers to the nuclear isotope of interest, for example $^{87}K_s$ refers to the Knight shift of the nuclear isotope ^{87}Rb

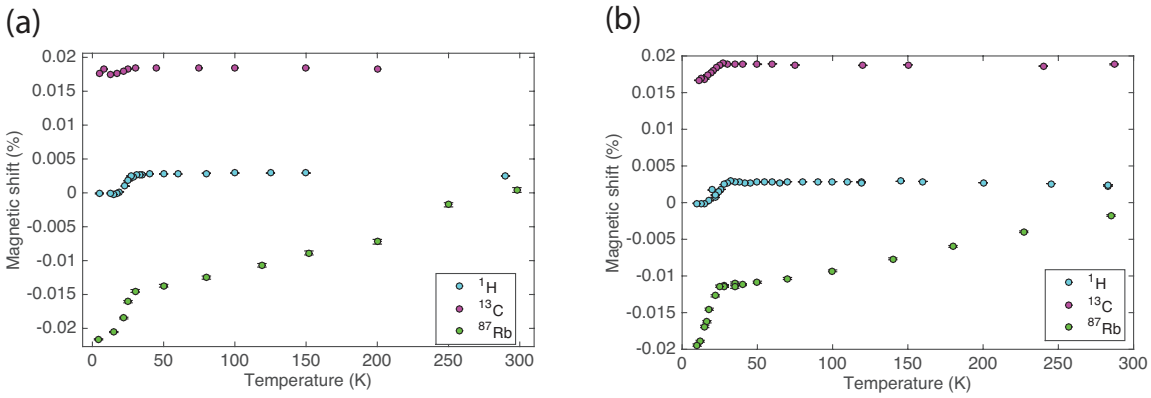

Figure 7.9: ^{1}H, ^{13}C and ^{87}Rb magnetic shift as a function of temperature at 14.1 T for expressed in % (a) $Rb_3(H_2@C_{60})$ and (b) $Rb_3(H_2O@C_{60})$

probe a region of different susceptibility to ^{1}H and ^{13}C. This is because the Knight shift, and therefore the total shift, is related to the spin susceptibility as described in section 7.3.1.

The ^{13}C NMR lineshift is shown in figure 7.10. The ^{13}C resonance is broad, and a weighted average is used to describe the peak position. There is a decay in Knight shift at a temperature in-line with the PPMS data and studies on ^{87}Rb NMR. There has been difficulty in the past obtaining an absolute value for the Knight shift for ^{13}C on the rubidium fullerides. Mehring et al. determined the value of the chemical shift by observing the shift in the superconducting state, which does not include the Knight shift contribution. However due to experimental uncertainty they use an interpolated value between insulating C_{60} and Rb_6C_{60} as 149 ppm.[90] By taking the difference between the ^{13}C normal-state shifts given in Fig. 7.10 and Mehring's interpolated value, gives $^{13}K_s \cong 37.2$ and 34.2 ppm for the H_2O and H_2 fulleride respectively.

The ^{1}H NMR magnetic shift of both endohedral fullerides was monitored as a function of temperature at 4.7 and 14.1 T, shown in Fig. 7.11. The inset shows the full range which includes the inhomogeneous broadening in the vortex state, only visible at 4.7 T. At 14.1 T, the magnetic shift is constant across the normal state and then decreases at the T_c, which is expected for a s-wave superconductor as the Knight shift decays. Both superconductors follow this trend with the deviation approximately at 29 K in both cases at 14.1 T. At 4.7 T for both superconductors there is a deviation from the normal state magnetic shift, for the H_2O endofulleride this occurs at 200 K, whereas the H_2 fulleride has a constant magnetic shift until 80 K.

The Knight shift then may be approximated by extracting the lowest temperature shift and taking the difference between this value and the normal state magnetic shift. This approximation is quite accurate however, as the shift tends to a zero slope as shown in Fig. 7.12, where the shift follows a Yosida function decay in the strong coupling

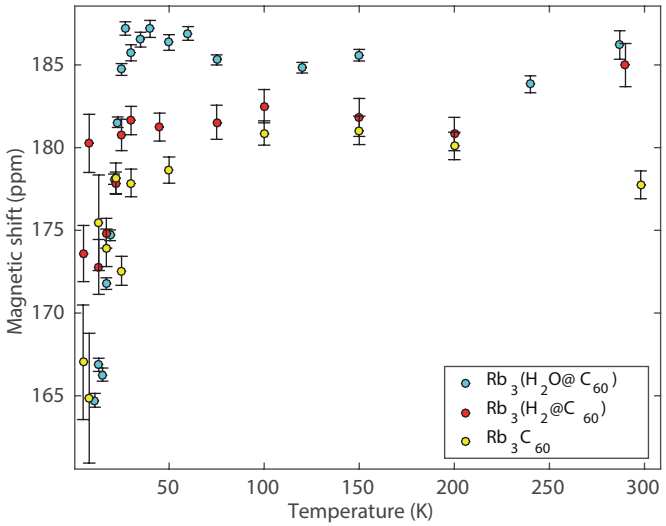

Figure 7.10: ^{13}C peak position vs. Temperature fit with a single Gaussian, data recorded at 14.1 T, the error margins indicate the uncertainty in peak position from a broad powder pattern.

regime ($2\Delta/k_BT_c = 5.5$). This is higher than reported in the past for studies which involve calculations of the Yosida function, although diamagnetic screening currents may not reveal the true decay curve, this is discussed further in the following section.

Following the argument that the lowest temperature shift has zero Knight shift, the Knight shift is determined by simple subtraction with the room temperature shift. The H_2O endofulleride has ^1K_s≈24 and 32 ppm and the H_2 endofulleride has K_{iso}≈25.5 and 32 ppm for 14.1 and 4.7 T respectively. The difference between fields might be ascribed to the diamagnetic contribution in the superconducting state which causes the applied field to be shielded. An alternative method to determine the Knight shift is to take the difference between the σ_{iso} of the parent insulator compounds H_2@C_{60} and H_2O@C_{60}, where the shifts are known accurately from MAS-NMR studies[197, 198], and the normal state values. This corresponds to ^1K_s≈26.8 and 28.2 ppm for the H_2 and H_2O fulleride respectively. These small Knight shifts suggests a small contribution from the Fermi-contact interaction, as has been suggested previously for MgB_2[207, 208].

7.2.3 Knight shift and Spin susceptibility

The diamagnetic contribution to the magnetic shift can be removed by subtracting the shifts of two different nuclei, the resulting quantity after normalisation is the normalised spin susceptibility as discussed in section 4.3. The result of this is shown in Fig. 7.13a and Fig. 7.13b. The solid and dashed line represent calculations of the Yosida function for $2\Delta_0/T_c k_B$=5.5 and 3.5 respectively. The decay is better fit to a gap ratio of 5.5 in

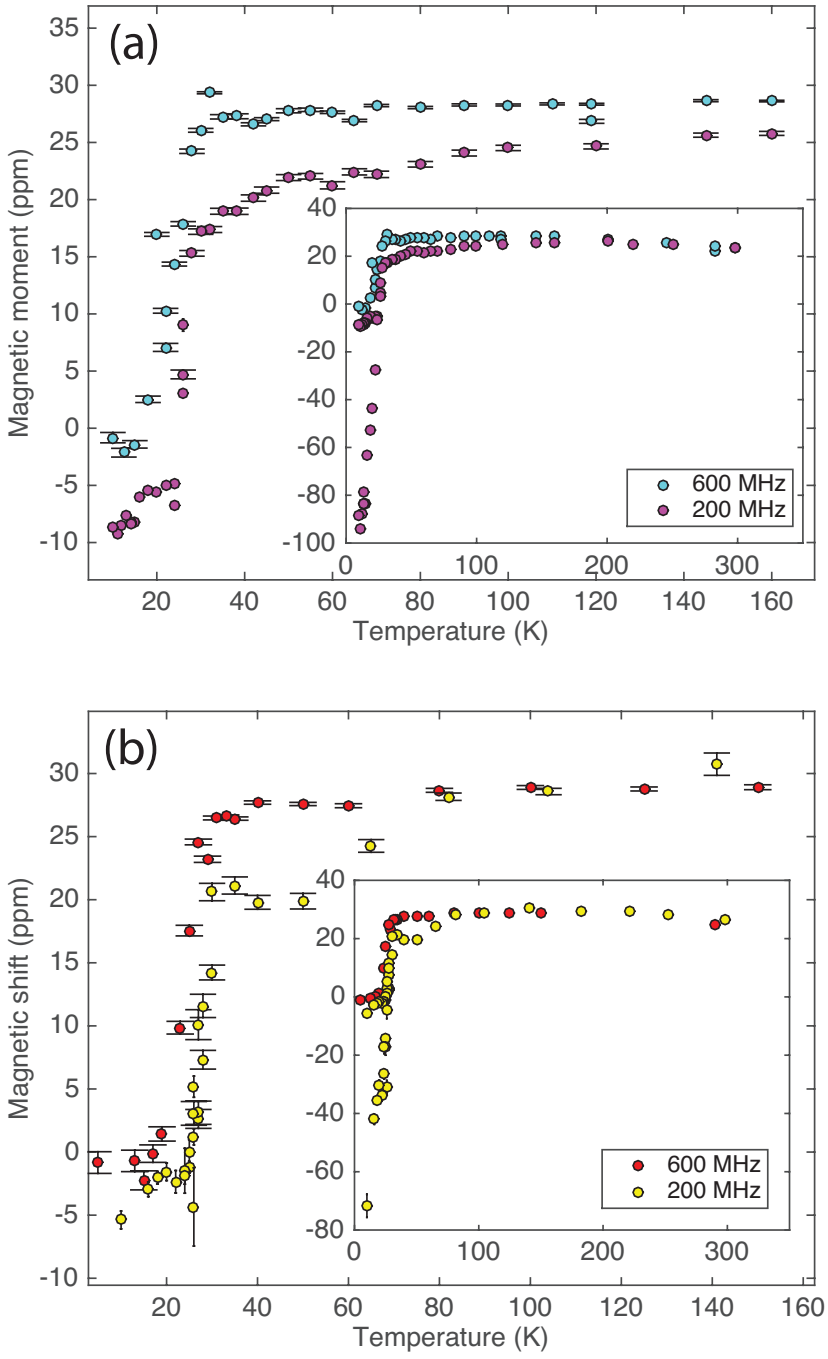

Figure 7.11: ^{1}H magnetic shift vs. temperature for $Rb_3(H_2@C_{60})$ and $Rb_3(H_2O@C_{60})$ at 4.7 and 14.1 T. The inset shows the full temperature range (a) $Rb_3(H_2O@C_{60})$ (b) $Rb_3(H_2@C_{60})$

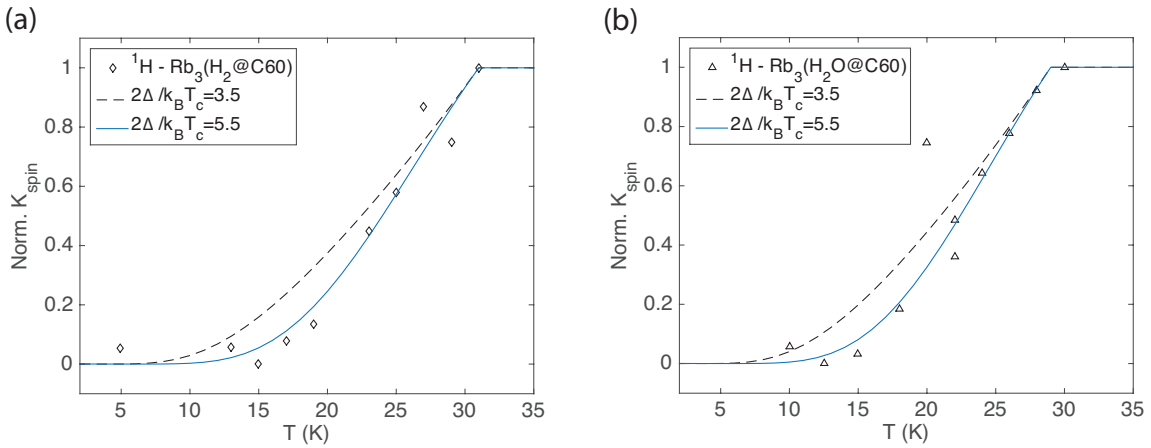

Figure 7.12: ^{1}H Knight shift decay below T_c $Rb_3(H_2@C_{60})$ and $Rb_3(H_2O@C_{60})$ at 4.7 and 14.1 T compared to Yosida functions calculated for BCS and strong coupling.(a) $Rb_3(H_2@C_{60})$ (b) $Rb_3(H_2O@C_{60})$

both cases but there is a large error which arises from describing the magnetic shift in a broad distribution due to a static powder sample. As discussed in section 4.3, any two NMR nuclei may be used for the analysis of the spin susceptibility. In this case, the magnetic shift data from ^{1}H NMR is not appropriate to use for this analysis, as at 14.1 T, there is a decay in shift at 30 K. This is a higher temperature than the ^{13}C and ^{87}Rb nuclei, which decay at 28 K, which is consistent with PPMS measurements as discussed in section 6.3. It is not known why this is, but it may be due to variations in local susceptibility experienced by the endohedral component. This is not the case for data collected at 4.7 T, in which the deviation in the NMR shift is the same for both ^{1}H and ^{87}Rb, shown in Fig. 7.13c. Again in this instance the decay is better fit to a Yosida function of $2\Delta_0/T_c k_B$=5.5, however the decay is even steeper than this and it was not possible to numerically fit.

The gap has previously been fit to a ratio of 4.1 from ^{13}C $1/T_1$ studies[81] and 3.5 from similar Knight shift subtractions[100]. This large discrepancy may be attributed to the differences in sample quality and accuracy of the method used to extract the gap value. In order to overcome these issues, single crystals allow more accurate determination of the magnetic shift, although they are difficult to grow. An alternative is the use of cryogenic MAS experiments[137] which allows high resolution NMR spectra to be collected at temperatures as low as 5 K. This has previously been done on a sample of Cs_3C_{60}, although the spin susceptibility was not reported.[15]

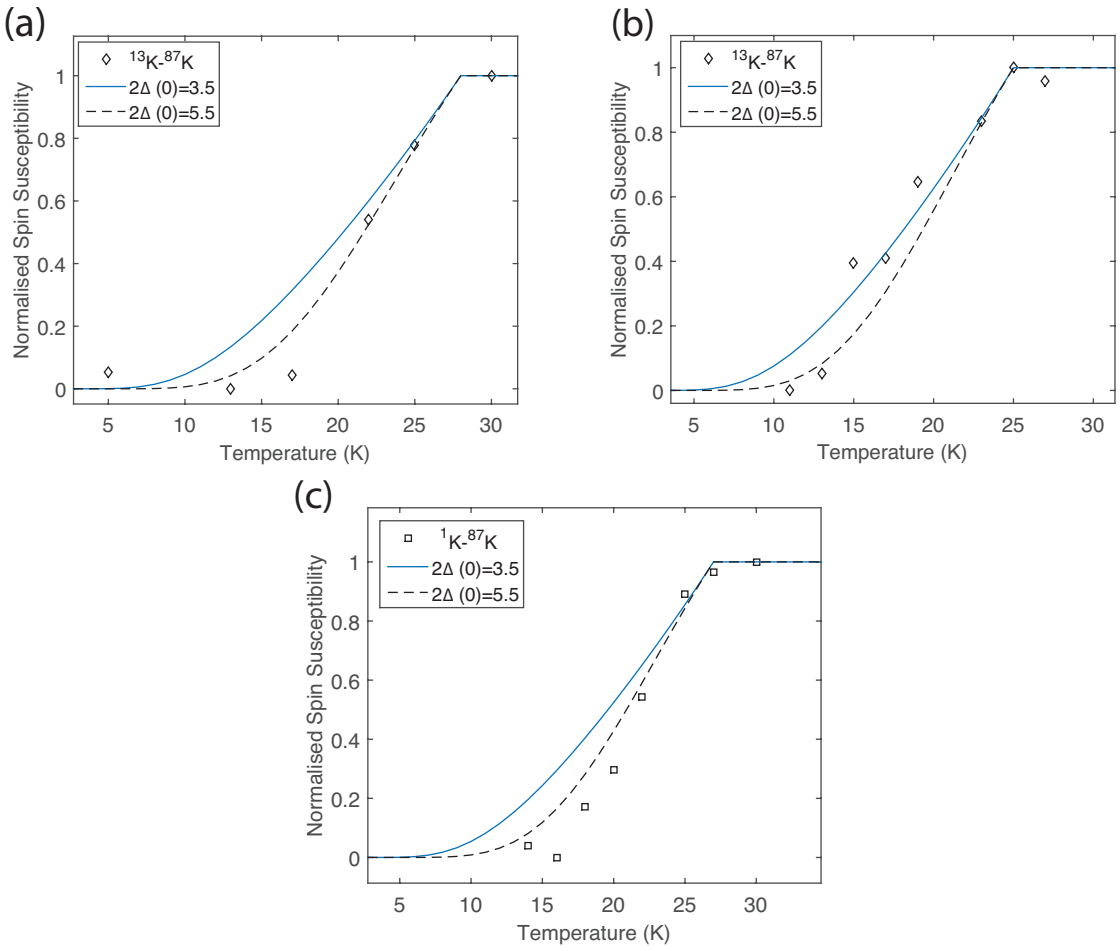

Figure 7.13: Normalised susceptibility for endohedral fullerides, extracted from subtraction of fractional shifts in NMR frequency for different nuclei, resulting decay is compared with Yosida function as described in text.(a) $Rb_3(H_2@C_{60})$ at 14.1 T (b) $Rb_3(H_2O@C_{60})$ at 14.1 T (c) $Rb_3(H_2O@C_{60})$ at 4.7 T

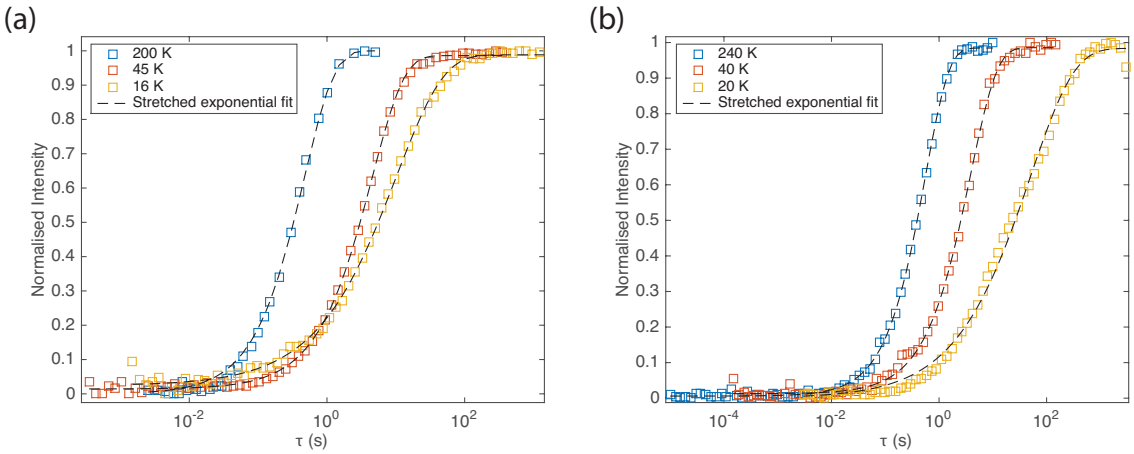

Figure 7.14: Stretched exponential fits of ^{1}H T_1 for H_2O endofulleride in the normal and superconducting states at (a) 4.7 T (200 MHz) (b) 14.1 T (600 MHz)

7.3 Nuclear Spin-lattice relaxation measurements

The nuclear spin lattice relaxation rate is followed as a function of temperature for ^{13}C, ^{87}Rb and ^{1}H nuclei for both H_2 and H_2O endohedral fullerides. The saturation recovery equation described in section 5.1.3 was used to fit ^{87}Rb and ^{13}C T_1 data. ^{1}H T_1 data was fit to either stretched exponential or bi-exponential functions, as discussed.

7.3.1 ^{1}H T_1 measurements on the H_2O endofulleride

Methodology

The ^{1}H T_1 was monitored as a function of temperature for the H_2O fulleride using a saturation recovery sequence, the T_1 was extracted using a single stretched exponential function. Given by

$$y(x) = A\exp(-x/T_1)^{\beta} + C \tag{7.1}$$

Where x is time. This is shown in Fig. 7.14 for both 4.7 and 14.1 T. At temperatures above T_c, the relaxation behaviour is described by the stretched exponential function with coefficient β equal to unity. This is the same as a single exponential function. At temperatures lower than T_c, the curve represents a superposition of relaxation curves and therefore becomes stretched. In this case β is lower than unity and this yields a better fit.

Results

Fig. 7.15 shows ^{1}H NMR $1/T_1$ on the metallic endofulleride and parent insulator endofullerene. In the endofulleride case the relaxation behaviour appears to follow

a linear dependence, which is expected for metallic systems[145]. The parent insulator endofullerene compound shows a similar decrease in relaxation rate, although the behaviour does not follow the same linear dependence. The mechanism of relaxation in the $H_2O@C_{60}$ parent compounds is governed by the spin-rotation mechanism of relaxation[209]. Interestingly, in the endofulleride there is a decrease in $1/T_1$ with respect to the endofullerene. The different contributions to relaxation are normally additive, but in this case the addition of Rb clearly damps the $1/T_1$. It is not clear if the spin-rotation mechanism is hindered or inhibited in this case. It has been speculated in the past that the addition of ions can affect the position of the H_2O molecule inside the cage[210], and this complements the observation of a reduced $1/T_1$ in the presence of Rb ions.

A brief summary of the relaxation behaviour is given, and then subsequent sections deal with each observation in more detail.

In terms of the temperature dependence, there appears to be a coupling between the conduction electrons and endohedral nuclei, this was apparent from a Knight shifted signal (section 7.2.2) but also the $1/T_1$ follows the Korringa law, which is also indicative of the Fermi-contact interaction. This is discussed in more detail in section 7.3.3 and 7.3.6.

There is also a deviation at T_c consistent with PPMS measurements (section 6.3.2). This is consistent with other NMR nuclei, and is discussed in more detail in section 7.3.4. There is also an enhancement at T_c which is observed at 4.7 T, this is assigned to the Hebel-Slichter coherence peak and is discussed in section 7.3.5.

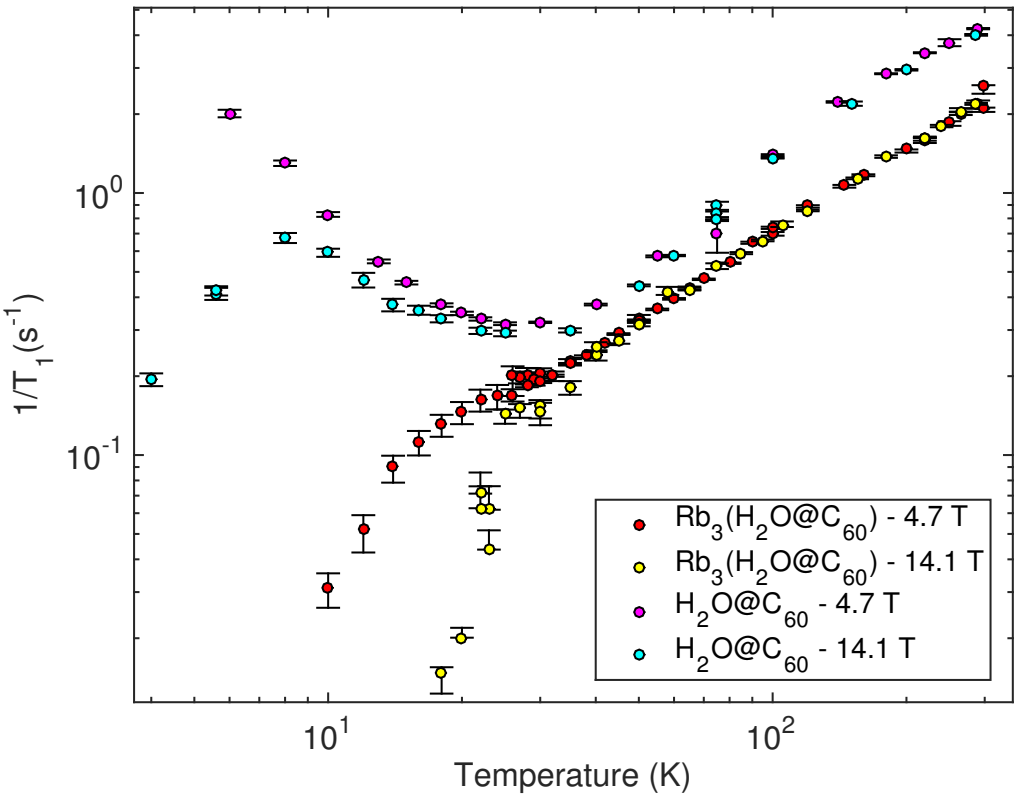

Figure 7.15: ^{1}H $1/T_1$ as a function of temperature at constant magnetic fields of 4.7 and 14.1 T, data is collected using the saturation recovery pulse sequence with an echo for magnetisation readout

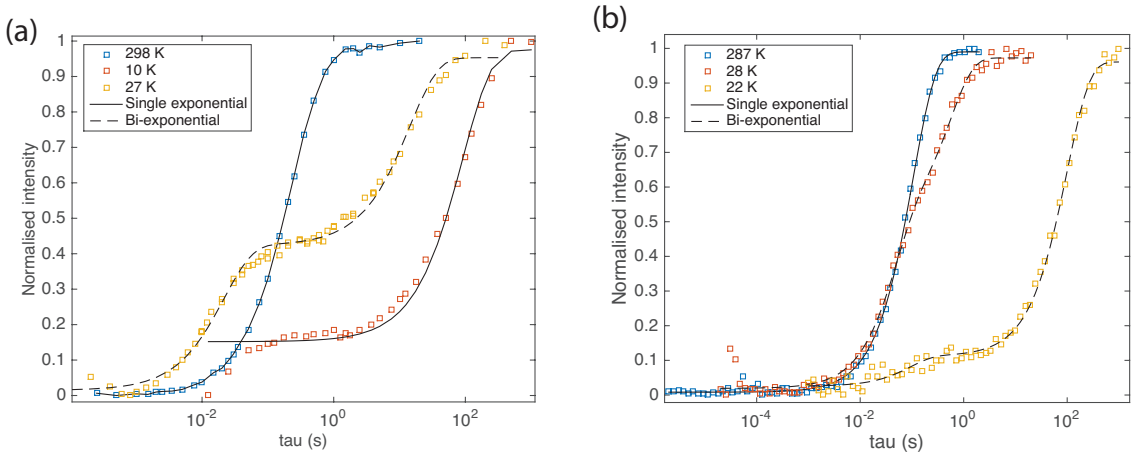

Figure 7.16: Single and bi-exponential fits for H_2 endofulleride in the normal and superconducting states at(a) 4.7 T (b) 14.1 T

7.3.2 ^{1}H T_1 measurements on the H_2 endofulleride

The ^{1}H T_1 was measured in the H_2 endofulleride, the results were quite different to the expected behaviour in metals, and the form more closely resembles some heavy fermion superconductors.[211] There was some difficulty in determining the most appropriate method for both the measurement and description of the nuclear spin relaxation, as there is a vast difference between the high and low temperature regimes as discussed.

Methodology

Initially an inversion recovery experiment was used, however this was found to be too time consuming as the relaxation rate becomes very long at low temperatures, i.e below 35 K for data collected at 14.1 T and 30 K for data at 4.7 T . Therefore the measurement of T_1 was done using a saturation recovery experiment and this was found to be more appropriate. Additionally, the variable delay list used was initially composed of 32 elements, however this was increased to 64 elements when it was clear that there were two components present at low temperatures. Increasing the variable delay list to 64 elements allowed the full relaxation curve to be recorded in one experiment, however the best fits were obtained by recording experiments with 32 elements in pairs, with one experiment sampling the first component which is very short and one experiment sampling the second component which is very long. This is now outlined in slightly more detail. Due to spurious background signals, initially the inversion recovery experiment to measure T_1 was selected. This selects components according to their pulse widths, advantageous if there are background signals, but requires the experiment time to be vastly increased relative to the saturation recovery method. This is due to the requirement that the cycle time between experiments has

to be 3-5×T_1, which can be long especially in superconductors at low temperatures.

This method was initially implemented at 14.1 T and allowed measurement of T_1 across a wide temperature range, given in Fig. 7.17. The saturation recovery method was implemented as well, in order to compare and contrast with inversion recovery. The result is given in Fig. 7.17 and immediately it becomes obvious there is an offset between the data points. This is most likely due to insufficient cycle times between experiments in the inversion recovery experiment, leading to an overestimation in the T_1. The saturation recovery experiment at 14.1 T was observed to be more consistent with data collected at other fields and also verified on a second occasion. Therefore all data presented in the following section was collected using a saturation recovery sequence, described in section 5.1.3.

It was found that for ^{1}H data recorded at 14.1 T, the region between 298-35 K was adequately described by a single exponential, however at temperatures below 35 K, there appeared to be a second contribution to the rate. A distribution of rates usually can be described using the stretched exponential method. However in this case there is a vast difference between the contributions and a second exponential is required. These fits are shown in Fig. 7.16, the fits are to a single exponential function in the region 298-35 K and a bi-exponential function at temperatures below 35 K where there were clearly two components. At all fields in some of the fits the first few points are excluded, due to insufficient saturation of the signal.

For data recorded at 4.7 T a similar methodology was adopted, with a single exponential function describing data between 298-30K and then two exponential functions below this temperature. In this case more data-points were recorded at lower temperatures, at temperatures <20 K a single exponential is found to be more appropriate to describe the data.

Data recorded at 8.5 T was fit to a single exponential at all temperature points, however shorter delay lists were used in this experiment and the true bi-exponentiality is not clearly observed.

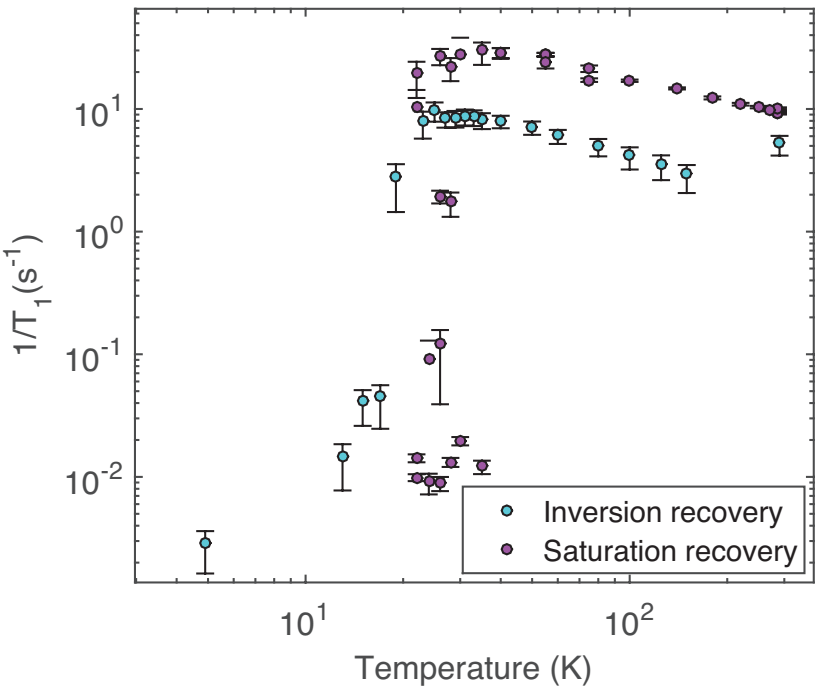

Figure 7.17: ^{1}H T_1 measurements on $Rb_3(H_2@C_{60})$ with inversion recovery and saturation recovery methods, measured in a constant magnetic field of 14.1 T

Results

Fig. 7.18a shows ^{1}H $1/T_1$ data at 4.7, 8.5 and 14.1 T on the H_2 endofulleride. Fig. 7.18b shows $1/T_1$ data for the parent insulator endohedral fullerene, $H_2@C_{60}$ and this is compared with $Rb_3(H_2@C_{60})$. Data on $H_2@C_{60}$ contributed by Salvatore Mamone at the University of Nottingham.

The ^{1}H $1/T_1$ of the H_2 endofulleride between temperatures 298-30 K increases, this appears to be field independent and is consistent across experimental sessions and described well by a single exponential. This is not observed in the parent endofullerene, which initially is constant between 300-200 K, where a large enhancement is observed, followed by a linear decay. Alternatively on the endofulleride material there is a large discontinuous decrease in relaxation rate at approximately 30 K, although this temperature appears to vary between fields[4]. It is not clear if this is an effect arising from the superconducting state, or some other currently unknown mechanism. Fig. 7.19 shows a comparison of $1/T_1$ and magnetic shift at 4.7 and 14.1 T, there appears to be similar temperature dependence between the transitions of the NMR parameters (i.e. both magnetic shift and T_1 decrease) and the temperature. This seems to indicate the involvement of the superconducting gap, but the more measurements are required to

[4]30 K at 4.7 T, 35 K at 14.1 T

further elucidate this point. In the normal state, it is immediately apparent that the data do not follow the standard Korringa behaviour for metals, although data collected on other nuclei do follow this law, a situation reminiscent of the cuprates[212, 213]. It is also clear that the alkali doped endofullerides have completely different $1/T_1$ than the parent endofullerene, which is governed by a dipolar and spin-rotation mechanism of relaxation[214, 215]. Interestingly the relaxation is initially slower in the endofulleride than in the endofullerene, one might expect the contrary, especially as the hyperfine interaction offers a powerful source of relaxation which is usually dominant[138]. Although at T<40 K the relaxation starts to become faster. One possible hypothesis is that the coupling between the phonons of the C_{60} cage and the spin-rotation of the endohedral molecule might be the dominant relaxation mechanism. One would expect a temperature dependence in this case, as the phonon modes change as temperature is reduced and this would especially be relevant below T_c where the phonon modes above and below the superconducting gap harden and soften respectively[216]. A sample of $Rb_3(HD@C_{60})$ is currently being prepared, which has different spin-rotational states than the H_2 derivative[217]. If the spin-rotation mechanism is a dominant contributor then the relaxation behaviour is expected to differ.

In general the form of relaxation presented here is quite different to the usual cases encountered in most superconductors, and superficially the form is most similar to the heavy fermion superconductor $PrOs_4Sb_{12}$[211]. In this superconductor, the $1/T_1$ increases as temperature is decreased, in a region still considered to be the normal state. A decay in $1/T_1$ is then observed at a temperature above T_c[218].

In metals the conduction electrons interact with the nuclei to cause a flip-flop and aid relaxation, as described in section 4.5. This form of relaxation holds for temperatures between the nuclear Zeeman splitting and electronic Fermi temperature ($\gamma B_0 < T < E_F$) and also assumes the Fermi-contact interaction is the dominant contribution, i.e. not the orbital or core polarisation term[219]. The Fermi-contact interaction may only be a small contribution to the total T_1 mechanism. The reason for this is as the Knight shift in both the H_2 and H_2O fullerides is of similar value. This indicates there is some similarity in the hyperfine interaction in both materials and from measurements of the Korringa ratio in the H_2O fulleride, deviating from unity (shown in section 7.3.6), is indicative of the presence of other relaxation mechanisms. The relaxation mechanism in the H_2 fulleride is currently unknown, but further experiments and ab-initio calculations are currently planned to elucidate these points further.

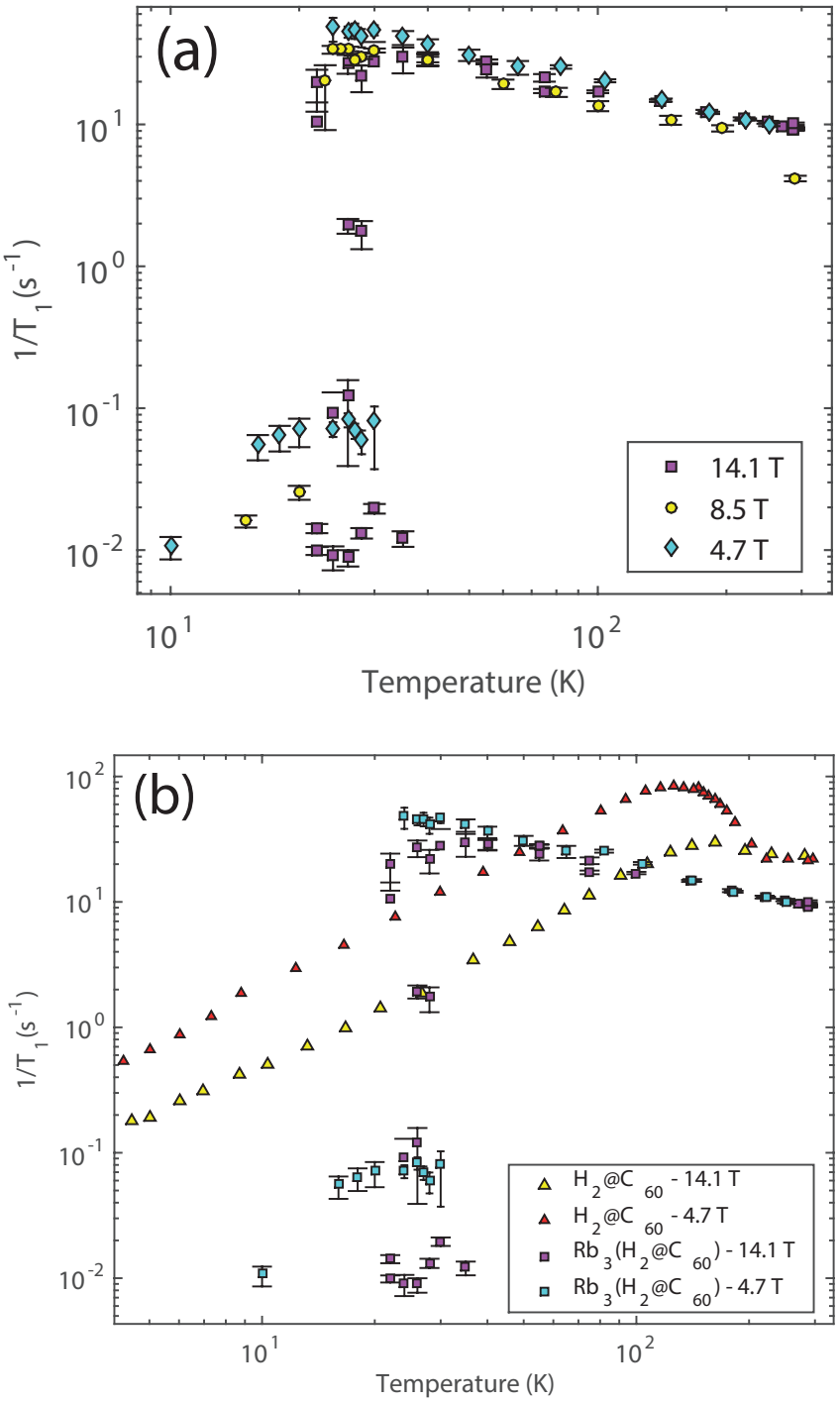

Figure 7.18: (a) ^{1}H $1/T_1$ on $Rb_3(H_2@C_{60})$ recorded at 4.7, 8.5 and 14.1 T using a saturation recovery sequence (b) ^{1}H $1/T_1$ on $Rb_3(H_2@C_{60})$ recorded at 4.7 and 14.1 T compared with parent insulator $H_2@C_{60}$

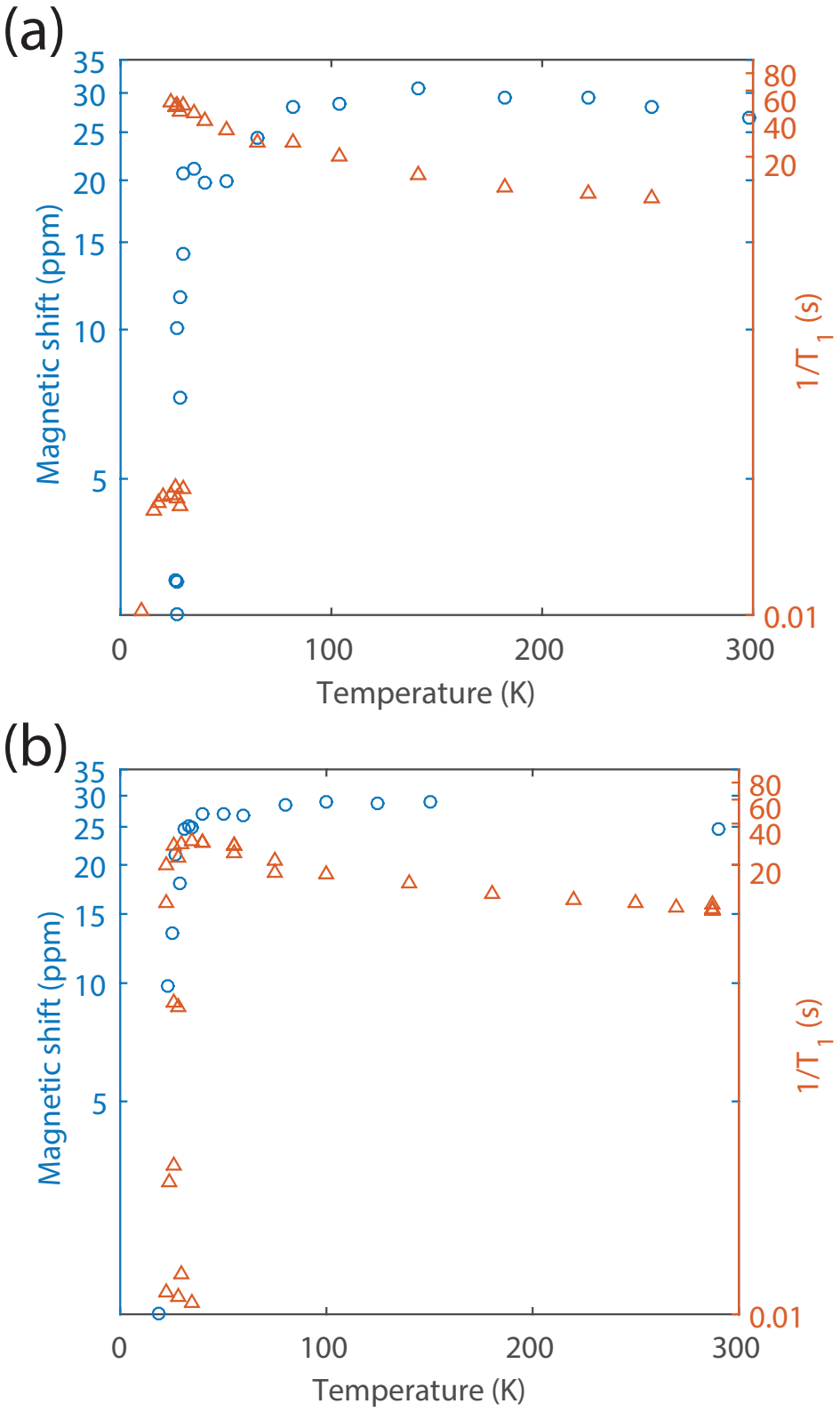

Figure 7.19: ^{1}H $1/T_1$ and magnetic shift on $Rb_3(H_2@C_{60})$ recorded using a saturation recovery sequence at (a) 4.7 and (b) 14.1 T

7.3.3 Korringa law

Figure 7.20 shows relaxation measurements of $Rb_3H_2O@C_{60}$ and $Rb_3H_2@C_{60}$ at fields of 4.7 and 14.1 T. The data is fit to determine the Korringa product using a least-squares fitting routine, allowing the exponent to vary from T^1 to allow better fits.

The temperature dependence of T_1 for ^{13}C, ^{87}Rb and ^{1}H is shown in Fig. 7.20. The normal-state temperature dependence shows $1/T_1T$ is constant between 298 and 30 K, which is consistent with the expected 'Korringa behaviour' of metals.

The fit determined $(T_1T)^{-1}$=0.072±0.0001 $(sK)^{-1}$ for ^{1}H NMR at 4.7 and 14.1 T, shown in Fig. 7.20a. This is expected to be the same between fields, as the relaxation behaviour in the normal-state is not field dependent. The best fit exponent is approximately 1.08, indicating near-linear relaxation.

^{13}C NMR gives fits as $(T_1T)^{-1}$=0.012±0.004 $(sK)^{-1}$, shown in Fig. 7.20b, with the exponent varying from 0.85-1.5. This large error is likely due to low S/N and lack of data points to define the Korringa product accurately enough although the value determined is consistent with previous works[155, 159, 162]

Fig. 7.20c shows ^{87}Rb NMR data collected on the H_2O fulleride at 4.7 T. The Korringa product is fit to $(T_1T)^{-1}$=0.045±0.02 $(sK)^{-1}$ and the exponent varies from 0.9-1.3. Similarly, Fig. 7.20d shows ^{87}Rb NMR data on the H_2 fulleride at 14.1 T. The Korringa product is fit to $(T_1T)^{-1}$=0.053±0.01 $(sK)^{-1}$ and the exponent varies from 1.02-1.13. The reported ^{87}Rb Korringa product[28] of non-endohedral Rb_3C_{60} is within the error margins of the value determined here.

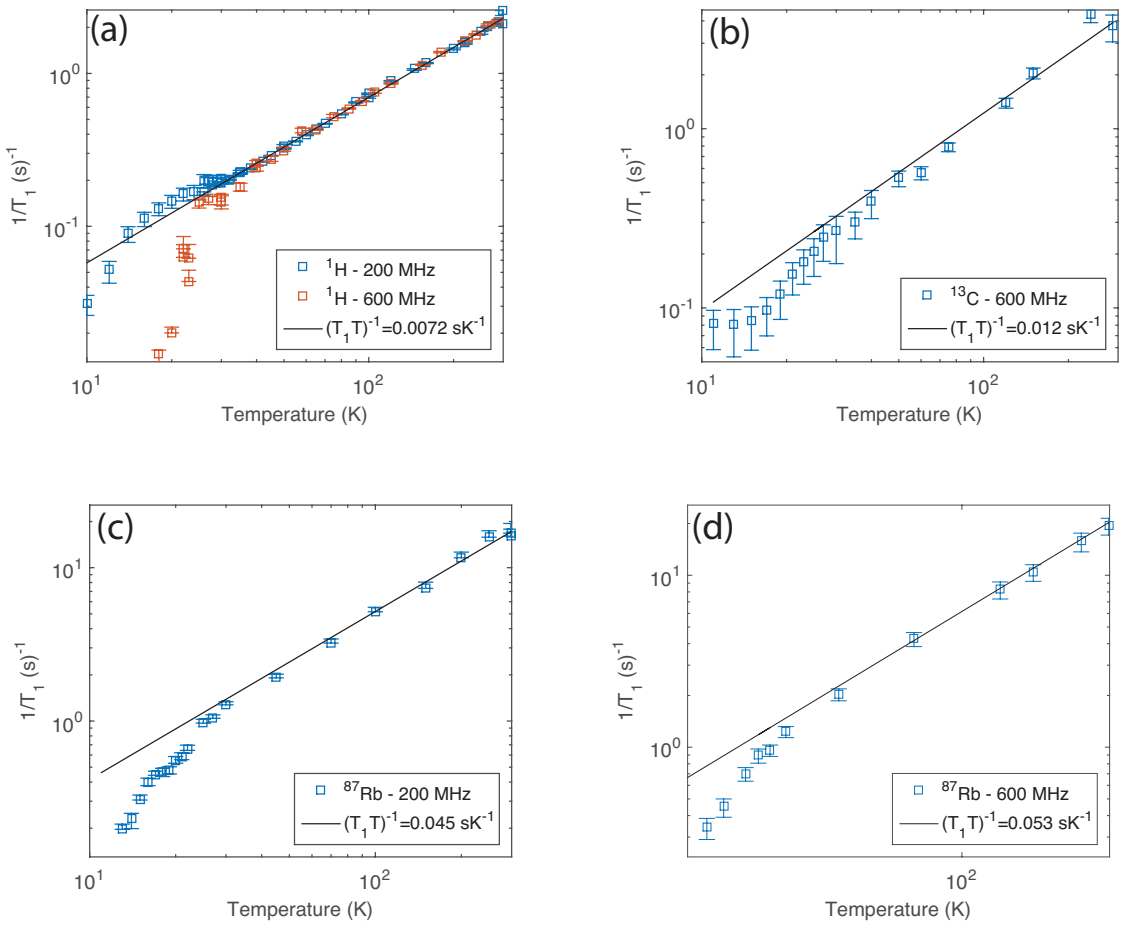

Figure 7.20: $1/T_1$ temperature dependence for ^{1}H, ^{87}Rb and ^{13}C $1/T_1$ nuclei for endohedral fullerides. (a) $Rb_3(H_2O@C_{60})$ at 4.7 and 14.1 T (b) $Rb_3(H_2O@C_{60})$ at 14.1 T(c) $Rb_3(H_2O@C_{60})$ at 4.7 T (d) $Rb_3(H_2@C_{60})$ at 14.1 T. Solid lines represent fits to determine Korringa product. Details on the fitting procedure are given in the main text. Error margins are given in the main text.

7.3.4 Arrhenius fits

The data in Figure 7.15 show metallic relaxation as discussed previously, at the T_c there is a deviation concomitant with the onset of the superconducting transition, consistent with PPMS studies. BCS s-wave superconductors usually show a deviation at T_c which may be fit to an Arrhenius law to extract Δ given by:

$$T_1^{-1} = W \exp(-\Delta/T) \tag{7.2}$$

Where Δ is the gap value given in K, T is temperature and W is relaxation rate. These fits have been done for both the H_2 and H_2O fulleride and are shown in Fig. 7.21. The procedure uses a non-linear least squares method and uses points below T_c, determined from PPMS measurements, for each field and sample. A comparison to literature is also given[81], where the gap is determined to be Δ=46.8 K and W is 1.04, from ^{13}C NMR measurements at 9.39 T. By taking the T_c, which they determine from NMR measurements (23±1), one arrives at $2\Delta_0/k_BT_c$=4.1, larger than the BCS ratio of 3.5. Each fit is now discussed with a comparison to these numbers.

Fig. 7.21a shows the fit for ^{1}H NMR T_1 at 4.7 (200 MHz) and 14.1 T (600 MHz). ^{1}H measurements at 200 MHz give W=0.72±0.18 and Δ_0=31.2±3.0. The T_c is 27.7 K which gives $2\Delta_0/k_BT_c$=2.25. This is lower than both the expected BCS and reported values from previous works[81]. Data at 14.1 T shows a sharp deviation from the expected behaviour and therefore is not fit to the Arrhenius law. There is no obvious reason for this deviation, although it may be related to a field dependent relaxation mechanism, as seen in the $H_2O@C_{60}$ parent compound at low temperatures. This is discussed in greater detail in section 7.3.1.

Fig. 7.21b shows ^{13}C measurements at 600 MHz which yields fits of W=1.11±0.20 and Δ_0=41.4±4.5. This is similar to the W and the gap value deduced from measurements from literature, discussed previously. This is expected in this case as the nuclei used to probe the gap are the same (^{13}C). There is a slight deviation from the law at lower temperatures to lower T_1 values and this is expected to be due to an additional relaxation mechanism due to vortices. Therefore the last two points in this dataset are not included in the fitting process, this is also taken into consideration in previous literature[81]. The superconducting gap ratio determined from the aforementioned values is $2\Delta_0/k_BT_c$=3.2, close to the BCS but lower than the literature values. The difference in H_{c2} and therefore T_c strongly affects the gap ratio and therefore the discrepancy may arise from differences in sample quality. Alternatively, H_{c2} may intrinsically be higher in the endohedral fullerides which may also contribute.

Fig. 7.21c and Fig. 7.21d shows ^{87}Rb NMR measurements at 4.7 and 14.1 T

for the H_2O and H_2 fulleride respectively. ^{87}Rb measurements at 200 MHz on the H_2O fulleride give W=5.36±1.0 and Δ_0 = 43.4±2.5. This value of Δ_0 is close to the literature value Δ_0=46.8 K, but lower when one calculates the gap ratio. The T_c from PPMS measurements at this field is 25.6 K, therefore $2\Delta_0/k_BT_c$=3.39, which is close to the BCS value. Contrastingly, ^{87}Rb measurements at 600 MHz for the H_2 fulleride give W=9.17±2.0 and Δ_0=50.5±2.0. This quite large difference in values is skewed by the last data point which deviates strongly from the previous trend. The gap value calculated using the PPMS value for T_c (26.5 K) at this field gives $2\Delta_0/k_BT_c$=3.8 which is more in-line with previous literature yielding a gap ratio of 4.1.[81]

To summarise, $2\Delta_0/k_BT_c$=3.5±0.3 for both H_2 and H_2O fullerides, according to ^{13}C and ^{87}Rb nuclei. This is consistent with optical reflectivity measurements which gives $2\Delta_0/k_BT_c$=3.52[220] and μSR which gives 3.52[220]. Tunnelling measurements on the other hand have proposed a higher gap of $2\Delta_0/k_BT_c$=5.2 [221] The discrepancy here may arise indirectly from the air sensitive nature of Rb_3C_{60}. Probes such as tunnelling may be subject to surface effects, with a gap value different on the surface layer than in the bulk. However, in bulk probes (NMR, optical reflectivity) there is distribution of normal and metallic regions, and the gap ratio has been interpreted using a distribution of gaps in the past[222]

In contrast to ^{13}C and ^{87}Rb NMR, the gap value for ^{1}H NMR is found to be $2\Delta_0/k_BT_c$=2.25. It is not obvious why this discrepancy arises, but it may be due to differing relaxation mechanisms between nuclei at low temperatures. However in a more general sense, the NMR probe that is used in this case is unconventional in terms of its interaction with the conduction electrons, i.e the endohedral molecule is 'freely floating' inside the cage. Therefore the gap ratio probed may be different, a similar effect has observed before on superconductors where there are two superconducting gaps[34]. Future work on different materials will attempt to clarify this point further.

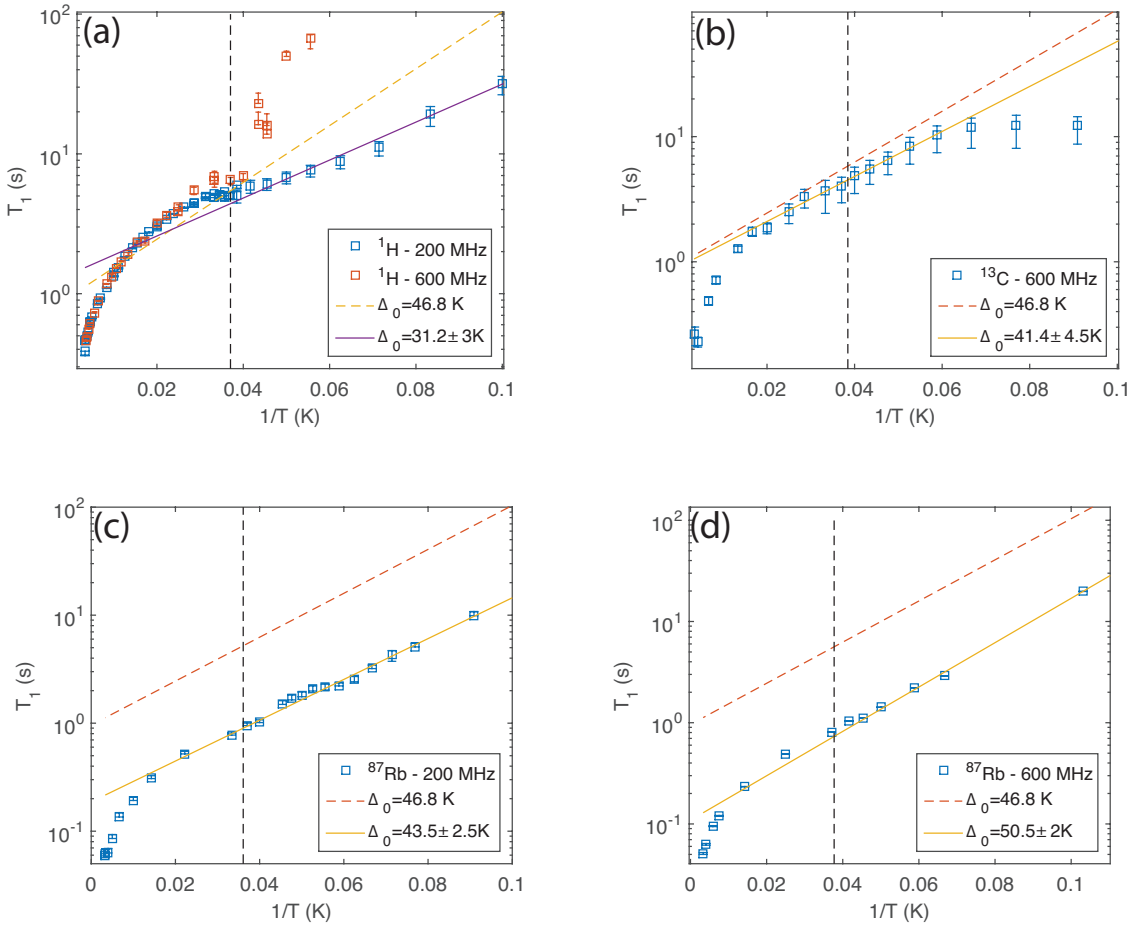

Figure 7.21: Temperature dependence of ^{1}H, ^{87}Rb and ^{13}C T_1 for endohedral fullerides. (a) $Rb_3(H_2O@C_{60})$ (b) $Rb_3(H_2O@C_{60})$ (c) $Rb_3(H_2O@C_{60})$ (d) $Rb_3(H_2@C_{60})$ Solid lines represent fits to Arrhenius laws, dashed lines from Tycko 1992[81]. Details on the fitting procedure are given in the main text.

7.3.5 Coherence peak in ^{1}H data

^{1}H T_1 shows behaviour consistent with metals, with a linear dependence of temperature[145], there is also an enhancement at T_c and then a fall in $1/T_1$ at low temperatures (15 K). This is plotted as R_s/R_n ($T_1T^{-1}{}_n/T_1T^{-1}{}_s$) in figure 7.22. The enhancement appears to rise to 1.4. An enhancement at T_c in R_s/R_n, followed by an exponential fall is usually considered strong evidence of BCS superconductivity[3].

This has been reported before in the fullerides in muon-spin resonance studies[91] and also in an ammonia intercalated fulleride using ^{1}H NMR.[167]. For fulleride superconductors the maximum enhancement of the relaxation rate (R_s/R_n) is expected to be 1.1-1.2[165], this is in zero applied field. μSR measurements have shown a similar enhancement to this, however if one takes into account the characteristic phonon frequency for fullerides then the expected max enhancment of R_s/R_n is 2-3.[8] The suppression of the coherence peak has been reported in other works[28, 81, 100].The very nature of high-T_c superconductors means there are numerous electron-phonon decay channels open to the electronic excitations[168], which can suppress the coherence peak.

Choi 1997 outlines the reasons for the suppression in fullerides[8], assigning it to damping arising from Coulomb interactions. In contrast to the ^{1}H results, the coherence peak is not seen in ^{87}Rb or ^{13}C NMR here and also more generally has not been observed in such high field before (4.7 T), for example it was seen to be suppressed at fields of 5 T for Rb_2CsC_{60}.

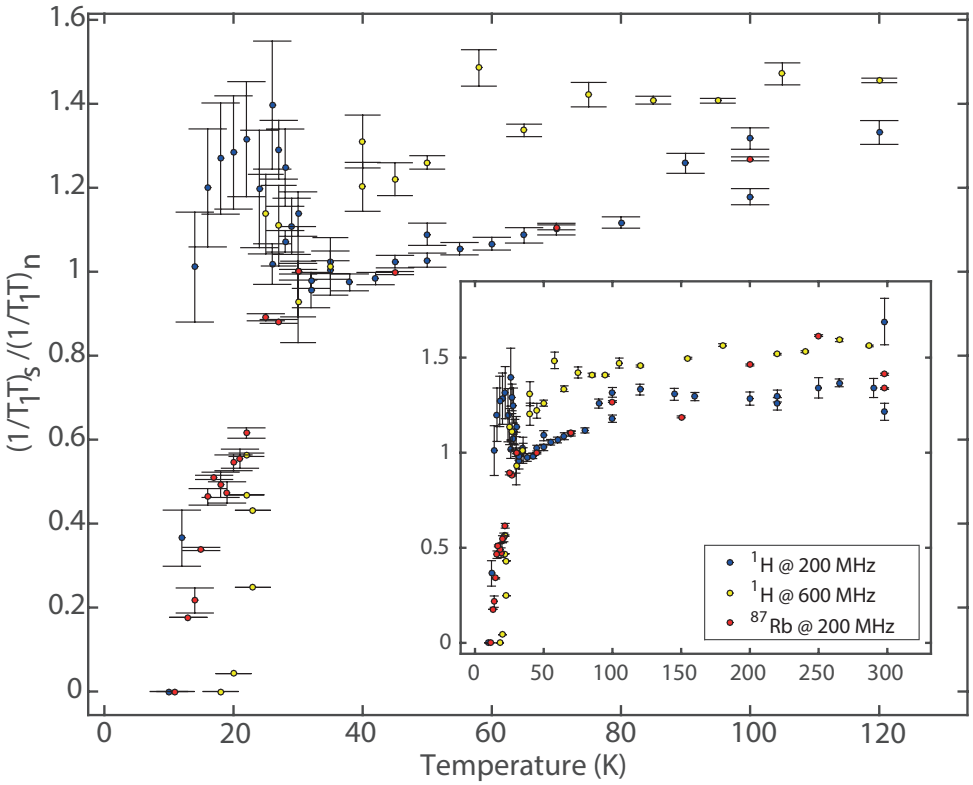

Figure 7.22: ^{1}H and ^{87}Rb $(T_1\mathrm{T})^{-1}$ as a function of temperature for $Rb_3H_2O@C_{60}$, data is normalised to normal state $(T_1\mathrm{T})^{-1}$ value. An enhancement is observed at T_c in ^{1}H data at 4.7 T

7.3.6 Korringa ratio

The ^{1}H Korringa ratio, discussed in section 4.4, for H_2O fulleride is analysed using the relation

$$R = (K^2 T_1 T)/S \tag{7.3}$$

Where K is the Knight shift, T_1 is the nuclear spin lattice relaxation time. S is made up of constants and is defined as:

$$S = \frac{\hbar}{4\pi k_B}\frac{\gamma_e^2}{\gamma_n^2} \tag{7.4}$$

where k_B is the Boltzman constant,γ_n and γ_e is the gyromagnetic ratio for nuclei and electrons respectively.

Taking the Knight shift value and $1/T_1$T to be 26.6 ppm and 0.0072 sK^{-1} respectively and $S = 2.70 \times 10^{-7}$, R=0.36. This is lower than the expected value of unity for relaxation driven by the Fermi-contact interaction, therefore other mechanisms may be important, typically the effects of strong correlations or other relaxation mechanisms are quoted to account for the discrepancy.[165]

It has been noted previously that the dominant relaxation mechanism in the ^{13}C NMR in the fullerides is the spin-dipolar mechanism[84, 155, 161]. This may also be relevant in the case of ^{1}H relaxation and may explain the deviation from unity in the Korringa ratio.

A direct method to test the appropriateness of the dipolar mechanism is to measure the anisotropy of the relaxation rate across the NMR lineshape. [162] This is done for ^{13}C and ^{1}H, for both endofullerides and is shown in figure 7.23. The variation in T_1 across the ^{13}C spectral lineshape (Fig. 7.23c) shows a clear anisotropy, with the $1/T_1$ ranging from 0.89 s^{-1} at the low frequency end and 1.5 s^{-1} at the high frequency end.

The anisotropy is similar to previously reported studies[28] however the magnitude of the high frequency T_1 is quite a lot higher in the data presented here. Actually the electron-nuclear dipole interaction predicts the ratio between high and low frequency sites to be 2.5, whereas the value found here is 1.7. Also in the study by Pennington the calculated ratio is lower than the theoretical value, and they assign the difference to an additional isotropic relaxation mechanism.

The suggested mechanisms in the case of ^{13}C relaxation are core polarisation of the 1s orbital and spin polarisation of the sp^2 orbitals involved in bonding. Another proposed mechanism arises from admixture of the 1s and 2p$_z$ orbitals from the curvature of the fullerene.[162]

Fig. 7.23a and 7.23b show the frequency dependence of $1/T_1$ for ^{1}H NMR on both the H_2 and H_2O endofullerides. The difference across the lineshape is minimal, the ratio

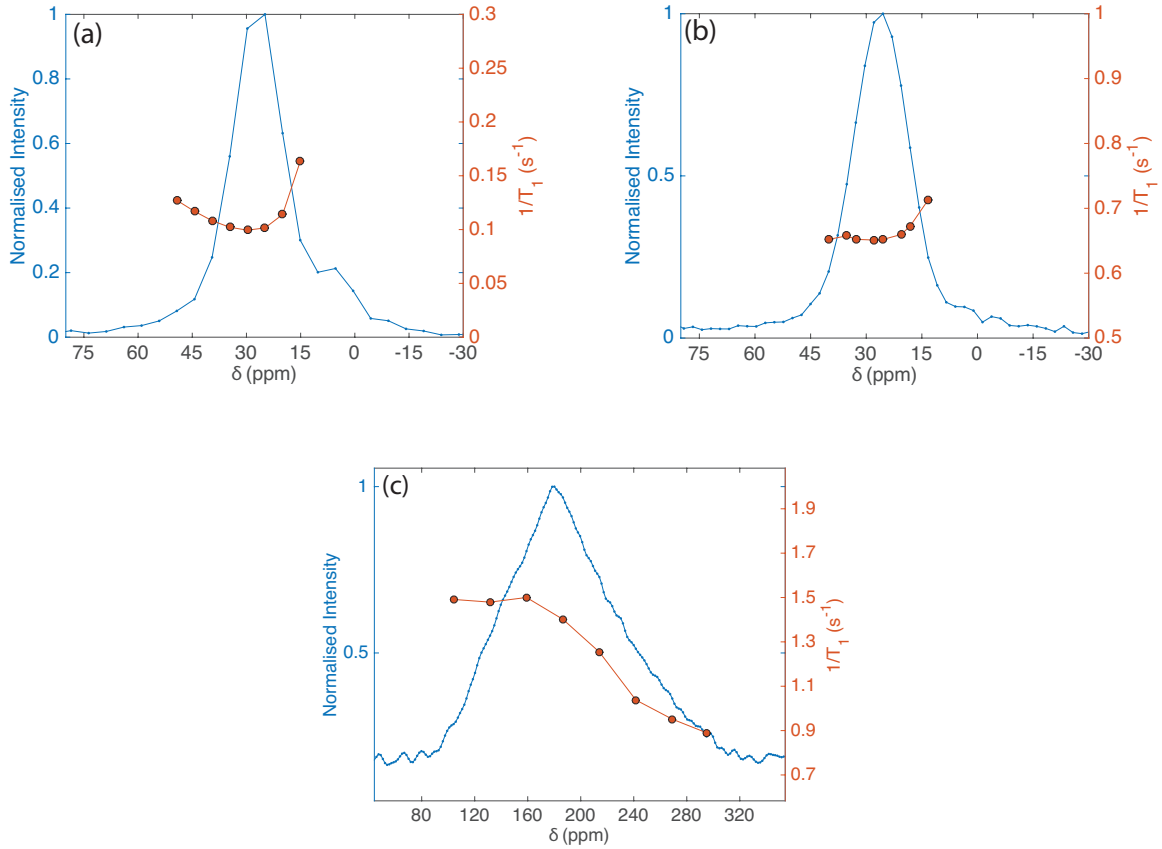

Figure 7.23: Frequency dependence of $1/T_1$ for endohedral fullerides. ^{1}H NMR collected at 4.7 T, and ^{13}C NMR at 14.1 T (a) ^{1}H - $Rb_3(H_2@C_{60})$ at 298 K (b) ^{1}H - $Rb_3(H_2O@C_{60})$ at 298 K (c) ^{13}C - $Rb_3(H_2O@C_{60})$ at 120 K

between high and low frequency sites is 1.3 and 1.1 for the H_2 and H_2O endofullerides respectively. Therefore the relaxation mechanism is unlikely to be dipolar in origin and there may then be an additional mechanism, such as a transferred hyperfine coupling. Ab-initio calculations are currently in progress to support this work and attempt to elucidate some of these points.

7.4 Conclusion

In conclusion, two new molecular endofulleride superconductors, $Rb_3(H_2O@C_{60})$ and $Rb_3(H_2@C_{60})$, were synthesised using a similar procedure to the vapour doping method[191]. The aims were as follows, first to establish the extent to which the normal and superconducting phases of Rb_3C_{60} are modified in the presence of an endohedral component. Specifically in terms of bulk properties such as T_c and lattice parameters, but also local properties probed using ^{1}H NMR measurements of Knight shift, T_1 and peak shape. Secondly to investigate the differences between endohedral molecules, H_2O and H_2, a point of interest here was the extent to which the electric dipole moment of H_2O affects the normal and/or superconducting states. The overarching purpose of this work was to seek out any unique information that can be extracted from endohedral NMR concerning superconductivity.

In terms of the bulk properties, the transition temperature was measured using VSM-PPMS, the H_2O and H_2 fulleride had a T_c in the lowest field (0.001 T) of 28.4 and 29.7 K respectively. The change in T_c in the H_2O fulleride is likely due to the presence of a larger endohedral component, as all other characterisation studies show a pure sample. The H_2 fulleride has a similar T_c value to the Rb_3C_{60} sample, this may be due to its smaller endohedral component which appears to exert less influence on the C_{60} cage. The most likely cause of decrease of T_c in the H_2O fulleride is the relatively larger influence on the C_{60} cage, and this is evidence that an endohedral-C_{60} interaction is present, this has also been reported previously for endofullerides containing Ar, which are also large relative to H_2[26]. Future work should address other alkali metals, such as Cs and K, and different incorporated endohedral molecules, for example HF. As H_2O clearly affects the superconducting state in a negative way in terms of bulk T_c, it is worth posturing whether a different combination can increase T_c. In both materials, NMR characterisation shows good agreement with both a standard sample synthesised using the same procedure and with experimental data from previous literature. The pXRD data collected here shows a phase pure sample with no other discernible phases. The presence of H_2O inside the C_{60} cage is only observed via a change in intensity of the peaks, future work should follow the temperature dependence of the pXRD spectrum, which might allow one to correlate some of the more novel aspects of the NMR data to any changes in structure, for example the $1/T_1$ for the H_2 fulleride discussed later shows a rapid decrease at temperatures similar to T_c. It is worth to investigate any structural transitions which take place in this region, comparing the standard sample, the H_2 and H_2O fullerides.

The ^{1}H NMR spectrum shows a single broad resonance for both materials, with ^{1}H Knight shifts determined to be 26.8 and 28.2 ppm for the H_2 and H_2O endofulleride

respectively. It is interesting that the observed shifts of both molecules are relatively close, and this reflects the apparently similar nature of the electronic structure inside the cage. This probably arises from the donated conduction electrons from Rb (Knight shift) and the small difference is likely due to the chemical shift. The notion that there is an interaction between the cage and endohedral component is ratified here again, but it is worth to clarify the nature of this interaction. Previous works have noted the electron cloud diameter of H_2 (and H_2O as well) exceeds the diameter of the C_{60} cage cavity[223]. This is evidenced by the Knight shifts in these experiments which shows there is an orbital overlap and charge transfer takes place. However as mentioned previously, only the T_c changes for the H_2O fulleride and this is indicative that the phonon modes are affected by H_2O but not H_2.

This information might address a wider issue of superconductivity in the fullerides, which is the specific mode relevant in the electron-phonon coupling mechanism. There are two distinct regions to consider, namely the intramolecular on-cage and intermolecular cage rotation phonon modes[224]. There are also the intermolecular optic phonon modes which are those vibrations between C_{60} and Rb. An isotope effect is present for ^{13}C but negligible for ^{87}Rb, which highlights the importance of the intramolecular phonon modes for the electron-phonon coupling mechanism. This is consistent with the reduction of T_c in the H_2O fulleride and similar T_c in the H_2 fulleride compared to the standard Rb_3C_{60} sample. In other words, the larger H_2O molecule exerts an influence on the intramolecular phonon modes and in some way slightly inhibits the electron-phonon coupling mechanism which reduces T_c. It is not clear exactly which phonon modes are relevant, and it may be that the intermolecular rotation modes are important. To clarify this further, ab-initio simulations of the phonon modes should be performed as a function of the molecule inside the cavity. This would allow one to observe which modes are altered in the presence of H_2O and not H_2, which would allow determination of the relevant phonon mode for the electron-phonon coupling mechanism. One might then simulate other molecules inside the cavity, such as HF or CH_4, to predict the effects on the superconducting state.

Local properties were studied by NMR. Variable temperature studies of the ^{13}C and ^{1}H lineshape in H_2 and H_2O fullerides shows broadly similar evolution, ^{87}Rb also shows a similar temperature dependence for the H_2 and non endohedral fullerides. The ^{87}Rb NMR spectra of the H_2O endofulleride shows a different temperature dependence, it is not clear why this is but it may be related to the endohedral component interacting with the C_{60} cage. This is supported by VSM-PPMS measurements which suggest the H_2O molecule does affect the structure as revealed from the change in T_c. The ^{1}H signal in both materials broadens at low temperatures, below T_c a second peak appears which is assigned to the inhomogeneous field distribution in the vortex state. This is

not observed in any other NMR active nucleus. The penetration depth, extracted from the second moment of the spectra, is 520±5 nm and 587±6 nm for the H_2O and H_2 fulleride respectively and this is similar to previous literature values.[81] The vortex structure observed by NMR has been reported previously but the ^{1}H NMR spectra recorded here shows clearly the variation of the vortex phases between solid and liquid types. This might be exploited more fully by synthesis of a single crystal of an molecular endohedral fulleride, which would allow one to study the vortex without the anisotropic broadening of the NMR line present in powders. This is useful as the NMR spectrum of the vortex state should show sharp discontinuities which can be fit according to Ginzburg-Landau theory and allows one to extract the penetration depth and coherence length.[225]

The local structure was also studied using ^{1}H, ^{13}C and ^{87}Rb T_1 measurements. The ^{13}C and ^{87}Rb T_1 measurements were consistent with previous literature and the control Rb_3C_{60} sample, this shows that the materials made are of high purity. The ^{1}H measurements were novel and therefore warrant further discussion. In the parent insulator compounds, ($H_2O@C_{60}$ and $H_2@C_{60}$) the ^{1}H nuclear spin relaxation is driven by a mixture of dipolar and spin-rotation mechanisms[214, 215], this may not be relevant in the case of the fullerides as the $1/T_1$ is slower than in the parent compounds. As the relaxation mechanism are usually additive, $1/T_1$ should be faster because of the additional hyperfine relaxation channel. The rate is slower and this means that one cannot assume that the endofullerene relaxation mechanisms are applicable in the endofullerides. In the H_2 and H_2O fullerides there is clearly a Fermi-contact interaction, as evidenced by the Knight shifted signal, but the relaxation mechanisms in both materials are clearly different, this is now discussed further.

The ^{1}H $1/T_1$ in the H_2O fulleride clearly follows a Korringa relaxation mechanism (a linear dependence with respect to temperature). There is a Hebel-Slichter coherence peak and a deviation of $1/T_1$ at lower temperatures which suggests $2\Delta_0/k_BT_c$=2.25. The Hebel-Slichter peak is a strong indication that the superconducting mechanism is BCS in origin and it would be worth exploring this at lower fields to observe an even greater enhancement. An additional task would be to fit the peak using the equation presented in section 4.5.1, which would yield a value for the superconducting gap ratio. The deviation of $1/T_1$ below T_c by the Arrhenius law suggests $2\Delta_0/k_BT_c$=2.25 and this in principle should be close to the gap value extracted from the Hebel-Slichter peak[164].

In the same sample, ^{87}Rb and ^{13}C measurements indicate a gap ratio more aligned with the BCS ratio of $2\Delta_0/k_BT_c$ ≈3.5. It is unknown why the ratio extracted using the Arrhenius law is lower using the ^{1}H NMR probe in the endohedral molecule. This should be investigated further and might be achieved by performing the same experi-

ments at lower field, this should yield the same ratio if there is an intrinsic mechanism. If the ratio is different however, it would be evidence of a relaxation channel which is field dependent, for example there is often a mechanism which arises from the vortices which can affect the deviation at temperatures below T_c. The gap ratio should be compared to the value extracted from the Hebel-Slichter peak as discussed previously. It is also worth synthesising additional endohedral fullerides with different alkali metals such as Cs or K which in principle should also show the coherence peak. Importantly the ^{1}H probe seems to be less affected by coherence peak suppression mechanisms, as the other NMR nuclei show no sign of the peak at the same fields (4.7 T). This would be useful in further investigating the Cs_3C_{60} system, which has not yet shown the Hebel-Slichter coherence peak.[226] An informative experiment would be to study this parameter as a function of pressure, the coherence peak should become more prevalent at higher pressures and this would be a very accurate and useful method to further confirm not only the s-wave mechanism but also to explore the Mott-Insulator transition. The increased pressure would decrease the interfullerene distance and increase the overlap between t_{1u} orbitals, which would favour electron delocalisation. A sample of $Cs_3(H_2O@C_{60})$ might be able to observe the transition from ^{1}H measurements if there is a similar behaviour to $Rb_3(H_2O@C_{60})$, for example relaxation in the metallic state would follow the Korringa law, whereas in the insulating region it would not. It has been noted before that the pressure induced changes are not explicable by BCS theory, and therefore the pressure dependent measurements of the Hebel-Slichter peak using ^{1}H NMR is a good tool to test this further.

An additional parameter determined was the Korringa ratio for the H_2O fulleride, it was found to deviate from unity and this may suggest the significance of electronic correlations, specifically of antiferromagnetic correlations. It has been noted previously that strong electronic correlations are important in the fulleride systems, and the ^{1}H NMR data recorded here agrees with this.[226] The data is consistent with the hypothesis that there is an electron orbital overlap between the C_{60} cage π electrons and the H_2O electron orbitals. Usually additional terms of the hyperfine coupling Hamiltonian, such as the dipolar or orbital contributions may also contribute to the relaxation rather than only the Fermi-contact term. In the case of the endofullerides, no appreciable anisotropy of the relaxation rate is found, indicating the hyperfine dipolar mechanism is not a dominant contributor, anisotropy is observed in ^{13}C NMR as reported before[161]. There may then be an additional transferred hyperfine coupling to the ^{1}H nuclei in the H_2O fulleride to account for the deviation from the Korringa ratio, this was suggested before in the case of ^{13}C $1/T_1$[162]. The core-polarisation term is also a possible source of relaxation and might explain the difference between the H_2O and H_2 fulleride, as H_2O has a π electron orbital and H_2 does not.

In terms of the H_2 fulleride the $1/T_1$ is enhanced on decreasing temperature and then a discontinuous drop is observed at temperatures similar to T_c although the transition point is not clearly defined. This is the most significant piece of data obtained during this investigation, it shows a clear difference in relaxation behaviour between the two molecules encapsulated inside the C_{60} cage. This is unlikely related to sample quality as other techniques, as well as other NMR active isotopes, show that both samples are pure. There is most likely a relaxation mechanism which is present in the H_2 fulleride, which is affected by the transition into the superconducting state. As mentioned in section 7.3.2, this may be due to a coupling between C_{60} phonon modes and the spin-rotation of the endohedral protons, a sample of $Rb_3(HD@C_{60})$ is currently being prepared in order to test this hypothesis, as HD has different rotational states than H_2. Future work should test both this sample as well as a sample of $Cs_3(H_2@C_{60})$. The advantage of studying Cs doped fullerides is that their transition into the superconducting state shows a pressure dependence which may be exploited here to study this possible phonon spin-rotation relaxation mechanism even further. For example the $1/T_1$ should be different in the metallic and insulating states, as well as the superconducting state, as the phonon modes vary across these phases.

CHAPTER

EIGHT

MAGNESIUM DIBORIDE SUPERCONDUCTORS

8.1 Characterization of MgB_2 and $MgB_{1.95}{}^{13}C_{0.05}$ nanoparticles

The samples studied in this chapter were synthesised by Maurizio Paolella at the Institute of Cryogenics, University Of Southampton, using the CVD procedure described in section 2.2.1. A modification was included in the synthesis, extra care was taken to immerse the samples in containers with argon gas to prevent degradation from reaction with O_2 and H_2O in the air. They were stored and handled in an argon glovebox in the short periods between experiments. The carbon doping is thought to be approximately 5%, from pXRD also performed by the Institute of Cryogenics. This is based on extracting the change in a-axis lattice parameter, which is affected by level of carbon doping as described in literature.[60, 61]

To determine the superconducting properties and confirm the level of carbon enrichment, magnetic susceptibility measurements were performed, shown in Fig. 8.1. This was carried out using the VSM option of the Quantum Design Physical Property Measurement System (PPMS) equipped with a 14 Tesla solenoid, measurements were carried out by Raivo Stern at the KBFI, Tallinn. The zero field T_c was measured (Fig. 8.1a) from the onset of the diamagnetism in zero field cooling (ZFC), with the field set to 0.01 T. The field was also set to a range of values including those used in the NMR experiments, then the T_c was measured during these field cooling runs. The T_c was determined to be 37 K in ZFC measurements which is in agreement with doping at $\sim$5 % [60].

The T_c decreases linearly with increasing magnetic field and at fields higher than 4.7 T the magnetization measurements become noisy and difficult to reliably interpret. This may be due to the large anisotropy of H_{c2} commonly reported for MgB_2 , which is in the range of 3-6[227].

The CVD procedure is thought to produce homogenous nanoparticles, and TEM measurements (Fig 8.2) show a particle size of 100 nm, however this is only an estimate

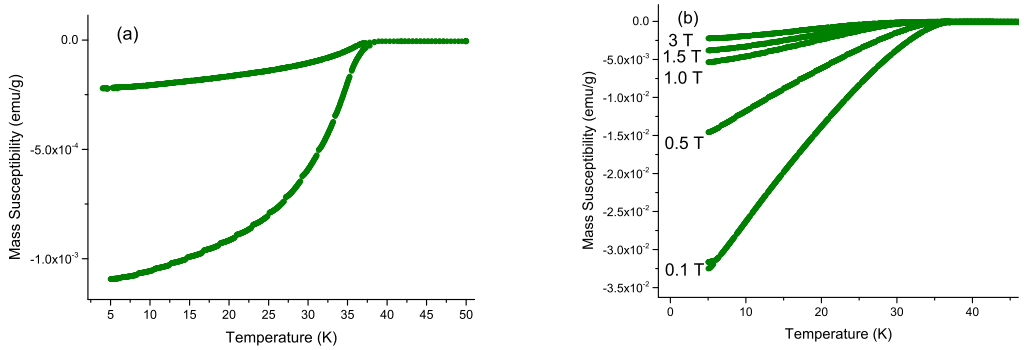

Figure 8.1: (a) ZFC and FC magnetic susceptibility measurements on $MgB_{1.95}{}^{13}C_{0.05}$. T_c was determined to be 37 K at 0.01 T. (b) FC magnetic susceptibility measurements on $MgB_{1.95}{}^{13}C_{0.05}$ between 0.1 T-3.0 T

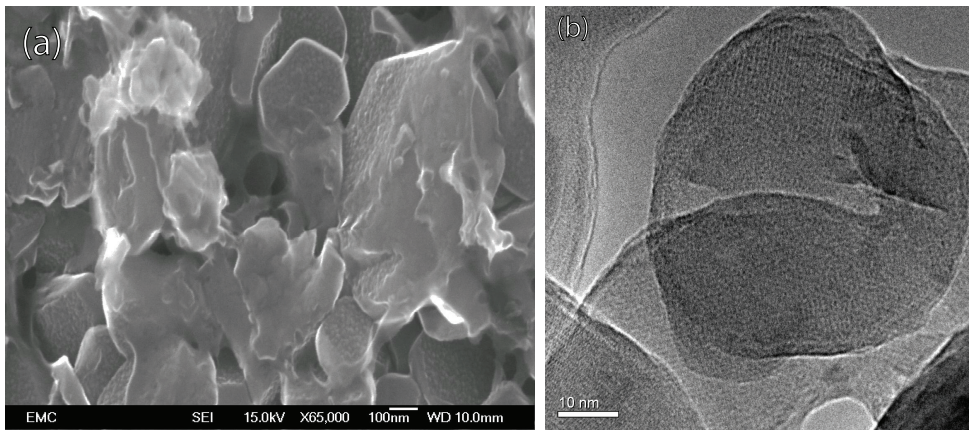

Figure 8.2: TEM images(a) Undoped MgB_2 bulk sample treated at 850°C (b) Carbon chemical vapour coated (C-CVD) $MgB_{1.95}{}^{13}C_{0.05}$ powder particles reacted at 900°C

and more measurements would be required to establish homogeneity.

8.1.1 NMR spectroscopy

NMR experiments at room temperature were used to characterise the carbon doped and undoped MgB_2 samples, at magnetic fields of 9.4 T and 14.1 T using the equipment described in section 5.1.1. ^{11}B NMR spectra were recorded at 9.4 T, 40 mg of $MgB_{1.95}{}^{13}C_{0.05}$ was packed into a 4 mm zirconium oxide rotor and spun at 8 kHz. Carbon spectra were recorded under MAS at 14.1 T, with 10 mg of $MgB_{1.95}{}^{13}C_{0.05}$ packed into a 2.5 mm rotor and spun at 30 kHz. MAS spectra were recorded using a Hahn echo[181] pulse sequence with 80 kHz amplitude pulse and 45μs echo time. All ^{11}B NMR data were referenced to BF_3OEt_2 (aq) at 0 ppm. Carbon was referenced to adamantane with a chemical shift of 38.23 ppm (CH_2 peak) [196].

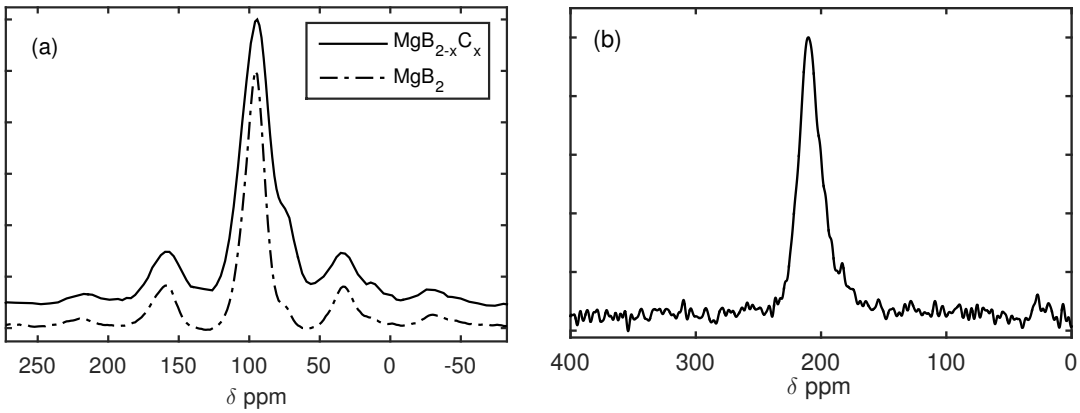

Figure 8.3: (a) MAS-NMR spectra at 298 K and 9.4 T. ^{11}B Hahn echo spectrum recorded with 80 kHz pulse amplitude, spectra are the result of 40 transients with 4 seconds between scans. (b) ^{13}C MAS-NMR spectrum at 298 K and 14.1 T. Sample is 10 mg $MgB_{1.95}{}^{13}C_{0.05}$ packed into a 2.5mm zirconium oxide rotor spinning at 30 kHz. ^{13}C Hahn echo spectrum recorded with 80 kHz pulse amplitude, spectrum is the result of 131072 transients with 1 second between scans

8.1.2 Room temperature NMR measurements

In order to further characterise the materials supplied by the Institute of Cryogenics, ^{11}B and ^{13}C NMR measurements were carried out at room-temperature. Boron has two NMR active nuclei, ^{11}B and ^{10}B, however ^{10}B NMR has a larger quadrupole moment, gyromagnetic ratio and has less naturally abundant and therefore was not used to characterise these materials. Also ^{25}Mg NMR is possible but was not used as it has a large quadrupole moment and relatively low gyromagnetic ratio.

NMR is a good technique to test purity in these materials because the boron NMR spectrum consists of a single resonance, this is due to MgB_2 containing one crystallographically unique boron site. The relevant NMR parameters for the ^{11}B isotope are I=3/2, natural abundance 80.1%, nuclear quadrupole moment ^{11}Q=0.04059(10)$\times 10^{-28}$ and gyromagnetic ratio γ_n=8.5847$\times 10^7$ rad(Ts)$^{-1}$. And for the ^{13}C isotope, I=1/2 and γ_n=6.7262$\times 10^7$ rad(Ts)$^{-1}$.

^{11}B NMR spectra

Fig. 8.3a shows the ^{11}B MAS NMR spectrum for the central transition (-1/2$\rightarrow$+1/2) of the spin 3/2 ^{11}B nucleus, for both MgB_2 and $MgB_{1.95}{}^{13}C_{0.05}$. The peak of interest is centered at 95 ppm, however in the carbon doped sample there is a clear asymmetry which may arise from boron nuclei in proximity of the substituted carbon. The spectrum in Fig 8.3a shows no obvious impurities, therefore one may conclude that the samples are of high purity, within the limits of detection of this measurement. In

non-pure samples, NMR can detect impurities arising due to the air sensitive nature of MgB_2 such as B_2O_3, which manifests as a resonance at 0 ppm.

There are four relevant interactions in the interpretation of the boron lineshape, these are the (a) dipolar interactions between neighbouring nuclei, (b) chemical shift anisotropy, (c) Knight-shift anisotropy and (d) the coupling between the nuclear quadrupole moment and electric field gradient.[169] Each of these interactions will now be considered:

The dipolar interaction between boron atoms leads to a splitting[36], however under MAS this interaction is averaged and is not present in Fig 8.3. The same is true for the Knight shift and chemical shift anisotropy, therefore the magnetic shift is just comprised of isotropic terms.

K_{spin} is an important quantity to determine, for example it can be used to test mechanisms of relaxation through the Korringa ratio, however there are a few caveats present in its evaluation. Separating the terms K_{orb} from K_{spin} is difficult A good approximation to determine the spin shift is to follow the peak position as a function of temperature, this circumvents reference related issues because the Knight shift is not field dependent. The spin shift disappears at low temperatures whilst in the superconducting state, the shift value that remains is a combination of orbital and second order quadrupolar terms. This is the method used to extract K_{spin} in section 8.2.2. The orbital contribution is thought to be small in MgB_2 however, only a small perturbation on the total shift.[147]

In general there is considerable disagreement in literature in evaluation of the Knight shift, which is likely due to various references used. It is also not completely clear if values reported are simply extracted from the room temperature shift, or use a procedure to determine K_{spin} based on low temperature measurements.

The magnetic shift (K_{tot}) in Fig. 8.3 is 95 ppm at 9.4 T, which is similar to values quoted previously referenced to $BF_3.OEt_3$[137]. Although this is much larger than other values, for example studies on non-oriented powders have reported 80 ppm referenced to $NaBH_4$ and 40 ppm referenced to BF_3[36], 70 ppm with respect to $B(OH)_3$[125] and 41 ppm with respect to $C_6H_{15}B$ [148]. A study[170] on a single crystal of MgB_2 gives $K_{iso}^{tot} = \frac{1}{3} \times (K_c^{tot} + 2K_{ab}^{tot}) = 81(5)$ppm and $K_{aniso}^{tot} = \frac{1}{3} \times (K_c^{tot} - K_{ab}^{tot}) = 19(4)$ppm.

An additional term that should be considered is the second order quadrupolar shift, which has an inverse field dependence. A good approach to isolate this term, is to study the shift at different fields and then fitting δ vs. ν_0 to the following equation enabling extraction of K_{iso}^{tot} and ν_Q:

$$\delta = \left(K_{iso}^{tot} - \frac{1}{10} \frac{\nu_Q^2}{(1 + K_{iso}^{tot} \nu_0^2)} \right) \times 10^6 \tag{8.1}$$

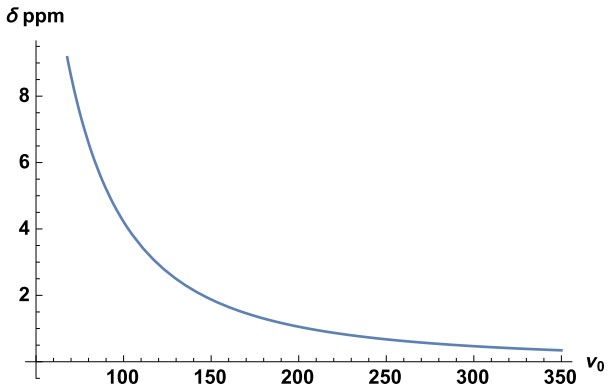

Figure 8.4: Second order Quadrupole shift vs. frequency

This has been done previously yielding K_{iso}^{tot}=83.85±1 and ν_Q=0.835 MHz, with the shift referenced to a saturated solution of H_3BO_3.[169]. Then by taking this value for ν_Q, one may subtract the quadrupolar shift. The EFG is axially symmetric along the c-axis direction, therefore η is zero.[170] The second order shift may be calculated using the following equation[133]

$$\nu_{Q,iso}^{(2)}(I,m) = -\frac{3\chi_Q^2}{40\nu_0 I^2(2I-1)^2}[I(I+1) - 9m(m-1) - 3]\left(1 + \frac{\eta^2}{3}\right) \tag{8.2}$$

Where χ_Q is the quadrupolar coupling frequency, ν_0 is the Larmor frequency (boron is 128.42 MHz at 9.4 T), I is the nuclear spin quantum number (I=3/2 for boron), m is the magnetic quantum number (m=1/2) and η is the asymmetry term (η=0 in this case). This equation is plotted in Fig.8.4. At a magnetic field of 9.4 T the expected second order quadrupole shift is 2.55 ppm.

^{13}C NMR spectra

^{13}C is a spin 1/2 nucleus and therefore circumvents some of the classical problems associated with quadrupolar nuclei. Fig 8.3b shows the ^{13}C MAS spectrum at room temperature, with a magnetic shift of 208 ppm. Even at 30 kHz the line-width is 2.8 kHz, this likely arises from a combination of the heteronuclear dipole interaction as well as a small distribution of shifts due to variations in the local environment and varying local susceptibility effects. The spin shift, as for ^{11}B is considered in section 8.2.2.

There are no other obvious carbon sites, therefore it is likely the doping with the CVD procedure selectively favours either a boron substitution in the lattice or interstitial grain boundaries where the electronic environment would be quite different, and not a mixture of both sites.

8.2 Cryogenic NMR experiments on $MgB_{1.95}{}^{13}C_{0.05}$

Experimental Methodology

Variable temperature ^{11}B and ^{13}C NMR experiments were performed using the equipment described in section 5.1.2. ^{11}B and ^{13}C NMR measurements were performed on 43 mg $MgB_{1.95}{}^{13}C_{0.05}$ packed into a 4 mm zirconium oxide rotor. Relaxation data were obtained using saturation recovery experiments with a comb of 80 pulses, with $\pi/2$ pulse durations of 1.25 μs using a Hahn-echo sequence with τ=20μs. Experiments were done in constant magnetic fields of 4.7 T and 8.4 T. For magnetic shift and peak shape analysis considered in the following chapter, the last slice of the 2D T_1 relaxation experiments is used.

Difficulty in tuning the probe during ^{13}C NMR experiments at 4.7 T below 25 K required dilution of the sample with an insulator (CsBr), which allowed further measurements. Initially CsBr was also added for use as a temperature calibration tool, for cryo-MAS. However these experiments did not take place. ^{13}C NMR experiments at 4.7 T took substantially longer and S/N in these datasets is reduced greatly compared to data at 8.5 T.

Ab-initio calculations

Ab-initio calulcations allow further understanding of the contributions to the Knight shift and relaxation rates, these calculations were done by Eva Pavarini at the Institute for Advanced Simulation, Julich. The simulations for both Knight shift and $1/T_1$T (discussed later) were performed on a supercell of $MgB_{1.95}{}^{13}C_{0.05}$ with one atom of boron substituted for carbon, reflecting x=0.04 and 0.07. Simulations were based on density functional theory in the local-density approximation and the linearised muffin-tin orbital (LMTO) method, this method is outlined in greater detail in Refs.[36, 147, 148].

8.2.1 Peak Shape analysis

Fig. 8.5 shows variable temperature NMR data on $MgB_{1.95}{}^{13}C_{0.05}$. For each temperature, spectra obtained at 8.5 T (blue) and 4.7 T (red) are superimposed for each isotopic species. For ^{11}B NMR at 4.7 T the signal is characteristic of a distribution of magnetic fields corresponding to the vortex structure and a contribution from diamagnetic screening currents.[173] At 8.5 T there are more vortices and therefore one sees mainly the normal state below T_c. The solid and liquid vortex phase, seen in NMR by a broad and relatively narrow peak respectively is also observed in Fig. 8.5. The liquid

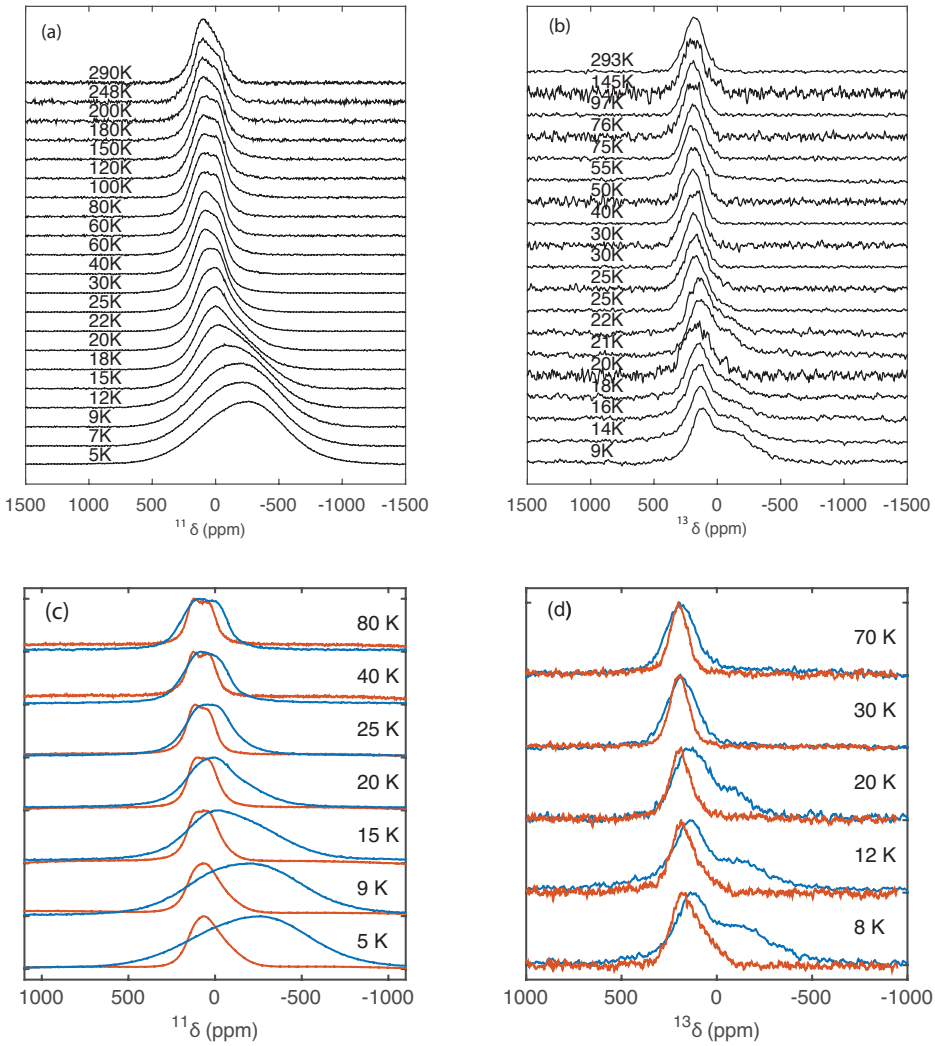

Figure 8.5: NMR peak shapes of $MgB_{1.95}{}^{13}C_{0.05}$ as a function of temperature. (a) ^{11}B NMR spectra at 4.7 T. (b) ^{13}C NMR spectra at 4.7 T. (c) ^{11}B NMR spectra at fields of 8.5 T (red) and 4.7 T (blue). (d) ^{13}C NMR spectra at fields of 8.5 T (red) and 4.7 T (blue).

phase vortex state has a correlation time which is faster than the signal acquisition, therefore the NMR signal is time-averaged and thus appears isotropic. Whereas in the solid phase, the correlation time is slower than the signal acquisition time and the peak shape has broadened[151, 173] However as noted previously[173], the distribution is also related to the anisotropy of H_{c2}, which arises from the temperature and orientation dependent superconducting gaps of MgB_2 [173], As

$$H_{c2}(\theta, T) = \frac{H_{c2}^{ab}(T)}{\sqrt{1 + (\gamma_\eta^2 - 1)\cos^2\theta}} \tag{8.3}$$

A polycrystalline powder has a distribution of crystal sites, and this means in MgB_2 the c-axis, which bisects the boron planes, will be oriented at a distribution of angles with respect to the applied magnetic field, B_0. Below T_c, at some angles H_{c2} will equal or be smaller than B_0 and the sample will remain in the normal state, there will also be a fraction which has a H_{c2} higher than the applied field and this part will be superconducting. As the temperature is lowered, H_{c2} increases and there is a point in which all H_{c2} distributions are larger than B_0 and all of the powder will enter the superconducting state. Although as B_0 is still higher than H_{c1}, the sample will be penetrated by vortices. The peak shape distribution will be reflective of the vortex structure as discussed in section 4.6. As in ^{11}B NMR spectra, ^{13}C spectra at 8.5 T show mostly the normal state signal below T_c, concomitant with the larger field. At 4.7 T and 9.2 K there is a lot of sample which appears to be in the normal state, with a smaller part in the vortex state. The difference may be due to the quadrupole contribution to the ^{11}B spectrum which broadens the peak masking the greater resolution which is achieved with ^{13}C NMR. Alternatively carbon's flux pinning properties may mean that it monitors more of the normal state contribution of the vortex structure. Both nuclei are thought to reside in the same position in the lattice, therefore they should experience the same distribution of c-axis angles. Therefore the difference must be due to vortex dynamics, which are expected to differ between boron and carbon. It is well known that carbon doping leads to a stronger pinning of the magnetic field and it is likely that on average more of the ^{13}C spins will be within the vortices. This may be the reason ^{13}C and ^{11}B NMR differ substantially at 10 K, where carbon defects act as flux pinning centres most of the vortex state is averaged and one sees mainly the normal state signal.

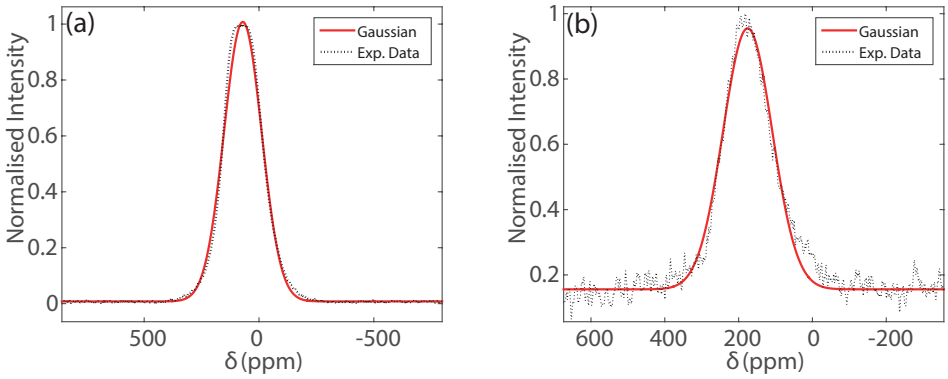

Figure 8.6: Gaussian fits to (a) ^{11}B at 18 K and (b) ^{13}C lineshape at 15 K for MgB_2. Spectra recorded at 8.5 T using a Hahn-echo sequence with τ=20μs. Experiments were run on a 43 mg sample of $MgB_{1.95}{}^{13}C_{0.05}$ packed into a zirconium oxide rotor.

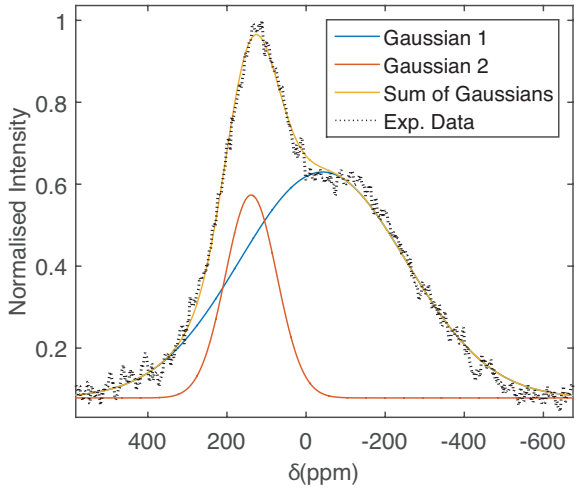

Figure 8.7: Example bi-Gaussian fit to ^{13}C lineshape at 9.2 K in a constant field of 4.7 T

8.2.2 Knight shift and spin susceptibility

Experimental methodology

The magnetic shift (K_{orb}+K_{spin}) of ^{11}B and ^{13}C NMR data as a function of temperature was determined by fitting a Gaussian line-shape, shown in Fig.8.6. In the case of ^{13}C data at 4.7 T, the data was fit to a bi-Gaussian model This model proved a better fit for this dataset, shown in Fig.8.7.

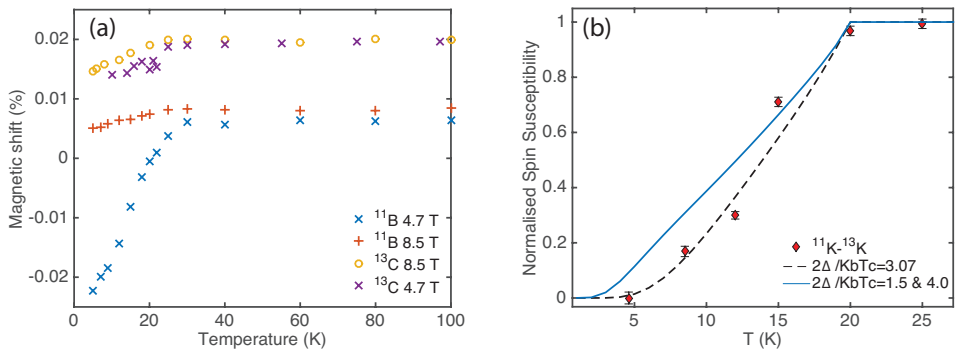

Figure 8.8: Knight shift (%) of ^{13}C and ^{11}B on $MgB_{1.95}{}^{13}C_{0.05}$ as a function of temperature at 4.7 and 8.5 T. Normalised spin susceptibility obtained by subtracting Knight shifts as described in text.

Knight shift in the superconducting state

Fig. 8.8a shows the dependence of the magnetic shift as a function of temperature for both boron and carbon. The difference in magnitude between field can be ascribed to the diamagnetic Meissner screening currents which are field dependent, the Knight shift is independent of field and temperature, but in the superconducting state it decays as discussed in section 4.3.1. The spin susceptibility should be the same for two nuclei in similar chemical environments and therefore after the diamagnetic subtraction procedure described in section 4.3.1, the resulting quantity is the normalised spin susceptibility shown in Fig. 8.8b. The fit of the data in Fig. 8.8b to the Yosida function yields a superconducting gap ratio of $2\Delta/k_BTc$=3.07±0.68, close to the usual BCS gap ratio of 3.53. In pure MgB_2, tunnelling spectroscopy studies[228, 229] report two gaps related to σ and π bands with superconducting gap ratios of $2\Delta/k_BTc$=5-6 and 1.2-1.5 respectively. Similarly point contact spectroscopy[123] gives $2\Delta/k_BTc$=4.1 and 1.7. The two band nature of MgB_2 is thought to be preserved upon doping with carbon in polycrystalline materials up to $x = 0.10$. However an isotropic gap function is found to be more appropriate in this case. A calculation of two superconducting gaps is given in Fig. 8.8b with typical values for each gap, there appears to be no obvious agreement which is in line with previous works[34] on ^{27}Al NMR, which has suggested $2\Delta/k_BTc$=1.5. As aluminium resides closer to the π bands, it is likely to be principally monitoring the relatively smaller gap ratio. In this case, ^{13}C probes the stronger σ bands and therefore this manifests as a stronger gap ratio. In neither case was the double gap model appropriate. Alternatively, interband scattering may play a key role and this is especially relevant in NMR studies of Knight shift and $1/T_1$, which have reported an isotropic gap. When interband scattering is large then one expects an average of the two gaps and more BCS like behaviour.[34] To determine the K_{spin}

term for both ^{11}B and ^{13}C, there are two main methods. (a) Compare the magnetic shift of the metallic compound with a parent insulating compound, the difference in magnetic shifts is K_{spin} or (b) Cryogenic experiments which allow extraction of K_{orb} and therefore by subtraction from the room temperature shift, K_{spin}. In this instance there is not similar insulating compound to MgB_2 available and method (b) must be adopted.

For ^{13}C, the room temperature shift is 208.6± 0.2ppm and the shift at the lowest temperature recorded (5 K) is 146.7± 0.2ppm, by simple subtraction K_{spin}≈62 ppm. A similar method is used for ^{11}B, there is an additional second order quadrupole shift term which may be extracted using the equations presented in section 8.1.2. The static room temperature shift is used at 8.5 T, which is 88.6±0.3 ppm and the lowest temperature (5 K) shift is 50.4± 0.4ppm, this then gives K_{spin}≈38±0.2 ppm.

Ab-initio calculations

To study the contributions to relaxation, ab-initio calculations were performed. The contributions are given in table 8.1.

		dipole (xy)	dipole (z)	Fermi-contact	Total
x=0.07	C	-0.0024	0.0048	0.0034	0.0058
x=0.07	B	-0.0008 ± 0.0004	0.0016 ± 0.0008	0.0030 ± 0.00125	0.0038
x=0.04	C	-0.0023	0.0046	0.0035	0.0058
x=0.04	B	-0.0011 ± 0.0005	0.0022 ±0.001	0.0035 ± 0.0013	0.0046

Table 8.1: Calculated dipole-dipole and contact contribution to the Knight shift in $MgB_{2-x}C_x$ in %. The label $\alpha = xy, z$ indicates the direction of the applied external magnetic field. Calculated using the approach described in Refs.[36, 148, 172].

The Knight shift extracted from Fig.8.8(a) is 0.0038% for ^{11}B and 0.0062% for ^{13}C. There is excellent agreement with the calculated values of total % Knight shift for ^{13}C (0.0058%) and ^{11}B (0.0036%). The Knight shift is dominated mainly by the Fermi-contact interaction for ^{11}B NMR, ^{13}C has a similar magnitude Fermi-contact contribution but the dominant contribution is the dipole term (z). Increasing the carbon doping level does not seem to affect the Knight shift contribution ratios for ^{13}C, but does have a small effect on the ^{11}B Knight shift.

Previous calculations for pure MgB_2[147] have indicated similar % Knight shift contributions, the only noticeable difference is for the Fermi-contact contribution. This contribution is 0.0027% for undoped MgB_2. In the carbon doped system, the contribution is higher (0.0035% at x=0.04) and decreases as more carbon is added (0.0030% at x=0.07), as shown in Table 8.1.

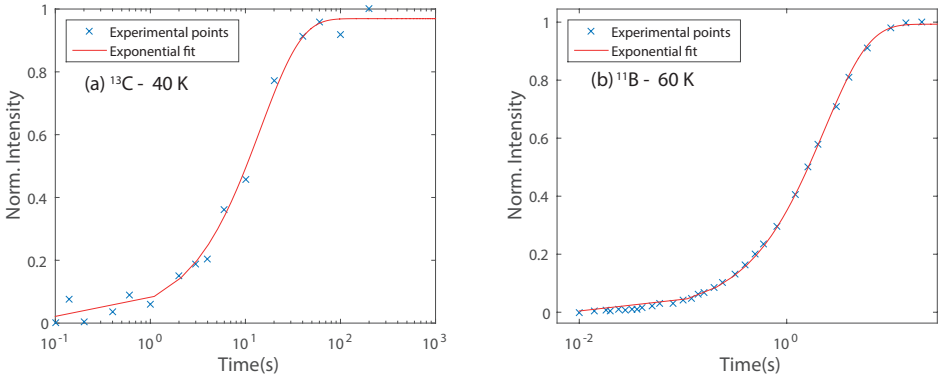

Figure 8.9: Saturation recovery experimental points and fit for (a) ^{13}C NMR at 8.5 T and 40 K (b) ^{11}B NMR at 8.5 T and 60 K

8.2.3 Nuclear spin relaxation in the normal and superconducting state

Experimental methodology

The NMR relaxation rate for both ^{11}B and ^{13}C were obtained using saturation recovery pulse sequences described in section 5.1.3. A saturation comb of 100 pulses with a saturation pulse length of 4μs and $\pi/2$ readout pulse of 3μs. The saturation recovery of a quadrupolar nuclei under static conditions, is expected to follow a bi-exponential model with the following form:

$$\frac{M(\infty) - M(t)}{M(\infty)} = \frac{1}{10}e^{-\tau/T_1} + \frac{9}{10}e^{-6t/T_1} \tag{8.4}$$

However it can be difficult to reliably extract different T_1 components, and the evidence from previous studies[137] indicates that under the conditions of strong pulse trains, a more mono-exponential fit is obtained of the following form:

$$\frac{M(\infty) - M(t)}{M(\infty)} = Ae^{-t/T_1} + C \tag{8.5}$$

This was also verified experimentally for ^{11}B NMR on MgB_2, no appreciable bi-exponentiality was found below T_c. Example fits for ^{11}B and ^{13}C NMR are shown in Fig. 8.9 in the normal state.

Normal state

The temperature dependence of the nuclear spin lattice relaxation rate (NSLR) is shown in Fig. 8.10. There is a linear temperature dependence in the normal phase,

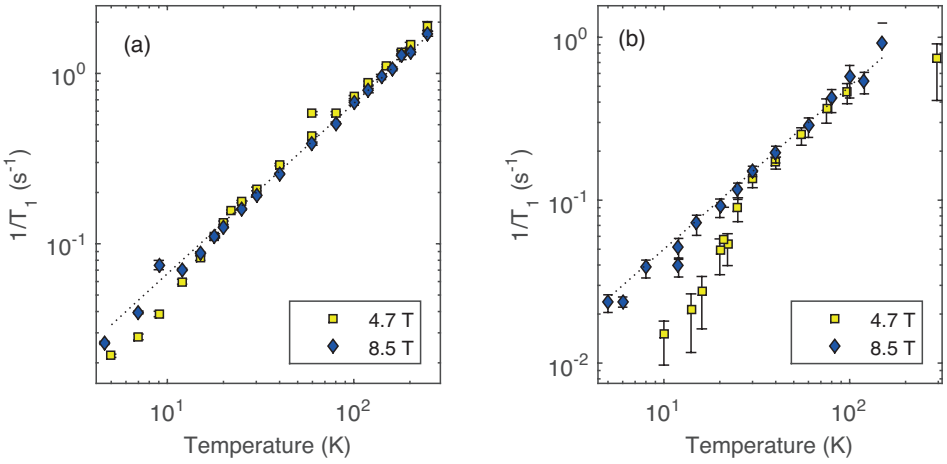

Figure 8.10: Spin-lattice relaxation rate of $MgB_{1.95}{}^{13}C_{0.05}$. Black dashed line is Korringa product, set to 150 s K and 200 s K for boron and carbon respectively. (a) ^{11}B NMR relaxation rate (b) ^{13}C NMR relaxation rate

which is typical for metallic systems and is known as the Korringa law [145]. This is the case for both ^{11}B and ^{13}C NMR data in the normal state. ^{11}B yields a Korringa product (T_1T) of 155 $\pm$ 10 K secK, in literature it is reported to be 178[174], 170[36], 165[171], 150[177] and 125[178] K sec.

^{13}C nuclei have a Korringa product of 200$\pm$20 K sec, but there is no other ^{13}C study for doped MgB_2 to compare this to. A suitable comparison can be made to aluminium doped MgB_2, where ^{27}Al NMR reveals $1/T_1T$=125-166 K sec with x=0.16-0.45.

The reduction in ^{27}Al Korringa product compared to ^{11}B Korringa product is thought to be due to filling of the σ hole band at the Fermi level.[34] The Korringa ratio (R) has been reported to be 0.2[171] and 0.1[36] for ^{11}B and near to unity for ^{25}Mg[176] and ^{27}Al, which is reflective of metals. From the experimental data collected, shown in Figures. 8.8 and 8.10, taking the Knight shift to be between 30-50 ppm, and from a Korringa product of 155 K sec, one may estimate the Korringa ratio as 0.05-0.15.

In terms of ^{13}C data, the Knight shift is taken to be 62 ppm and T_1T= 200 $\pm$ 20 K sec, this reveals a Korringa ratio of 0.17-0.21, closer to the ^{11}B ratio reported previously[36, 171]. The $1/R$ values reported for ^{27}Al range from 1-2.5 depending on ^{27}Al doping [35], other literature reports [148] $1/R \approx 2$.

Ab-initio calculations

To study the contributions to relaxation, ab-initio calculations were performed using the method described earlier. The calculated relaxation rates expressed as $1/T_1$T are given in Table 8.2 and are shown in terms of contributions from the Fermi-contact, orbital and dipole mechanisms. Usually the strongest contribution is the Fermi-contact

		orbital	dipole	Fermi-contact	Total
x=0.07	C	4.4	1.86	0.57	6.83
x=0.07	B	3.3 ± 1.15	1.08 ± 0.2	0.62± 0.27	5
x=0.04	C	1.8	1.1	0.60	3.5
x=0.04	B	3.25 ± 1.35	1.13 ± 0.16	0.62± 0.23	5

Table 8.2: Calculated relaxation rate $1/T_1T$ in 10^{-3}/(K sec). Calculated using the approach described in Refs.[36, 148, 172].

interaction for most metals, however this is not the case for MgB_2.

In general the strongest contribution to the relaxation rate for ^{11}B nuclei is the orbital term, as reported previously[147] and is due to states at the Fermi level consisting mainly of B p-orbitals. The contributions to $1/T_1$T for ^{13}C also show similar behaviour with the orbital term being the dominant contributor. However the difference is more marked with doping level, higher % carbon in the lattice corresponds to a larger orbital contribution to $1/T_1$T.

A comparison can be drawn between experimental and calculated values, for ^{13}C $1/T_1$T is 0.005 (K sec)$^{-1}$, higher than the total for x=0.04 but lower than x=0.07. The level of doping is approximately x=0.05, and therefore the experimental value may be consistent with ab-initio values. From ^{11}B NMR, the experimentally determined $1/T_1$T is 0.0065 K sec^{-1}, which is higher than the calculated values presented in table 8.2

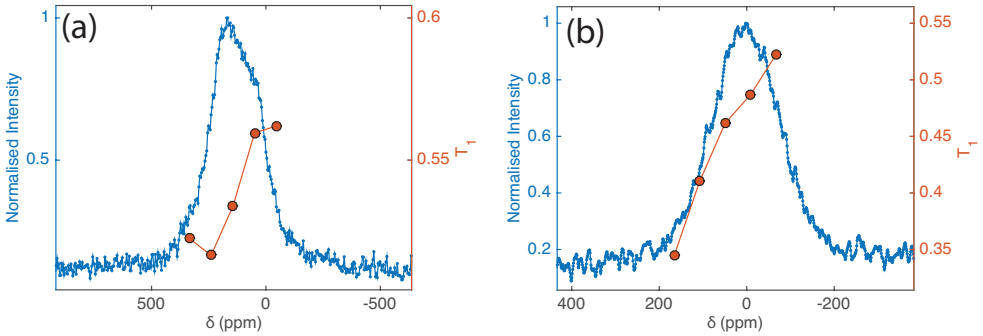

Figure 8.11: Variation of T_1 across (a) ^{11}B lineshape at 200 K and (b) ^{13}C lineshape at 150 K

The Fermi-contact term is the smallest contribution for both nuclei and this means that the dipole term is now relatively large, which leads to an anisotropy of the relaxation rate. This can be seen experimentally in 8.11, which shows the variation of T_1 across lineshape. This is also consistent with previous calculations.[147] The situation is different for nuclei such as ^{27}Al and ^{25}Mg where the Fermi-contact term dominates, and there is not an appreciable dipolar contribution.

Superconducting state

BCS s-wave superconductors usually show an exponential decrease in both $1/T_1$ and a Hebel-Slichter coherence peak usually manifests just below T_c due to the opening of the superconducting gap [3]. These two features will now be considered.

Fig. 8.10 shows $1/T_1$ data for both ^{11}B and ^{13}C NMR. There is an expected difference in behaviour between fields because of the field dependence of T_c. At 8.5 T, the majority of the sample is in the normal state, as shown in fig. 8.10, although some of the sample is still superconducting and this is manifested in a slight deviation from Korringa like behavior, as expected.[145]

At 4.7 T $1/T_1$ there is a more marked deviation from the Korringa law at 25 K. In boron this deviation is enhanced from the presence of a dopant (carbon), this has also been noted in previous works[137]. This is probably due to enhancement of H_{c2}. The ^{13}C relaxation rate data at 4.7 T deviates more substantially below T_c however there are large error bars, making more meaningful analysis difficult. The S/N is greatly reduced because the sample required dilution with an insulator for the experiments to continue. As the experiments for each data-point were extremely long (approx 1 day each), there was difficulty in estimating the longest variable delay time and consequently data below T_c is not well defined. Qualitatively one may say that there is a deviation consistent with boron data, however no more quantitative analysis could be done.

A coherence peak is not observed in either ^{11}B or ^{13}C data. This agrees with previous measurements on MgB_2, [36, 171, 177] Although is in contrast with others[125, 126, 180] and also with similar analogues, $MgB_{2-x}{}^{12}C_x$[174] and $MgB_{2-x}Al_x$[34, 126, 180].

The difference between studies may be due to the large anisotropy of MgB_2, which is well known. Therefore H_{c2} and thus T_c will differ according to the directional orientation of crystallites and the coherence peak will effectively be 'smeared' out, this is especially prevalent at high fields where the estimated T_c difference between $Hc_{c2\perp}$ and $H_{c2\parallel}$ directions will be greater.[34]

8.3 Conclusion

In conclusion, a sample of $MgB_{1.95}{}^{13}C_{0.05}$ was synthesised in order to probe the doping site and superconducting state using ^{13}C NMR. The specific aims of this exercise were twofold, firstly to establish the extent of carbon-boron substitution and/or carbon build up at the grain boundaries using ^{13}C NMR on a sample made using the CVD method of nanoparticle synthesis. The second aim was to extract novel information using ^{13}C NMR, specifically in terms of Knight shift, T_1 and peak shape measurements with comparison to ab-initio calculations where applicable. Another point of interest was the normalised spin-susceptibility probed using the Knight shift of ^{11}B and ^{13}C NMR, which has not been determined previously due to other NMR active nuclei residing in different areas of the lattice.

In terms of the position of carbon, there is only a single peak in the ^{13}C NMR spectrum and this seems to imply that when MgB_2 is doped with carbon it substitutes favourably in one position (substitution with boron, or collects at grain boundary). However it is not immediately obvious which is preferential as pXRD measurements show the a-axis parameter shrinks as reported previously[60] but this could occur from either type of substitution. Toward determining a specific substitution scenario, ab-initio simulations were performed. The good match between simulations and experimental evidence suggests that one carbon is substituted for one boron, as the simulations were based upon the single substitution scenario. Alternative scenarios for example would be carbon clustering or grain boundary/stacking faults, these are unlikely to be present in significant number as then ^{13}C and ^{11}B NMR parameters, such as T_1T and K_s would have rather different numerical values. This of course would result from the different electronic and magnetic structures in each scenario. Therefore it is likely that this single-substitution scenario is representative of carbon doping using the CVD method of nanoparticle synthesis. To corroborate this further, ab-initio simulations of other carbon doping scenarios (such as clustering) are currently being carried out. There have been previous electronic studies that have suggested that substitution is more energetically favourable than interstitial positions [230]. Although it is clear that this is dependent on the type of synthesis, e.g. the CVD method seems to favour substitution over interstitial positions, but samples synthesised using malic acid and toluene show more interstitial positions and negligible carbon-boron substitution.[131] This is an important point as ^{13}C NMR can help to distinguish the source of flux pinning, i.e. in boron-carbon substituted samples the pinning centre is the carbon defect, but in samples with carbon in interstitial positions, flux pinning arises from boron vacancies causing stacking faults, which in turn cause defect pinning centres[131]. Future work should focus on a series of ^{13}C labelled samples synthesised using other methods

to the CVD synthesis with ab-initio calculations to support ^{13}C NMR data. This would allow determination of the carbon distribution using other chemical synthesis routes. This is especially interesting because J_c does not increase linearly with carbon doping content and this may be investigated using ab-initio calculations and ^{13}C NMR. One may match the experimental and calculated NMR parameters with different carbon doping scenarios, for example the highest J_c is with carbon doping of x=0.08. If the carbon content is increased to x=0.20 then the J_c *decreases*. It is not completely clear why this is, but if one could simulate the carbon distribution (perhaps carbon begins to cluster at x=0.20) and match with ^{13}C NMR parameters (such as T_1T and Knight shift) it may become more clear.

Ab-initio calculations show good agreement with experimental values for ^{13}C, but there is a slight deviation between ^{11}B experimental and calculated numbers. It is not clear why this arises. The main contribution to the ^{11}B Knight shift is the orbital term as reported before, but for ^{13}C the most substantial term is the dipole (z) one. There is a clear dependence on ^{11}B Knight shift contributions as the carbon doping level is changed, but from ^{13}C the relative Knight shift contributions stay fairly constant. Future work should seek to understand the effect of carbon doping in more detail, a series of different ^{13}C should be made and then compared to the ab-initio values, a similar exercise has been done for ^{27}Al NMR.[34]

The relaxation rate shows metallic Korringa like behaviour in the normal state and a deviation at T_c concomitant with entering the superconducting state. This is more prevalent at lower fields, where the deviation occurs at similar temperatures for both nuclei. There is also an anisotropy in T_1 across the lineshape which is supported by ab-initio calculations which suggest there is a substantial dipolar contribution to the relaxation rate. The strongest contribution to the relaxation rate for both ^{13}C and ^{11}B is the orbital term, this has been reported before for ^{11}B NMR.

The peak shape as a function of temperature shows an expected shift into the superconducting state, but there is a large diamagnetic contribution which masks the true Knight shift and changes the peak shape dramatically. This is better resolved using ^{13}C NMR which allows one to seperate both terms at 4.7 T. An alternative hypothesis is that as carbon is a pinning centre for vortices and therefore will reside inside more vortex cores, on average when compared to boron. ^{13}C NMR then reveals more of the normal state, when compared to ^{11}B NMR which shows an inhomogenous distribution of fields characteristic of the outer vortex structure. Future work might attempt to study a ^{13}C doped single crystal of MgB_2 which may be able to distinguish the features of the vortex lineshape and allow one to fit the penetration depth and coherence length using theoretical methods.[225]

The Knight shift decay in the superconducting state follows a BCS-like trend, with

$2\Delta/k_BTc$=3.07±0.68. The gap is better fit to an isotropic Yosida function, which could be either (a) enhanced interband scattering yielding a more average isotropic value or (b) boron and carbon sit in a position more descriptive of the Δ_σ band and therefore probe only this superconducting gap. This supports the view that MgB_2 is a typical BCS superconductor, but future work should be done at different magnetic fields to further validate this gap ratio. Again samples with varying carbon content should also be tested to see if the gap ratio varies.

CHAPTER

NINE

APPENDIX

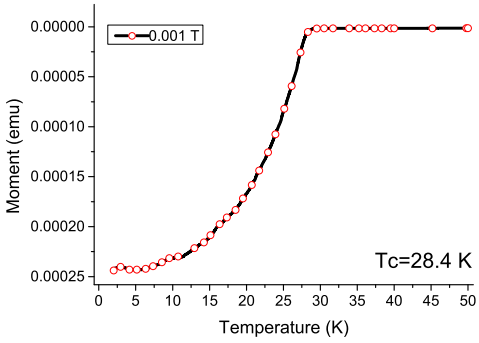

(a) ZFC measurement at 1000 nT

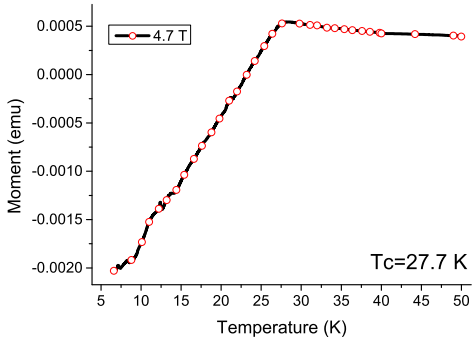

(b) FC measurement at 4.7 T

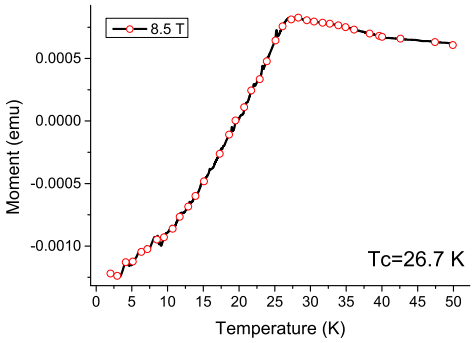

(c) FC measurement at 8.5 T

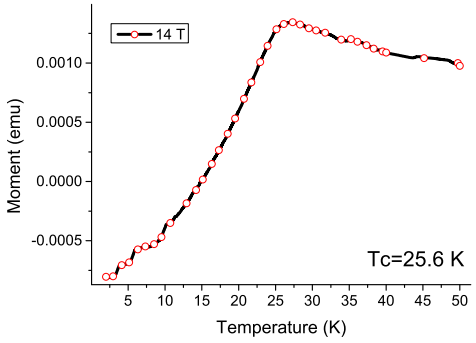

(d) FC measurement at 14 T

Figure 9.1: Magnetic susceptibility measurements of $Rb_3(H_2O@C_{60})$ collected using VSM-PPMS. ZFC - Zero field cooled and FC - Field cooled

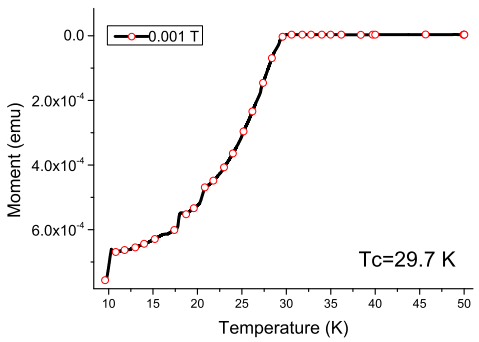

(a) ZFC measurement at 0.001 T

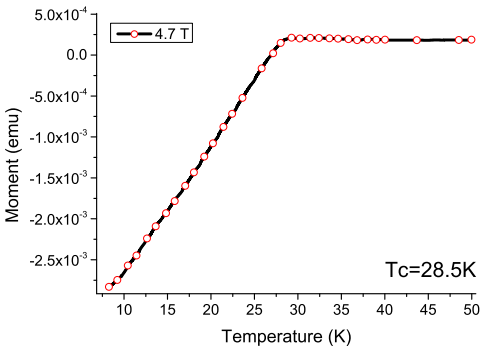

(b) FC measurement at 4.7 T

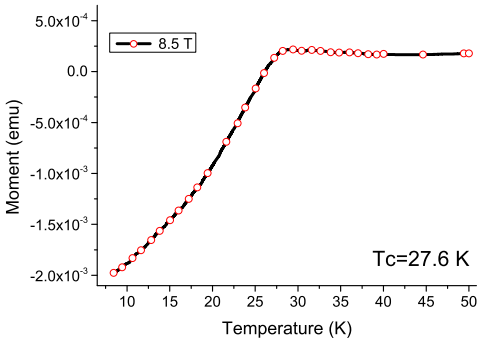

(c) FC measurement at 8.5 T

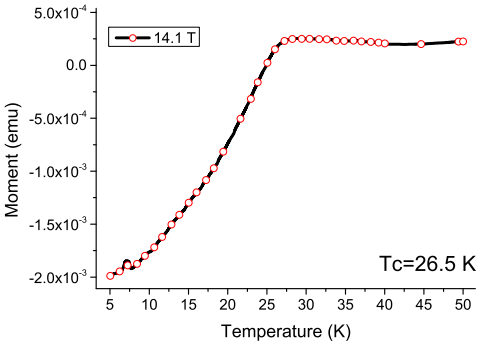

(d) FC measurement at 14 T

Figure 9.2: Magnetic susceptibility measurements of $Rb_3(H_2@C_{60})$ collected using VSM-PPMS. ZFC - Zero field cooled and FC - Field cooled

```
Data File C:\HPLC DATA\LC18\OCT2015\DEF_LC18 2015-10-13 10-02-26\13_010000003.D
Sample Name: SAS175G after sub

    ======================================================================
    Acq. Operator   : Shamim Alom                   Seq. Line :   3
    Acq. Instrument : LC18                          Location : Vial 2
    Injection Date  : 13/10/2015 10:26:20                Inj :   1
                                                   Inj Volume : 10.000 µl
    Sequence File   : C:\HPLC Data\LC18\OCT2015\DEF_LC18 2015-10-13 10-02-26\DEF_LC18.S
    Method          : C:\HPLC DATA\LC18\OCT2015\DEF_LC18 2015-10-13 10-02-26\TOLUENE10MIN.M (
                      Sequence Method)
    Last changed    : 13/10/2015 10:02:26 by Shamim Alom
    Method Info     : 100% Toluene in D
```

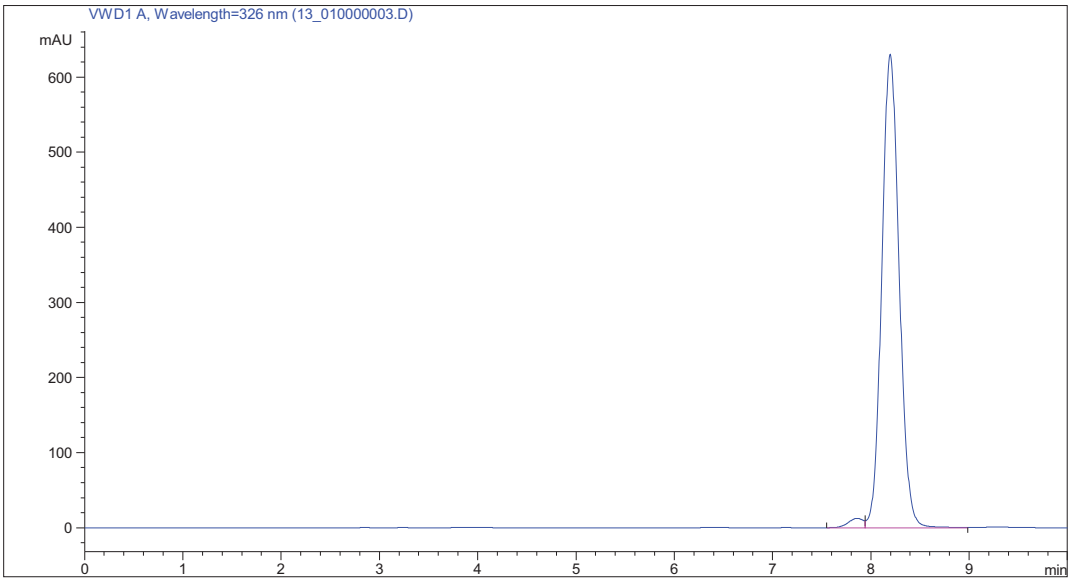


```
    ======================================================================
                            Area Percent Report
    ======================================================================

    Sorted By             :      Signal
    Multiplier:                   :      1.0000
    Dilution:                     :      1.0000
    Do not use Multiplier & Dilution Factor with ISTDs


    Signal 1: VWD1 A, Wavelength=326 nm

    Peak RetTime Type  Width     Area      Height     Area
      #   [min]        [min]   [mAU*s]     [mAU]       %
    ----|-------|----|-------|----------|----------|--------|
       1   7.858 BV    0.1603  132.00569   12.58226   1.6748
       2   8.196 VB    0.1916 7749.99170  630.04614  98.3252

    Totals :                   7881.99739  642.62841


    ======================================================================

LC18 13/10/2015 10:36:25 Shamim Alom                          Page   1 of 1
```

Figure 9.3: HPLC trace of $H_2O@C_{60}$ starting material, peak with retention time 7.8 minutes is C_{60} and peak at 8.2 minutes is $H_2O@C_{60}$

CHAPTER

TEN

BIBLIOGRAPHY

Bibliography

[1] J. Bardeen, L. N. Cooper, and J. R. Schrieffer. Theory of superconductivity. *Physical Review*, 108:1175–1204, 1957.

[2] L. C. Hebel and C. P. Slichter. Nuclear relaxation in superconducting aluminum. *Physical Review*, 107(3):901–902, 1957.

[3] L. C. Hebel and C. P. Slichter. Nuclear spin relaxation in normal and superconducting aluminum. *Physical Review*, 113(6), 1959.

[4] S. L. Bud'ko and P. C. Canfield. Superconductivity of magnesium diboride. *Physica C*, 514:142–151, 2014.

[5] P. A. Marchetti, F. Ye, Z. B. Su, and L. Yu. Non-BCS superconductivity for underdoped cuprates by spin-vortex attraction. *Journal of Physics and Chemistry of Solids*, 72:337–340, 2011.

[6] E. Cappelluti, C. Grimaldi, L. Pietronero, S. Strässler, and G. A. Ummarino. Superconductivity of Rb_3C_{60}: Breakdown of the Migdal-Eliashberg theory. *The European Physical Journal B*, 21(3):9, 2001.

[7] J. L. Tallon, J. G. Storey, and B. Mallett. The design of High-T_c superconductors - Room-temperature superconductivity? *Physica C*, 482:45–49, 2012.

[8] H. Y. Choi. Coulomb suppression of NMR coherence peak in fullerene superconductors. *Physical Review Letters*, 81(2), 1997.

[9] E. Barthel, G. Quirion, P. Wzietek, D. Jérome, J. B. Christensen, M. Jørgensen, and K. Bechgaard. NMR in commensurate and incommensurate spin density waves. *Europhysics Letters*, 21(1):87, 1993.

[10] A. M. Mounce, S. Oh, S. Mukhopadhyay, W. P. Halperin, a. P. Reyes, P. L. Kuhns, K. Fujita, M. Ishikado, and S. Uchida. Spin-density wave near the vortex cores in the high-temperature superconductor $Bi_2Sr_2CaCu_2O_8$. *Physical Review Letters*, 106(5):4–7, 2011.

[11] T. Wu, H. Mayaffre, S. Kramer, M. Horvatic, C. Berthier, W. N. Hardy, R. Liang, D. A. Bonn, and M. H. Julien. Magnetic-field-induced charge-stripe order in the high-temperature superconductor $YBa_2Cu_3O_y$. *Nature*, 477(7363):191–194, 2011.

[12] Takayoshi S., Hidekazu M., Masahiro U., Fuko E., Mitsuharu Y., Yoshio K., Kwing T. L., Hidetomo U., Kazuhiko K., Shigeki M., and Setsuko T. Multiple Antiferromagnetic Spin Fluctuations and Novel Evolution of T_c in Iron-Based Superconductors $LaFe(As_{1-x}P_xO_{1-y}F_y)$ Revealed by ^{31}P-NMR Studies. *Journal of the Physical Society of Japan*, 85(5):053706, 2016.

[13] J. Crocker, A. P. Dioguardi, N. Roberts-Warren, A. C. Shockley, H.-J. Grafe, Z. Xu, J. Wen, G. Gu, and N. J. Curro. NMR studies of pseudogap and electronic inhomogeneity in $Bi_2Sr_2CaCu_2O_{8+\delta}$. *Physical Review B*, 84:224502, Dec 2011.

[14] P. Wzietek, T. Mito, H. Alloul, D. Pontiroli, M. Aramini, and M. Riccò. NMR Study of the Superconducting Gap Variation near the Mott Transition in Cs_3C_{60}. *Physical Review Letters*, 112(6):066401, 2014.

[15] A. Potocnik, A. Y. Ganin, Y. Takabayashi, M. T. McDonald, I. Heinmaa, P. Jeglic, R. Stern, M. J. Rosseinsky, K. Prassides, and D. Arcon. Jahn-Teller orbital glass state in the expanded fcc Cs_3C_{60} fulleride. *Chemical Science*, 5:3008–3017, 2014.

[16] C. M. Varma, J. Zaanen, and K. Raghavachari. Superconductivity in the fullerenes. *Science*, 254(5034):989–992, 1991.

[17] K. Tanigaki, T. W. Ebbesen, S. Saito, J. Mizuki, J. S. Tsai, Y. Kubo, and S. Kuroshima. Superconductivity at 33 K in $Cs_xRb_yC_{60}$, 1991.

[18] A. Y. Ganin, Y. Takabayashi, Y. Z. Khimyak, S. Margadonna, A. Tamai, M. J. Rosseinsky, and K. Prassides. Bulk superconductivity at 38 K in a molecular system. *Nature Materials*, 7(5):367–371, 2008.

[19] Y. Takabayashi, A. Y. Ganin, P. Jeglic, D. Arcon, T. Takano, Y. Iwasa, Y. Ohishi, M. Takata, N. Takeshita, K. Prassides, and M. J. Rosseinsky. The disorder-free non-BCS superconductor Cs_3C_{60} emerges from an antiferromagnetic insulator parent state. *Science*, 323(5921):1585–90, 2009.

[20] Y. Ihara, H. Alloul, P. Wzietek, D. Pontiroli, M. Mazzani, and M. Riccò. NMR study of the Mott transitions to superconductivity in the two Cs_3C_{60} phases. *Physical Review Letters*, 104(25):7–10, 2010.

[21] H. Alloul. Electronic Correlations, Jahn-Teller Distortions and Mott Transition to Superconductivity in Alkali-C_{60} Compounds. *EPJ Web Conferences*, 23:00015, 2012.

[22] Y. Nomura, S. Sakai, M. Capone, and R. Arita. Unified understanding of superconductivity and Mott transition in alkali-doped fullerides from first principles. *Science Advances*, 1(7):e1500568–e1500568, 2015.

[23] K. Komatsu, M. Murata, and Y. Murata. Encapsulation of molecular hydrogen in fullerene C_{60} by organic synthesis. *Science*, 307(5707):238–240, 2005.

[24] K. Kurotobi and Y. Murata. A Single Molecule of Water Encapsulated in Fullerene C_{60}. *Science*, 333(6042):613–616, 2011.

[25] C. Beduz, M. Carravetta, J. Chen, M. Concistrè, M. Denning, M. Frunzi, A. J. Horsewill, O. G. Johannessen, R. Lawler, X. Lei, M. H. Levitt, Y. Li, S. Mamone, Y. Murata, U. Nagel, T. Nishida, J. Ollivier, S. Rols, T. Rõõm, R. Sarkar, N. J. Turro, and Y. Yang. Quantum rotation of ortho and para-water encapsulated in a fullerene cage. *Proceedings of the National Academy of Sciences of the United States of America*, 109(32):12894–8, 2012.

[26] A. Takeda, Y. Yokoyama, S. Ito, T. Miyazaki, H. Shimotani, K. Yakigaya, T. Kakiuchi, H. Sawa, H. Takagi, K. Kitazawa, and N. Dragoe. Superconductivity of doped Ar@C_{60}. *Chemical Communications*, pages 912–914, 2006.

[27] A. Krachmalnicoff, M. H. Levitt, and R. J Whitby. An optimised scalable synthesis of H_2O@C_{60} and a new synthesis of H_2@C_{60}. *Chemical communications*, 50(86):13037–13040, 2014.

[28] C. H. Pennington and V. A. Stenger. Nuclear magnetic resonance of C_{60} and fulleride superconductors. *Review of Modern Physics*, 60(3):855–910, 1996.

[29] J. Nagamatsu, N. Nakagawa, T. Muranaka, Y. Zenitani, and J. Akimitsu. Superconductivity at 39 K in magnesium diboride. *Nature*, 410(6824):63–4, 2001.

[30] T. Matsushita. *Flux pinning in Superconductors*, volume 146. Springer-Verlag Berlin Heidelberg, 2014.

[31] S. Hahn, Y. lwasa, J. Bascunan, J.P. Voccio, J. Ling, J. Song, and Y. Kim. Persistent-Mode MRI Magnet Fabricated From Reacted, Monofilamentary MgB_2 Wires And Joints, January 15 2015. US Patent App. 14/330,689.

[32] Dou S. X., Pan A. V., Zhou S., Ionescu M., Liu H. K., and Munroe P. R. Substitution-induced pinning in MgB_2 superconductor doped with SiC nanoparticles. *Superconductor Science and Technology*, 15(11):1587, 2002.

[33] A. Yamamoto, J. Shimoyama, S. Ueda, Y. Katsura, I. Iwayama, S. Horii, and K. Kishio. Universal relationship between crystallinity and irreversibility field of MgB_2. *Applied Physics Letters*, 86(21), 2005.

[34] M. Saeed, K. Kumagai, M. Filippi, and A. Bianconi. ^{27}Al and ^{11}B NMR Study of the Two-Band Superconductor Mg_{1-x} Al_xB_2. *Journal of the Physical Society of Japan*, 79(12):124711, 2010.

[35] G. Papavassiliou, M. Pissas, M. Karayanni, M. Fardis, S. Koutandos, and K. Prassides. ^{11}B and ^{27}Al NMR spin-lattice relaxation and Knight shift of $Mg_{1-x}Al_xB_2$: Evidence for an anisotropic Fermi surface. *Physical Review B*, 66(14):140514, oct 2002.

[36] S. H. Baek, B. J. Suh, E. Pavarini, F. Borsa, R. G. Barnes, S. L. Bud'ko, and P. C. Canfield. NMR spectroscopy of the normal and superconducting states of MgB_2 and comparison to AlB_2. *Physical Review B*, 66(10):104510, 2002.

[37] G. A. Ummarino, D. Daghero, R. S. Gonnelli, and A. H. Moudden. Carbon substitutions in MgB_2 within the two-band Eliashberg theory. *Physical Review B*, 71(13):134511, 2005.

[38] H. W. Kroto, J.R. Heath, S. C. O'Brien, R. F. Curl, and R. E. Smalley. C_{60}: Buckminsterfullerene. *Nature*, 318(14):162–163, 1985.

[39] R. Tycko, R. C. Haddon, G. Dabbagh, S. H. Glarum, D. C. Douglas, and A. M. Musce. Solid-State Magnetic Resonance Spectroscopy of Fullerenes. *Journal of Physical Chemistry*, 95(2):518–520, 1991.

[40] R. Tycko, G. Dabbagh, R. Fleming, R. Haddon, A. Makhija, and S. Zahurak. Molecular dynamics and the phase transition in solid C_{60}. *Physical Review Letters*, 67(14):1886–1889, 1991.

[41] W. P. Beyermann, M. F. Hundley, J. D. Thompson, F. N. Diederich, and G. Grüner. Low-temperature specific heat of C_{60}. *Physical Review Letters*, 68(13):2046–2049, 1992.

[42] W. Krätschmer, K. Fostiropoulos, and D. R. Huffman. The Infrared and Ultraviolet-Absorption Spectra of Laboratory- Produced Carbon Dust - Evidence For the Presence of the C_{60} Molecule. *Chemical Physics Letters*, 170(2):167, 1990.

[43] M. H. Levitt and A. J. Horsewill. Nanolaboratories: physics and chemistry of small-molecule endofullerenes. *Philosophical Transactions of the Royal Society A*, 371(1998):20130124, 2013.

[44] B. A. Dicamillo, R. L. Hettich, G. Guiochon, R. N. Compton, M. Saunders, H. A. Jimenez-Vazquez, A. Khong, and R. J. Cross. Enrichment and characterization of a noble gas fullerene: ArC_{60}. *Journal of Physical Chemistry*, 100(22):9197–9201, 1996.

[45] T. Suetsuna, N. Dragoe, W. Harneit, A. Weidinger, H. Shimotani, S. Ito, H. Takagi, and K. Kitazawa. Separation of $N_2@C_{60}$ and $N@C_{60}$. *Chemistry*, 8(22):5079–83, 2002.

[46] Y. Rubin, T. Jarrosson, G. W. Wang, M. D. Bartberger, K. N. Houk, G. Schick, M. Saunders, and R. J. Cross. Insertion of helium and molecular hydrogen through the orifice of an open fullerene. *Angewandte Chemie International Edition*, 40(8):1543–1546, 2001.

[47] Y. Murata, M. Murata, and K. Komatsu. 100% encapsulation of a hydrogen molecule into an open-cage fullerene derivative and gas-phase generation of $H_2@$ C_{60}. *Journal of the American Chemical Society*, 125:7152–7153, 2003.

[48] G. Schick, T. Jarrosson, and Y. Rubin. Formation of an effective opening within the fullerene core of C_{60} by an unusual reaction sequence. *Angewandte Chemie International Edition*, 38(16):2360–2363, 1999.

[49] M. Carravetta, Y. Murata, M. Murata, I. Heinmaa, R. Stern, A. Tontcheva, A. Samoson, Y. Rubin, K. Komatsu, and M. H. Levitt. Solid-State NMR Spectroscopy of Molecular Hydrogen Trapped Inside an Open-Cage Fullerene. *Journal of the American Chemical Society*, 126(13):4092–4093, 2004.

[50] M. Ge, U. Nagel, D. Hüvonen, T. Rõõm, S. Mamone, M. H. Levitt, M. Carravetta, Y. Murata, K. Komatsu, J. Y C Chen, and N. J. Turro. Interaction potential and infrared absorption of endohedral H_2 in C_{60}. *Journal of Chemical Physics*, 134(5):1–13, 2011.

[51] M. Carravetta, O. G. Johannessen, M. H. Levitt, I. Heinmaa, R. Stern, A. Samoson, A. J. Horsewill, Y. Murata, and K. Komatsu. Cryogenic NMR spec-

troscopy of endohedral hydrogen-fullerene complexes. *Journal of Chemical Physics*, 124(10), 2006.

[52] Malcolm H Levitt. Spectroscopy of light-molecule endofullerenes. *Philosophical Transactions of the Royal Society A*, 2013.

[53] P. W. Stephens, L. Mihaly, P. L. Lee, R. L. Whetten, S M. Huang, R. Kaner, F. Deiderich, and K. Holczer. Structure of single-phase superconducting K_3C_{60}. *Nature*, 351(6328):632–634, 1991.

[54] P. W. Stephens, L. Mihaly, J. B. Wiley, S. M. Huang, R. B. Kaner, F. Diederich, R. L. Whetten, and K. Holczer. Structure of RbC_{60} compounds. *Physical Review B*, 45(1):543–546, 1992.

[55] R. Tycko, G. Dabbagh, M. J. Rosseinsky, D. W. Murphy, R. M. Fleming, A. P. Ramirez, and J. C. Tully. ^{13}C NMR Spectroscopy of K_xC_{60}: Phase Separation, Molecular Dynamics, and Metallic Properties. *Science*, 253(5022):884–886, 1991.

[56] A. Auerbach, N. Manini, and E. Tosatti. Electron-Vibron Interactions and Berry Phases in Charged Buckminsterfullerene: Part I. *Physical Review B*, 49(18):29, 1993.

[57] X. H. Li, X. J. Du, M. Qiu, Y. W. Ma, and L. Y. Xiao. Design and experimental demonstration of an MgB_2 based 1.5 T MRI test magnet. *Physica C*, 463-465:1338–1341, 2007.

[58] S. L. Bud'ko, G. Lapertot, C. Petrovic, C. E. Cunningham, N. Anderson, and P. C. Canfield. Boron isotope effect in superconducting MgB_2. *Physical Review Letters*, 86(9):1877–1880, 2001.

[59] H. J. Choi, D. Roundy, H. Sun, M. L. Cohen, and S. G. Louie. The origin of the anomalous superconducting properties of MgB_2. *Nature*, 418(6899):758–60, 2002.

[60] E. A. Young and Y. Yang. Preparation and Properties of Using $Mg(B_{1-x}C_x)_2$ Carbon Chemical Vapor Coated Boron. *Applied Superconductivity*, 17(2):2794–2797, 2007.

[61] S. Soltanian, J. Horvat, X. L. Wang, P. Munroe, and S. X. Dou. Effect of nanocarbon particle doping on the flux pinning properties of MgB_2 superconductor. *Physica C*, 390(3):185–190, 2003.

[62] J. H. Kim and S. Choi. Carbon doping induced imperfections on MgB_2 superconducting wire. *Journal of Analytical Science and Technology*, 6(1):0–4, 2015.

[63] M. A. Susner, S. D. Bohnenstiehl, S. A. Dregia, M. D. Sumption, Y. Yang, J. J. Donovan, and E. W. Collings. Homogeneous carbon doping of magnesium diboride by high-temperature, high-pressure synthesis. *Applied Physics Letters*, 104(16), 2014.

[64] M. E. Jones and R. E. Marsh. The preparation and structure of magnesium boride, MgB_2. *Journal of the American Chemical Society*, 76(1936):1434–1436, 1953.

[65] C. Buzea and T. Yamashita. Review of the superconducting properties of MgB_2. *Superconductor Science and Technology*, 14(11):R115–R146, Nov 2001.

[66] M. Cyrot and D. Pavuna. *Introduction to Superconductivity and High-T_c Materials*. 1992.

[67] C. P. Slichter. Magnetic Resonance and Superconductivity: Some History, Ancient and in the Making. *Journal of Superconductivity and Novel Magnetism*, 19(3-5):159–166, 2006.

[68] M. Tinkham. *Introduction to Superconductivity: Second Edition*. Dover Publications, 2004.

[69] W. Meissner and R. Ochsenfeld. Ein neuer Effekt bei Eintritt der Supraleitfähigkeit. *Naturwissenschaften*, 21(44):787–788, 1933.

[70] D. S. Ginley, G. Crabtree, W. K. Kwok, D. Lopez, U. Welp, E. H. Brandt, and P. H. Kes. Chapter Four. In *Handbook Superconducting Materials*, Handbook of Superconducting Materials, pages 171–205. Taylor and Francis, dec 2002.

[71] H. Safar, P. L. Gammel, D. A. Huse, D. J. Bishop, M. Hill, and J. P. Rice. Evidence for a First-Order Vortex-Lattice-Melting. *Physical Review Letters*, 69(5), 1992.

[72] M. S. Fuhrer, K. Cherrey, A. Zettl, M. L. Cohen, and V. H. Crespi. Carbon isotope effect in single-crystal Rb_3C_{60}. *Physical Review Letters*, 83(2):11–14, 1999.

[73] B. Burk, Vincent H. Crespi, A. Zettl, and Marvin L. Cohen. Rubidium isotope effect in superconducting Rb_3C_{60}. *Physical Review Letters*, 72(23):3706–3709, 1994.

[74] T. W. Ebbesen, J. S. Tsai, K. Tanigaki, H. Hiura, Y. Shimakawa, Y. Kubo, I. Hirosawa, and J. Mizuki. Dopant isotope effect on superconductivity in Rb_3C_{60}. *Physica C*, 203(1-2):163–166, dec 1992.

[75] A. S. Alexandrov. *Theory of Superconductivity: From Weak to Strong Coupling*. CRC Press, 2003.

[76] A. F. Hebard, M. J. Rosseinsky, R. C. Haddon, D. W. Murphy, S. H. Glarum, T. Palstra, A. P. Ramirez, and A. R. Kortan. Superconductivity at 18 K in potassium-doped C_{60}. *Nature*, 350:600–601, 1991.

[77] S. P. Kelty, C. C. Chen, and C. M. Lieber. Superconductivity at 30 K in caesium-doped C_{60}. *Nature*, 352(6332):223–225, 1991.

[78] T. T M. Palstra, O. Zhou, Y. Iwasa, P. E. Sulewski, R. M. Fleming, and B. R. Zegarski. Superconductivity at 40K in cesium doped C_{60}. *Solid State Communications*, 93(4):327–330, 1995.

[79] M. J. Rosseinsky, A. P. Ramirez, S. H. Glarum, D. W. Murphy, R. C. Haddon, A. F. Hebard, T. T. M. Palstra, A. R. Kortan, S. M. Zahurak, and A. V. Makhija. Superconductivity at 28 K in Rb_xC_{60}. *Physical Review Letters*, 66(21):2830–2832, may 1991.

[80] M. J. Rosseinsky. Recent developments in the chemistry and physics of metal fullerides. *Chemical Materials*, 10:2665–2685, 1998.

[81] R. Tycko, G. Dabbagh, and M. J. Rosseinsky. Electronic properties of normal and superconducting alkali fullerides probed by C^{13} nuclear magnetic resonance. *Physical Review*, 68(12):1912–1915, 1992.

[82] T. W. Ebbesen, J. S. Tsai, and K. Tanigaki. Isotope effect on superconductivity in Rb_3C_{60}. *Nature*, 255:620–622, 1992.

[83] A. P. Ramirez and A. R. Kortan. Isotope effect in superconducting Rb_3C_{60}. *Physical Review*, 68:1058–1060, 1992.

[84] R. Tycko, G. Dabbagh, D. W. Murphy, Q. Zhu, and J. E. Fischer. Electronic properties and phase transitions of RbC_{60} and CsC_{60}: Investigation by NMR spectroscopy. *Physical Review B*, 48(12):9097–9105, 1993.

[85] K. Tanigaki and K. Prassides. Conducting and superconducting properties of alkali-metal C_{60} fullerides. *Journal of Materials Chemistry*, 5:1515, 1995.

[86] C. Pennington, C. Hahm, V. Stenger, K. Gorny, C. Recchia, J. Martindale, D. Buffinger, and R. Ziebarth. Double-resonance NMR probes of structural distortions in alkali-metal-fulleride superconductors. *Physical Review B*, 54(10):R6853–R6856, 1996.

[87] D. Jung, J. Ren, and M. H. Whangbo. Structural and electronic factors influencing the superconductivity in alkali-metal-doped superconductors A_3C_{60}. *Synthetic Metals*, 78:7–10, 1996.

[88] M. Kanowski, H. Werner, and R. Schlögl. ^{87}Rb NMR investigations on binary and ternary fullerene compounds: Rb_3C_{60}, K_2RbC_{60} and Rb_2CsC_{60}. *Applied Magnetism*, 11:285–292, 1996.

[89] G. Zimmer, M. Mehring, F. Rachdi, and J. E. Fischer. Vortex dynamics in Rb_3C_{60} observed by Rb and C NMR. *Physical Review B*, 54(6):3768–3771, 1996.

[90] G. Zimmer, K. F. Thier, M. Mehring, and F. Rachdi. NMR on alkali fullerides. *Applied Magnetic Resonance*, 11:263–283, 1996.

[91] W. MacFarlane, R. Kiefl, S. Dunsiger, J. Sonier, J. Chakhalian, J. Fischer, T. Yildirim, and K. Chow. Muon-spin-relaxation studies of the alkali-fulleride superconductors. *Physical Review B*, 58(2):1004–1024, 1998.

[92] P. Klupp, G.and Matus, K. Kamarás, A. Y. Ganin, A. McLennan, M. J. Rosseinsky, Y. Takabayashi, M. T. McDonald, and K. Prassides. Dynamic Jahn–Teller effect in the parent insulating state of the molecular superconductor Cs_3C_{60}. *Nature Communications*, 3:912, 2012.

[93] Y. Nomura, K. Nakamura, and R. Arita. Ab-initio derivation of electronic low-energy models for C_{60} and aromatic compounds. *Physical Review B*, 85(15):1–12, 2012.

[94] Y. Nomura and R. Arita. Ab-initio downfolding for electron-phonon-coupled systems: Constrained density-functional perturbation theory. *Physical Review B*, 92(24):1–15, 2015.

[95] J. Robert, P. Petit, T. Yildirim, and J. E. Fischer. Experimental lattice dependence of the density of states in alkali fullerides. *Physical Review B*, 57(2):1226–1230, 1998.

[96] J. Winter and H. Kuzmany. Landau damping and lifting of vibrational degeneracy in metallic potassium fulleride. *Physical Review B*, 53(2):655–661, 1996.

[97] D. S. Bethune, G. Meijer, W. C. Tang, H. J. Rosen, W. G. Golden, H. Seki, C. A. Brown, and M. S. de Vries. Vibrational Raman and infrared spectra of chromatographically separated C_{60} and C_{70} fullerene clusters. *Chemical Physics Letters*, 179(1-2):181–186, 1991.

[98] M. Schluter, M. Lannoo, M. Needels, G. A. Baraff, and D. Tomnek. Electron-phonon coupling and superconductivity in alkali-intercalated C_{60} solid. *Physical Review Letters*, 68(4):526–529, Jan 1992.

[99] I. I. Mazin, S. N. Rashkeev, V. P. Antropov, O. Jepsen, A. I. Liechtenstein, and O. K. Andersen. Quantitative theory of superconductivity in doped C_{60}. *Physical Review B*, 45(9):5114, 1992.

[100] V. A. Stenger. NMR Studies of Alkali C_{60} Superconductors. *Journal of Superconductivity*, 7(6):1–6, 1994.

[101] R. H. Zadik, Y. Takabayashi, G. Klupp, R. H. Colman, A. Y. Ganin, A. Potočnik, P. Jeglič, D. Arčon, P. Matus, K. Kamarás, Y. Kasahara, Y. Iwasa, A. N. Fitch, Y. Ohishi, G. Garbarino, K. Kato, M. J. Rosseinsky, and K. Prassides. Optimized unconventional superconductivity in a molecular Jahn-Teller metal. *Science Advances*, 1(3), 2015.

[102] G. Sparn, J. D. Thompson, R. L. Whetten, S. M. Huang, R. B. Kaner, F. Diederich, G. Grüner, and K. Holczer. Pressure and Field-Dependence of Superconductivity in Rb_3C_{60}. *Physical Review Letters*, 68(18):1228–1231, 1992.

[103] J. E. Schirber, D. L. Overmyer, H. H. Wang, J. M. Williams, K. D. Carlson, A. M. Kini, U. Welp, and W. K. Kwok. Pressure dependence of the superconducting transition temperature of potassium fullerene, K_xC_{60}. *Physica C*, 178(1-3):137–139, 1991.

[104] G. Sparn, J. D. Thompson, S. M. Huang, R. B. Kaner, F. Diederich, R. L. Whetten, G. Grüner, and K. Holczer. Pressure Dependence of Superconductivity in Single-Phase K_3C_{60}. *Science*, 252(5014):1829–31, 1991.

[105] M. Capone, M. Fabrizio, C. Castellani, and E. Tosatti. Strongly Correlated Superconductivity. *Science*, 296(June), 2002.

[106] R. W. Lof, M. A. van Veenendaal, B. Koopmans, H. T. Jonkman, and G. A. Sawatzky. Band Gap, Excitons, and Coulomb Interaction in Solid C_{60}. *Physical Review Letters*, 68(26):3924–3927, 1992.

[107] M Fabrizio and E Tosatti. Nonmagnetic molecular Jahn-Teller Mott insulators. *Physical Review B*, 55(20):13465–13472, 1997.

[108] S. Chakravarty, M. P. Gelfand, and S. Kivelson. Electronic correlation-effects and superconductivity in doped fullerenes. *Science*, 254(5034):970–974, 1991.

[109] Y. Takada. Consideration of the mechanism of superconductivity in fullerenes: Beyond Migdal's theorem and the dynamic Coulomb effect. *Journal Physical Chemistry of Solids*, 54(12):1779–1788, 1993.

[110] J. E. Han, O. Gunnarsson, and V. H. Crespi. Strong Superconductivity with local Jahn-Teller Phonons in C_{60} Solids. *Physical Review Letters*, 90(16):167006, 2003.

[111] M. Capone, M. Fabrizio, and E. Tosatti. Direct transition between a singlet Mott insulator and a superconductor. *Physical Review Letters*, 86(23):5361–5364, 2001.

[112] Y.J. Uemura, L.P. Le, and G.M. Luke. Muon spin relaxation studies in organic superconductors and organic magnets. *Synthetic Metals*, 56(2-3):2845–2852, apr 1993.

[113] A. M. Neminsky, D. V. Shovkun, and O. T. Vyaselev. AC susceptibility of Rb_3C_{60} fine powder. *Physical Review B*, 54(1):454–461, 1996.

[114] I. I. Mazin and V. P. Antropov. Electronic structure , electron–phonon coupling and multiband effects in MgB_2. *Physica C*, 385:49–65, 2003.

[115] H. Kohno, K. Miyake, and H. Harima. An electronic mechanism for superconductivity in MgB_2. *Physica B: Condensed Matter*, 312-313:148–149, 2002.

[116] H. J. Choi, D. Roundy, H. Sun, M. L. Cohen, and S. G. Louie. First-principles calculation of the superconducting transition in MgB_2 within the anisotropic Eliashberg formalism. *Physical Review B*, 66(2):020513, 2002.

[117] Amy Y. Liu, I. I. Mazin, and J. Kortus. Beyond Eliashberg Superconductivity in MgB_2: Anharmonicity, Two-Phonon Scattering, and Multiple Gaps. *Physical Review Letters*, 87(8):087005, 2001.

[118] J. Kortus, I. Mazin, K. D. Belashchenko, V. P. Antropov, and L. Boyer. Superconductivity of Metallic Boron in MgB_2. pages 1–4, 2001.

[119] J. An and W. Pickett. Superconductivity of MgB_2: Covalent Bonds Driven Metallic. *Physical Review Letters*, 86(19):4366–4369, may 2001.

[120] F. Bouquet, R. A. Fisher, N. E. Phillips, D. G. Hinks, and J. D. Jorgensen. Specific Heat of $Mg^{11}B_2$: Evidence for Second Energy Gap. *Physical Review Letters*, 87(4), 2001.

[121] X. K. Chen, M. J. Konstantinovic, J. C. Irwin, D. D. Lawrie, and J. P. Franck. Evidence for two superconducting gaps in MgB_2. *Physical Review Letters*, 87(15):157002, 2001.

[122] S. Tsuda, T. Yokoya, T. Kiss, Y. Takano, K. Togano, H. Kito, H. Ihara, and S. Shin. Evidence for a Multiple Superconducting Gap in MgB_2 from High-Resolution Photoemission Spectroscopy. *Physical Review Letters*, 87(17):177006, 2001.

[123] P. Szabó, P. Samuely, J. Kačmarčík, T. Klein, J. Marcus, D. Fruchart, S. Miraglia, C. Marcenat, and A. G. M. Jansen. Evidence for Two Superconducting Energy Gaps in MgB_2 by Point-Contact Spectroscopy. *Physical Review Letters*, 87(13):137005, 2001.

[124] F. Giubileo, D. Roditchev, W. Sacks, R. Lamy, D. X. Thanh, J. Klein, S. Miraglia, D. Fruchart, J. Marcus, and P. Monod. Two-Gap State Density in MgB_2: A True Bulk Property Or A Proximity Effect? *Physical Review Letters*, 87(17):177008, 2001.

[125] H. Kotegawa, K. Ishida, Y. Kitaoka, T. Muranaka, and J. Akimitsu. Evidence for Strong-Coupling s-Wave Superconductivity in MgB_2: B^{11} NMR Study. *Physical Review Letters*, 87(12):127001, 2001.

[126] H. Kotegawa, K. Ishida, Y. Kitaoka, T. Muranaka, N. Nakagawa, H. Takagiwa, and J. Akimitsu. Evidence for high-frequency phonon mediated S-wave superconductivity: ^{11}B NMR study of Al-doped MgB_2. *Physical Review B*, 66(6):064516, 2002.

[127] C. H. Cheng and C. Sorrell. Defect control at nanoscale andx flux pinning enhancement in MgB_2 superconductor. *Journal of Modern Transportation*, 20(2):65–69, 2012.

[128] T. M. Silver, J. Horvat, M. Reinhard, Yao P., S. Keshavarzi, P. Munroe, and S. X. Dou. Uranium doping and thermal neutron irradiation flux pinning effects in mgb_2. *IEEE Transactions on Applied Superconductivity*, 14(1):33–39, 2004.

[129] Y. Bugoslavsky, G. K. Perkins, X. Qi, L. F. Cohen, and A. D. Caplin. Vortex dynamics in superconducting MgB_2 and prospects for applications. *Nature*, 410:563–565, 2001.

[130] M. Mudgel, V. P. S. Awana, H. Kishan, and G. L. Bhalla. Significant improvement of flux pinning and irreversibility field in nano-carbon-doped MgB_2 superconductor. *Solid State Communications*, 146(7-8):330–334, 2008.

[131] J. H. Kim, S. Oh, Y. U. Heo, S. Hata, H. Kumakura, A. Matsumoto, M. Mitsuhara, S. Choi, Y. Shimada, M. Maeda, J. L. MacManus-Driscoll, and S. X. Dou. Microscopic role of carbon on MgB_2 wire for critical current density comparable to NbTi. *NPG Asia Materials*, 4(1):3, 2012.

[132] Malcom H Levitt. *Spin Dynamics: Basics of Nuclear Magnetic Resonance*. John Wiley and Sons, 2011.

[133] K. J. D. MacKenzie and M. E. Smith. *Multinuclear solid-state NMR of inorganic materials*. Pergamon, Oxford; New York, 2002.

[134] R. Bhattacharyya, B. Key, H. Chen, A. S. Best, A. F. Hollenkamp, and C. P. Grey. In-situ NMR observation of the formation of metallic lithium microstructures in lithium batteries. *Nature Materials*, 9(6):504–510, 2010.

[135] S. Deguchi, S. Mukai, M. Tsudome, and K. Horikoshi. Facile generation of fullerene nanoparticles by hand-grinding. *Advanced Materials*, 18(6):729–732, 2006.

[136] H. Tanaka, A. Yamamoto, J. I. Shimoyama, H. Ogino, and K. Kishio. Strongly connected ex situ MgB_2 polycrystalline bulks fabricated by solid-state self-sintering. *Superconductor Science and Technology*, 25(11):115022, 2012.

[137] P. Beckett, M. S. Denning, I. Heinmaa, M. C. Dimri, E. A. Young, R. Stern, and M. Carravetta. High resolution ^{11}B NMR of magnesium diboride using cryogenic magic angle spinning. *Journal of Chemical Physics*, 137(11):114201, 2012.

[138] C. P. Slichter. *Principles of Magnetic Resonance*, volume 28. John Wiley and Sons, Ltd., 1990.

[139] K. Matano, Z. A. Ren, X. L. Dong, L. L. Sun, Z. X. Zhao, and G Zheng. Spin-singlet superconductivity with multiple gaps in $PrFeAsO_{0.89}$ $F_{0.11}$. *EPL (Europhysics Letters)*, 83(5):57001, 2008.

[140] K. Ishida, H. Mukuda, Y. Kitaoka, K. Asayama, Z. Q. Mao, Y. Mori, and Y. Maeno. Spin-triplet superconductivity in Sr_2RuO_4 identified by ^{17}O Knight shift. *Nature*, 396(6712):658–660, 1998.

[141] K. Yosida. Paramagnetic susceptibility in superconductors [3]. *Physical Review*, 110(3):769–770, 1958.

[142] S. Oh, A. Mounce, J. Lee, and W. Halperin. Spin pairing and penetration depth measurements from nuclear magnetic resonance in $NaFe_{0.975}Co_{0.025}As$. *Physical Review B*, 87:2–6, 2013.

[143] B. Muhlschlegel. Die thermodynamischen Funktionen des Supraleiters. *Zeitschrift fur Physik*, 155(3):313–327, 1959.

[144] D. F. Smith and C. P. Slichter. The Study of Mechanisms of Superconductivity by NMR Relaxation. *Lecture Notes on Physics*, 684:243–295, 2006.

[145] J. Korringa. Nuclear magnetic relaxation and resonnance line shift in metals. *Physica*, 16(7–8):601–610, 1950.

[146] T. Shiroka, M. Pikulski, N. D. Zhigadlo, B. Batlogg, J. Mesot, and H. R. Ott. Pairing of weakly correlated electrons in the platinum-based centrosymmetric superconductor $SrPt_3P$. *Physical Review B*, 91(24):245143, 2015.

[147] E. Pavarini and I. I. Mazin. NMR relaxation rates and Knight shifts in MgB_2. *Physical Review B*, 64(14):140504, 2001.

[148] S. Serventi, G. Allodi, C. Bucci, R. De Renzi, G. Guidi, E. Pavarini, P. Manfrinetti, and A. Palenzona. NMR determination of the partial density of states and of the electronic correlation in $Mg_{1-x}Al_xB_2$. *Physical Review B*, 67(13):2–5, 2003.

[149] V. A. Stenger, C. H. Pennington, D. R. Buffinger, and R. P. Ziebarth. Nuclear Magnetic Resonance of A_3C_{60} Superconductors. 74(9):1649–1652, 1995.

[150] D. E. MacLaughlin. Magnetic Resonance in the Superconducting State. *Solid State Physics*, 31:1–69, 1976.

[151] A. P. Reyes, X. P. Tang, and H. N. Bachman. Vortex melting in polycrystalline $YBa_2Cu_3O_7$ from O ^{17} NMR. *Physical Review B*, 55(22):737–740, 1997.

[152] P. Pincus, A.C. Gossard, V. Jaccarino, and J.H. Wernick. NMR measurements of the flux distribution in type II superconductors. *Physical Review Letters*, 13(1):21–22, nov 1964.

[153] G. Zimmer, M. Mehring, F. Rachdi, and J. E. Fischer. ^{87}Rb NMR and the T" problem in Rb_3C_{60}. *Physical Review B*, 53(9):5620–5625, 1996.

[154] R. E. Walstedt, D. W. Murphy, and M. Rosseinsky. Structural Distortion in Rb_3C_{60} Revealed By ^{87}Rb NMR. *Nature*, 362(6421):611–613, 1993.

[155] G. Zimmer, M. Helmle, and M. Mehring. Analysis of ^{87}Rb and ^{13}C Hyperfine Interaction in Rb_3C_{60}. *Europhysics letters*, 24:59–64, 1993.

[156] M. Kraus, O. Klein, G. Buntkowsky, and K. Lüders. New aspects in the interpretation of the T" and T NMR lines in Rb_3C_{60}. *Physical Review B*, 271:7–14, 1999.

[157] M. Kanowski, H. Werner, R. Schlögl, H. M. Vieth, and K. Lüders. ^{13}C MAS NMR investigations of alkali doped C_{60}. *Applied Magnetic Resonance*, 8:173–180, 1995.

[158] M. Carravetta, A. Danquigny, S. Mamone, F. Cuda, O. G. Johannessen, I. Heinmaa, K. Panesar, R. Stern, M. C Grossel, A. J. Horsewill, A. Samoson, M. Murata, Y. Murata, K. Komatsu, and M. H. Levitt. Solid-state NMR of endohedral hydrogen-fullerene complexes. *Physical chemistry chemical physics : PCCP*, 9(35):4879–4894, 2007.

[159] D. W. Murphy, M. J. Rosseinsky, R. M. Fleming, R. Tycko, A. P. Ramirez, R. C. Haddon, T. Siegrist, G. Dabbagh, J. C. Tully, and R E Walstedt. Synthesis and Characterisation of Alkali Metal Fullerides: A_xC_{60}. *Journal of Physical Chemistry Solids*, 53(11):1321–1332, 2012.

[160] J. Reichenbach, F. Rachdi, I. Luk'yanchuk, M. Ribet, G. Zimmer, and M. Mehring. High-resolution ^{13}C nuclear magnetic resonance in alkali intercalated fullerene C_{60}. *Journal of Chemical Physics*, 101(1994):4585, 1994.

[161] V. P. Antropov, I. I. Mazin, O. K. Andersen, A. I. Liechtenstein, and O. Jepsen. Dominance of the spin-dipolar NMR relaxation mechanism in fullerene superconductors. *Physical Review B*, 47(12):373–376, 1993.

[162] C. H. Pennington, V. A. Stenger, C. H. Recchia, C. Hahm, K. Gorny, V. Nandor, D. R. Buffinger, S. M. Lee, and R. P. Ziebarth. ^{13}C NMR hyperfine couplings, T_1 anisotropy, and Korringa relations in Rb_2CsC_{60}. *Physical Review B*, 53(6):2967–2970, 1996.

[163] F. Tabak and M. Corti. ^{87}Rb NMR relaxation and vortex dynamics in Rb3C60. *Turkish Journal of Physics*, 24:587–592, 2000.

[164] R. F. Kiefl, W. A. MacFarlane, K. H. Chow, S. Dunsiger, T. L. Duty, T. M. S. Johnston, J. W. Schneider, J. Sonier, L. Brard, R. M. Strongin, J. E. Fischer,

and A. B. Smith. Coherence peak and superconducting energy gap in rb_3c_{60} observed by muon spin relaxation. *Physical Review Letters*, 70:3987–3990, 1993.

[165] S. Sasaki, A. Matsuda, and C. W. Chu. Fermi-liquid behavior and BCS s-wave pairing of K_3C_{60} observed by ^{13}C NMR. *Journal of the Physical Society of Japan*, 63(5):1670–1673, 1994.

[166] V. A. Stenger and C. H. Pennington. Nuclear Magnetic Resonance of A_3C_{60} Superconductors. *Physical Review Letters*, 74(9):1649–1652, 1995.

[167] M. Riccò, L. Menozzi, R. De Renzi, and F. Bolzoni. Korringa relation and Hebel–Slichter peak in ammonia intercalated fullerides by NMR. *Physica C*, 306:136–142, 1998.

[168] P. B. Allen and D. Rainer. Phonon Suppression of Coherence Peak in Nuclear-Spin Relaxation Rate of Superconductors. *Nature*, 349(6308):396–398, 1991.

[169] T. Yamaji, M. Murakami, J. Fukazawa, T. Shimizu, and K. Takegoshi. Analysis of ^{11}B NMR Powder Lineshape of MgB_2 in the Normal Conductive Phase. *Journal of the Physical Society of Japan*, 77(4):044711, apr 2008.

[170] S. Strässle, J. Roos, M. Mali, H. Keller, and J. Karpinski. ^{11}B NMR study of single-crystal MgB_2 in the normal conducting phase. *Physica C*, 466(1-2):168–173, 2007.

[171] J. Jung, S. Baek, F. Borsa, S. Bud'ko, G. Lapertot, and P. Canfield. ^{11}B NMR and relaxation in the MgB_2 superconductor. *Physical Review B*, 64(1):012514, 2001.

[172] E. Pavarini and I. I. Mazin. First-principles study of spin-orbit effects and NMR in Sr_2RuO_4. *Physical Review B*, 74(3):1–11, 2006.

[173] B. Chen, P. Sengupta, W. P. Halperin, E. E. Sigmund, V. F. Mitrović, M. H. Lee, K. H. Kang, B. J. Mean, J. Y. Kim, and B. K. Cho. Anisotropy and penetration depth of MgB_2 from ^{11}B NMR. *New Journal of Physics*, 8(11):274–274, nov 2006.

[174] M. Karayanni, G. Papavassiliou, M. Pissas, M. Fardis, K. Papagelis, K. Prassides, T. Takenobu, and Y. Iwasa. ^{11}B NMR Study of Pure and Lightly Carbon-Doped MgB_2 Superconductors. *Journal of Superconductivity*, 18(4):521–528, 2005.

[175] M. Pissas, G. Papavassiliou, M. Karayanni, M. Fardis, I. Maurin, I. Margiolaki, K. Prassides, and C. Christides. Magnetization and ^{11}B NMR study of $Mg_{1-x}Al_xB_2$ superconductors. *Physical Review B*, 65(18):184514, apr 2002.

[176] M. Mali, J. Roos, A. Shengelaya, H. Keller, and K. Conder. ^{25}Mg NMR study of the MgB_2 superconductor. *Physical Review B*, 65(10):100518, 2002.

[177] A. P. Gerashenko and K. N. Mikhalev. Electronic states of boron in superconducting MgB_2 studied by ^{11}B NMR. *Applied Magnetism*, 163:157–163, 2001.

[178] S. Serventi, G. Allodi, C. Bucci, R. D. Renzi, G. Guidi, E. Pavarini, P. Manfrinetti, and A. Palenzona. NMR relaxation rates and Knight shifts in the alloy $Mg_{1-x}Al_xB_2$. *Superconductor Science and Technology*, 16(2):152, 2003.

[179] A. Rigamonti, F. Borsa, and P. Carretta. Basic aspects and main results of NMR-NQR spectroscopies in high-temperature superconductors. *Reports of Progress in Physics*, 61:1367–1439, 1998.

[180] H. Kotegawa. Evidence for strong-coupling s-wave superconductivity and the related materials. *Science and Technology*, 381:25–32, 2002.

[181] E. L. Hahn. Spin echoes. *Physical Review*, 80(4):580–594, 1950.

[182] J. D. van Beek. matNMR: A flexible toolbox for processing, analyzing and visualizing magnetic resonance data in Matlab. *Journal of Magnetic Resonance*, 187(1):19–26, 2007.

[183] V. Brouet, H. Alloul, S. Garaj, and L. Forro. Gaps and excitations in fullerides with partially filled bands : NMR study of Na_2C_{60} and K_4C_{60}. page 12, 2002.

[184] K. Holczer, O. Klein, H. Alloul, Y. Yoshinari, and F. Hippert. Non-Korringa ^{13}C nuclear relaxation in the normal state of K_3C_{60} superconductor. *Europhys. Lett.*, 23:63, 1993.

[185] A. Y. Ganin, Y. Takabayashi, P. Jeglič, D. Arčon, A. Potočnik, P. J. Baker, Y. Ohishi, M. T. McDonald, M. D. Tzirakis, A. McLennan, G. R. Darling, M. Takata, M. J. Rosseinsky, and K. Prassides. Polymorphism control of superconductivity and magnetism in Cs_3C_{60} close to the Mott transition. *Nature*, 466(7303):221–225, 2010.

[186] R. Jenkins and Robert L. Snyder. Diffraction Theory. In *Introd. to X-ray Powder Diffractometry*, pages 47–95. John Wiley and Sons, Inc., 1996.

[187] H. M. Rietveld. A profile refinement method for nuclear and magnetic structures. *Journal of Applied Crystallography*, 2(2):65–71, 1969.

[188] A.C. Larson, R.B. Von Dreele, and B. H. Toby. General Structure Analysis System - GSAS / EXPGUI, A Graphical user interface for GSAS. *Journal of Applied Crystallography*, 748(1994):2001, 2001.

[189] D. R. Buffinger and R. P. Ziebarth. Rapid and efficient synthesis of alkali metal-C_{60} compounds in liquid ammonia. *Journal of the American Chemical Society*, 115:9267–9270, 1993.

[190] J. B. Howard, J. T. Mckinnon, Y. Makarovsky, and A. L. Lafleur. Production of C_{60} and C_{70} Fullerenes in Benzene-Oxygen Flames. *Journal of Physical Chemistry*, 96:6657–6662, 1992.

[191] K. Holczer, O. Klein, S. Huang, and R. Kaner. Alkali-fulleride superconductors: synthesis, composition, and diamagnetic shielding. *Science*, 252(5009):1154–1157, 1991.

[192] M. J. Rosseinsky, A. P. Ramirez, S. H. Glarum, D. W. Murphy, R. C. Haddon, A. F. Hebard, T. T. M. Palstra, A. R. Kortan, S. M. Zahurak, and A. V. Makhija. Superconductivity at 28 K in Rb_xC_{60}. *Physical Review Letters*, 66(21):2830–2832, 1991.

[193] R. C. Haddon. Electronic structure, conductivity and superconductivity of alkali metal doped C_{60}. *Pure and Applied Chemistry*, 65(13):11–15, 1993.

[194] J. P. McCauley, Q. Zhu, and N. Coustel. Synthesis, structure, and superconducting properties of single-phase Rb_3C_{60}. A new, convenient method for the preparation of M_3C_{60} superconductors. *Journal of the American Chemical Society*, 113(8):8537–8538, 1991.

[195] X. Liu, W. C. Wan, S. M. Owens, and W. E. Broderick. Superconducting Alkali Metal Fullerides: Development of a Versatile Solution-Phase Route from Soluble M_3C_{60} Precursors. *Journal of the American Chemical Society*, 116:5489–5490, 1994.

[196] C. R. Morcombe and K. W. Zilm. Chemical shift referencing in MAS solid state NMR. *Journal of Magnetic Resonance*, 162(2):479–486, 2003.

[197] M. Concistrè, S. Mamone, M. Denning, G. Pileio, X. Lei, Y. Li, M. Carravetta, N. J. Turro, and M. H. Levitt. Anisotropic nuclear spin interactions in $H_2O@C_{60}$ determined by solid-state NMR. *Philosophical Transactions of the Royal Society A*, 371(1998):20120102, 2013.

[198] M. Carravetta, A. Danquigny, S. Mamone, F. Cuda, O. G. Johannessen, I. Heinmaa, K. Panesar, R. Stern, M. C. Grossel, A. J. Horsewill, A. Samoson, M. Murata, Y. Murata, K. Komatsu, and M. H. Levitt. Solid-state NMR of endohedral hydrogen-fullerene complexes. *Physical Chemistry Chemical Physics*, 9(35):4879–4894, 2007.

[199] M. J. Duer. *Solid-state NMR spectroscopy. Principles and applications.*, volume 1. John Wiley and Sons, Ltd., 2002.

[200] G. Maroulis. Tuning the conductance of $H_2O@C_{60}$ by position of the encapsulated H_2O. *Journal Chemical Physics*, 94(2):1182–1190, 1991.

[201] L. H. Bennett, R. E. Watson, and G. C. Carter. Relevance of knight shift measurements to the electronic density of states. *Journal of Research of the National Bureau of Standards*, 74A(4):569, 1970.

[202] R. M. Fleming, M. J. Rosseinsky, A. P. Ramirez, D. W. Murphy, J. C. Tully, R. C. Haddon, T. Siegrist, R. Tycko, S. H. Glarum, P. Marsh, G. Dabbagh, S. M. Zahurak, A. V. Makhija, and C. Hampton. Preparation and structure of the alkali-metal fulleride, A_4C_{60}. *Nature*, 353(6347):868, 1991.

[203] S. Chu and M. E. Mchenry. Synthesis and superconducting properties of a Rb_3C_{60} single crystal. *Physical Review B*, 55(17):722–729, 1997.

[204] H. He, J. Teixeira Dias, J. Foulkes, and J. Klinowski. ^{13}C solid-state MAS NMR studies of the low temperature phase transition in fullerene C_{60}. *Physical Chemistry Chemical Physics*, 2(13):2651–2654, 2000.

[205] M. Carravetta, O. G. Johannessen, M. H. Levitt, I. Heinmaa, R. Stern, A. Samoson, A. J. Horsewill, Y. Murata, and K. Komatsu. Cryogenic NMR spectroscopy of endohedral hydrogen-fullerene complexes. *Journal of Chemical Physics*, 124(10):1–13, 2006.

[206] A. M. Neminsky, P. N. Nikolaev, D. V. Shovkun, E. E. Laukhina, and E. B. Yagubskii. Temperature Dependence of the Magnetic Field Penetration Depth in Rb_3C_{60} Measured by ac Susceptibility. *Physical Review Letters*, 72(19):0–3, 1994.

[207] B. J. Suh, X. Zong, Y. Singh, A. Niazi, and D. C. Johnston. ^{11}B NMR in the layered diborides OsB_2 and RuB_2. *Physical Review B*, 76(14):1–4, 2007.

[208] C. S. Lue, Y. F. Tao, and T. H. Su. Comparative NMR investigation of the Re-based borides. *Physical Review B*, 78(3):9–12, 2008.

[209] Y. Li, J. Chen, and X. Lei. Comparison of nuclear spin relaxation of H_2O@ C_{60} and H_2@ C_{60} and their nitroxide derivatives. *Journal of Chemical Physics*, 3:1165–1168, 2012.

[210] G. Maroulis. Tuning the conductance of $H_2O@C_{60}$ by position of the encapsulated H_2O. *Journal of Chemical Physical*, 94(2):1182–1190, 1991.

[211] H. Kotegawa, M. Yogi, Y. Imamura, Y. Kawasaki, G. Zheng, S. Kitaoka, Y .and Ohsaki, H. Sugawara, Y. Aoki, and H. Sato. Evidence for Unconventional Strong-Coupling Superconductivity in $PrOs_4Sb_{12}$: An Sb Nuclear Quadrupole Resonance Study. *Physical Review Letters*, 90(2):27001, 2003.

[212] A. J. Millis, D. Pines, and H. Monien. Phenomenological model of nuclear relaxation in the normal state of $YBa_2Cu_3O_7$. *Physical Review B*, 42(1):167, 1990.

[213] R E Walstedt, B S Shastry, and Murray Hill. NMR, Neutron Scattering, and the One-Band Model of $La_{2-x}Sr_xCuO_4$. *Physical Review Letters*, 72(22):0–3, 1994.

[214] E. Sartori, M. Ruzzi, N. J. Turro, J. D. Decatur, D. C. Doetschman, R. G. Lawler, A. L. Buchachenko, Y. Murata, and K. Komatsu. Nuclear Relaxation of H_2 and $H_2@C_{60}$ in Organic Solvents. *Journal American Chemical Society*, 128(46):14752–14753, 2006.

[215] I. Oppenheim and M. Bloom. Nuclear Spin Relaxation in Gases and Liquids: I. Correlation functions. *Canadian Journal Physics*, 42(1):70–83, oct 1964.

[216] K. H. Bennemann and J. Ketterson. *Superconductivity: Conventional and Unconventional Superconductors*, volume 1. Springer-Verlag Berlin Heidelberg, 2008.

[217] J. Y. C. Chen, A. A. Martí, N. J. Turro, K. Komatsu, Y. Murata, and R. G. Lawler. Comparative NMR properties of H_2 and HD in toluene-d8 and in H_2/HD@C_{60}. *Journal of Physical Chemistry B*, 114(45):14689–14695, 2010.

[218] G. Seyfarth, J. P. Brison, M. A. Méasson, J. Flouquet, K. Izawa, Y. Matsuda, H. Sugawara, and H. Sato. Multiband superconductivity in the heavy fermion compound $PrOs_4Sb_{12}$. *Physical Review Letters*, 95(10), 2005.

[219] D. Kölbl, D. M. Zumbühl, A. Fuhrer, G. Salis, and S. F. Alvarado. Breakdown of the Korringa Law of Nuclear Spin Relaxation in Metallic GaAs. *Physical Review Letters*, 109(8):86601, 2012.

[220] L. Degiorgi, P. Wachter, G. Gruner, S. M. Huang, J. Wiley, and R. B Kaner. Optical Response of the Superconducting State of K_3C_{60} and Rb_3C_{60}. *Physical Review Letters*, 69(16):2987–2990, 1992.

[221] Z. Zhang, C. Chen, S. P. Kelty, H. Dai, and C. M. Lieber. The superconducting energy gap of Rb_3C_{60}. *Nature*, 353(6342):333–335, 1991.

[222] S. A. Fitzgerald, S. G. Kaplan, A. Rosenberg, A. J. Sievers, and R. A. S. McMordie. Far-infrared transmission of superconducting K_3C_{60} films. *Physical Review B*, 45(17):10165–10168, may 1992.

[223] K. Sattler. *Handbook of Nanophysics: Functional Nanomaterials*. CRC Press, 2010.

[224] D. Varshney, R. Jain, and N. Singh. Phonon-induced superconductivity and physical properties in intercalated fullerides Rb_3C_{60}. *Journal of Theoretical and Applied Physics*, pages 1–23, 2012.

[225] E. Brandt. Precision Ginzburg-Landau Solution of Ideal Vortex Lattices for Any Induction and Symmetry. *Physical Review Letters*, 78(11):2208–2211, 1997.

[226] A. Potočnik, A. Krajnc, P. Jeglič, Y. Takabayashi, A. Y. Ganin, K. Prassides, M. J. Rosseinsky, and D. Arčon. Size and symmetry of the superconducting gap in the FCC Cs_3C_{60} polymorph close to the metal-Mott insulator boundary. *Scientific reports*, 4:4265, 2014.

[227] M. Zehetmayer, M. Eisterer, J. Jun, S.M. Kazakov, J. Karpinski, a. Wisniewski, and H.W. Weber. Anisotropy in superconducting MgB_2: a comparison of SQUID and torque measurements. *Physica C*, 408-410:111–113, 2004.

[228] T. Ekino, T. Takasaki, T. Muranaka, J. Akimitsu, and H. Fujii. Tunneling spectroscopy of the superconducting gap in MgB_2. *Physical Review B*, 67(9):094504, 2003.

[229] T. Takasaki, T. Ekino, and T. Muranaka. Superconducting gap in polycrystalline MgB_2 studied by electron tunneling. *Physica C*, 378-381:229–233, 2002.

[230] D. Kasinathan, K. W. Lee, and W. E. Pickett. On heavy carbon doping of MgB_2. *Physica C*, 424(3-4):116–124, 2005.